

**DEVELOPMENT OF CONJUGATED COPOLYMERS FOR
CARBON NANOTUBE-BASED SOLAR CELLS**

by

Thomas Meredith Kraft

A thesis submitted to the Department of Chemistry

In conformity with the requirements for

the degree of Master of Science

Queen's University

Kingston, Ontario, Canada

(February, 2011)

Copyright ©Thomas Meredith Kraft, 2011

Abstract

The investigation carried out in this project allowed for the development of eleven regioregular π -conjugated alternating copolymers and their implementation in organic solar cells. The eleven synthesized polymers, poly[(2,7-(9-(heptadecan-9-yl)-9H-carbazole))-alt-(4,7-dithien-2-yl-2,1,3-benzothiadiazole)] (**CB**), poly[(2,7-(9,9-dioctyl-9H-fluorene-2,7-diyl))-alt-(1,6-pyrene)] (**LP**), poly[(2,7-(9-(heptadecan-9-yl)-9H-carbazole))-alt-(5,5''-(3,3''-dihexyl-2,2':5',2":5",2'''-quarterthiophene))] (**CT**), poly[(2,7-(9-(heptadecan-9-yl)-9H-carbazole))-alt-(2,7-9H-fluoren-9-one)] (**CF**), poly[(2,7-(9-(heptadecan-9-yl)-9H-carbazole))-alt-(1,6-pyrene)] (**CP**), poly[(2,7-(9,9-dioctyl-9H-fluorene-2,7-diyl))-alt-(4,7-dithien-2-yl-2,1,3-benzothiadiazole)] (**LB**), poly[(2,7-(9,9-dioctyl-9H-fluorene-2,7-diyl))-alt-(2,7-9H-fluoren-9-one)] (**LF**), poly[(5,5''-(3,3''-dihexyl-2,2':5',2":5",2'''-quarterthiophene))-alt-(2,7-9H-fluoren-9-one)] (**TF**), poly[(2,7-(9,9-dioctyl-9H-fluorene-2,7-diyl))-alt-(4,4'-dioctyl-2,2'-bithiophene)] (**oTLT**), poly[(2,7-(9-(heptadecan-9-yl)-9H-carbazole))-alt-(4,4'-dioctyl-2,2'-bithiophene)] (**oTCT**), poly[(2,7-(9-(heptadecan-9-yl)-9H-carbazole))-alt-(4,4'-dihexyl-2,2'-bithiophene)] (**TCT**), were investigated using theoretical methods that included semi-empirical geometry optimizations, density functional theory (DFT) energy calculations, and time-dependent density functional theory (TD-DFT) optical absorption predictions. The absorption predictions gave credence to our experimental results in which the absorption of the longer polymer chains underwent a redshift from the monomer absorption.

With several of the prepared polymers, bulk-heterojunction photovoltaic cells were fabricated and their photovoltaic activity was investigated. Several of the fabricated cells exhibited photovoltaic efficiencies including polymer/PCBM composites with an aluminum back electrode (CF, CT, P3HT, and MEH-PPV), and also inverted cells with a silver back electrode

(CT, P3HT, and MEH-PPV). Several polymers (CF, CT, TCT, LP, oTCT, oTLT, P3HT, and MEH-PPV) were used to solubilize single-walled carbon nanotubes (SWNTs). The solubility of the nanotubes occurred by the polymers' ability to wrap the tubes, disrupt the bundles (ropes of tubes), and allow for the creation of a homogeneous mixture. Polymer:PCBM:SWNT mixtures were prepared and utilized as the active layer in BHJ solar cells. Some of the inverted cells (with a silver back electrode) that incorporated the nanotube composites (CT, oTCT, oTLT, P3HT, and MEH-PPV) displayed photovoltaic activity. These preliminary results illuminate the photovoltaic behavior of the polymer and provide evidence for their future use in polymer solar cells.

Acknowledgements

Over the past two years I have been conducting my studies at Queen's University to complete my M.Sc. in chemistry. This enlightening journey has opened my eyes to the vast applications of organic photovoltaics. Specifically, my exposure to the chemistry involved in polymer solar cells has provided me with remarkable insight into this growing scientific field. This experience would not have been possible without the support of my supervisors (Drs. Nunzi and Buncel). I would like to thank Dr. Jean-Michel Nunzi for providing me with his expertise in the field of organic photovoltaics and Dr. Erwin Buncel for his wisdom and guidance throughout the project. The successful completion of my thesis would not have been possible without their support. I would also like to thank Dr. Gregory Jerkiewicz and Dr. Suning Wang for being on my thesis committee.

My project began with help from Dr. Gabriela Aldea, whose collaboration will always be remembered. The theoretical calculations would not have been possible without the assistance of Dr. Nick Mosey. I am thankful for all my group members and lab mates (Feng Liu, Konrad Piskorz, Nicole Day, Matthew Schuster, and Ian Rupar) who were always there to talk with. I would especially like to thank Feng Liu for his help with electrode deposition and solar cell characterization. I extend gratitude to all those who assisted me with various instrumentation including Dr. Jiayi Wang (mass spectroscopy), Mr. David McLoed (MALDI), Dr. François Sauriol (NMR), Dr. Guojun Liu (GPC), Yang Gao (GPC), and Xiaoyu Li (GPC).

Throughout my time as a graduate student I have been endlessly supported by my family. I would specifically like to thank my mom (Deborah) for her eternal love and support, my dad (Jouni) who has inspired me, my grandpa (MO) who always gives me good advice, and my lovely fiancée (Ingrid) whose motivation, love, and support is unwavering.

Table of Contents

Abstract.....	ii
Acknowledgements.....	iv
Chapter 1 Introduction.....	1
1.1 Solar Cells.....	1
1.1.1 A Historical Context of Solar Cells.....	1
1.1.2 General Introduction to Solar Cells.....	1
1.1.3 Current solar cell technologies.....	4
1.1.4 Organic Photovoltaics.....	6
1.1.5 Solar Cell Characterization.....	11
1.2 Conjugated Polymers.....	12
1.2.1 Historical Context of Conjugated Polymers.....	12
1.2.2 Introduction to Conjugated Polymers.....	13
1.2.3 Synthesis of Conjugated Polymers.....	15
1.2.4 Electronic Applications of Conjugated Polymers.....	19
1.3 Carbon Nanotubes.....	22
1.3.1 A brief history of carbon nanotubes (CNTs).....	22
1.3.2 Properties of single-walled carbon nanotubes.....	23
1.3.3 Properties of multi-walled carbon nanotubes.....	25
1.3.4 Synthetic Methods.....	26
1.4 Modification of Carbon Nanotubes.....	28
1.4.1 Functionalization of Carbon Nanotubes.....	28
Covalent Functionalization.....	28
Non-Covalent Functionalization.....	30
1.4.2 Polymer/CNT Composites.....	31
1.4.3 Polymer/Carbon Nanotube Composites for Photovoltaic Cells.....	32
Chapter 2 Project Objectives.....	36
Chapter 3 Experimental.....	38
3.1 Theoretical Calculations.....	38
3.2 Materials.....	40

3.3 Instruments.....	41
3.4 Solar Cell Fabrication Methods	42
3.4.1 Etching of indium tin oxide (ITO) layer	42
3.4.2 Preparation of polymer composites for BHJ active layer	43
3.4.2.1 Polymer and PCBM solutions.....	43
3.4.2.2 Polymer, PCBM, and CNT solutions.....	43
3.4.3 Solar Cell Fabrication	44
3.4.3.1 Aluminum Electrode	44
3.4.3.2 Silver Electrode – Inverted Cell.....	45
3.5 Synthetic Methods	46
3.5.1 Synthesis of 3,3''-dihexyl-2,2':5',2'':5'',2'''-quarterthiophene	46
3.5.2 Synthesis of 5,5''-dibromo-3,3''-dihexyl-2,2':5',2'':5'',2'''-quarterthiophene.....	48
3.5.3 Synthesis of 2,7-dibromophenanthrene-9,10-dione	49
3.5.4 Synthesis of (3,3'''-dihexyl-[2,2':5',2'':5'',2'''-quarterthiophene]-5,5'''-diyl)bis(tributylstannane).....	50
3.5.5 Synthesis of 2,2'-(3,3'''-dihexyl-[2,2':5',2'':5'',2'''-quarterthiophene]-5,5'''-diyl)bis(4,4,5,5-tetramethyl-1,3,2-dioxaborolane).....	51
3.5.6 Synthesis of 1,6-bis(3-hexylthiophen-2-yl)pyrene.....	53
3.5.7 Synthesis of 2,7-bis(3-hexylthiophen-2-yl)phenanthrene-9,10-dione	54
3.5.8 Synthesis of 2,7-bis(3-hexylthiophen-2-yl)-9H-fluoren-9-one	55
3.5.9 Synthesis of 9-(heptadecan-9-yl)-2,7-bis(3-hexylthiophen-2-yl)-9H-carbazole.....	57
3.5.10 Synthesis of 9-(heptadecan-9-yl)-2,7-bis(3-octylthiophen-2-yl)-9H-carbazole	58
3.5.11 Synthesis of 2,2'-(9,9-dioctyl-9H-fluorene-2,7-diyl)bis(3-octylthiophene).....	59
3.5.12 Synthesis of poly[(2,7-(9-(heptadecan-9-yl)-9H-carbazole))-alt-(4,4'-dihexyl-2,2'-bithiophene)] (TCT).....	61
3.5.13 Synthesis of poly[(2,7-(9-(heptadecan-9-yl)-9H-carbazole))-alt-(4,4'-dioctyl-2,2'-bithiophene)] (oTCT).....	62
3.5.14 Synthesis of poly[(2,7-(9,9-dioctyl-9H-fluorene-2,7-diyl))-alt-(4,4'-dioctyl-2,2'-bithiophene)] (oTLT).....	63
3.5.15 Synthesis of poly[(5,5''-(3,3''-dihexyl-2,2':5',2'':5'',2'''-quarterthiophene))-alt-(2,7-9H-fluoren-9-one)] (TF)	64

3.5.16 Synthesis of poly[(5,5''-(3,3''-dihexyl-2,2':5',2'':5'',2'''-quarterthiophene))-alt-(2,7-9H-fluoren-9-one)] (TF)	65
3.5.17 Synthesis of poly[(2,7-(9,9-dioctyl-9H-fluorene-2,7-diyl))-alt-(2,7-9H-fluoren-9-one)] (LF).....	66
3.5.18 Synthesis of poly[(2,7-(9,9-dioctyl-9H-fluorene-2,7-diyl))-alt-(4,7-dithien-2-yl-2,1,3-benzothiadiazole)] (LB)	67
3.5.19 Synthesis of poly[(2,7-(9-(heptadecan-9-yl)-9H-carbazole))-alt-(1,6-pyrene)] (CP) .	69
3.5.20 Synthesis of poly[(2,7-(9-(heptadecan-9-yl)-9H-carbazole))-alt-(2,7-9H-fluoren-9-one)] (CF)	70
3.5.21 Synthesis of poly[(2,7-(9-(heptadecan-9-yl)-9H-carbazole))-alt-(5,5''-(3,3''-dihexyl-2,2':5',2'':5'',2'''-quarterthiophene))] (CT)	72
3.5.22 Synthesis of poly[(2,7-(9,9-dioctyl-9H-fluorene-2,7-diyl))-alt-(1,6-pyrene)] (LP)....	73
3.5.23 Synthesis of poly[(2,7-(9-(heptadecan-9-yl)-9H-carbazole))-alt-(4,7-dithien-2-yl-2,1,3-benzothiadiazole)] (CB)	75
Chapter 4 Results and Discussion.....	77
4.1 Theoretical Study	77
4.1.1 Oligomer Band Gaps.....	77
4.1.2 Optical Absorptions	85
4.1.3 Calculation Cost.....	86
4.1.4 Fragment Interactions	87
4.2 Polymer Synthesis.....	90
4.2.1 Synthetic Process	90
4.2.2 Absorption and Emission Spectra	94
4.2.3 MALDI analysis.....	97
4.2.4 GPC results	99
4.3 Solar Cells.....	101
4.3.1 Fabrication without SWCNTs.....	101
4.3.2 Fabrication with SWCNTs.....	103
Chapter 5 Conclusions and Future Work.....	106
5.1 Conclusions.....	106
5.2 Future Work.....	107

References.....	108
Appendix A Supplementary Data	114
HOMO and LUMO energy levels of oligomers determined theoretically using DFT calculations (6-31G (d)).....	114
UV-Visible absorption spectra (theoretical and experimental) and fluorescence of polymers	120
Theoretical optical absorption of polymers not synthesized.....	129
GPC Results	131
¹ H NMR Spectra of Polymers.....	145
MALDI-TOF results for selected polymers.....	151
Solar Cells.....	157
Aluminum electrode.....	157
Silver Electrode.....	170
Silver Electrode – Variation in Intensity.....	186

List of Figures

Figure 1.1: Comparison of current solar cell efficiencies achieved in the laboratory	2
Figure 1.2: Summary of semiconductors	3
Figure 1.3: The average solar spectrum at the surface of the earth with semiconductor band gaps indicated.....	5
Figure 1.4: Flexible solar cells produced by Konarka	7
Figure 1.5: Interpenetrating network of donor and acceptor active layer in BHJ cell (left) and general polymer solar cell composition (right).....	8
Figure 1.6: Optimized geometry (Semi-empirical Austin Model 1) of [C ₆₀]PCBM.....	8
Figure 1.7: Photo-induced charge transfer within BHJ solar cell.	9
Figure 1.8: Structure of BHJ solar cell with Al back electrode	9
Figure 1.9: Reverse BHJ solar cell with high work function back electrode (Ag)	11
Figure 1.10: Current versus voltage curve for a photovoltaic cell.....	11
Figure 1.11: A semi-conducting diblock copolymer (PPV:PS derivative).....	16
Figure 1.12: Suzuki cross-coupling reaction scheme.....	18
Figure 1.13: Structure of MEH-PPV	20
Figure 1.14: PEDOT with anion PSS (commonly used as a water suspension).....	21
Figure 1.15: Description of carbon nanotube formation.....	24
Figure 1.16: Armchair and zigzag single-walled carbon nanotube morphologies.....	24
Figure 1.17: An AFM image of two SWCNTs connected in sequence	29
Figure 3.1: ITO (gray) mask.	42
Figure 3.2: Bulk-heterojunction polymer solar cell with aluminum back electrode.....	44
Figure 3.3: Inverted bulk-heterojunction polymer solar cell with silver back electrode.	45
Figure 3.4: 3,3''''-dihexyl-2,2':5',2":5",2'''-quarterthiophene.	46
Figure 3.5: Reaction scheme for the synthesis of 3,3''''-dihexyl-2,2':5',2":5",2'''-quarterthiophene.	47
Figure 3.6: 5,5''''-dibromo-3,3''''-dihexyl-2,2':5',2":5",2'''-quarterthiophene.....	48
Figure 3.7: Reaction Scheme for the synthesis of 5,5''''-dibromo-3,3''''-dihexyl-2,2':5',2":5",2'''-quarterthiophene.....	48
Figure 3.8: 2,7-dibromophenanthrene-9,10-dione.	49

Figure 3.9: Reaction scheme for the synthesis of 2,7-dibromophenanthrene-9,10-dione.....	49
Figure 3.10: (3,3'''-dihexyl-[2,2':5',2'':5'',2'''-quaterthiophene]-5,5'''-diyl)bis(tributylstannane)	50
Figure 3.11: Reaction scheme for the synthesis of (3,3'''-dihexyl-[2,2':5',2'':5'',2'''-quaterthiophene]-5,5'''-diyl)bis(tributylstannane).	50
Figure 3.12: 2,2'-(3,3'''-dihexyl-[2,2':5',2'':5'',2'''-quaterthiophene]-5,5'''-diyl)bis(4,4,5,5-tetramethyl-1,3,2-dioxaborolane).	51
Figure 3.13: Reaction scheme for the synthesis of 2,2'-(3,3'''-dihexyl-[2,2':5',2'':5'',2'''-quaterthiophene]-5,5'''-diyl)bis(4,4,5,5-tetramethyl-1,3,2-dioxaborolane).	52
Figure 3.14: 1,6-bis(3-hexylthiophen-2-yl)pyrene.....	53
Figure 3.15: Reaction scheme for the synthesis of 1,6-bis(3-hexylthiophen-2-yl)pyrene.	53
Figure 3.16: 2,7-bis(3-hexylthiophen-2-yl)phenanthrene-9,10-dione.	54
Figure 3.17: Reaction scheme for the synthesis of 2,7-bis(3-hexylthiophen-2-yl)phenanthrene-9,10-dione.	54
Figure 3.18: 2,7-bis(3-hexylthiophen-2-yl)-9H-fluoren-9-one.	55
Figure 3.19: Reaction scheme for the synthesis of 2,7-bis(3-hexylthiophen-2-yl)-9H-fluoren-9-one.....	56
Figure 3.20: 9-(heptadecan-9-yl)-2,7-bis(3-hexylthiophen-2-yl)-9H-carbazole.....	57
Figure 3.21: Reaction scheme for the synthesis of 9-(heptadecan-9-yl)-2,7-bis(3-hexylthiophen-2-yl)-9H-carbazole.	57
Figure 3.22: 9-(heptadecan-9-yl)-2,7-bis(3-octylthiophen-2-yl)-9H-carbazole.....	58
Figure 3.23: 9-(heptadecan-9-yl)-2,7-bis(3-octylthiophen-2-yl)-9H-carbazole.....	58
Figure 3.24: 2,2'-(9,9-dioctyl-9H-fluorene-2,7-diyl)bis(3-octylthiophene).	59
Figure 3.25: Reaction scheme for the synthesis of 2,2'-(9,9-dioctyl-9H-fluorene-2,7-diyl)bis(3-octylthiophene).	59
Figure 3.26: poly[(2,7-(9-(heptadecan-9-yl)-9H-carbazole))-alt-(4,4'-dihexyl-2,2'-bithiophene)].	61
Figure 3.27: Reaction scheme for the synthesis of poly[(2,7-(9-(heptadecan-9-yl)-9H-carbazole))-alt-(4,4'-dihexyl-2,2'-bithiophene)].	61
Figure 3.28: poly[(2,7-(9-(heptadecan-9-yl)-9H-carbazole))-alt-(4,4'-dioctyl-2,2'-bithiophene)].	62
Figure 3.29: Reaction scheme for the synthesis of poly[(2,7-(9-(heptadecan-9-yl)-9H-carbazole))-alt-(4,4'-dioctyl-2,2'-bithiophene)].	62

Figure 3.30: poly[(2,7-(9,9-dioctyl-9H-fluorene-2,7-diyl))-alt-(4,4'-dioctyl-2,2'-bithiophene)]... 63	63
Figure 3.31: Reaction scheme for the synthesis of poly[(2,7-(9,9-dioctyl-9H-fluorene-2,7-diyl))-alt-(4,4'-dioctyl-2,2'-bithiophene)]..... 63	63
Figure 3.32: poly[(5,5''''-(3,3''''-dihexyl-2,2':5',2'':5'',2'''-quarterthiophene))-alt-(2,7-9H-fluorene-9-one)]..... 64	64
Figure 3.33: Reaction scheme for the synthesis of poly[(5,5''''-(3,3''''-dihexyl-2,2':5',2'':5'',2'''-quarterthiophene))-alt-(2,7-9H-fluorene-9-one)]..... 64	64
Figure 3.34: poly[(5,5''''-(3,3''''-dihexyl-2,2':5',2'':5'',2'''-quarterthiophene))-alt-(2,7-9H-fluorene-9-one)]..... 65	65
Figure 3.35: Reaction scheme for the synthesis of poly[(5,5''''-(3,3''''-dihexyl-2,2':5',2'':5'',2'''-quarterthiophene))-alt-(2,7-9H-fluorene-9-one)]..... 65	65
Figure 3.36: poly[(2,7-(9,9-dioctyl-9H-fluorene-2,7-diyl))-alt-(2,7-9H-fluorene-9-one)]..... 66	66
Figure 3.37: Reaction scheme for the synthesis of poly[(2,7-(9,9-dioctyl-9H-fluorene-2,7-diyl))-alt-(2,7-9H-fluorene-9-one)]..... 66	66
Figure 3.38: poly[(2,7-(9,9-dioctyl-9H-fluorene-2,7-diyl))-alt-(4,7-dithien-2-yl-2,1,3-benzothiadiazole)]..... 67	67
Figure 3.39: Reaction scheme for the synthesis of poly[(2,7-(9,9-dioctyl-9H-fluorene-2,7-diyl))-alt-(4,7-dithien-2-yl-2,1,3-benzothiadiazole)]. 68	68
Figure 3.40: poly[(2,7-(9-(heptadecan-9-yl)-9H-carbazole))-alt-(1,6-pyrene)]..... 69	69
Figure 3.41: Reaction scheme for the synthesis of poly[(2,7-(9-(heptadecan-9-yl)-9H-carbazole))-alt-(1,6-pyrene)]. 69	69
Figure 3.42: poly[(2,7-(9-(heptadecan-9-yl)-9H-carbazole))-alt-(2,7-9H-fluorene-9-one)]. 70	70
Figure 3.43: Reaction scheme for the synthesis of poly[(2,7-(9-(heptadecan-9-yl)-9H-carbazole))-alt-(2,7-9H-fluorene-9-one)]..... 71	71
Figure 3.44: poly[(2,7-(9-(heptadecan-9-yl)-9H-carbazole))-alt-(5,5''''-(3,3''''-dihexyl-2,2':5',2'':5'',2'''-quarterthiophene))] 72	72
Figure 3.45: Reaction scheme for the synthesis of poly[(2,7-(9-(heptadecan-9-yl)-9H-carbazole))-alt-(5,5''''-(3,3''''-dihexyl-2,2':5',2'':5'',2'''-quarterthiophene))]..... 72	72
Figure 3.46: poly[(2,7-(9,9-dioctyl-9H-fluorene-2,7-diyl))-alt-(1,6-pyrene)]. 73	73
Figure 3.47: Reaction scheme for the synthesis of poly[(2,7-(9,9-dioctyl-9H-fluorene-2,7-diyl))-alt-(1,6-pyrene)]. 74	74

Figure 3.48: poly[(2,7-(9-(heptadecan-9-yl)-9H-carbazole))-alt-(4,7-dithien-2-yl-2,1,3-benzothiadiazole)].....	75
Figure 3.49: Reaction scheme for the synthesis of poly[(2,7-(9-(heptadecan-9-yl)-9H-carbazole))-alt-(4,7-dithien-2-yl-2,1,3-benzothiadiazole)].	75
Figure 4.1: Band gap of oligomers as length (n) increases.	82
Figure 4.2: Calculated (DFT 6-31G (d)) HOMO and LUMO energy levels of the co-oligomers.	83
Figure 4.3: Conversion of absorption peaks to Gaussian functions.	85
Figure 4.4: Optimized geometry of three oTLT (n=3) oligomers.....	88
Figure 4.5: Armchair single-walled carbon nanotubes (n=1, 3, and 6) with semi-empirically (AM1) determined geometries.	89
Figure 4.6: CNT interaction with TP (quaterthiophene-pyrene co-oligomer)	89
Figure 4.7: Fluorescence of synthesized conjugated polymers.....	90
Figure 4.8: TCT monomer	91
Figure 4.9: Stille cross-coupling mechanism.....	93
Figure 4.10: Oxidative coupling radical mechanism	93
Figure 4.11: LP absorption comparison (theoretical and experimental).....	95
Figure 4.12: Structures of the LP monomer and oligomer (n=3).....	95
Figure 4.13: Absorbance and fluorescence comparison of CT.	96
Figure 4.14: Structure of the CT monomer.....	96
Figure 4.15: MALDI matrices (DHB and CHCA).	98
Figure 4.16: MALDI-TOF spectrum of the polymer TCT with a DHB matrix.....	99
Figure 4.17: P3HT:PCBM solar cell with Al back electrode.....	102
Figure 4.18: Non-functional CP:PCBM solar cell with Al back electrode.	102
Figure 4.19: Functioning CT:PCBM:CNT solar cell with silver electrode.	104
Figure 4.20: Short Circuit Solar Cell (CF:PCBM:CNT).	105

List of Tables

Table 4.1: Oligomers studied using theoretical calculations.	77
Table 4.2: Number of atoms within oligomeric units.	80
Table 4.3: Highest occupied molecular orbital (HOMO) and lowest unoccupied molecular orbital (LUMO) energies of the oligomers with six repeat units.	84
Table 4.4: Cost of TD-DFT energy calculations.....	86
Table 4.5: Polymerization reaction conditions	92
Table 4.6: Polymer band gaps (E_g) (determined by theoretical calculations and UV/Vis absorption spectroscopy) and their fluorescence emission (λ_{max}).	97
Table 4.7: GPC determined masses and polydispersity of the synthesized polymers.	100
Table 4.8: Parameters of BHJ solar cells (no SWNTs) with an aluminum back-electrode.	103
Table 4.9: Parameters of BHJ solar cells (no SWNTs) with a silver back-electrode.	103
Table 4.10: Parameters of BHJ solar cells with a silver back-electrode that contain SWNTs. ...	105

Chapter 1

Introduction

1.1 Solar Cells

1.1.1 A Historical Context of Solar Cells

1839 – Becquerel – Photovoltage produced by light interacting with an electrode in an electrolyte solution [1].

1877 – Adams and Day – Photovoltaic effect observed in selenium [1].

1914 – Solar cells composed of selenium and copper oxide reach efficiencies of about 1% [1].

1954 – Chapin, Fuller, and Pearson – Prepared a silicon junction cell with an efficiency of 6% [1].

1954 – Reynolds *et al.* – Created the first all-thin-film cell composed of a $\text{Cu}_x\text{S}/\text{CdS}$ junction which achieved an efficiency of 6% [1].

1956 – Jenny *et al.* – Produced a p-n homojunction GaAs cell with 4% efficiency [1].

1958 - Chapin, Fuller, and Pearson – Reached 14% efficiency with a silicon junction cell [1].

1980 – Bragnolo *et al.* – Prepared a $\text{Cu}_x\text{S}/\text{CdS}$ cell with 9% efficiency [1].

1988 – Verlinden *et al.* – Achieved 28% with a silicon junction solar cell [1].

1.1.2 General Introduction to Solar Cells

Solar cells have seen vast improvements since the notion of harvesting direct electrical energy from the sun was first discovered in the middle of the 19th century in France by Antoine César Becquerel. At present, there are numerous types of solar cells that include but are not limited to crystalline silicon cells, thin film technologies, multijunction concentrators, and organic photovoltaics (OPVs).

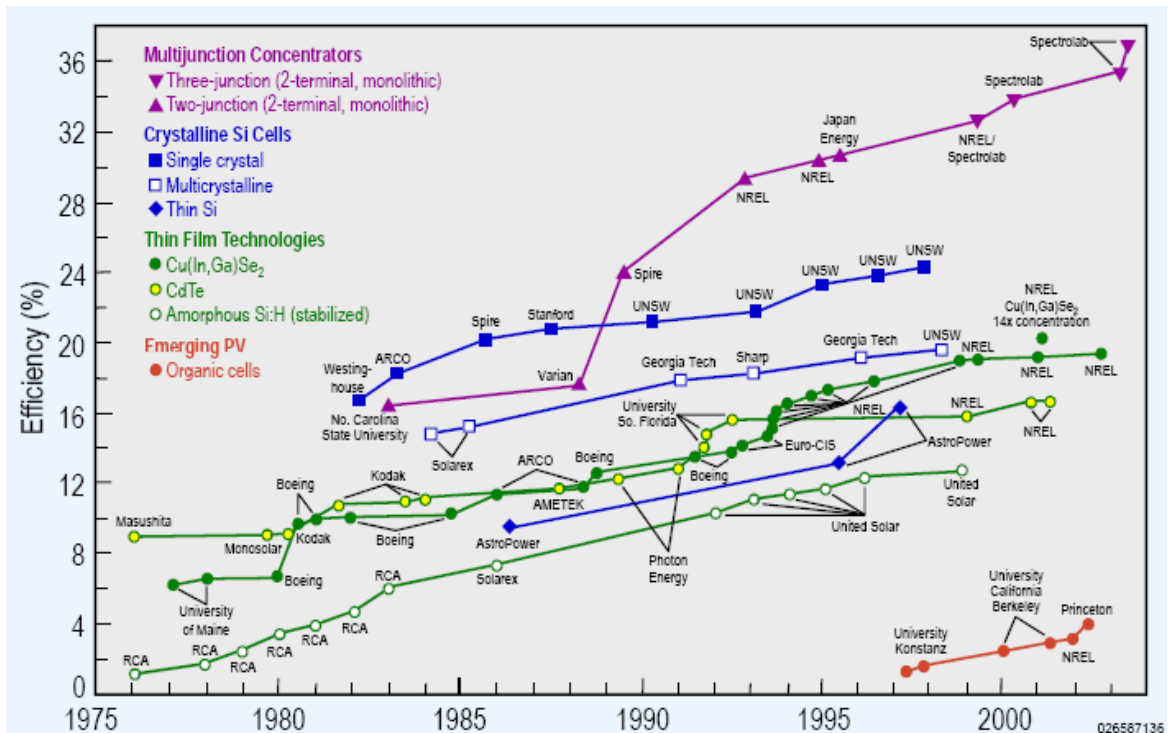


Figure 1.1: Comparison of current solar cell efficiencies achieved in the laboratory (National Renewable Energy Laboratory (USA))

Although the cell designs may vary, there is one component that they all have in common; the ability to convert photons into electricity. This phenomenon, in which light interacts with a solid semiconductor, is known as the photovoltaic effect.

Semiconductors can be defined loosely by either their energy gap (energy difference between the valence and conduction band energy levels, HOMO-LUMO band gap) or their resistivity. The energy gap of a semiconductor lies in the range of 0 eV - 4 eV and its resistivity (inverse of conductivity) is between $10^{-2} - 10^9 \Omega\text{cm}$ [2].

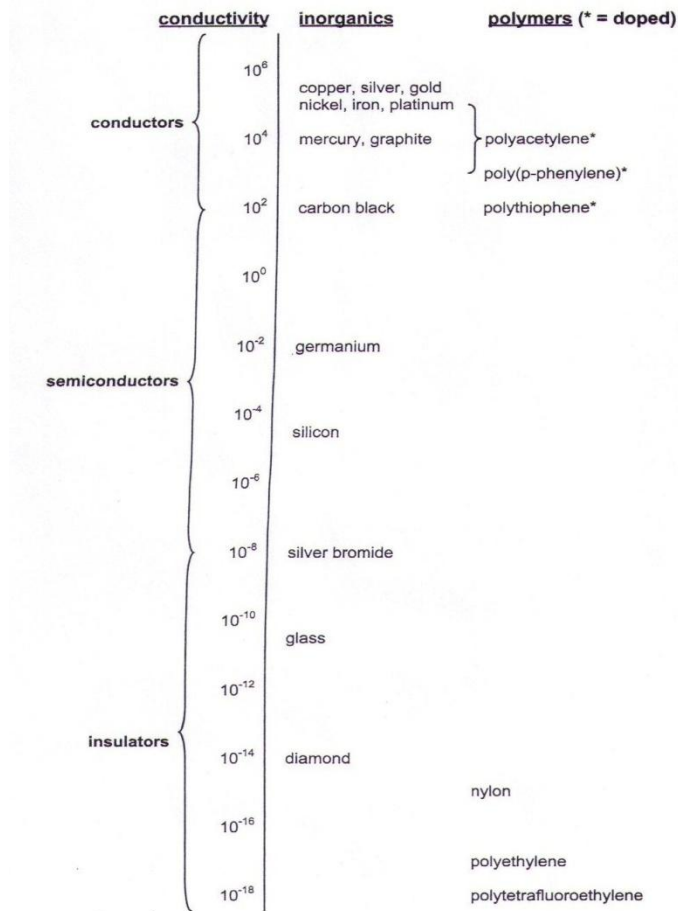


Figure 1.2: Summary of semiconductors [3]

The band gap energy of a semiconductor lies between that of a metal (0 eV band gap) and an insulator (band gap greater than 3 eV). The semiconductors electronic properties can be altered via doping to prepare either an n-type or p-type semiconductor. Essentially, an n-type semiconductor has a majority of free electrons, whereas the majority of free carriers in a p-type semiconductor are holes (a hole is what is left in the absence of an electron) [2]. Electrons in the semiconductor's conduction band and holes in its valence band are known as free carriers due to their ability to carry electrical current [2]. The electronic characteristic of the semiconducting

material within the solar cell is of paramount importance for the ability to convert sunlight into electricity (photovoltaic activity).

The photovoltaic effect describes the fundamental interaction of light with matter to produce electricity. Light with photon energy greater than the band gap is absorbed by a semiconductor material. Within the semiconductor, electrons and holes are formed by the optical excitation provided by light. It is necessary for an internal electric field to separate the electrons and holes so that they do not recombine within the semiconductor. The electric field, which exerts a force on electrically charged particles, is created when holes and electrons form a band opposite one another on either side of the junction. The holes (from the p-type region) form a band in a small area in the n-type region and the electrons (from the n-type region) in the p-type material. To generate electricity, the electrons and holes must pass out of the material into the external circuit via opposite electrodes [1]. This fundamental process in photovoltaic cells can occur through various mechanisms depending on cell type and morphology.

1.1.3 Current solar cell technologies

There are several different solar cell junctions (interfaces) in which holes and electrons are separated. These designs include the homojunction, heterojunction, heteroface junction (buried homojunction), metal-semiconductor junction (Schottky barrier), p-i-n junction, semiconductor-electrolyte junction, and the bulk-heterojunction (multiple junctions within the active layer). The most common cell morphologies are fabricated with crystalline silicon, amorphous silicon, gallium arsenide and other III-V materials, cadmium telluride and other II-VI materials, copper indium deselenide and other I-III-VI materials, and various organic compounds [1].

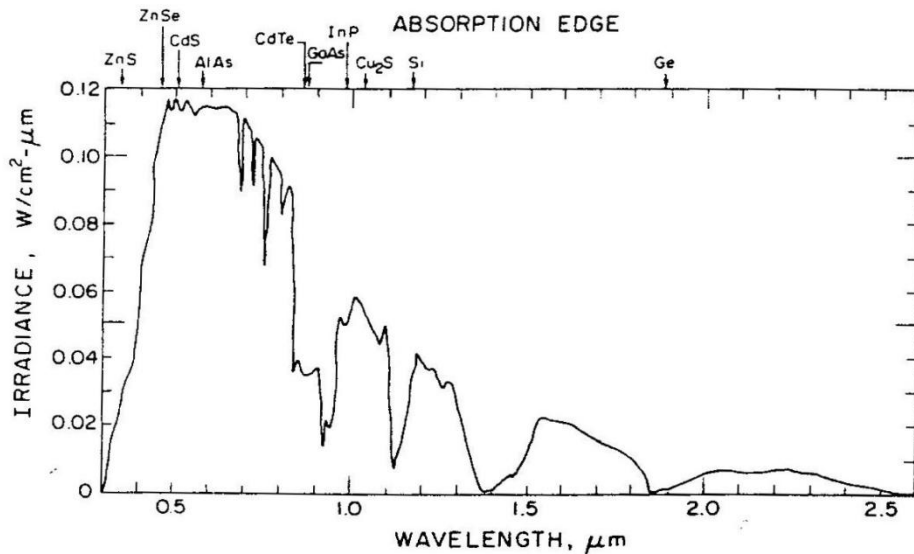


Figure 1.3: The average solar spectrum at the surface of the earth with semiconductor band gaps indicated [1].

The most common cells currently in production are composed of crystalline silicon. Silicon is non-toxic, stable, highly abundant in the earth's crust, and has dominated semiconductor applications for over 50 years. The Si p-n homojunction cell was the only solar cell widely available to consumers in the early 1980s. The homojunction cell contains one semiconductor material in which there are two fractions, doped either p-type or n-type [1]. Silicon is commonly doped with boron (acceptor impurity) to form a p-type semiconductor and phosphorous (donor impurity from PH_3) is the dopant used to prepare the n-type material. When light hits the silicon, photoexcitation creates free minority carrier electrons in the p-type portion and free minority carrier holes in the n-type portion. The free carriers diffuse toward the junction and pass over it, as long as they are not removed by recombination before arriving at the junction. The carriers are then collected by the junction's electric field and pass into the external circuit after they have traveled through the other region of the semiconductor. The p-n junction of the homojunction is similar to that of the p-n heterojunction, the major difference being that the

heterojunction is composed of two different semiconductor materials; one that is p-type and the other n-type. A common combination used in heterojunction cells is the n-type semiconductor CdS and the p-type CdTe. In 1976, the n-CdS/p-CdTe cell reached efficiencies of 6 – 7% by Bube and in 1993 Ferekides' group was able to produce an all thin-film n-CdS/p-CdTe cell that had a 15.8% efficiency. Although the efficiency of these types of cells is high, there are major drawbacks related to cost, fabrication, and health. Not only are the inorganic materials needed for the solar cells expensive but many heavy metals, like cadmium, are toxic. An alternative to the inorganic photovoltaics are organic solar cells.

1.1.4 Organic Photovoltaics

Organic photovoltaics are an emerging technology that uses organic compounds in order to decrease cost and increase ease of processing solar cells. These solar cells provide the promise of ultra-low cost, production via continuous printing process, and large area coverage (i.e. roof tops). Organic solar cells have the potential to be semitransparent, flexible and extremely light weight, which makes them an ideal candidate for personal use (i.e. incorporation into cell phones and clothing). The efficiencies of OPVs have seen great improvements throughout the last decade, from less than 1% to over 8%.



Figure 1.4: Flexible solar cells produced by Konarka

The most efficient and mature OPV is the dye-sensitized solar cell (DSSC) that uses an organic dye to absorb light and undergo a fast electron transfer to a nanostructure oxide (e.g. TiO_2). The largest disadvantage of the DSSCs is that hole transport is achieved by a liquid electrolyte. Another type of OPV that does not rely on a liquid electrolyte, and is more promising for large scale applications is the solid-state bulk-heterojunction device (BHJ), which is a polymer based solar cell.

Currently, Konarka holds the world record for preparing a polymer solar cell (PSC) with an overall efficiency of $8.3 \pm 0.3 \%$ (certified by the National Renewable Energy Laboratory in November 2010). The polymer OPV contains a bulk-heterojunction (BHJ) within the cell's active layer. An important characteristic within the BHJ is the photoinduced charge transfer phenomenon [4]. The BHJ active layer is composed of an interpenetrating network of a donor (conjugated polymer) and an acceptor (fullerene derivatives), sandwiched between two electrodes.

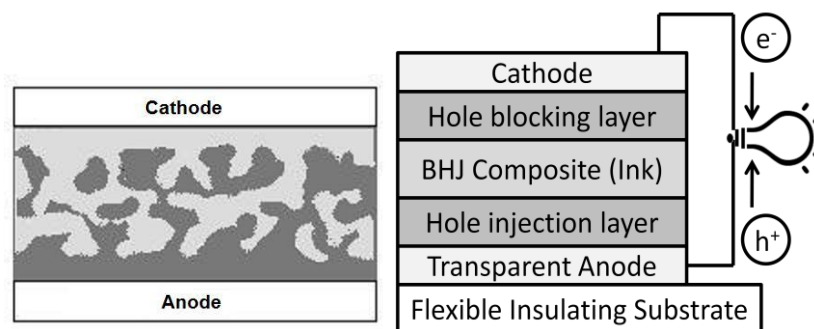


Figure 1.5: Interpenetrating network of donor and acceptor active layer in BHJ cell (left) and general polymer solar cell composition (right).

The most common buckminsterfullerene derivative is [6,6]-phenyl-C₆₁-butyric acid methyl ester ([C₆₀]PCBM or PCBM) which is miscible with conjugated polymers, a great electron acceptor, and has good electron mobility.

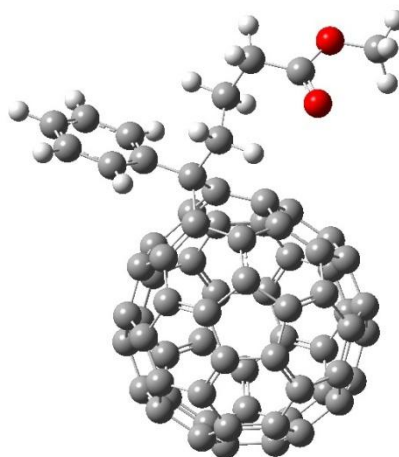


Figure 1.6: Optimized geometry (Semi-empirical Austin Model 1) of [C₆₀]PCBM

For the BHJ solar cell to function, photons pass through the transparent electrode (commonly an indium tin oxide thin-film) and are absorbed by the polymer. The energy stimulates a coulombically bound electron-hole pair, known as an exciton, from the highest occupied molecular orbital (HOMO) to the lowest unoccupied molecular orbital (LUMO).

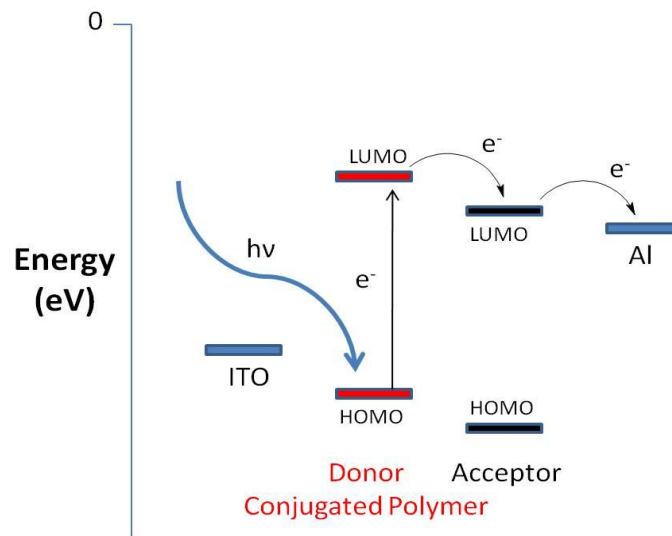


Figure 1.7: Photo-induced charge transfer within BHJ solar cell.

This is followed by exciton dissociation that occurs due to electron transfer from the LUMO of the donor to the LUMO of the acceptor. Charge transport of the hole (from the donor) to the anode and the electron (from the acceptor) to the cathode enables the hole and electron to enter the external circuit and create electricity [5].

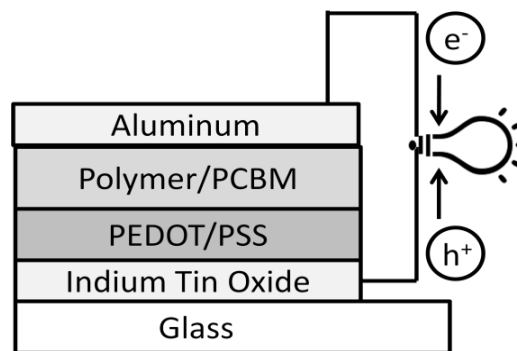


Figure 1.8: Structure of BHJ solar cell with Al back electrode

Most commonly charge extraction occurs using indium tin oxide (ITO), which has a high work function, as the positive electrode (anode) and aluminum, which is a metal with a low work

function, as the negative electrode (cathode). The positive electrode (e.g. ITO) extracts the positive holes from the active layer with the help of a hole transport layer (e.g. poly(3,4-ethylenedioxythiophene) poly(styrenesulfonate) (PEDOT:PSS)), while simultaneously the negative electrode (e.g. Al) extracts the electrons.

One of the most prominent concerns for polymer photovoltaics is their performance lifetime (longevity in air). Problems can arise from both excessive sunlight and also the use of a low work function back electrode (e.g. Al) that can be easily oxidised in the presence of oxygen [6]. Not only can sunlight alter the morphology of the layers within the cell but it can also induce interfacial degradation over the cells lifetime. Potentially, the cells can be made more durable by including polymers in the BHJ layer that are designed to have an increased T_g (glass transition temperature) or induce cross linking of the polymers. The oxidation of the electrode can be reduced by either encapsulating the low work function metal (e.g. capping with a less reactive metal) or by using a metal electrode that has a higher work function. When a high work function metal (e.g. Ag) is used the charge extraction within the cell must be inverted. This implies that the ITO will be used to extract electrons and that the silver back electrode will collect holes. To ensure that this process works efficiently, a hole blocking layer must be added between ITO and the BHJ layer to ensure only electrons reach the negative electrode (ITO). Sean Shaheen and coworkers deposited a zinc acetate film (via spin coating) and subsequently performed a thermal conversion to form a zinc oxide (ZnO) hole blocking layer [6]. On the silver electrode a silver oxide (Ag_xO) layer forms between the organic layer and the metal electrode. The silver oxide is a p-type semiconductor with a high work function that can effectively extract holes from the cell, whose efficiency can be further increased by the introduction of a hole transport layer (PEDOT:PSS) between the silver electrode and BHJ layer.

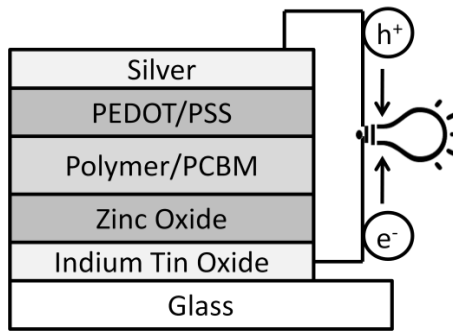


Figure 1.9: Reverse BHJ solar cell with high work function back electrode (Ag)

1.1.5 Solar Cell Characterization

The solar cell's performance can be characterized by several parameters (V_{oc} , I_{sc} , FF, and P_{max}) that can be used to calculate the cell's overall efficiency (power conversion efficiency, PCE) or external quantum efficiency (EQE) [7].

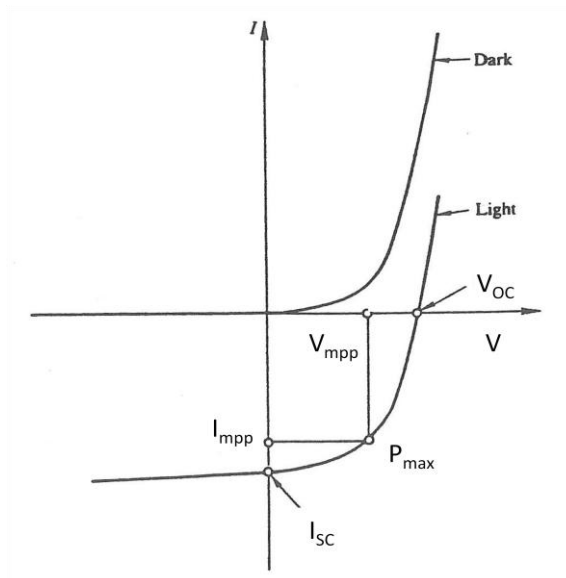


Figure 1.10: Current versus voltage curve for a photovoltaic cell [1]

The PCE provides the efficiency of the cell under illumination by the standard light source, AM 1.5. AM 1.5 is 100 mW cm^{-2} white light matching the spectral intensity distribution on the earth's

surface when it is tilted at an angle of 37°. EQE is the ratio of collected charge carriers (electrons) per incident photon at a specific wavelength.

$$\text{PCE} = (V_{\text{OC}} \times I_{\text{SC}} \times \text{FF}) / P_{\text{in}}$$

$$\text{EQE} = (1240 \times I_{\text{SC}}) / (\lambda \times P_{\text{in}})$$

V_{OC} - open-circuit voltage

I_{sc} - short-circuit current

$$\text{FF} = (I_{\text{mpp}} \times V_{\text{mpp}}) / (V_{\text{OC}} \times I_{\text{SC}})$$

P_{in} - incident light power

$$I_{\text{mpp}} \times V_{\text{mpp}} = P_{\text{max}} - \text{maximum power output of solar cell}$$

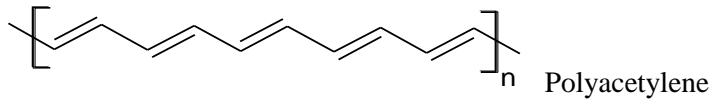
$$hc/e = 1240 \text{ W*nm/A} \text{ --- } (1\text{eV} = 1240 \text{ nm})$$

1.2 Conjugated Polymers

1.2.1 Historical Context of Conjugated Polymers

1906 – Pochettino – Discovered the photoconductivity of anthracene.

1968 – Berets and Smith – Investigated the electronic properties of linear polyacetylene (PA) [8].

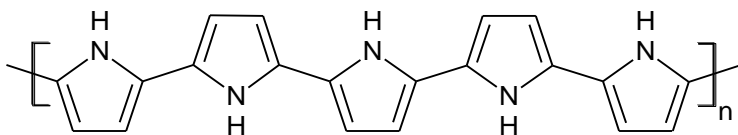


1977 – Heeger et al. – Explored the metallic conductivity of PA. The driving force of the research was to prepare conducting PA wires. The major drawback of PA is that it is difficult to process, due to its insolubility and its ease of oxidation which decreases conductivity [8].

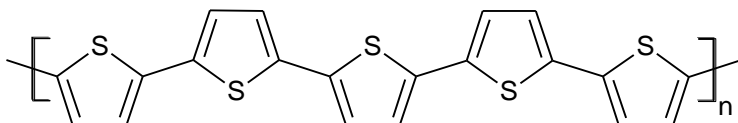
1980 – Narmaan – Produced highly conductive PA (σ approximately 100000 Scm^{-1}) [8].

1990's (early) – New polymers (and variations to control steric effects, electronic properties and solubility) were synthesized:

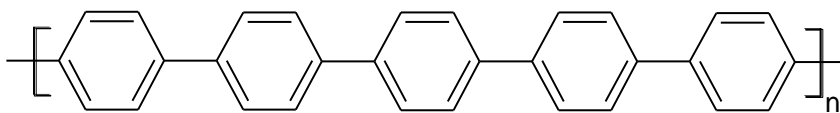
- Polypyrrole (PPy)



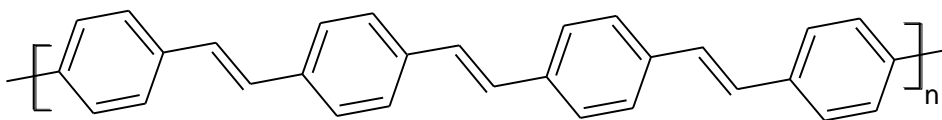
- Polythiophene (PT)



- Polyparaphenylene (PPP)



- Polyphenylenevinylene (PPV)



1990's – Groups began tailoring the electronic and physical properties of conjugated polymers by altering various aspects of the polymer [8].

- Monomer core
- Side chain lengths/steric hindrances
- Control of optical band gap

2000 – Heeger, MacDiarmid and Shirakawa – Awarded Nobel prize for work done on PA [8].

1.2.2 Introduction to Conjugated Polymers

The unique electronic properties of conjugated polymers allow them to be used for various electronic applications which include xerography, multi-element sensors, batteries, and

organic electronics. Organic electronics, also known as soft electronics, can be fabricated with conjugated polymers or small molecules to create field effect transistors (FET), organic light emitting diodes (OLED), and organic photovoltaic devices (OPV). Their use in such devices is enabled by the semiconducting electronic characteristic of the conjugated polymers.

Semiconducting polymers have an unsaturated carbon based backbone with alternating single and double bonds [4]. Each carbon atom has one electron in a p_z orbital that is not involved in the σ -bond. The p_z orbitals between adjacent carbon atoms overlap to create a π -system. These overlapping p_z orbitals form a delocalized π -electron cloud along the backbone of the polymer. The molecular energy levels of the π -band (HOMO) and the π^* -band (LUMO) provide a critical characteristic of the polymer. The energy difference between the HOMO and LUMO is known as the band gap, which is responsible for various characteristics including absorption, photoluminescence, and the photo-induced charge transfer (essential to the bulk-heterojunction (BHJ) solar cell).

The electronic transport properties of a conjugated polymer are affected by several intrinsic and extrinsic properties. Intrinsic molecular level properties include ionization potentials, electron affinity, coulomb correlations, and, as previously mentioned, the HOMO-LUMO π -bands. The HOMO-LUMO band gap energy can also be described as the energy difference between the valence band and the conduction band ($E_G = E_V - E_C$). The energy associated with the valence band is equivalent to the ionization potential (energy required to remove an electron from the highest occupied state to vacuum) and the energy of the conduction band is equivalent to the electron affinity (energy gained when an electron is added to the lowest unoccupied state from vacuum). Extrinsic properties that have an effect on a polymer's transport

properties include crystallinity, morphology, disorder, intermolecular interactions, and impurities [4]. These properties can be controlled by carefully engineering the polymer's structure.

1.2.3 Synthesis of Conjugated Polymers

When designing the π -conjugated polymer it is important to recognize the different synthetic methods. In 1958, Natta and coworkers were the first to synthesize polyacetylene by polymerizing acetylene [8]. This was accomplished by using $\text{Ti}(\text{OPr})_4$ and $\text{Al}(\text{Et})_3$, in which a Ti-C bond is formed on the growing polymer chain that allows for monomer insertion. The challenge presented by the insolubility of PA encouraged other polymerization techniques which include Ring Opening Metathesis Polymerization (ROMP) and the grafting approach. The approach using ROMP was developed by J. Feast in the early 1980's. He was able to prepare a soluble precursor of PA by using ROMP, in which the reaction was catalyzed by WCl_6 and the precursor was thermally treated to produce PA. Another method to prepare PA was by grafting PA onto a soluble polymer backbone. More complicated polymers can be prepared with more control by step-growth polymerization.

There are numerous methods of step-growth polymerizations that proceed through various mechanisms. The common methods are oxidative coupling with FeCl_3 , and cross-coupling reactions in the presence of a metal catalyst (e.g. Yamamoto, Suzuki, Stille, Negishi, Sonogashira coupling). The use of FeCl_3 is an efficient method of polymer preparation, although the mechanism only allows for the production of alternating copolymers if a symmetric monomer is used. The monomers used for the oxidative coupling method are relatively simple to prepare because it is not necessary to add reactive functional groups on the ends. The polymers formed by this synthetic method are in the doped state due to the conductive metal catalyst. It is imperative that the catalyst impurity be removed to avoid quenching of the polymer's photo- and

electroluminescence (PL and EL). To prepare more complex polymers such as block copolymers, the synthetic methods must be altered to achieve a well defined structure.

Block copolymers consist of two or more blocks of one polymeric unit successively attached (i.e. $A_nB_nC_n$). With two polymer units attached to one another (in a diblock copolymer), nanophase separation of the blocks in the solid state can occur due to unfavourable mixing enthalpy and small mixing entropy. Control of the solid state morphology can be obtained by varying the blocks within the diblock copolymer. The polymer's head/tail properties can be hydrophobic/hydrophilic, soft/hard, or semiconducting/insulating. Various semiconducting/insulating diblock copolymers have been synthesized, which include polyparaphenylene - polystyrene (PPP:PS), polyparaphenylene - polymethylmethacrylate (PPP:PMMA), polyphenylenevinylene - polystyrene (PPV:PS), poly(3-alkylthiophenes) - polymethylmethacrylate (PAT:PMMA), and poly(3-alkylthiophenes) - polystyrene (PAT:PS). PPP:PS and PPP:PMMA has been successfully prepared by François and coworkers via living anionic polymerization initiated with *sec*-BuLi [9]. Hadziioannou utilized polymerizations mediated by 2,2,6,6-tetramethyl-1-piperidinyloxy (TEMPO), which is a nitroxide free radical, to synthesize derivatives of the diblock copolymer PPV:PS [10].

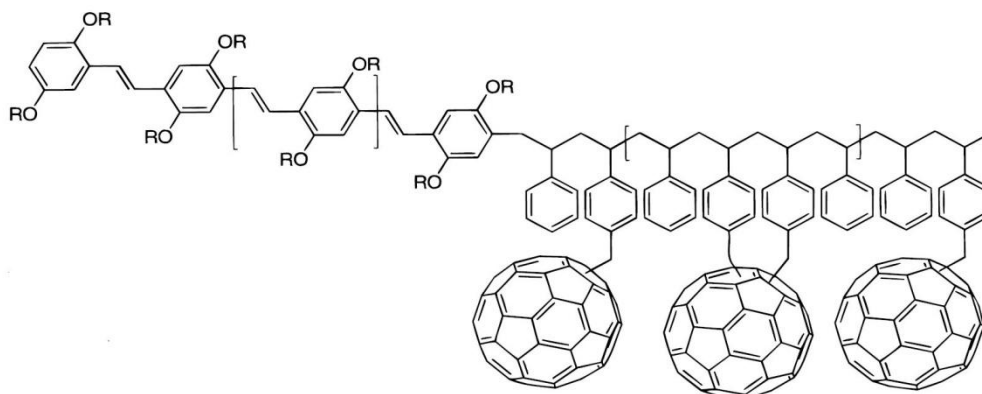


Figure 1.11: A semi-conducting diblock copolymer (PPV:PS derivative) [9].

The critical component of the preparation method was the synthesis of the macroinitiator, which involved coupling a PPV chain to a TEMPO-styrene unit. This TEMPO-styrene-PPV macroinitiator was subsequently used to polymerise the styrene moiety to prepare a well ordered PPV:PS polymer. TEMPO is a stable free radical that is used in the free radical polymerization process developed at the Xerox Research Centre of Canada by Georges, Kazmaier and coworkers [11]. Another approach that can be used to prepare diblock copolymers is atom transfer radical polymerization (ATRP). With ATRP a metal complex is needed for the homolytic and reversible cleavage of a carbon-halogen bond to produce a radical (on the growing polymer chain) that adds to the monomer. Liu and coworkers used ATRP to prepare PAT:PMMA and PAT:PS by attaching a PMMA or PS tail to a halogenated PAT unit [12]. Block copolymers, such as the ones aforementioned can provide polymers with interesting and valuable properties; however, alternating copolymers with well designed monomers are essential in providing fine control of the electronic and physical properties of the polymer.

Greater control of the polymer synthesis and subsequent structure is granted by metal catalyzed reactions used to couple monomers together in a controlled sequence. The monomer, A or B, must have the same reactive group on both ends (with A's reactive group different from B's). Yamamoto polymerization involves the use of a nickel catalyst (commonly $\text{NiCl}_2(\text{dppp})$), a disubstituted Grignard reagent (RMgX), and a dihalide. The major drawback of the Yamamoto synthesis is that the monomer with MgX at both ends cannot be purified due to the inherent reactivity of the Grignard reagent. Yamamoto polymerizations are most successful to prepare a polymer with one dihalogenated monomer. A more effective method to prepare well ordered alternating copolymers is via Suzuki coupling.

Suzuki cross-coupling reactions involve carbon-carbon bond formation between organoboron and organohalogen compounds in the presence of a Pd⁰ catalyst and a base.

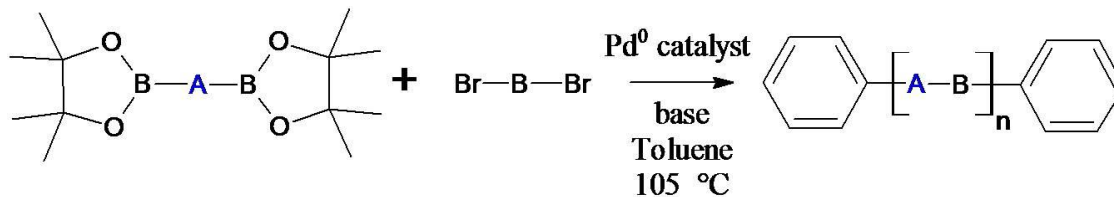


Figure 1.12: Suzuki cross-coupling reaction scheme

The reactions were first developed by Norio Miyaura and Akira Suzuki. For polymerization reactions, a dihalogenated monomer (with either Br or I at both ends) is reacted with a disubstituted boronic ester (or boronic acid) monomer. It is advantageous to prepare polymers via the Suzuki cross-coupling reaction because both reagents can be purified prior to the polymerization reaction. The disubstituted monomers' stability allows for their purification via flash column chromatography. The purity of the reactants in a polymerization reaction is critical in achieving polymers with a high molecular weight and low polydispersity. The presence of mono-substituted reactants will terminate the polymerization by end-capping the polymers which results in the formation of many oligomers. The benefit provided by the ability to purify the monomers is also seen when performing Stille cross-coupling polymerizations. The synthesis using Stille coupling involves the use of a disubstituted organostannane (similar to the Suzuki method's use of monomers that are disubstituted with boron derivatives) and a dihalide. Not only are the reactants similar but the same catalysts can be used for Stille and Suzuki cross-coupling reactions. Most Pd(0) catalysts will work, although Pd(PPh₃)₄ is most frequently used and is widely available.

1.2.4 Electronic Applications of Conjugated Polymers

Many electronic devices can be made with the synthesized conjugated polymers, which include a number of organic electronics. Three of the most common organic electronics that use conjugated polymers include field effect transistors (FET), light emitting diodes (LED), and photovoltaics (PV). These soft electronics capitalize on the thin, light-weight semiconducting materials that can be prepared with π -conjugated polymers.

The basic configuration of an organic field-effect transistor (OFET) consists of three electrodes; a source, drain, and gate. The gate electrode is separated from the semiconductor thin-film by an insulating layer. The OFET is considered a thin-film transistor (TFT) because it contains a thin-film deposit of an organic semiconductor layer on the neutral substrate (unlike the bulk solid found in inorganic FETs). Although, not all TFTs utilize organic semiconductors, they can also be prepared from hydrogenated amorphous silicon (a-Si:H) and polycrystalline silicon thin-films. Unlike inorganic field effect transistors, the OFET has no p-n junction at the source and drain. The electrodes are metals that can easily inject charge into the semiconductor which results in current enhancement in accumulation, unlike an inorganic FET in which this occurs in the inversion regime. Also, due to the low conductivity of the organic semiconductor and its thinness, there is low current at zero gate voltage [10]. The OFET's use of conjugated polymer films is useful in the miniaturization of electronics, which is similar to the improvement these polymers has provided to display technologies.

Organic light emitting diodes (OLED) have allowed for the production of ultra-low cost, energy efficient, colour flat panel displays. OLEDs can produce emissions of wavelengths from ultraviolet to near infrared with nearly 100% internal quantum efficiencies. The limits of OLEDs have not yet been reached, although OLEDs with luminous efficiencies of 60 lm/W and operating

lifetimes of 100 000 hours have already been produced. In 1990, the first practical polymer light emitting diodes (PLED) were fabricated with PPV by Richard Friend's group at Cambridge University, which started a trend in PLED research [13]. Polymers like PPV were modified with side chains to increase solubility and aided in the incorporation of the active layer in the LED [14]. The modified PPV polymer, poly[2-methoxy-5-(2-ethylhexyloxy)-1,4-phenylenevinylene] (MEH-PPV), has been widely studied and has become a popular polymer for PLED fabrication.

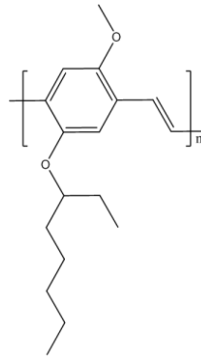


Figure 1.13: Structure of MEH-PPV

The simplest PLED can be fabricated with three layers (with forward bias): metal transparent anode (ITO) on a glass substrate, polymer film (~100 nm), metal cathode (Ca, Al, etc.). A layer can be added between the polymer film and both electrodes to either perform as a hole injection or hole blocking layer. Poly(3,4-diethyloxy)thiophene with polystyrenesulfonic acid as a counterion (PEDOT:PSS) is used as a hole injection layer between the anode and the polymer.

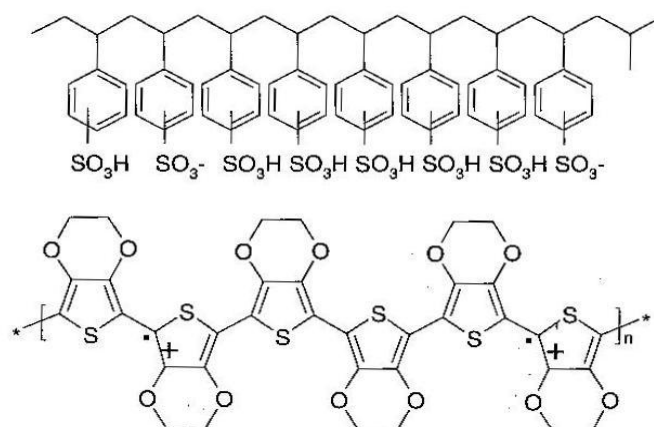


Figure 1.14: PEDOT with anion PSS (commonly used as a water suspension) [8].

Within the PLED, electrons are injected from the cathode and holes from the anode which results in recombination in the polymer which produces light. When choosing electrodes it is necessary to consider their work functions (energy required to remove an electron from the metal). High work function metals inject holes more efficiently than electrons, just as low work function metals inject electrons more efficiently than holes. To inject holes (remove electrons) the metal contact (anode) must be able to accept electrons from the polymer's E_V and to inject electrons the cathode must be able to donate electrons into the E_C . The energy barrier ($\Phi_{e(h)}$) associated with either the electron (e) or hole injection (h) is described by the Ideal Schottky model.

$$\Phi_{e(h)} = |E_{v(c)} - W|$$

This model illustrates how the energy barrier is related to the work function of the metal contact and either the conduction (for electron injection) or valence band (for hole injection) energy level. The electronic characteristics of the polymer based OLED in which a charge is applied, holes and electrons are injected in the polymer, and light is produced upon hole-electron recombination; opposite to what occurs in a polymer bulk-heterojunction solar cell. In the solar cell, the desire is

that the polymer absorbs light, electron-hole dissociation occurs, the charges are carried to opposite electrodes, and charge is created.

1.3 Carbon Nanotubes

1.3.1 A brief history of carbon nanotubes (CNTs)

1889 – Hughes and Chambers – Preparation of carbon filaments.

1896 – Edward Acheson – First to synthesize graphite.

1952 – Radushkevich *et al.* – Nanofilaments that exhibited an inner cavity were investigated by transmission electron microscopy (TEM). The filaments were prepared by the action of a catalyst on the gaseous species originating from the thermal decomposition of hydrocarbons.

1976 – Endo *et al.* – Prepared multi-walled carbon fibres via the decomposition of benzene. The structures were examined by high resolution electron microscopy which clearly showed that the fibres exhibited a hollow core with multiple concentric sheets arranged around the central axis [15].

1985 – Richard E. Smalley, Robert F. Curl, and Sir Harold W. Kroto – Discovered buckminsterfullerene (fullerene) for which they received the Nobel Prize in Chemistry (1996). This discovery was of great consequence for subsequent research of novel carbon architectures.

1991 – Sumio Iijima - Catalyst free formation of concentric multi-walled carbon nanotubes (c-MWNT) was reported. The c-MWNTs were by-products of fullerene synthesis via the electric-arc technique.

1993 – Iijima *et al.* and Bethune *et al.* – Discovered single-walled carbon nanotubes (SWNT) while attempting to fill MWNTs in situ with various metals.

2001 – Richard E. Smalley – Described carbon nanotubes as the “strongest, stiffest, toughest molecule ever produced, the best possible molecular conductor of both heat and electricity”. [16]

1.3.2 Properties of single-walled carbon nanotubes

A single-walled carbon nanotube (SWNT) is best described as a graphene sheet that has been rolled into a cylinder with half a fullerene sealing both ends. Graphene is a polyaromatic monoatomic layer consisting of sp^2 -hybridized carbon atoms arranged in hexagons (graphite is composed of multiple layers of graphene). The diameter of most SWNT is about 1.4 nm, although there have been reports of tubes synthesized with diameters as small as 0.4 nm (the tubular morphology is not favoured beyond 2.5 nm). The carbon nanotubes have very high aspect ratios (length/diameter) with lengths in the micrometer or millimetre range (200 nm – 10 μ m) [17]. The chemical reactivity of the nanotubes is more prevalent among the carbons at the tips. The increase in reactivity is because these carbons are arranged in six pentagonal rings, whereas all the other carbons within the tube are involved in hexagonal rings. Unlike planar graphene, whose carbon atoms are all sp^2 -hybridized, the sp^2 -hybridized carbons in the nanotubes have a small degree of sp^3 character due to the tubes radius of curvature. This tubular morphology provides the CNTs with unique electronic behaviour that can vary depending on how the graphene sheet is rolled into a tube.

The morphology of SWNTs can be divided into two broad categories; either chiral or achiral. A chiral carbon nanotube (just like any chiral molecule) cannot be superimposed on its own mirror image and is known as a helical nanotube. The cylindrical folding of the graphene sheet can be described by a vector (and the corresponding vector integers: n and m) and the angle of helicity (θ).

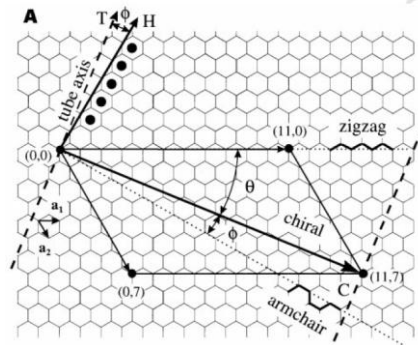


Figure 1.15: Description of carbon nanotube formation [18]

Chiral nanotubes can take various forms with an angle of helicity between 0° (zigzag type $(n,0)$) to 30° (armchair type (n,n)). Approximately 1/3 of produced single-walled carbon nanotubes have a metallic electronic characteristic, whereas 2/3 is semiconducting [19]. As a general rule, armchair (n,n) tubes are metals (band gap = 0), zigzag $(n,0)$ tubes are semiconducting, chiral (n,m) tubes with $n-m$ equivalent to an integer of 3 ($n-m = 3y$; $y = \text{non-zero integer}$) are small (tiny) gap semiconductors, and all other chiral tubes are large gap semiconductors [16].

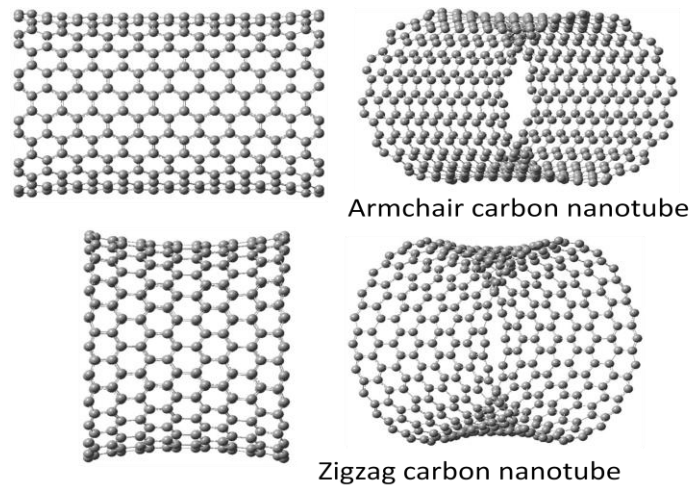


Figure 1.16: Armchair and zigzag single-walled carbon nanotube morphologies

However, the band gap energy of the semiconducting tubes is inversely proportional to the tube diameter. Therefore, armchair and about 1/3 of zigzag SWNTs should be metallic with the rest

being semiconducting [20]. Although SWNT can have unique electronic properties amongst themselves, there is a common attraction among all CNT. This attraction, van der Waals forces, is caused by the π -electrons that interact between adjacent nanotubes. The van der Waals forces cause the native state of the SWNT to be in ropes rather than separate tubes. Similarly, DWNT and MWNT can either become entangled with each other or exist as individual moieties [17]. The ropes (also known as bundles) of single-walled carbon nanotubes exhibit hexagonal arrangements and are rather difficult to disrupt due to the van der Waals forces which provide an intertube binding energy of approximately 900 meV/nm. The diameter of the ropes can range from 5-100 nm but normally exhibit a diameter close to 30 nm [17].

1.3.3 Properties of multi-walled carbon nanotubes

As the name suggests, multi-walled carbon nanotubes (MWNT) can have any number of walls upwards from two layers (double-walled carbon nanotube, DWNT). MWNT can acquire various morphologies during synthesis and commonly fall into two categories. The morphology of the tube is described as either a concentric multi-walled carbon nanotube (c-MWNT) or a herringbone multi-walled carbon nanotube (h-MWNT). c-MWNT's consist of any number of SWNTs coaxially arranged around one another with increasing diameter (one SWNT within a larger SWNT). The tubes have a metallic characteristic with the outer tube primarily involved in conduction. The intertube distance between nanotubes is approximately 0.34 nm, which is slightly larger than graphite's inter-graphene sheet distance of 0.335 nm. The increase in packing distance is caused by the curvature of the nanotubes, which does not allow for quite as neat packing. h-MWNT's have a herringbone texture caused by the graphene sheets making an angle with respect to the nanotube axis varying the inner diameter of the CNTs. This variation in the angle of the graphene sheets distorts the tubular arrangement of the nanotubes. The angle, which

determines the ultimate morphology of the MWNTs, is controlled by the synthetic conditions (i.e. catalyst morphology, composition of atmosphere). If the angle is 0° then a c-MWNT is formed, although if the angle is 90° the structure is no longer a tube. CNTs can be altered to carbon nanofibers when perpendicular graphene sheets (that make a 90° angle relative to the CNT axis) are incorporated by c-MWNT and h-MWNT. When this anomaly occurs, a bamboo structure is formed creating divided internal cavities within the tube.

1.3.4 Synthetic Methods

Single-walled carbon nanotubes can be prepared using various methods that include the use of solar energy, metal catalysts, dc electric arc, laser vaporisation (ablation), CO disproportionation, and three-phase ac arc plasma. MWNTs are commonly prepared using electric arc, CO disproportionation, or catalyst enhanced thermal cracking of gaseous hydrocarbons. All three methods can be used for the preparation of c-MWNT, whereas the latter two methods produce h-MWNT. The mechanism involving solar energy, dc electric arc, or laser vaporisation all involve energy transfer resulting from the interaction between either the target material and an external energy source (solar energy and laser vaporisation) or the electrode and the plasma (dc electric arc). This interaction causes target or anode erosion that leads to plasma formation (plasma is an electrically neutral ionized gas comprised of neutral atoms, charged particles and electrons). Subsequently, the vaporized (sublimed) material is swept away by an inert gas to collect as soot.

A successful method to prepare both MWNT and SWNT is catalytic chemical vapour deposition (CCVD). This synthetic method involves the catalysis-enhanced thermal cracking of a gaseous carbon source (i.e. hydrocarbons, CO). High purity SWNTs are produced using a variation of this process (developed at Rice University) that differs from other CCVD methods

because it only uses a gaseous carbon species and does not require a solid phase in the reactor. This floating catalyst technique, called the HiPco (high-pressure carbon monoxide) process, involves a gas phase catalytic reaction in which CO₂ (derived from Fe(CO)₅) is used to prepare the CNTs. In this reaction, heat is applied which causes Fe(CO)₅ to decompose and condense into larger clusters. The SWNTs nucleate and grow on these newly formed particles in the gas phase via CO disproportionation (also known as the Boudouard equilibrium ($2\text{CO} \rightleftharpoons \text{C} + \text{CO}_2$)).

Synthetic methods using CVD historically produced SWNT with diameters ranging from 0.4-5.0 nm, whereas the HiPco process produces nanotubes with a narrow diameter range. The production of tubes with a small diameter range is attributed to a rational catalyst design, deterministic single-nanoparticle formation, and the fine-tuning of growth conditions [17]. Unlike tube length the chirality of the tubes is much more difficult to control, although increased chiral selectivity in the bulk production of SWNTs is possible. Daniel Resasco and colleagues at the University of Oklahoma investigated a controlled production method for SWNT by the catalytic decomposition of CO on bimetallic Co-Mo catalysts [21]. This synthetic method uses a mesoporous silica support with CO as a feedstock gas and varying ratios of Co and Mo. This bulk supported catalyst became known as CoMoCAT which can produce SWNT samples that have only one or two types of semiconducting chiralities. About 50% of the tubes prepared by the CoMoCAT method have the (5,6) and (7,5) structures [22]. With the success of this preparation method the company Southwest Nano was created to commercially prepare SWNTs via CoMoCAT.

1.4 Modification of Carbon Nanotubes

1.4.1 Functionalization of Carbon Nanotubes

The physical and electrical properties of carbon nanotubes can be exploited through covalent bonding or non-covalent interactions (i.e van der Waals). These modifications can be performed to increase the tube's solubility in various solvents, for their incorporation in a matrix (polymer, ceramic, metal), or with proteins to enable the tubes to cross cell membranes [23]. Nucleic acids have also been used for both non-covalent and covalent functionalization of nanotubes. Ming Zheng and colleagues from DuPont, MIT and the University of Illinois at Urbana-Champaign were some of the first researchers to explore DNA wrapping of single-walled carbon nanotubes [24-26]. The interest in CNT functionalization has grown enormously in an effort to explore and utilize the unique electronic and physical properties of carbon nanotubes.

Covalent Functionalization

The tips and sidewalls of carbon nanotubes can be functionalized through covalent bonding, with the ends of the tubes being the most reactive. Acids (such as HNO_3 , $\text{HNO}_3 + \text{H}_2\text{SO}_4$, H_2SO_4 in conjunction with KMnO_4) that are often used for the purification and end opening of CNTs can also be oxidized to functionalize the tips and defects of tubes with carboxylic (-COOH) and alcohol (-OH) groups. Oxidation of the tubes surface can allow for their electrostatically stabilized colloidal dispersion in water and ethanol [17]. Further functionalization of the tubes with organic or inorganic materials can be achieved by reacting with the -OH and -COOH groups. Functionalization of the nanotube can serve to achieve enhanced solubility, self assembly, or even use as a chemical sensor.

There are numerous examples of nanotube functionalization, some workers attaching long aliphatic amines to tube ends and others attaching CNTs to each other forming macromolecules.

In 1998, Smalley and coworkers connected nanotubes together in sequence by attaching NH_2 - $(\text{CH}_2)_{11}$ -SH groups via an amide linkage to the tips of single-walled carbon nanotubes [27]. Subsequently gold particles were introduced to anchor the thiol chain ends which provided the link between the tubes.



Figure 1.17: An AFM image of two SWCNTs connected in sequence [27].

Not only is it possible to add functional groups to the tube ends, but sidewall functionalization can also be achieved.

When highly reactive reagents are used it is possible to covalently modify the tube walls. The reactivity of the tube's sidewall is increased as the diameter of the tube is decreased because the curvature increases. The sidewalls can be functionalized in many different ways which include fluorination, formation of carbenes and nitrenes, alkylation and arylation, 1,3-dipolar cycloaddition of azomethine ylides, solution phase ozonolysis, addition of radicals, silylation, electrochemical reactions, and attachment of polymers. Polymer grafting (involving the attachment of polymers) can be accomplished via amide linkages when the carboxyl group on the nanotube is reacted with an aminopolymer (i.e poly(propionylethylenimine-co-vinyl alcohol) (PPEI-EI). In a similar fashion highly soluble linear polymers can also be attached via ester linkages, which can be accomplished with poly(vinyl acetate-co-vinyl alcohol) (PVA-VA). This attachment of polymers can increase the solubility of the NT in many different solvents.

Polymers can also be grafted to improve the nanotube's bonding in CNT/polymer composites. Ajayan and collaborators treated SWNTs with sec-butyllithium to create an initiator for the anionic polymerization of styrene [28]. This resulted in polystyrene grafted SWNT prepared in a single-step.

Even though the covalent modifications of nanotubes (such as those previously mentioned) provide a means to incorporate these unique carbon structures into various applications, there is one major drawback. The downside is that covalent bond formation disrupts the native electronic structure of the tube.

Non-Covalent Functionalization

To modify carbon nanotubes, while retaining the original electronic structure, non-covalent functionalization can be used. Non-covalent modifications are particularly important when pursuing applications that exploit the unique electronic properties of CNTs. This electronically mild functionalization normally occurs via van der Waals forces between the tubes and surfactants, planar aromatics (such as pyrene), or by helical wrapping by polymers around the tube [20].

Surfactants (anionic, cationic, or non-ionic) and diblock copolymers (hydrophilic:hydrophobic) are often used to solubilize both multi-walled and single-walled carbon nanotubes in water [17]. A commonly used ionic surfactant is sodium dodecyl sulphate (SDS) which coats the tube, transfers charge to the NT surface and disperses the tubes in water by electrostatic forces. This dispersion can be performed by addition of 1% SDS to an aqueous suspension of CNTs followed by ultrasonication. Other surfactants used to solubilise CNTs include the use of triton-X-100 with sodium dodecyl benzene sulphonate (SDBS) and a

poly(acrylic acid)-CTAB (hexadecyltrimethylammonium bromide) complex to form a lamellar structure on the surface of MWNTs [29].

Small molecules have also been used to bind non-covalently to the surface of nanotubes. One of the first research groups to try this was that of Hongjie Dai in 2001. Dai's group used a pyrene derivative to form π - π interactions between the π -orbitals of the planar pyrene and those of the CNT sidewall [30]. Other groups have used various heterocyclic polyaromatic molecules, such as porphyrins and phthalocyanines to modify the tube surface through van der Waals interactions.

Another method to functionalize CNTs without covalent bonding is by polymer wrapping. Polymers are used to helically wrap around the nanotube surface to aid in the tubes possible application. In 2001, Smalley's group used polyvinyl pyrrolidone (PVP) and polystyrene sulphonate (PSS) to solubilise SWNTs [31]. This work was published in the same year as research performed by Fraser Stoddart and James Heath from UCLA in which polymer wrapping was performed with poly(*m*-phenylenevinylene) (PPV) with octyloxy side chains to achieve soluble nanotube complexes [32].

1.4.2 Polymer/CNT Composites

For over ten years research has been conducted to develop high performance functional materials using composites of carbon nanotubes and polymers. The CNTs can be incorporated with or without previous functionalization. The pristine, functionalized, or polymer grafted nanotubes can be dispersed in polymer matrices through various methods that include melt-processing (disperses CNTs in melted thermoplastic polymer), solution processing, or in situ polymerization. CNT composites have been prepared with thermosetting resins and polymers that are solvent-processable, semicrystalline, amorphous, liquid crystalline, and π -conjugated. It has

been shown that the CNTs can enhance many different properties of the materials. Properties such as strength, stiffness, thermal stability, solvent resistance, glass transition temperature (T_g), crystallization time, crystallinity, electrical conductivity, reduced thermal shrinkage, and optical anisotropy can be enhanced by the presence of CNTs.

The improved qualities provided by the incorporation of CNTs in different materials can be exploited by numerous applications. These applications include chemical and physical sensors, probe tips for atomic force microscopy (AFM), electrically and thermally conducting fibres for functional textiles, nanowires, quantum wires, nanoscopic levers, components in molecular motors and other molecular devices. CNT composites in the biomedical field can be used as scaffolds for tissue growth, substrates for neuron growth, actuators, and novel micro- and mesoporous carbon structures for filtration. In the electronics field these CNT-enabled materials can be used in field emission display devices, as packaging materials for thermal management, supercapacitors for charge storage devices, for electromagnetic interference shielding, and in photovoltaic cells. In 2000, Hiroki Ago and fellow researchers were the first to investigate the electronic properties of a conjugated polymer/CNT composite composed of PPV and MWNTs [33]. They demonstrated that there was a strong interaction (energy transfer) between the photoexcited conducting polymer (PPV) and MWNT. The main electronic interaction was found to be the nonradiative energy transfer of singlet excitons from the polymer to the nanotube. Since this initial work a decade ago other groups have investigated π -conjugated polymer/CNT composites in bulk heterojunction solar cells.

1.4.3 Polymer/Carbon Nanotube Composites for Photovoltaic Cells

Polymer solar cells (PSCs) consist of a donor-acceptor film (bulk heterojunction (BHJ) layer) sandwiched between two electrodes. The anode is commonly indium tin oxide (ITO)

which is a transparent conducting oxide that transports holes from the donor within the BHJ. Just like the anode, the cathode's composition can vary but is commonly Al which is used to draw electrons from the BHJ's acceptor. The PSC utilizes a low band gap π -conjugated polymer as a donor (D) that must have a smaller ionization potential than the acceptor (A) (commonly PCBM). The acceptor, which must have a greater electron affinity than the polymer, can be PCBM, single-walled, double-walled, or multi-walled nanotubes. CNTs have a high surface area which provides an ideal morphological architecture for exciton dissociation. The nanotubes high aspect ratio (greater than 1000) allows for the creation of percolation pathways at low doping levels and this provides a means for high carrier mobility and efficient charge transfer to the appropriate electrodes.

SWNTs were first used as the acceptor in the PSC's BHJ by Kymakis and Amaratunga who blended poly(3-octylthiophene) (P3OT) with 1 weight % nanotube [34]. The performance of the solar cells was increased with respect to the open circuit voltage (V_{OC}) and short circuit current density (I_{SC}). This variation to the PSC introduced internal polymer/nanotube junctions, which allowed for exciton dissociation, and a continuous path for electron transport to the cathode. The semiconducting SWNT has a p-type character and the ability to promote charge separation and electron transport. Low efficiencies of SWNT based solar cells can be associated with a few factors such as the presence of metallic SWNT that short-circuit the cell (reducing the shunt resistance), impurities (mostly metal catalyst residue), SWNT aggregation, and low charge carrier mobility in the polymer matrix. Nogueira and colleagues tried to mitigate some of these potential problems by the covalent functionalization of SWNT ends and defects with thiophene moieties [35]. The thiophene pendent groups were used to increase the dispersion of the tubes in a P3OT matrix. It is critical that the nanotubes are dispersed homogeneously throughout the

polymer matrix to achieve an optimized interfacial area for charge transfer. Hümmelgen and colleagues also used a P3OT/SWNT composite to prepare a solar cell that reached power conversion efficiencies of 1.48% under 15.5 Wm^{-2} light [36]. The solar cell had a CNT composite layer deposited on a polybithiophene layer between the two electrodes. Pal and coworkers also used two layers within their photovoltaic devices [37]. The solar cells produced by their group had a C_{60} layer vacuum evaporated on a spin coated MWNT/P3HT composite. The nanotubes were used to aid in exciton dissociation and extract charges toward the ITO electrode. Fullerenes were also used by Mitra and coworkers to functionalize SWNTs for their incorporation into a P3HT composite to be used as the active layer in a BHJ solar cell [38]. There was an improvement in both the I_{SC} and FF by taking advantage of the accepting nature of fullerene and the charge transport capability of SWNTs. Polymer photovoltaics that used CNT/P3HT composites were studied by Arranz-Andrés and Blau who used SWNT, DWNT, and MWNT [39]. It was found that the CNTs induced local order of the polymer chains and that there was an increase in the power conversion efficiency (PCE), V_{OC} , I_{SC} , and FF as compared to cells without CNTs.

The carbon nanotubes within the cell should make exciton dissociation and charge extraction easier. Multi-component composites of CNT/P3HT/PCBM were used as the active layer in BHJ cells prepared by Joussetme and fellow researchers [40]. They prepared dilute solutions of single- and multi-walled carbon nanotube solutions which they added to solutions of P3HT/PCBM. This three component mixture, dissolved in chlorobenzene, was spin coated to prepare the thin film active layer in various photovoltaic devices. A power conversion efficiency of 2.0% was achieved with a 1:1 P3HT/PCBM solution with 0.1 weight % MWNTs. It was found that thermal treatment of the D-A layer was necessary to ensure high current density. The thermal

annealing of the BHJ active layer produces a nanostructured morphology that reduces charge carrier recombination that can occur in the polymer composite (due to the proximity of the donor and acceptor). The polymer/CNT solutions used to prepare the BHJ thin film must be stable and free of CNT aggregates. This is successfully achieved with conjugated polymers whose chains interact with the nanotubes via π - π stacking.

When single-walled nanotubes are used as the acceptor in the BHJ internal polymer-nanotube junctions are present which allow for the photoinduced electron transfer from the polymer to the SWNT. Kymakis and colleagues who used SWNTs as an acceptor with P3OT found that the solar cell's had an increase photoresponse and that the photocurrent increased by more than two orders of magnitude [41, 42]. The introduction of SWNTs ensured that a bi-continuous network was present for the electrons and holes to travel to their respective electrodes. The internal electric field created within the BHJ causes the excitons to dissociate into electrons and holes which travel in opposite directions. The free holes travel through the polymer to the anode and the free electrons travel to the cathode through the nanotubes. The nanotubes presence within the BHJ layer is critical to achieve ordered phase segregation and self-organization of the bi-continuous internal pathway

Chapter 2

Project Objectives

The research performed in this project will be used to investigate the interaction between various regioregular π -conjugated alternating copolymers and single-walled carbon nanotubes (SWNTs). The interaction between SWNTs and polymer is specifically important within the active layer of a bulk-heterojunction organic photovoltaic cell. The carbon nanotubes will be beneficial for the ordered phase segregation of the BHJ composite layer within the polymer solar cell. Not only will the nanotubes increase the order within the active layer, but the semi-conducting SWNTs can also act as an acceptor and promote exciton dissociation.

Several low-band gap polymers will be prepared to help investigate the role that the carbon nanotubes play within the BHJ layer. The polymer's electronic properties will be predicted using density functional theory calculations. The theoretical calculations will provide insight into the HOMO and LUMO energy levels, which are critical when designing conjugated polymers appropriate for BHJ solar cells. It is preferred that the solar cell has a large open-circuit voltage (V_{OC}) which can be established by a low-band gap polymer with a low HOMO energy level. The theoretical calculations will also be used to determine the optical absorption of the polymers and also morphological properties.

With the synthesized polymers, composites are to be prepared with a fullerene derivative (PCBM) and single-walled carbon nanotubes. The composites will be used to fabricate the active layer within the BHJ photovoltaic cell. Solar cells will be prepared with composites that are either comprised of the polymer and PCBM or polymer, PCBM, and SWCNTs. This study will

shed light on the photo-induced charge transfer process within the bulk-heterojunction polymer solar cell and what impact carbon nanotubes have on this critical process.

Chapter 3

Experimental

3.1 Theoretical Calculations

Theoretical calculations were performed in this study with Gaussian03 to investigate various physical properties of the polymers [43]. Specifically, the investigation focused on the morphological and electronic properties of oligomers ranging from $n=1$ to $n=9$. The calculations provide results which can be used to determine the electronic band gap (difference in the HOMO and LUMO energy levels) and optical absorption of the molecules.

The number of atoms contained in the co-oligomers is large and requires a significant amount of computational effort. The oligomers' sizes vary from 86 to 1199 atoms. To reduce cost, geometry optimizations for all of the compounds studied were performed using semi-empirical methods (SE). Specifically, the semi-empirical method used for this investigation was the Austin model 1 (AM1) [44]. With the semi-empirically derived optimized geometries Hartree-Fock (HF) and hybrid density functional theory (DFT) calculations were performed to examine and compare the energies and band gaps of three of 15 oligomers. The basis set chosen for the Hartree-Fock calculations was the 6-31G (d) [45]. For the DFT calculations the B3LYP functional was chosen with the 6-31G (d) basis set [46].

It is clearly shown that the semi-empirical and Hartree-Fock methods drastically overestimate the difference in the HOMO and LUMO energy levels whereas the hybrid DFT method is much closer to analogous experimental results. The optimal band gap for conjugated polymers, that are to be used in solar cells, ranges from 1.2 eV to 2.1 eV, with the LUMO level between -3.7 eV to -4.0 eV and an ideal HOMO level between -5.2 eV to -5.8 eV. The SE and

HF methods overestimate the band gap by approximately three times more than the DFT method. Based on these results, the geometries of the remaining oligomers were optimized semi-empirically and their energy levels were deduced by DFT calculations.

The geometries of the molecules needed to be optimized by the semi-empirical method before calculations of molecular energies and band gaps could be performed. This method proved to be successful and allowed for over 100 calculations to be completed in a timely and cost effective manner. Since the DFT calculations only focused on the molecule's energy and not its geometry, the energy calculations were successfully completed in a reasonable time frame. The data clearly illustrates that the B3LYP functional of the DFT method gives a good estimate of the experimental band gap. The data also shows that as the size of the oligomers increase the band gap decreases, which is due to the increased conjugation within the molecule. It was found that when very large molecules are studied, like polymers, it is best to optimize the geometries semi-empirically and then subsequently analyze the energies with the hybrid DFT method, as approximated by the B3LYP functional.

Theoretical optical absorption curves were determined using time-dependent self-consistent field density functional theory (TD-SCF-DFT, TD-DFT) performed using the B3LYP functional and 6-31G (d,p) basis set. These energy calculations were performed on the semi-empirically optimized geometries and were calculated for 40 excited states. The data obtained from the TD-DFT calculations was processed with Gauss Sum 2.2 to construct the UV-visible absorption spectra by fitting the calculated peaks to Gaussian functions [47]. To produce realistic looking spectra the full width at half maximum of the Gaussian functions was set at 3000 cm^{-1} .

Further theoretical studies were pursued to investigate the interaction between identical oligomers and also between single-walled carbon nanotube (SWNT) fragments and oligomers.

Oligomer group geometry optimizations were performed via the Austin model 1 semi-empirical method due to the large number of atoms involved in the calculations. Fragments of SWNTs were investigated, but due to their large size geometry optimizations using density functional (DFT B3LYP/6-31G (d)) theory were not feasible. Therefore, the carbon nanotubes' geometries were optimized semi-empirically (SE AM1) followed by a DFT energy calculation (B3LYP/6-31G (d)). Subsequently, the interaction between a single-walled carbon nanotube fragment and an oligomer was studied by performing a semi-empirical (AM 1) geometry optimization. For details of the theoretical results the reader is directed to section 1 of chapter 4 (results and discussion).

3.2 Materials

2-bromo-3-hexylthiophene, 2-bromo-3-octylthiophene, 5,5'-dibromo-2,2'-bithiophene, n-butyllithium, anhydrous FeCl₃, iodine, isopropoxy pinacolborane, N,N,N',N'-tetramethyl-ethane-1,2-diamine, phenylboronic acid, tetrabutylammonium hydroxide (1M in methanol), tri-butyltin chloride (Bu₃SnCl), magnesium turnings, magnesium sulphate, 1,3-bis((diphenylphosphino)propane)dichloronickel(II) (Ni(dppp)Cl₂), tri(*o*-tolyl)phosphine, Pd₂(dba)₃, Pd(PPh₃)₄, were used as received from Sigma-Aldrich. 4,7-bis(5-bromothiophen-2-yl)benzo[c][1,2,5]thiadiazole, 1,6-dibromopyrene, 2,7-dibromo-9H-fluoren-9-one, 9-(heptadecan-9-yl)-2,7-bis(4,4,5,5-tetramethyl-1,3,2-dioxaborolan-2-yl)-9H-carbazole, 2,2'-(9,9-dioctyl-9H-fluorene-2,7-diyl)bis(4,4,5,5-tetramethyl-1,3,2-dioxaborolane) were used as received from LumTech.

N-bromosuccinimide (NBS) was purchased from Sigma-Aldrich and purified via recrystallization from water. Phenanthrene-9,10-dione was prepared in the laboratory by Ian Rupar from the reduction of phenanthrene (Aldrich).

Tetrahydrofuran (THF), diethyl ether, hexanes, and toluene were purchased as dry solvents stored over molecular sieves from Sigma-Aldrich or filtered through a silica gel drying column under an inert atmosphere.

Dichloromethane, *o*-dichlorobenzene, chlorobenzene, bromobenzene, hexanes, ethyl acetate, dimethyl sulfoxide (DMSO), N, N-dimethylformamide, ethanol, methanol, diethyl ether (for extractions), acetonitrile, acetone, sodium hydroxide, sodium bicarbonate, celite, ammonium chloride, KF and aqueous HCl and H₂SO₄ were used as received from Fisher.

Single-walled carbon nanotubes (SWCNTs) were used as received from Unidym (grade: P0901).

3.3 Instruments

Characterization of the prepared monomers and polymers was accomplished by several techniques. Absorption spectra were determined on an HP 8542 diode array spectrophotometer and fluorescence measurements were detected with a USB2000-Ocean Optics Spectrometer. Nuclear magnetic resonance (NMR) spectroscopy was performed with a Bruker Avance-400 MHz system with a 5mm probe. NMR samples were prepared with deuterated chloroform as received from Aldrich.

Due to the large size variation in the molecules studied, two methods of mass spectroscopy were used. For the polymer intermediates that were prepared, electron impact time of flight (EI-TOF) spectroscopy was utilized. For the polymers matrix assisted laser desorption/ionization time of flight (MALDI-TOF) spectroscopy was used with either a 2,5-dihydroxybenzoic acid (DHB) or α -cyano-4-hydroxycinnamic acid (CHCA) matrix. Further polymer characterization was performed by gel permeation chromatography (GPC or SEC) on a size exclusion column with both a light scattering (Heleos-II (LS)) and refractive index (Optilab

rex (RI) detectors. Three successive 5 micron AM Gel GPC columns from the American Polymer Standards Corporation (pore size: 100000 Å, 10000 Å, and 500 Å) were used with either tetrahydrofuran (THF) or chloroform as the eluent. The GPC results were analyzed with Wyatt Technology Corporation's Astra V (© 2008).

The solar cells were characterized with a Keithley 4200-SCS Semiconductor Parameter Analyzer. The cells were connected to the analyzer via a negative and positive alligator clip. The light source used to test the cells was a halogen lamp with an intensity of 65 +/- 1 mW/cm². The initial test distance from the light source was 45 cm, although to decrease the intensity the distance was varied to 85 and 140 cm.

3.4 Solar Cell Fabrication Methods

3.4.1 Etching of indium tin oxide (ITO) layer

The first step in preparing a bulk-heterojunction solar cell is to etch the ITO substrate (transparent and electrically conducting). Glass slides were purchased that have a thin layer of ITO deposited on one side. To avoid short circuits in the completed solar cell the ITO electrode needed to be etched. Firstly, the ITO was masked with masking tape to protect the desired ITO substrate.

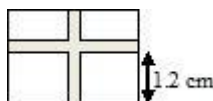


Figure 3.1: ITO (gray) mask.

The exposed ITO was covered in powdered zinc metal and placed in 2 M HCl (aq) for approximately two minutes. Subsequently, the slide was washed thoroughly with water and then the masking tape was removed. The slide was washed with a cotton pad soaked in toluene then

placed in several sonication baths of toluene, ethanol, dichloromethane, and finally acetone (1/2 hour each). The slides were dried under nitrogen and stored in an oven until further use.

3.4.2 Preparation of polymer composites for BHJ active layer

3.4.2.1 Polymer and PCBM solutions

Solutions of the polymer were prepared using chlorobenzene as solvent (15 mg polymer/mg of solvent). The polymer was carefully weighed, sonicated for 50 minutes, and then the solution was extracted via syringe. The solution was filtered with a 0.45 μm filter tip into a new vial that contained [C₆₁]PCBM (15 mg). The 99% pure PCBM was purchased from SES Research (now Nanos Research).

3.4.2.2 Polymer, PCBM, and CNT solutions

Prior to the preparation of the polymer:PCBM:SWCNT solutions a CNT dispersion was needed. A single-walled carbon nanotube solution was prepared to ensure that the SWNTs were fully dispersed in the solvent and that the final polymer:PCBM:SWCNT would contain a precise CNT concentration of 0.12 weight %. To achieve this concentration, SWCNTs (0.422 mg) were dispersed via sonication in chlorobenzene (20 mL).

Solutions of the polymer were prepared using chlorobenzene as solvent (15 mg/mL). The polymer was carefully weighed, sonicated for 50 minutes, and then the solution was extracted via syringe. The solution was filtered with a 0.45 μm filter tip into a new vial that contained [C₆₁]PCBM (15 mg). The solvent was subsequently evaporated and replaced with 0.9 mL of the CNT:chlorobenzene solution. The polymer:PCBM:SWCNT mixture was then sonicated for 45 minutes prior to use.

3.4.3 Solar Cell Fabrication

3.4.3.1 Aluminum Electrode

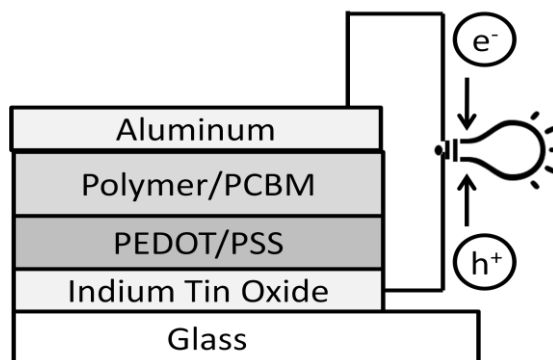


Figure 3.2: Bulk-heterojunction polymer solar cell with aluminum back electrode.

Method A

Dry ITO glass slides were spin coated with an aqueous PEDOT:PSS solution (2500 rpm for 60 seconds) and then a q-tip dipped in water was used to clean the ITO electrode contact. The slide was then put in vacuum oven (100 °C) for 2 hours. The Polymer:PCBM composites were spin coated (2500 rpm for 60 seconds) followed by the use of a q-tip dipped in dichloromethane to ensure that a small portion of the ITO electrode is kept clean. Subsequently the slide was put in vacuum oven (100 °C) for 1 hour. The Al electrode was deposited via physical vapour deposition (PVD) with a layer thickness of 200 nm and a 0.2 cm² surface area.

Method B

The etched ITO glass slide was washed with isopropanol and dried under a stream of nitrogen gas prior to use. The application of a PEDOT:PSS layer followed by spin coating an aqueous solution of PEDOT:PSS at 2500 rpm for three minutes. The slide was then placed in a vacuum oven for 30 minutes at 110 °C to ensure all water was removed. The Polymer:PCBM composite was spin coated (2500 rpm for three minutes) on top of the hole transport layer and put

in a vacuum oven for 12 minutes at 110 °C. The slide was then placed in a PVD apparatus for the evaporation of the 0.2 cm² Al electrode (200 nm thick).

3.4.3.2 Silver Electrode – Inverted Cell

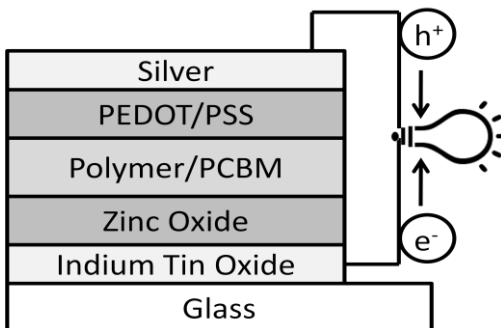


Figure 3.3: Inverted bulk-heterojunction polymer solar cell with silver back electrode.

The zinc oxide layer was prepared by spin coating a precursor solution of zinc acetate at 2000 rpm for 40 seconds. The zinc acetate layer was thermally converted into a nanocrystalline zinc oxide film via annealing at 275 °C for 5 minutes. The zinc oxide coated ITO slide was washed with water, acetone, and isopropanol. The slide was dried with a stream of nitrogen gas and subsequently placed in an oven.

The bulk-heterojunction composite layer was deposited via spin casting at 2500 rpm for 60 seconds. The slide was placed in a vacuum oven for 10 minutes at 100 °C. The polymer/PCBM layer was followed by a layer of PEDOT:PSS that was also spun coat at 2500 rpm for 60 seconds and annealed at 100 °C for 10 minutes. The PEDOT:PSS solution had to be modified with a surfactant so that it could be successfully added on top of the hydrophobic polymer layer. It was necessary to add Triton X-100 (a non-ionic surfactant) and DMSO (dimethyl sulfoxide) to the aqueous solution in quantities of 1%/weight and 5%/volume

respectively. Following the thermal treatment, the slide was placed under high vacuum in the PVD apparatus to allow for the 0.2 cm^2 silver electrode (anode) deposition (thickness of 100 nm).

3.5 Synthetic Methods

Literature references were used for the direction of synthetic reactions which involved Kumada coupling [48], stannylation [49] and borylation [50] of 3,3''-dihexyl-2,2':5',2'':5'',2'''-quarterthiophene, bromination of phenanthrene-9,10-dione [51], chemical oxidative polymerization [52,53], Stille coupling [54,55], and Suzuki coupling [50, 56, 57].

3.5.1 Synthesis of 3,3''-dihexyl-2,2':5',2'':5'',2'''-quarterthiophene

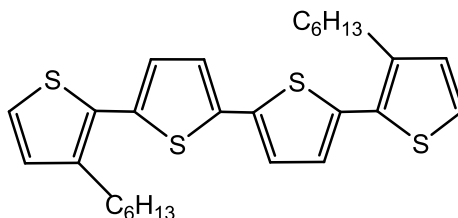


Figure 3.4: 3,3''-dihexyl-2,2':5',2'':5'',2'''-quarterthiophene.

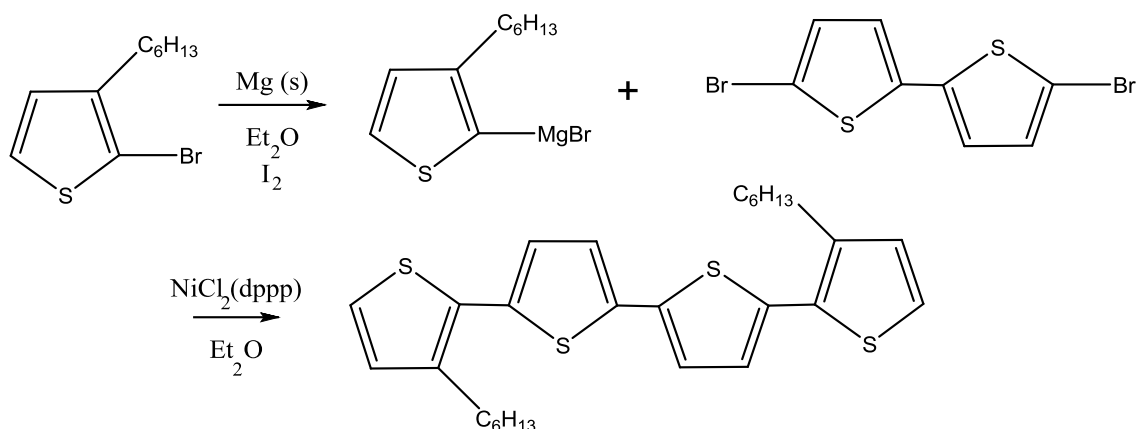


Figure 3.5: Reaction scheme for the synthesis of 3,3''-dihexyl-2,2':5',2'':5'',2'''-quarterthiophene.

Under dry nitrogen, a three-necked round bottom flask was flame dried following the addition of magnesium turnings (24.31 g/mol, 16.8 mmol, 0.408 g). One crystal of iodine was added followed by dry diethyl ether (20 mL). 2-bromo-3-hexylthiophene (247.20 g/mol, 16.0 mmol, 3.96 g, 1.24 g/mL, 3.19 mL) was added drop wise via syringe. This solution was refluxed for two hours to prepare the Grignard reagent. In another round bottom flask, 5,5'-dibromo-2,2'-bithiophene (324.06 g/mol, 7.8 mmol, 2.53 g) and Ni(dppp)Cl₂ (541.88 g/mol, 0.4 mmol, 0.217 g) were stirred in dry diethyl ether (10 mL) and dry Toluene (30 mL). The Grignard reagent was subsequently added to the red nickel solution via syringe and stirred overnight at reflux. The reaction mixture was hydrolyzed with cold HCl (aq) (0.5 M). The aqueous layer was extracted with dichloromethane (3 x 100 mL). The organic layers were combined, washed with an aqueous solution of NaHCO₃ (saturated) and water. The organic layer was subsequently dried with MgSO₄, filtered through a celite plug and evaporated under reduced pressure. The product, an orange-yellow solid, was purified via silica gel chromatography (hexanes:dichloromethane (9:1)) (83.18 %).

^1H NMR (400 MHz, CDCl_3): δ 7.18 (d, 2H), δ 7.13 (d, 2H), δ 7.03 (d, 2H), δ 6.95 (d, 2H), δ 2.78 (t, 4H), δ 1.65 (m, 4H), δ 1.33 (m, 12H), δ 0.89 (t, 6H). ^{13}C NMR (400 MHz, CDCl_3): δ 140.02, 130.44, 130.23, 126.66, 126.64, 123.99, 123.96, 115.51, 31.82, 30.80, 29.43, 29.37, 22.77, 14.25

3.5.2 Synthesis of 5,5''''-dibromo-3,3''''-dihexyl-2,2':5',2'':5'',2'''-quaterthiophene

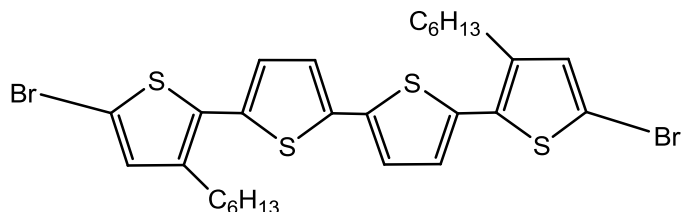


Figure 3.6: 5,5''''-dibromo-3,3''''-dihexyl-2,2':5',2'':5'',2'''-quaterthiophene.

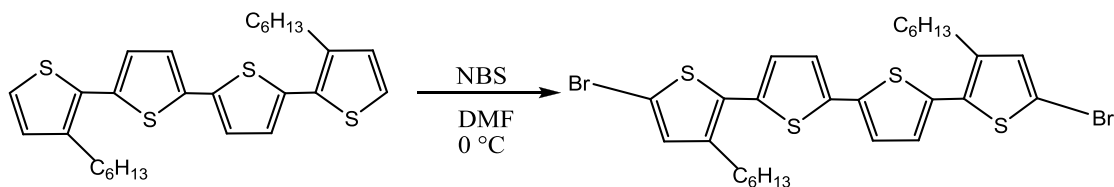


Figure 3.7: Reaction Scheme for the synthesis of 5,5''''-dibromo-3,3''''-dihexyl-2,2':5',2'':5'',2'''-quaterthiophene.

In a 100 mL three-necked round bottom flask under a nitrogen atmosphere, 3,3''''-dihexyl-2,2':5',2'':5'',2'''-quaterthiophene (498.83 g/mol, 1.1 mmol, 0.549 g) was added to DMF (50 mL) and cooled to 0 °C with an ice bath. While the solution stirred in the dark, a dropping funnel was used for the drop wise addition of N-bromosuccinimide (178.98 g/mol, 2 mmol, 0.358 g) dissolved in DMF (15 mL). After the solution stirred for two hours at 0 °C the ice bath was removed. The solution warmed to room temperature and stirred overnight. A saturated aqueous solution of NaHCO_3 (50 mL) was added to the reaction mixture. The organic layer was separated and the aqueous layer was extracted with dichloromethane (3 x 50 ml). The

combined organic layers were washed with water, dried over MgSO_4 and evaporated under reduced pressure. The product, an orange solid, was purified via silica gel chromatography (hexanes) (97.41 %).

^1H NMR (400 MHz, CDCl_3): δ 7.11 (d, 2H), δ 6.96 (d, 2H), δ 6.90 (s, 2H), δ 2.71 (t, 4H), δ 1.61 (m, 4H), δ 1.33 (m, 12H), δ 0.88 (t, 6H). ^{13}C NMR (400 MHz, CDCl_3): δ 137.17, 132.85, 127.35, 127.13, 124.36, 124.14, 119.16, 110.90, 31.77, 30.67, 29.25, 22.83, 14.29, 1.17
HRMS (EI) calculated for $\text{C}_{28}\text{H}_{32}\text{Br}_2\text{S}_4$ m/z 655.9733 [M^+], found m/z 657.0257

3.5.3 Synthesis of 2,7-dibromophenanthrene-9,10-dione

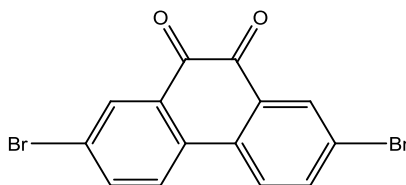


Figure 3.8: 2,7-dibromophenanthrene-9,10-dione.

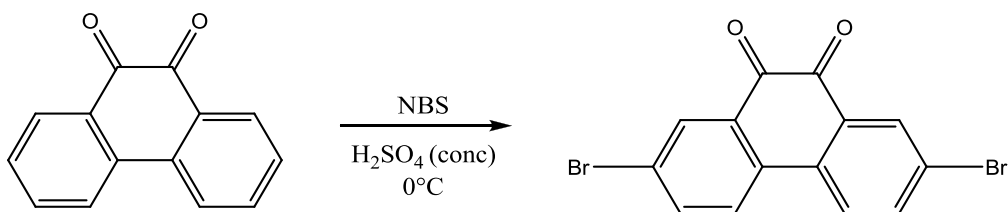


Figure 3.9: Reaction scheme for the synthesis of 2,7-dibromophenanthrene-9,10-dione.

In a 250 mL three-necked round bottom flask under a nitrogen atmosphere, concentrated H_2SO_4 (35 mL) was added drop wise to phenanthrene-9,10-dione (208.21 g/mol, 4.71 mmol, 0.98 g) and subsequently the black solution cooled to 0°C with an ice bath. N-bromosuccinimide (178.98 g/mol, 8.56 mmol, 1.532 g) was added in portions over 30 minutes. After the solution stirred for two hours, water (150 mL) was added carefully over a one hour period. The orange

solid precipitated was vacuum filtered followed by recrystallization from acetonitrile (300 mL) (68.86 %).

$^1\text{H NMR}$ (400 MHz, CDCl_3): δ 8.31 (s, 2H), δ 7.85 (s, 4H).

HRMS (EI) calculated for $\text{C}_{14}\text{H}_6\text{Br}_2\text{O}_2$ m/z 365.8715 [M^+], found m/z 365.8685

3.5.4 Synthesis of (3,3''-dihexyl-[2,2':5',2'':5'',2'''-quaterthiophene]-5,5'''-diyl)bis(tributylstannane)

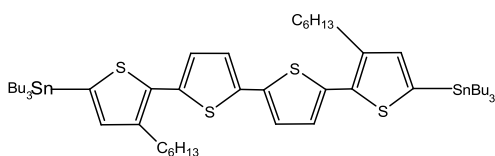


Figure 3.10: (3,3''-dihexyl-[2,2':5',2'':5'',2'''-quaterthiophene]-5,5'''-diyl)bis(tributylstannane)

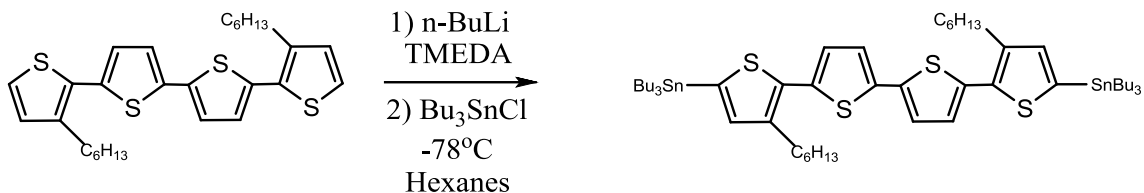


Figure 3.11: Reaction scheme for the synthesis of (3,3''-dihexyl-[2,2':5',2'':5'',2'''-quaterthiophene]-5,5'''-diyl)bis(tributylstannane).

In a 100 mL flame dried three-necked round bottom flask, 3,3''-dihexyl-2,2':5',2'':5'',2'''-quaterthiophene (498.83 g/mol, 0.591 mmol, 0.295 g) was stirred in dry hexanes (25 mL) and N,N,N',N'-tetramethyl-ethane-1,2-diamine (116.24 g/mol, 1.77 mmol, 0.78 g/mL, 0.264 mL) under argon. The solution was cooled to $-78\text{ }^\circ\text{C}$ for the drop wise addition of n-BuLi (1.6 M in hexanes, 1.77 mmol, 1.11 mL). The acetone/dry ice bath was removed to allow

the reaction mixture to reflux for one hour. Subsequently the solution was cooled to -78 °C for the addition of tributyltin chloride (325.49 g/mol, 1.207 g/mol, 2.96 mmol, 0.798 mL). After the addition of Bu₃SnCl, the acetone bath was removed and the solution stirred at room temperature overnight. An aqueous ammonium chloride solution (2M) was added. The aqueous layer was extracted with dichloromethane (3 x 40 ml). The organic layers were combined, washed with saturated NaHCO₃ (aq), water, and dried over MgSO₄. The solvent was evaporated under reduced pressure producing a dark red-brown oil.

¹H NMR (400 MHz, CDCl₃): δ 7.11 (d, 2H), δ 7.01 (d, 2H), δ 6.96 (s, 2H), δ 2.80 (t, 4H), δ 1.70 – 0.80 (overlap with ClSnBu₃). ¹³C NMR: δ 140.86, 138.82, 136.66, 136.10, 136.04, 135.95, 125.95, 123.80, 31.84, 30.84, 29.11, 27.99, 27.41, 27.00, 22.79, 17.68, 13.77, 10.99

3.5.5 Synthesis of 2,2'-(3,3'''-dihexyl-[2,2':5',2'':5'',2''':5''',2''''-quaterthiophene]-5,5''''-diyl)bis(4,4,5,5-tetramethyl-1,3,2-dioxaborolane)

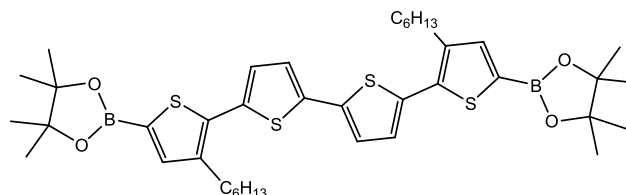


Figure 3.12: 2,2'-(3,3'''-dihexyl-[2,2':5',2'':5'',2''':5''',2''''-quaterthiophene]-5,5''''-diyl)bis(4,4,5,5-tetramethyl-1,3,2-dioxaborolane).

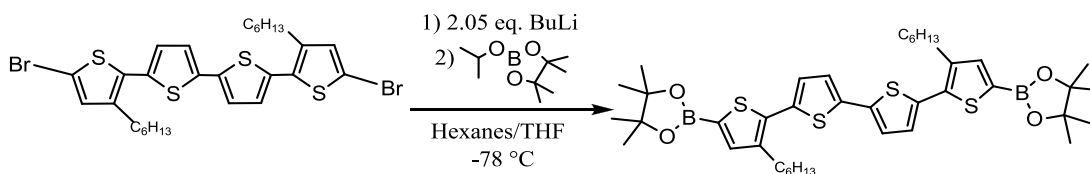


Figure 3.13: Reaction scheme for the synthesis of 2,2'-(3,3''-dihexyl-[2,2':5',2'':5'':2'''-quaterthiophene]-5,5'''-diyl)bis(4,4,5,5-tetramethyl-1,3,2-dioxaborolane).

In a 100 mL flame dried three-necked round bottom flask, 5,5'''-dibromo-3,3'''-dihexyl-2,2':5',2'':5'':2'''-quaterthiophene (656.62 g/mol, 1.5 mmol, 0.985 g) was stirred in dry THF (10 mL) and hexanes (25 mL) under argon. The solution was cooled to -78 °C for the drop wise addition of n-BuLi (1.6 M in hexanes, 3.075 mmol, 1.92 mL). Following two hours of stirring, isopropoxy pinacolborane (186.06 g/mol, 0.912 g/mL, 4.5 mmol, 0.837 g, 0.918 mL) was added via syringe. The acetone/dry ice bath was removed after 90 minutes to allow the reaction mixture to stir at room temperature overnight. The reaction mixture was poured into ice water, which was followed by an extracted with dichloromethane (3 x 40 ml). The organic layers were combined and dried over MgSO₄. The solvent was evaporated under reduced pressure producing the solid brown product (97.41 %).

¹H NMR (400 MHz, CDCl₃): δ 7.14 (d, 2H), δ 7.08 (d, 2H), δ 7.06 (s, 2H), δ 2.78 (t, 4H), δ 1.66 (m, 4H), δ 1.35 (s, 24H), δ 1.31 (m, 12H), δ 0.89 (t, 6H).

3.5.6 Synthesis of 1,6-bis(3-hexylthiophen-2-yl)pyrene

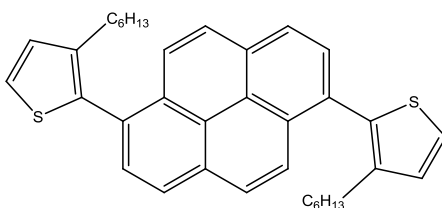


Figure 3.14: 1,6-bis(3-hexylthiophen-2-yl)pyrene.

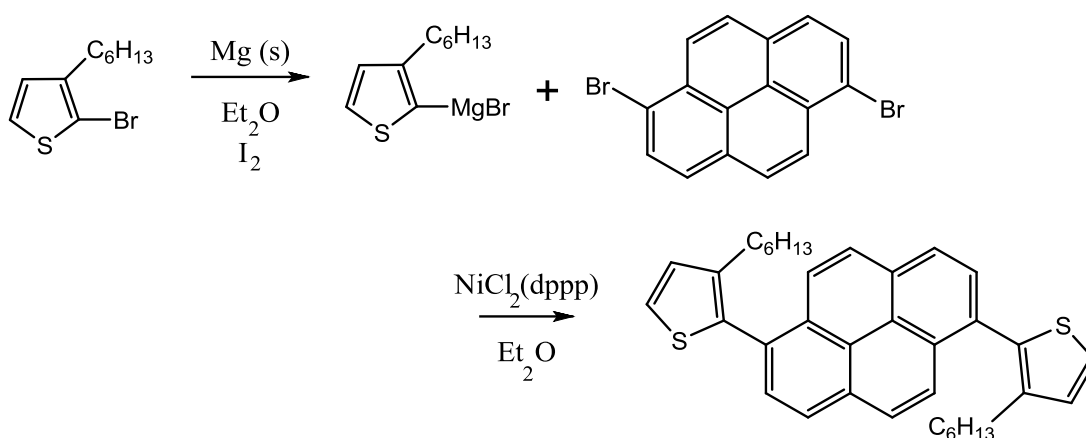


Figure 3.15: Reaction scheme for the synthesis of 1,6-bis(3-hexylthiophen-2-yl)pyrene.

Under dry nitrogen, a three-necked round bottom flask was flame dried following the addition of magnesium turnings (24.31 g/mol, 2.15 mmol, 0.052 g). One crystal of iodine was added followed by dry THF (15 mL). 2-bromo-3-hexylthiophene (247.20 g/mol, 2.1 mmol, 0.519 g, 1.24 g/mL, 0.42 mL) was added drop wise via syringe. This solution was refluxed for two hours to prepare the Grignard reagent. In another round bottom flask, 1,6-dibromopyrene (360.04 g/mol, 1.0 mmol, 0.360 g) and Ni(dppp)Cl₂ (541.88 g/mol, 0.1 mmol, 0.054 g) were stirred in dry THF (15 mL). The Grignard reagent was subsequently added to the red nickel solution via

syringe and stirred overnight at reflux. The reaction mixture was hydrolyzed with cold HCl (aq) (0.5 M). The aqueous layer was extracted with dichloromethane (3 x 50 mL). The organic layers were combined, washed with an aqueous solution of NaHCO₃ (saturated) and water. The organic layer was subsequently dried with MgSO₄, filtered through a celite plug and evaporated under reduced pressure. The product, a brown solid, was unsuccessfully purified after several purification attempts via silica gel chromatography (hexanes).

HRMS (EI) calculated for C₃₆H₃₈S₂ m/z 534.2415 [M⁺], found m/z 534.2418

3.5.7 Synthesis of 2,7-bis(3-hexylthiophen-2-yl)phenanthrene-9,10-dione

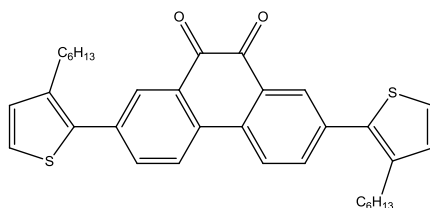


Figure 3.16: 2,7-bis(3-hexylthiophen-2-yl)phenanthrene-9,10-dione.

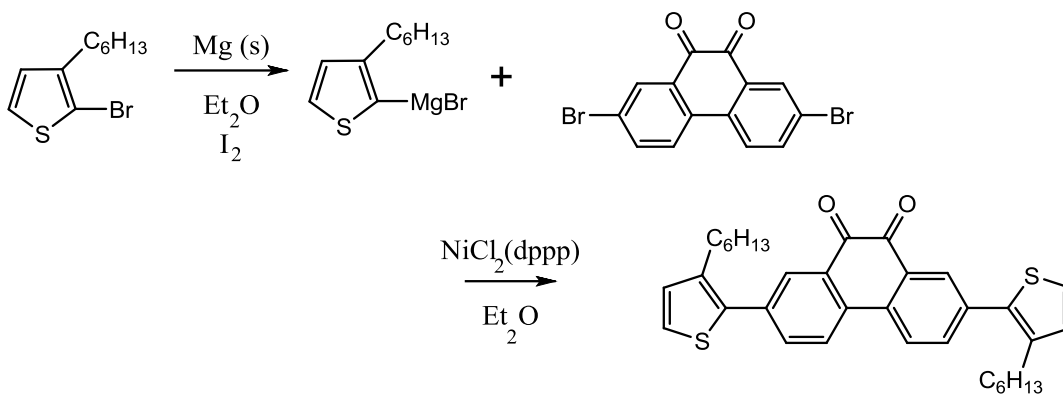


Figure 3.17: Reaction scheme for the synthesis of 2,7-bis(3-hexylthiophen-2-yl)phenanthrene-9,10-dione.

Under dry nitrogen, a three-necked round bottom flask was flame dried following the addition of magnesium turnings (24.31 g/mol, 2.15 mmol, 0.052 g). One crystal of iodine was added followed by dry diethyl ether (10 mL). 2-bromo-3-hexylthiophene (247.20 g/mol, 2.1 mmol, 0.519 g, 1.24 g/mL, 0.42 mL) was added drop wise via syringe. This solution was refluxed for two hours to prepare the Grignard reagent. In another round bottom flask, 2,7-dibromophenanthrene-9,10-dione (366.0 g/mol, 1.1 mmol, 0.403 g) and Ni(dppp)Cl₂ (541.88 g/mol, 0.1 mmol, 0.054 g) were stirred in dry Toluene (35 mL). The Grignard reagent was subsequently added to the red nickel solution via syringe and stirred overnight at reflux. The green reaction mixture was hydrolyzed with cold HCl (aq) (0.5 M) producing a brown solution. The aqueous layer was extracted with dichloromethane (3x 50 mL). The organic layers were combined, washed with an aqueous solution of NaHCO₃ (saturated) and water. The organic layer was subsequently dried with MgSO₄, filtered through a celite plug and evaporated under reduced pressure. The product, an orange-brown solid, was unsuccessfully purified by silica gel chromatography (hexanes).

3.5.8 Synthesis of 2,7-bis(3-hexylthiophen-2-yl)-9H-fluoren-9-one

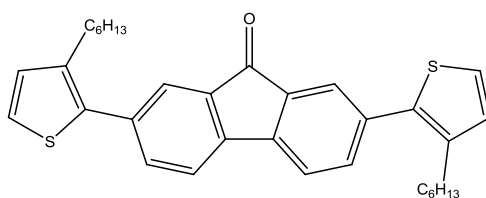


Figure 3.18: 2,7-bis(3-hexylthiophen-2-yl)-9H-fluoren-9-one.

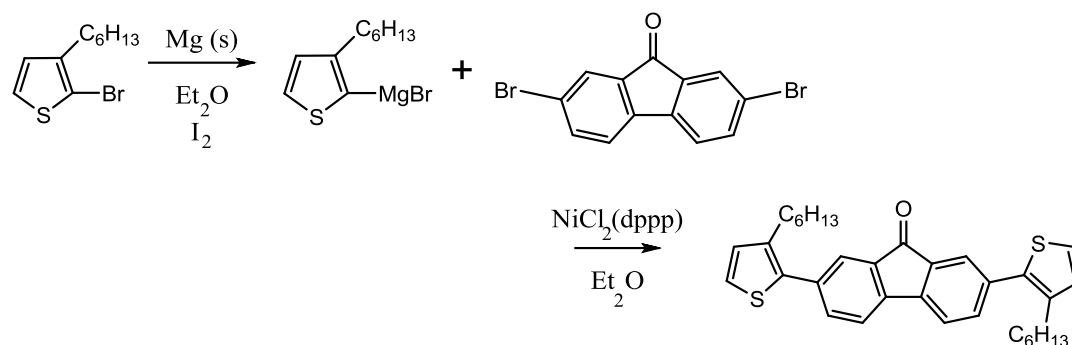


Figure 3.19: Reaction scheme for the synthesis of 2,7-bis(3-hexylthiophen-2-yl)-9H-fluoren-9-one.

Under dry nitrogen, a three-necked round bottom flask was flame dried following the addition of magnesium turnings (24.31 g/mol, 2.15 mmol, 0.052 g). One crystal of iodine was added followed by dry diethyl ether (10 mL). 2-bromo-3-hexylthiophene (247.20 g/mol, 2.1 mmol, 0.519 g, 1.24 g/mL, 0.42 mL) was added drop wise via syringe. This solution was refluxed for two hours to prepare the Grignard reagent. In another round bottom flask, 2,7-dibromo-9H-fluoren-9-one (337.99 g/mol, 1.0 mmol, 0.338 g) and Ni(dppp)Cl₂ (541.88 g/mol, 0.1 mmol, 0.054 g) were stirred in dry Toluene (30 mL). The Grignard reagent was subsequently added to the red nickel solution via syringe and stirred overnight at reflux. The reaction mixture was hydrolyzed with cold HCl (aq) (0.5 M) with the aqueous layer being extracted with dichloromethane (3 x 50 mL). The organic layers were combined, washed with an aqueous solution of NaHCO₃ (saturated) and water. The organic layer was subsequently dried with MgSO₄, filtered through a celite plug and evaporated under reduced pressure. The product, a brown-orange solid, was unsuccessfully purified even after several attempts by silica gel chromatography (hexanes).

3.5.9 Synthesis of 9-(heptadecan-9-yl)-2,7-bis(3-hexylthiophen-2-yl)-9H-carbazole

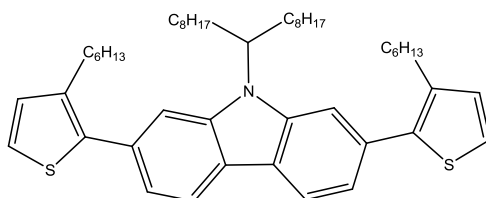


Figure 3.20: 9-(heptadecan-9-yl)-2,7-bis(3-hexylthiophen-2-yl)-9H-carbazole.

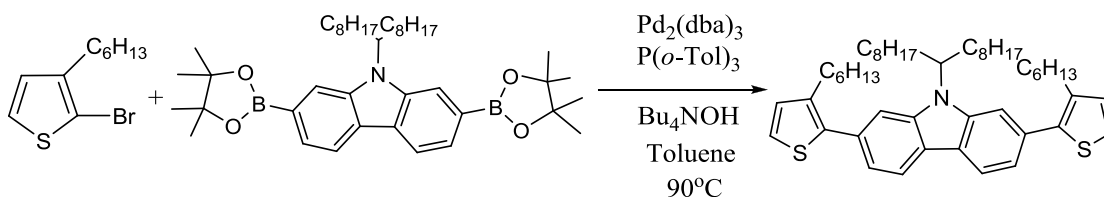


Figure 3.21: Reaction scheme for the synthesis of 9-(heptadecan-9-yl)-2,7-bis(3-hexylthiophen-2-yl)-9H-carbazole.

In a flame dried round bottom flask fitted with a reflux condenser, 9-(heptadecan-9-yl)-2,7-bis(4,4,5,5-tetramethyl-1,3,2-dioxaborolan-2-yl)-9H-carbazole (657.58 g/mol, 0.5 mmol, 0.329 g), Pd₂(dba)₃ (915.72 g/mol, 0.01 mmol, 0.009 g), tri(*o*-tolyl)phosphine (304.38 g/mol, 0.02 mmol, 0.006 g) and 15 mL of dry toluene were stirred under dry nitrogen. Following the addition of 2-bromo-3-hexylthiophene (247.20 g/mol, 1.0 mmol, 0.248 g, 1.24 g/mL, 0.2 mL), tetrabutylammonium hydroxide (1.0 mmol, 1.0 mL, 1 M in methanol) was added via syringe and subsequently the reaction mixture was stirred at 90 °C overnight. The following day the reaction mixture was cooled to room temperature, extracted with dichloromethane, dried with MgSO₄ and filtered through celite. The solvent was evaporated under reduced pressure to yield a brown solid which was purified via silica gel chromatography (hexanes, hexanes - ethyl acetate (9:1)) (75.48 %).

^1H NMR (400 MHz, CDCl_3): δ 8.10 (dd, 2H), δ 7.54 (d, 2H), δ 7.31 (dd, 2H), δ 7.27 (d, 2H), δ 7.03 (d, 2H), δ 4.56 (m, 1H), δ 2.75 (t, 4H), δ 2.30 (m, 2H), δ 1.93 (t, 2H), δ 1.66 (m, 4H), δ 1.20 (m, 34H), δ 0.97 (d, 2H), δ 0.85 (m, 12H).

HRMS (EI) calculated for $\text{C}_{49}\text{H}_{71}\text{NS}_2$ m/z 737.5028 [M^+], found m/z 737.5026.

3.5.10 Synthesis of 9-(heptadecan-9-yl)-2,7-bis(3-octylthiophen-2-yl)-9H-carbazole

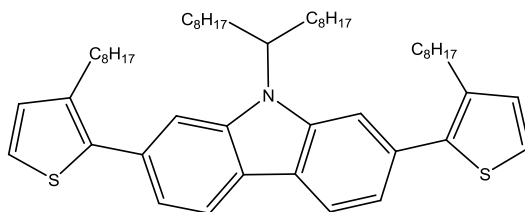


Figure 3.22: 9-(heptadecan-9-yl)-2,7-bis(3-octylthiophen-2-yl)-9H-carbazole.

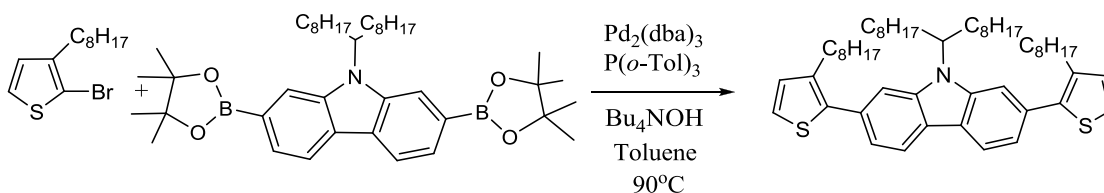


Figure 3.23: 9-(heptadecan-9-yl)-2,7-bis(3-octylthiophen-2-yl)-9H-carbazole.

In a flame dried round bottom flask fitted with a reflux condenser, 9-(heptadecan-9-yl)-2,7-bis(4,4,5,5-tetramethyl-1,3,2-dioxaborolan-2-yl)-9H-carbazole (657.58 g/mol, 1.0 mmol, 0.658 g), $\text{Pd}_2(\text{dba})_3$ (915.72 g/mol, 0.02 mmol, 0.018 g), tri(*o*-tolyl)phosphine (304.38 g/mol, 0.04 mmol, 0.012 g) and 20 mL of dry toluene were stirred under dry nitrogen. Following the addition of 2-bromo-3-octylthiophene (275.25 g/mol, 2.0 mmol, 0.551 g, 1.206 g/mL, 0.46 mL), tetrabutylammonium hydroxide (2.0 mmol, 2.0 mL, 1 M in methanol) was added via syringe and subsequently the reaction mixture was stirred at 90 °C overnight. The following day the reaction mixture was cooled to room temperature, extracted with dichloromethane, dried with MgSO_4 and

filtered through celite. The solvent was evaporated under reduced pressure to yield a brown solid which was purified via silica gel chromatography (hexanes, hexanes - ethyl acetate (9:1)) (31.47 %).

^1H NMR (400 MHz, CDCl_3): δ 8.06 (dd, 2H), δ 7.51 (d, 2H), δ 7.29 (dd, 2H), δ 7.22 (d, 2H), δ 6.99 (d, 2H), δ 4.56 (m, 1H), δ 2.75 (t, 4H), δ 2.30 (m, 2H), δ 1.93 (t, 2H), δ 1.65 (m, 4H), δ 1.22 (m, 20H), δ 1.12 (m, 22H) δ 0.96 (d, 2H), δ 0.82 (m, 12H). ^{13}C NMR (400 MHz, CDCl_3): δ 139.30, 138.52, 129.79, 125.65, 123.70, 120.77, 120.09, 112.34, 109.85, 108.09, 56.70, 33.98, 32.04, 31.91, 31.74, 31.38, 30.46, 29.88, 29.61, 29.52, 29.34, 27.09, 22.82, 22.74, 14.24, 14.19, 1.18

HRMS (EI) calculated for $\text{C}_{53}\text{H}_{79}\text{NS}_2$ m/z 793.5654 [M^+], found m/z 793.5651.

3.5.11 Synthesis of 2,2'-(9,9-dioctyl-9H-fluorene-2,7-diyl)bis(3-octylthiophene)

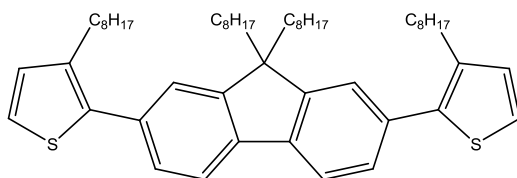


Figure 3.24: 2,2'-(9,9-dioctyl-9H-fluorene-2,7-diyl)bis(3-octylthiophene).

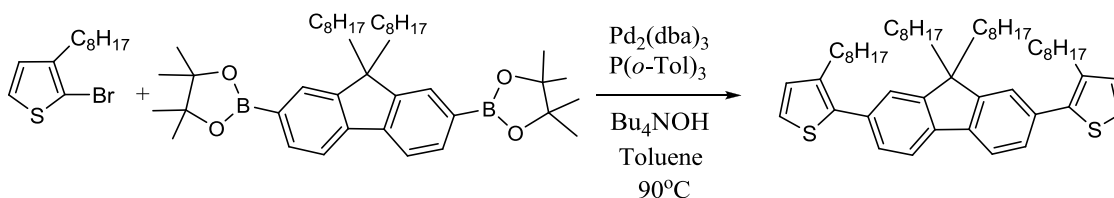


Figure 3.25: Reaction scheme for the synthesis of 2,2'-(9,9-dioctyl-9H-fluorene-2,7-diyl)bis(3-octylthiophene).

In a flame dried round bottom flask fitted with a reflux condenser, 2,2'-(9,9-dioctyl-9H-fluorene-2,7-diyl)bis(4,4,5,5-tetramethyl-1,3,2-dioxaborolane) (642.57 g/mol, 1.0 mmol, 0.643 g),

$\text{Pd}_2(\text{dba})_3$ (915.72 g/mol, 0.02 mmol, 0.018 g), tri(*o*-tolyl)phosphine (304.38 g/mol, 0.04 mmol, 0.012 g) and 20 mL of dry toluene were stirred under dry nitrogen. Following the addition of 2-bromo-3-octylthiophene (275.25 g/mol, 2.0 mmol, 0.551 g, 1.206 g/mL, 0.46 mL), tetrabutylammonium hydroxide (2.0 mmol, 2.0 mL, 1 M in methanol) was added via syringe and subsequently the reaction mixture was stirred at 90 °C overnight. The following day the reaction mixture was cooled to room temperature, extracted with dichloromethane, dried with MgSO_4 and filtered through celite. The solvent was evaporated under reduced pressure to yield a brown solid which was purified via silica gel chromatography (hexanes, hexanes - ethyl acetate (9:1)) (19.25 %).

^1H NMR (400 MHz, CDCl_3): δ 7.71 (d, 2H), δ 7.40 (d, 2H), δ 7.24 (d, 2H), δ 7.17 (d, 2H), δ 7.00 (d, 2H), δ 2.68 (t, 4H), δ 1.93 (m, 4H), δ 1.62 (m, 6H), δ 1.26 (m, 20H), δ 1.09 (m, 22H), δ 0.87 (m, 6H), δ 0.80 (m, 6H). ^{13}C NMR (400 MHz, CDCl_3): δ 151.24, 140.45, 138.74, 138.64, 129.80, 128.42, 128.29, 125.66, 123.87, 123.51, 119.85, 55.27, 40.72, 34.82, 34.37, 31.93, 31.74, 31.32, 30.46, 29.79, 29.64, 29.45, 23.97, 22.81, 22.75, 14.20, 1.17

HRMS (EI) calculated for $\text{C}_{53}\text{H}_{78}\text{S}_2$ m/z 778.5545 [M^+], found m/z 778.5542.

3.5.12 Synthesis of poly[(2,7-(9-(heptadecan-9-yl)-9H-carbazole))-alt-(4,4'-dihexyl-2,2'-bithiophene)] (TCT)

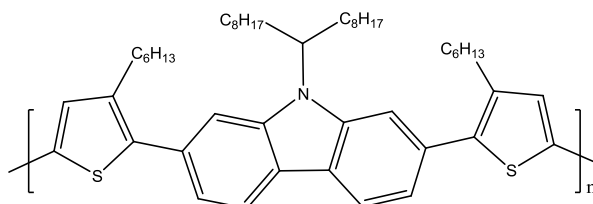


Figure 3.26: poly[(2,7-(9-(heptadecan-9-yl)-9H-carbazole))-alt-(4,4'-dihexyl-2,2'-bithiophene)].

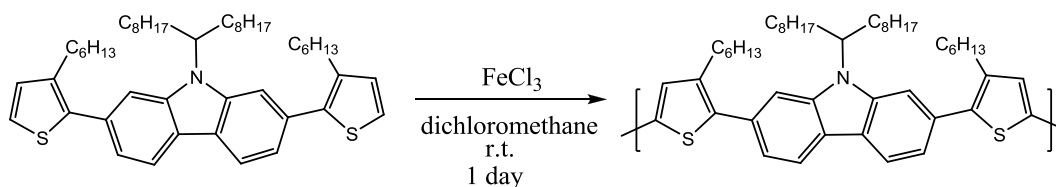


Figure 3.27: Reaction scheme for the synthesis of poly[(2,7-(9-(heptadecan-9-yl)-9H-carbazole))-alt-(4,4'-dihexyl-2,2'-bithiophene)].

In a flame dried round bottom flask 9-(heptadecan-9-yl)-2,7-bis(3-hexylthiophen-2-yl)-9H-carbazole (738.2 g/mol, 0.38 mmol, 0.279 g) was dissolved in freshly distilled dichloromethane (3 mL) and stirred under dry nitrogen. Following the addition of anhydrous FeCl₃ (162.2 g/mol, 1.52 mmol, 0.247 g) the orange solution turned black. The reaction mixture was stirred at room temperature overnight. After cold methanol (10 mL) was added to the reaction mixture the dark forest green precipitate was vacuum filtered. The polymer was dissolved in dichloromethane and the insoluble fraction was removed via filtration. The solvent of the filtrate was evaporated yielding a dark green solid (41.82 %). Please refer to the appendix for both the MALDI-TOF MS and ¹H NMR (400 MHz, CDCl₃) spectra.

3.5.13 Synthesis of poly[(2,7-(9-(heptadecan-9-yl)-9H-carbazole))-alt-(4,4'-dioctyl-2,2'-bithiophene)] (oTCT)

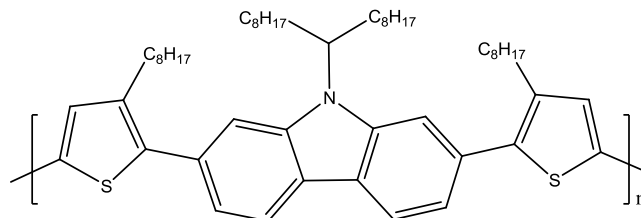


Figure 3.28: poly[(2,7-(9-(heptadecan-9-yl)-9H-carbazole))-alt-(4,4'-dioctyl-2,2'-bithiophene)].

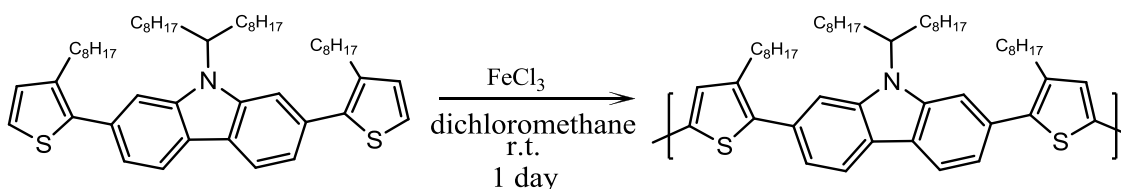


Figure 3.29: Reaction scheme for the synthesis of poly[(2,7-(9-(heptadecan-9-yl)-9H-carbazole))-alt-(4,4'-dioctyl-2,2'-bithiophene)].

In a flame dried round bottom flask 9-(heptadecan-9-yl)-2,7-bis(3-octylthiophen-2-yl)-9H-carbazole (794.33 g/mol, 0.315 mmol, 0.25 g) was dissolved in freshly distilled dichloromethane (5 mL) and stirred under dry nitrogen. Following the addition of anhydrous FeCl_3 (162.2 g/mol, 1.26 mmol, 0.204 g) the brown-yellow solution turned dark purple. The reaction mixture was stirred at room temperature overnight. After cold methanol (10 mL) was added to the dark purple reaction mixture the solution turned brownish-black and the polymer was precipitated in methanol (40 mL). The polymer was vacuum filtered, dissolved in dichloromethane and the insoluble fraction was removed via filtration. The solvent of the filtrate was evaporated yielding a dark brown solid (70.91 %). Please refer to the appendix for both the MALDI-TOF MS and ^1H NMR (400 MHz, CDCl_3) spectra.

3.5.14 Synthesis of poly[(2,7-(9,9-dioctyl-9H-fluorene-2,7-diyl))-alt-(4,4'-dioctyl-2,2'-bithiophene)] (oTLT)

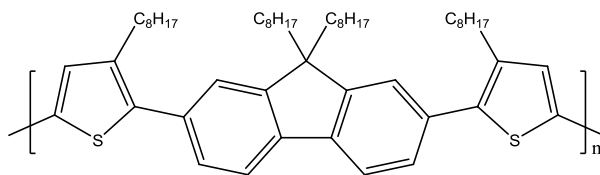


Figure 3.30: poly[(2,7-(9,9-dioctyl-9H-fluorene-2,7-diyl))-alt-(4,4'-dioctyl-2,2'-bithiophene)].

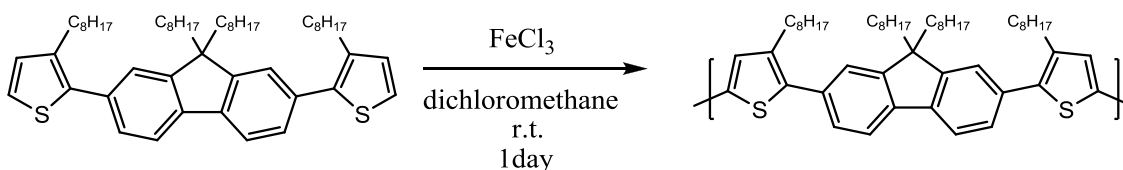


Figure 3.31: Reaction scheme for the synthesis of poly[(2,7-(9,9-dioctyl-9H-fluorene-2,7-diyl))-alt-(4,4'-dioctyl-2,2'-bithiophene)].

In a flame dried round bottom flask 2,2'-(9,9-dioctyl-9H-fluorene-2,7-diyl)bis(3-octylthiophene) (779.32 g/mol, 0.167 mmol, 0.13 g) was dissolved in freshly distilled dichloromethane (4 mL) and stirred under dry nitrogen. Following the addition of anhydrous FeCl₃ (162.2 g/mol, 0.668 mmol, 0.108 g) the brown solution turned navy blue. The reaction mixture was stirred at room temperature overnight. After cold methanol (10 mL) was added to the dark blue reaction mixture the solution turned dark green and the polymer was precipitated in 40 mL of cold methanol. The polymer was vacuum filtered (53.93 %), dissolved in dichloromethane and the insoluble fraction was removed via filtration. Please refer to the appendix for both the MALDI-TOF MS and ¹H NMR (400 MHz, CDCl₃) spectra.

3.5.15 Synthesis of poly[(5,5''-(3,3''-dihexyl-2,2':5',2'':5'',2''''-quarterthiophene))-alt-(2,7-9H-fluoren-9-one)] (TF)

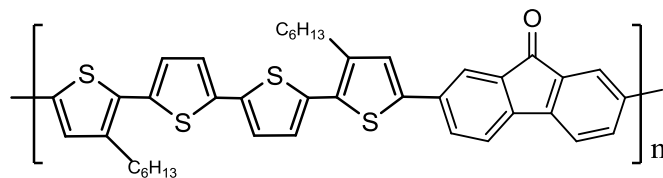


Figure 3.32: poly[(5,5''-(3,3''-dihexyl-2,2':5',2'':5'',2''''-quarterthiophene))-alt-(2,7-9H-fluoren-9-one)].

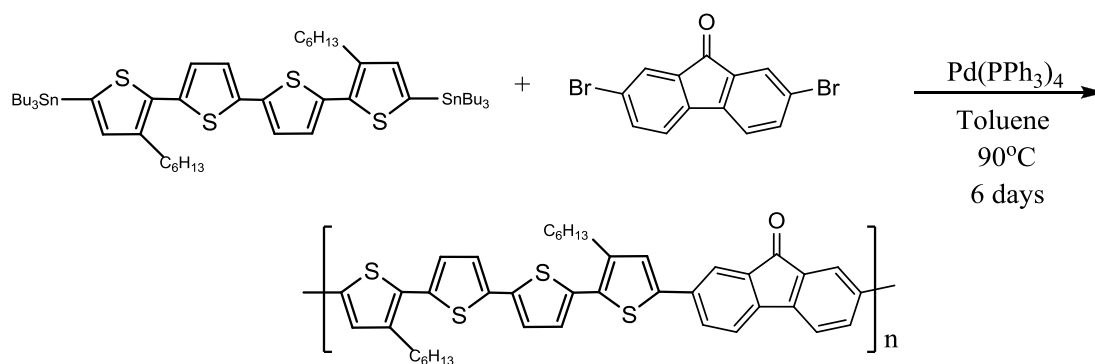


Figure 3.33: Reaction scheme for the synthesis of poly[(5,5''-(3,3''-dihexyl-2,2':5',2'':5'',2''''-quarterthiophene))-alt-(2,7-9H-fluoren-9-one)].

In a flame dried round bottom flask fitted with a reflux condenser, (3,3''-dihexyl-[2,2':5',2'':5'',2''''-quarterthiophene]-5,5''-diyl)bis(tributylstannane) (1076.92 g/mol, 0.6 mmol, 0.646 g), 2,7-dibromo-9H-fluoren-9-one (337.99 g/mol, 0.6 mmol, 0.203 g), Pd(PPh₃)₄ (1155.58 g/mol, 0.03 mmol, 0.034 g), and 50 ml of dry toluene were stirred under reflux for 6 days. Upon cooling to room temperature, KF (aq) (5 g in 10 mL water) was added and stirred for two hours, this was followed by an extraction with dichloromethane (3 x 100 mL). The organic layer was washed with water, dried over MgSO₄ and evaporated under reduced pressure. The reddish-brown solid was dissolved in dichloromethane (20mL) and precipitated in methanol (300mL).

The precipitate was vacuum filtered and washed with cold methanol. Please refer to the appendix for both the MALDI-TOF MS and ^1H NMR (400 MHz, CDCl_3) spectra.

3.5.16 Synthesis of poly[(5,5''-(3,3''-dihexyl-2,2':5',2'':5'',2'''-quaterthiophene))-alt-(2,7-9H-fluoren-9-one)] (TF)

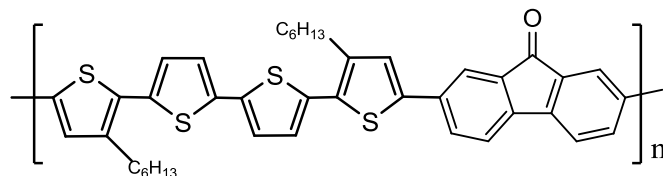


Figure 3.34: poly[(5,5''-(3,3''-dihexyl-2,2':5',2'':5'',2'''-quaterthiophene))-alt-(2,7-9H-fluoren-9-one)].

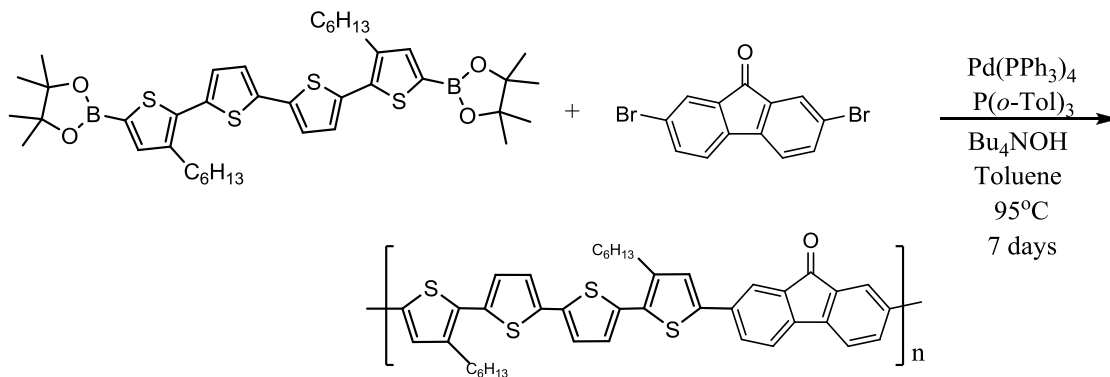


Figure 3.35: Reaction scheme for the synthesis of poly[(5,5''-(3,3''-dihexyl-2,2':5',2'':5'',2'''-quaterthiophene))-alt-(2,7-9H-fluoren-9-one)].

In a flame dried round bottom flask fitted with a reflux condenser, 2,2'-(3,3''-dihexyl-[2,2':5',2'':5'',2'''-quaterthiophene]-5,5''-diyl)bis(4,4,5,5-tetramethyl-1,3,2-dioxaborolane) (750.75 g/mol, 1.0 mmol, 0.751 g), 2,7-dibromo-9H-fluoren-9-one (337.99 g/mol, 1.1 mmol, 0.372 g), $\text{Pd}(\text{PPh}_3)_4$ (1155.58 g/mol, 0.02 mmol, 0.023 g), tri(*o*-tolyl)phosphine (304.38 g/mol, 0.022 mmol, 0.007 g) and 11 mL of dry toluene were stirred under dry nitrogen. Following the addition of tetrabutylammonium hydroxide (0.74 mmol, 0.74 mL, 1 M in methanol) via syringe, the reaction

mixture was stirred at 95°C for 7 days. Upon cooling to room temperature, the polymer was precipitated in methanol/H₂O (9:1). The precipitate was vacuum filtered and washed with cold methanol. Please refer to the appendix for both the MALDI-TOF MS and ¹H NMR (400 MHz, CDCl₃) spectra.

3.5.17 Synthesis of poly[(2,7-(9,9-dioctyl-9H-fluorene-2,7-diyl))-alt-(2,7-9H-fluoren-9-one)] (LF)

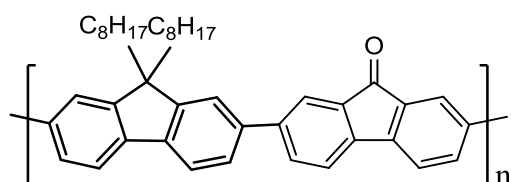


Figure 3.36: poly[(2,7-(9,9-dioctyl-9H-fluorene-2,7-diyl))-alt-(2,7-9H-fluoren-9-one)].

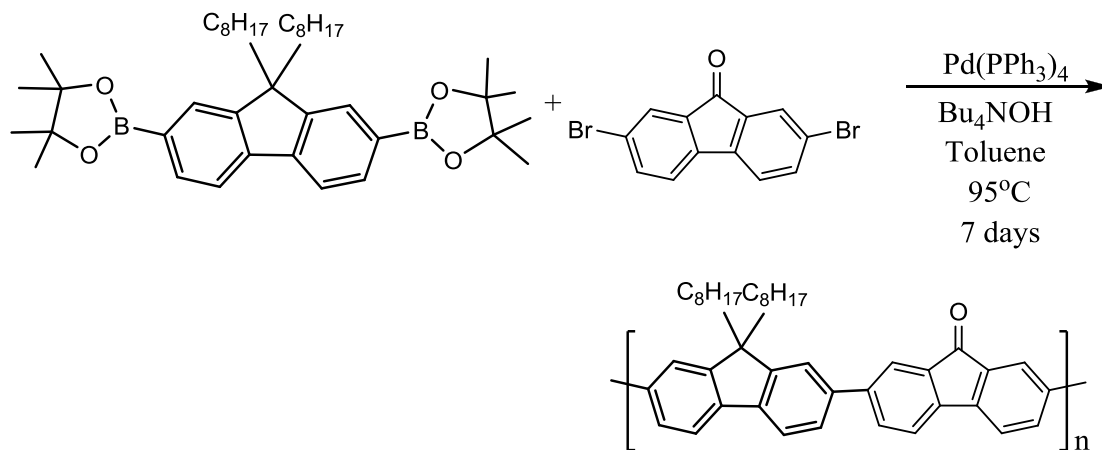


Figure 3.37: Reaction scheme for the synthesis of poly[(2,7-(9,9-dioctyl-9H-fluorene-2,7-diyl))-alt-(2,7-9H-fluoren-9-one)].

In a flame dried round bottom flask fitted with a reflux condenser, 2,2'-(9,9-dioctyl-9H-fluorene-2,7-diyl)bis(4,4,5,5-tetramethyl-1,3,2-dioxaborolane) (642.57 g/mol, 2.0 mmol, 1.286 g),

2,7-dibromo-9H-fluoren-9-one (337.99 g/mol, 2.1 mmol, 0.710 g), Pd(PPh₃)₄ (1155.58 g/mol, 0.1 mmol, 0.116 g) and 25 mL of dry toluene were stirred under dry nitrogen. Following the addition of tetrabutylammonium hydroxide (1.48 mmol, 1.48 mL, 1 M in methanol) via syringe, the reaction mixture was stirred at 95 °C for 7 days. Upon cooling to room temperature, the orange polymer was precipitated in methanol (75 mL). The precipitate was vacuum filtered and washed with cold methanol. The polymer (soluble in THF) was further purified by precipitation in methanol, followed by acetone and then a dialysis membrane (3.5kDa). Please refer to the appendix for both the MALDI-TOF MS and ¹H NMR (400 MHz, CDCl₃) spectra.

3.5.18 Synthesis of poly[(2,7-(9,9-dioctyl-9H-fluorene-2,7-diyl))-alt-(4,7-dithien-2-yl-2,1,3-benzothiadiazole)] (LB)

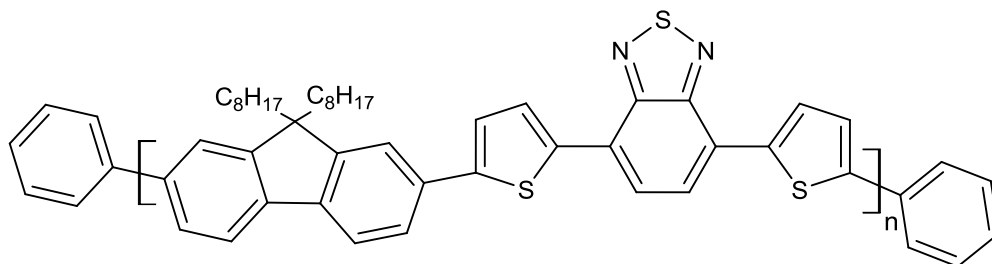


Figure 3.38: poly[(2,7-(9,9-dioctyl-9H-fluorene-2,7-diyl))-alt-(4,7-dithien-2-yl-2,1,3-benzothiadiazole)].

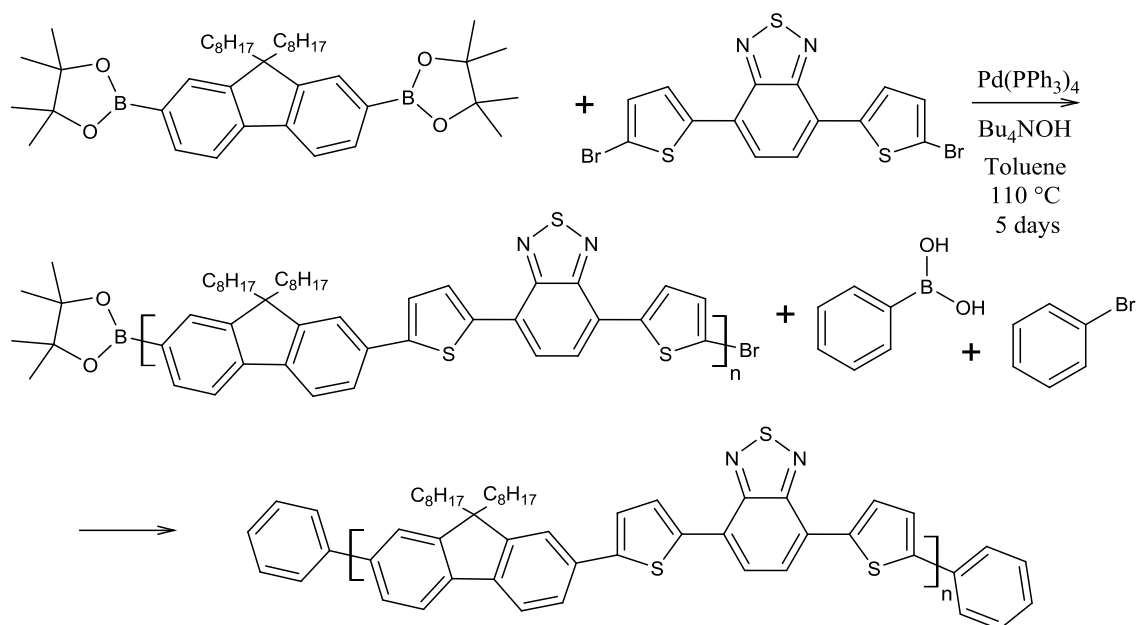


Figure 3.39: Reaction scheme for the synthesis of poly[(2,7-(9,9-dioctyl-9H-fluorene-2,7-diyl))-alt-(4,7-dithien-2-yl-2,1,3-benzothiadiazole)].

In a flame dried round bottom flask fitted with a reflux condenser, 2,2'-(9,9-dioctyl-9H-fluorene-2,7-diyl)bis(4,4,5,5-tetramethyl-1,3,2-dioxaborolane) (642.57 g/mol, 2.0 mmol, 1.286 g), 4,7-bis(5-bromothiophen-2-yl)benzo[*c*][1,2,5]thiadiazole (458.21 g/mol, 2.1 mmol, 0.962 g), Pd(PPh₃)₄ (1155.58 g/mol, 0.2 mmol, 0.023 g) and 40 mL of dry toluene were stirred under dry nitrogen. Following the addition of tetrabutylammonium hydroxide (2.2 mmol, 2.2 mL, 1 M in methanol) via syringe, the yellow turned brown reaction mixture was stirred at 110 °C for 5 days. End capping of the polymer was achieved with the addition of phenylboronic acid (121.93 g/mol, 0.66 mmol, 0.081 g in 1 mL methanol) which was followed one hour later with bromobenzene (157.01 g/mol, 1.495 g/mL, 0.66 mmol, 0.104 g, 0.07 mL). After another hour the reaction mixture was cooled to room temperature and the polymer was precipitated in methanol (75 mL). The brown precipitate was vacuum filtered and washed with cold methanol. Please refer to the appendix for the ¹H NMR (400 MHz, CDCl₃) spectrum.

3.5.19 Synthesis of poly[(2,7-(9-(heptadecan-9-yl)-9H-carbazole))-alt-(1,6-pyrene)] (CP)

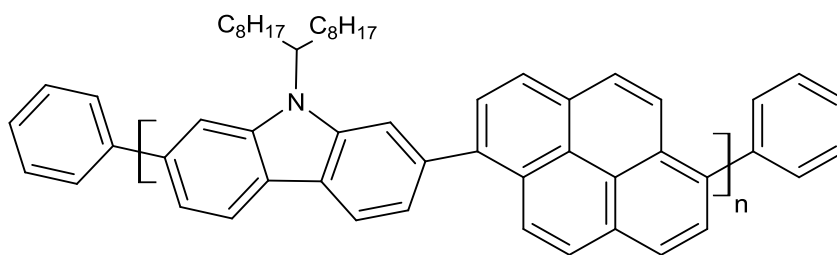


Figure 3.40: poly[(2,7-(9-(heptadecan-9-yl)-9H-carbazole))-alt-(1,6-pyrene)]

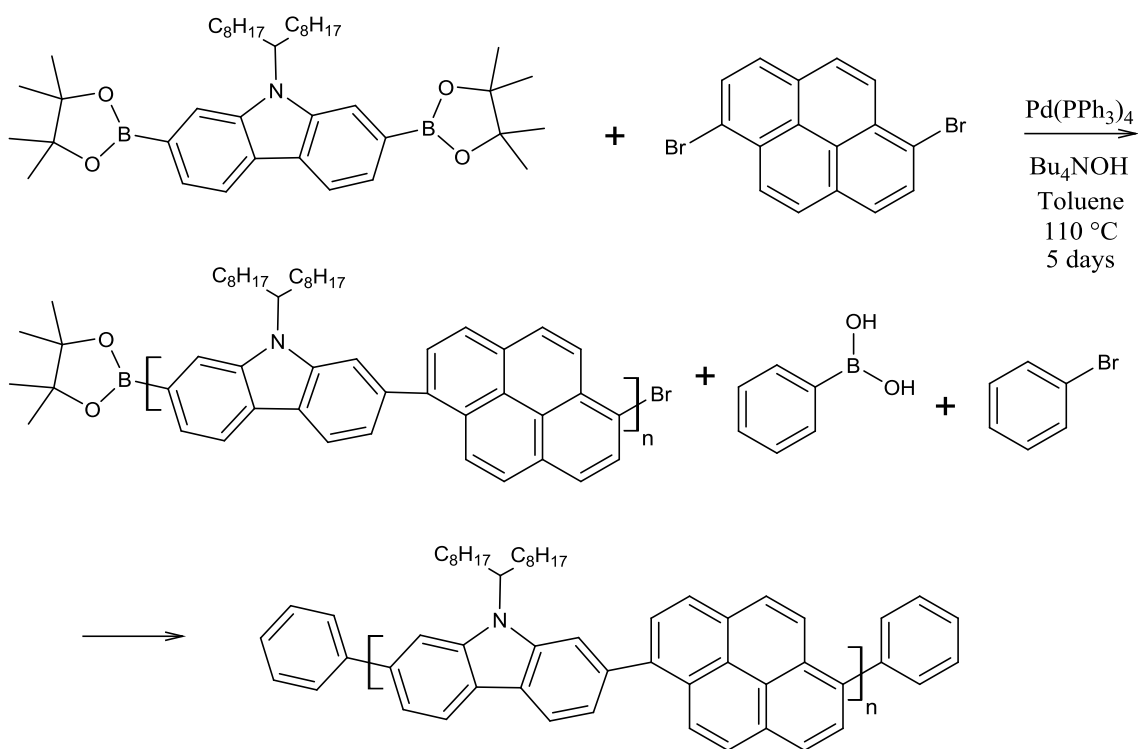


Figure 3.41: Reaction scheme for the synthesis of poly[(2,7-(9-(heptadecan-9-yl)-9H-carbazole))-alt-(1,6-pyrene)].

In a flame dried round bottom flask fitted with a reflux condenser, 9-(heptadecan-9-yl)-2,7-bis(4,4,5,5-tetramethyl-1,3,2-dioxaborolan-2-yl)-9H-carbazole (657.58 g/mol, 2.0 mmol, 1.315 g), 1,6-dibromopyrene (360.04 g/mol, 2.0 mmol, 0.720 g), Pd(PPh₃)₄ (1155.58 g/mol, 0.2

mmol, 0.023 g) and 40 mL of dry toluene were stirred under dry nitrogen. Following the addition of tetrabutylammonium hydroxide (2.0 mmol, 2.2 mL, 1 M in methanol) via syringe, the reaction mixture was stirred at 110 °C for 5 days. End capping of the polymer was achieved with the addition of phenylboronic acid (121.93 g/mol, 0.66 mmol, 0.081 g in 1 mL methanol) which was followed one hour later with bromobenzene (157.01 g/mol, 1.495 g/mL, 0.66 mmol, 0.104 g, 0.07 mL). After another hour the reaction mixture was cooled to room temperature and the polymer was precipitated in cold methanol (75 mL). The yellow precipitate was vacuum filtered, dissolved in THF and purified with a dialysis membrane (3.5kDa). Please refer to the appendix for both the MALDI-TOF MS and ^1H NMR (400 MHz, CDCl_3) spectra.

3.5.20 Synthesis of poly[(2,7-(9-(heptadecan-9-yl)-9H-carbazole))-alt-(2,7-9H-fluoren-9-one)] (CF)

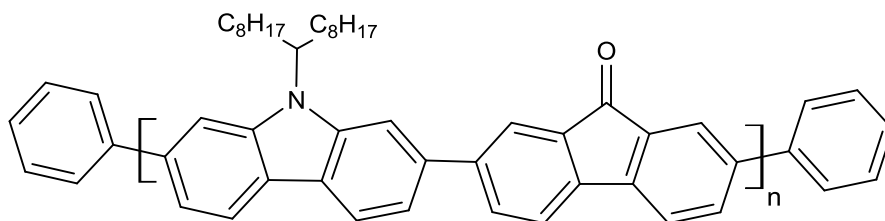


Figure 3.42: poly[(2,7-(9-(heptadecan-9-yl)-9H-carbazole))-alt-(2,7-9H-fluoren-9-one)].

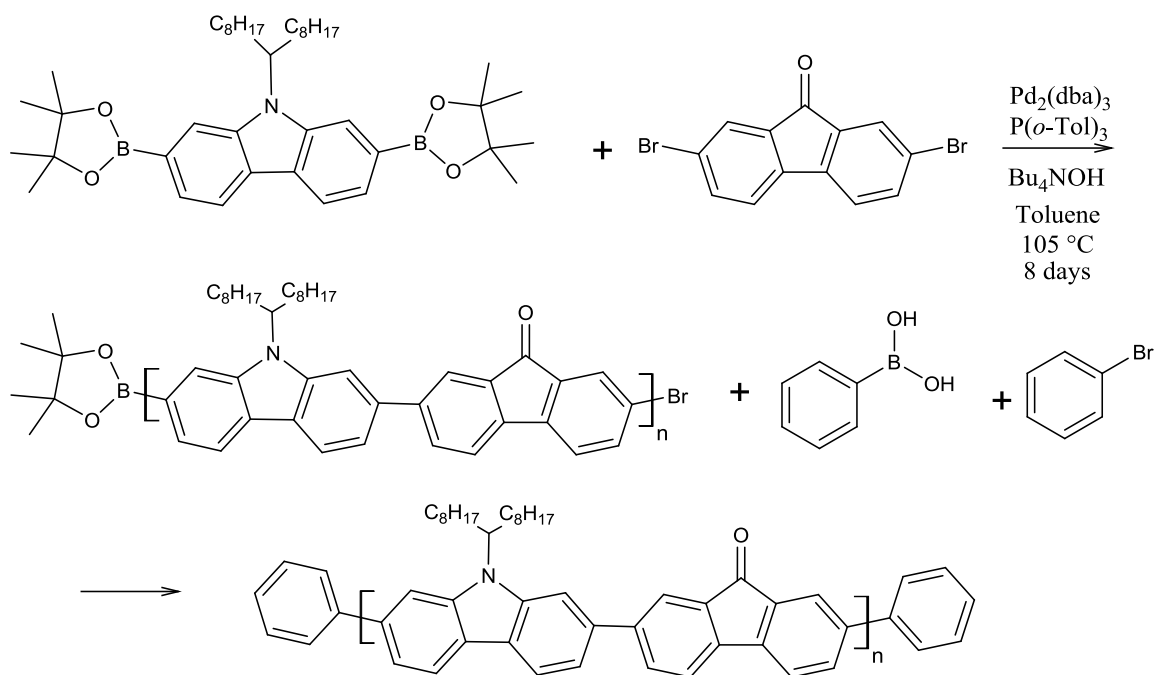


Figure 3.43: Reaction scheme for the synthesis of poly[(2,7-(9-(heptadecan-9-yl)-9H-carbazole))-alt-(2,7-9H-fluoren-9-one)].

In a flame dried round bottom flask fitted with a reflux condenser, 9-(heptadecan-9-yl)-2,7-bis(4,4,5,5-tetramethyl-1,3,2-dioxaborolan-2-yl)-9H-carbazole (657.58 g/mol, 2.0 mmol, 1.315 g), 2,7-dibromo-9H-fluoren-9-one (337.99 g/mol, 2.0 mmol, 0.676 g), Pd₂(dba)₃ (915.72 g/mol, 0.1 mmol, 0.0916 g), tri(*o*-tolyl)phosphine (304.38 g/mol, 0.1 mmol, 0.030 g) and 15 mL of dry toluene were stirred under dry nitrogen. Following the addition of tetrabutylammonium hydroxide (2.0 mmol, 2.2 mL, 1 M in methanol) via syringe, the reaction mixture was stirred at 105 °C for 8 days. End capping of the polymer was achieved with the addition of phenylboronic acid (121.93 g/mol, 0.50 mmol, 0.061 g in 2 mL toluene) which was followed one hour later with bromobenzene (157.01 g/mol, 1.495 g/mL, 0.66 mmol, 0.104 g, 0.07 mL). After another hour the reaction mixture was cooled to room temperature and the polymer was precipitated in cold methanol (75 mL). Please refer to the appendix for the ¹H NMR (400 MHz, CDCl₃) spectrum.

3.5.21 Synthesis of poly[(2,7-(9-(heptadecan-9-yl)-9H-carbazole))-alt-(5,5''-(3,3''-dihexyl-2,2':5',2'':5'',2'''-quarterthiophene))] (CT)

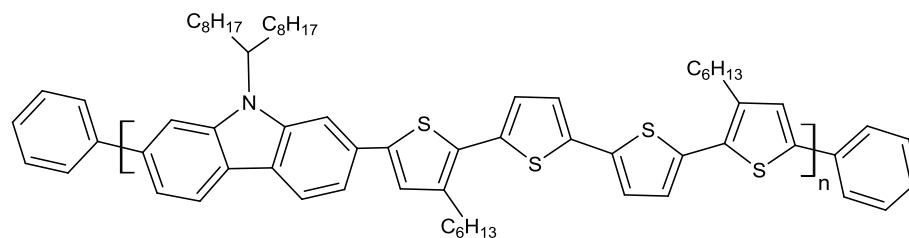


Figure 3.44: poly[(2,7-(9-(heptadecan-9-yl)-9H-carbazole))-alt-(5,5''-(3,3''-dihexyl-2,2':5',2'':5'',2'''-quarterthiophene))]

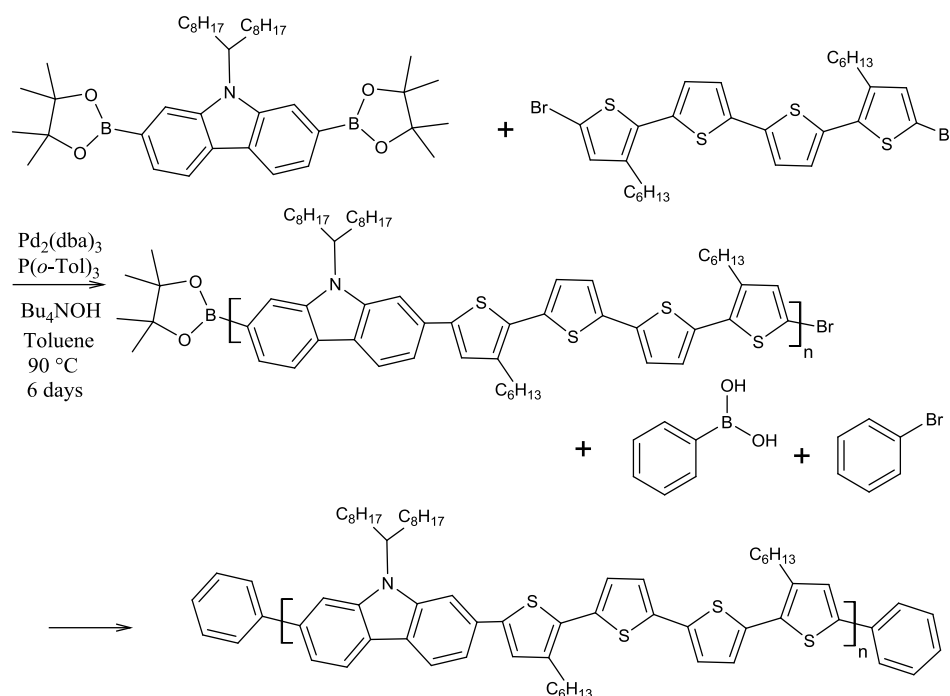


Figure 3.45: Reaction scheme for the synthesis of poly[(2,7-(9-(heptadecan-9-yl)-9H-carbazole))-alt-(5,5''-(3,3''-dihexyl-2,2':5',2'':5'',2'''-quarterthiophene))].

In a flame dried round bottom flask fitted with a reflux condenser, 9-(heptadecan-9-yl)-2,7-bis(4,4,5,5-tetramethyl-1,3,2-dioxaborolan-2-yl)-9H-carbazole (657.58 g/mol, 0.442 mmol,

0.291 g), 5,5''-dibromo-3,3''-dihexyl-2,2':5',2'':5'',2'''-quaterthiophene (656.62 g/mol, 0.442 mmol, 0.290 g), Pd₂(dba)₃ (915.72 g/mol, 0.0022 mmol, 0.002 g), tri(*o*-tolyl)phosphine (304.38 g/mol, 0.0088 mmol, 0.003 g) and 15 mL of dry toluene were stirred under dry nitrogen. Following the addition of tetrabutylammonium hydroxide (0.44 mmol, 0.44 mL, 1 M in methanol) via syringe, the reaction mixture was stirred at 90 °C for 6 days. End capping of the polymer was achieved with the addition of bromobenzene (157.01 g/mol, 1.495 g/mL, 0.0442 mmol, 0.0046 mL) which was followed two hours later with phenylboronic acid (121.93 g/mol, 0.0442 mmol, 0.005 g in 2 mL toluene). After another day the reaction mixture was cooled to room temperature and the polymer was precipitated in cold methanol (75 mL). Please refer to the appendix for the ¹H NMR (400 MHz, CDCl₃) spectrum.

3.5.22 Synthesis of poly[(2,7-(9,9-dioctyl-9H-fluorene-2,7-diyl))-alt-(1,6-pyrene)] (LP)

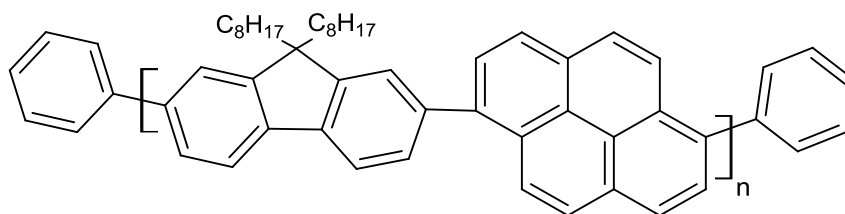


Figure 3.46: poly[(2,7-(9,9-dioctyl-9H-fluorene-2,7-diyl))-alt-(1,6-pyrene)].

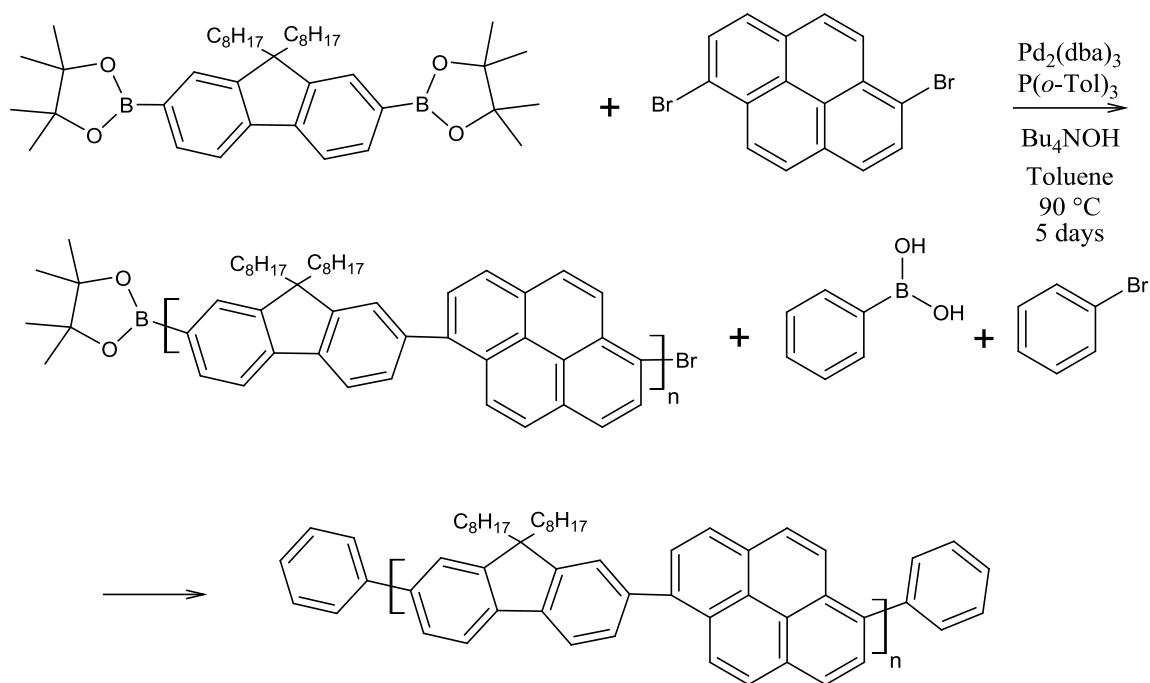


Figure 3.47: Reaction scheme for the synthesis of poly[(2,7-(9,9-dioctyl-9H-fluorene-2,7-diyl))-alt-(1,6-pyrene)].

In a flame dried round bottom flask fitted with a reflux condenser, 2,2'-(9,9-dioctyl-9H-fluorene-2,7-diyl)bis(4,4,5,5-tetramethyl-1,3,2-dioxaborolane) (642.57 g/mol, 1.0 mmol, 0.643 g), 1,6-dibromopyrene (360.04 g/mol, 2.0 mmol, 0.720 g), Pd₂(dba)₃ (915.72 g/mol, 0.0022 mmol, 0.002 g), tri(*o*-tolyl)phosphine (304.38 g/mol, 0.0088 mmol, 0.003 g) and 10 mL of dry toluene were stirred under dry nitrogen. Following the addition of tetrabutylammonium hydroxide (1.0 mmol, 1.0 mL, 1 M in methanol) via syringe, the reaction mixture was stirred at 90 °C for 5 days. End capping of the polymer was achieved with the addition of bromobenzene (157.01 g/mol, 1.495 g/mL, 0.1 mmol, 0.0105 mL) which was followed two hours later with phenylboronic acid (121.93 g/mol, 0.1 mmol, 0.012 g in 1 mL toluene). The following day the reaction mixture was cooled to room temperature and the polymer was precipitated in cold methanol (75 mL) and

stirred for one hour. The precipitate was vacuum filtered and washed with cold methanol. Please refer to the appendix for the ^1H NMR (400 MHz, CDCl_3) spectrum.

3.5.23 Synthesis of poly[(2,7-(9-(heptadecan-9-yl)-9H-carbazole))-alt-(4,7-dithien-2-yl-2,1,3-benzothiadiazole)] (CB)

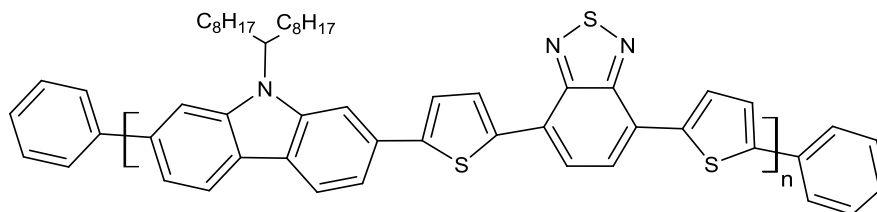


Figure 3.48: poly[(2,7-(9-(heptadecan-9-yl)-9H-carbazole))-alt-(4,7-dithien-2-yl-2,1,3-benzothiadiazole)].

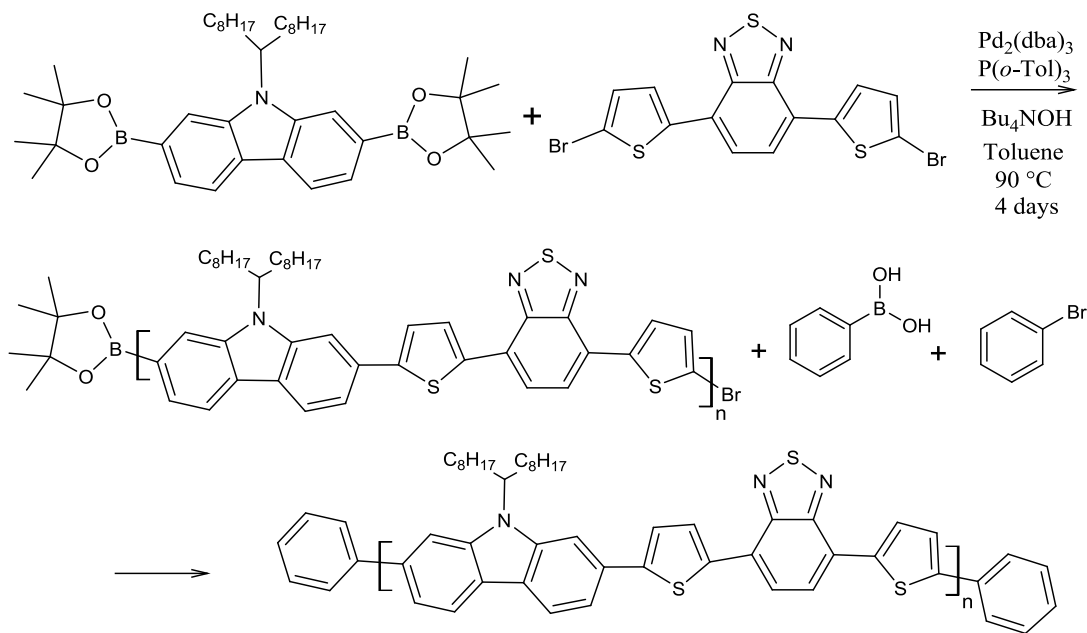


Figure 3.49: Reaction scheme for the synthesis of poly[(2,7-(9-(heptadecan-9-yl)-9H-carbazole))-alt-(4,7-dithien-2-yl-2,1,3-benzothiadiazole)].

In a flame dried round bottom flask fitted with a reflux condenser, 9-(heptadecan-9-yl)-2,7-bis(4,4,5,5-tetramethyl-1,3,2-dioxaborolan-2-yl)-9H-carbazole (657.58 g/mol, 0.5 mmol, 0.329 g), 4,7-bis(5-bromothiophen-2-yl)benzo[c][1,2,5]thiadiazole (458.21 g/mol, 0.5 mmol, 0.229 g), Pd₂(dba)₃ (915.72 g/mol, 0.0025 mmol, 0.002 g), tri(*o*-tolyl)phosphine (304.38 g/mol, 0.01 mmol, 0.003 g) and 10 mL of dry toluene were stirred under dry nitrogen. Following the addition of tetrabutylammonium hydroxide (0.5 mmol, 0.5 mL, 1 M in methanol) via syringe, the reaction mixture, which turned from pink-red to brown upon heating, was stirred at 90 °C for 4 days. End capping of the polymer was achieved with the addition of bromobenzene (157.01 g/mol, 1.495 g/mL, 0.05 mmol, 0.0053 mL) which was followed two hours later with phenylboronic acid (121.93 g/mol, 0.05 mmol, 0.006 g in 1 mL toluene). The following day the reaction mixture was cooled to room temperature and the polymer was precipitated in cold methanol (75 mL) and stirred for one hour. The precipitate was vacuum filtered and washed with cold methanol. Please refer to the appendix for the ¹H NMR (400 MHz, CDCl₃) spectrum.

Chapter 4

Results and Discussion

4.1 Theoretical Study

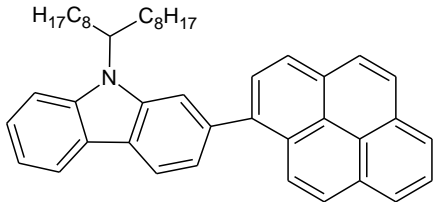
4.1.1 Oligomer Band Gaps

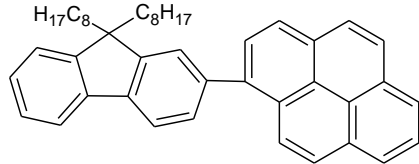
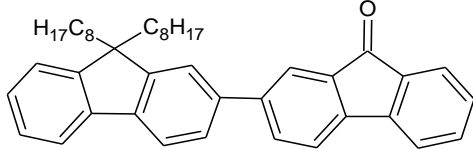
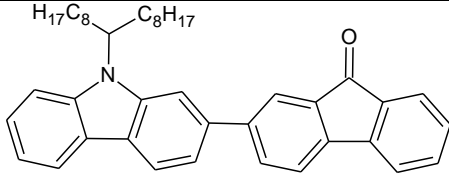
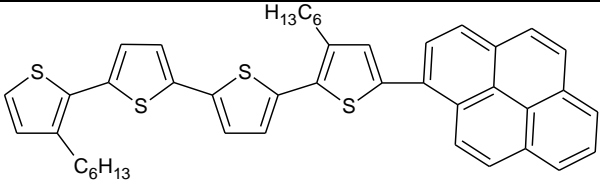
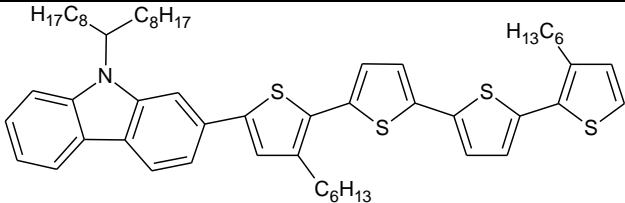
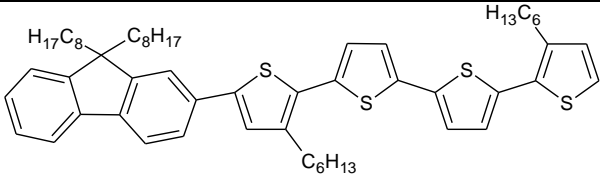
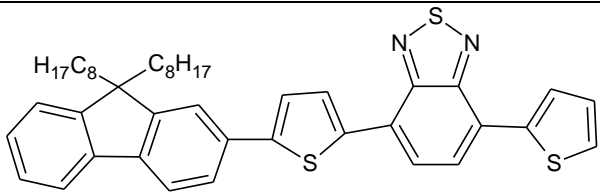
In this theoretical study, fifteen different alternating conjugated copolymers were investigated. Due to the large number of atoms contained in polymers it was necessary to study oligomeric units (fragments) of the polymers. The monomers used in this study are:

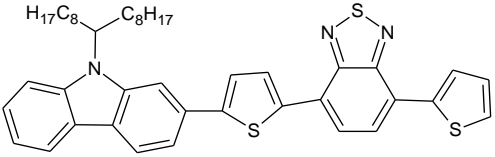
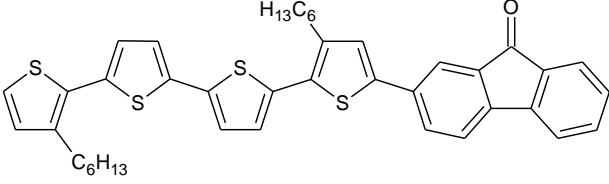
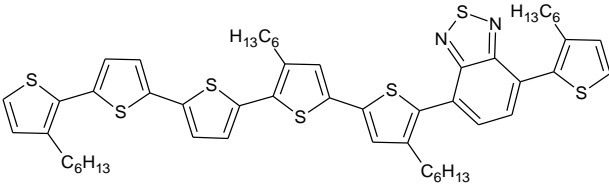
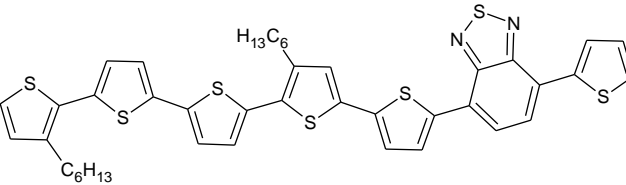
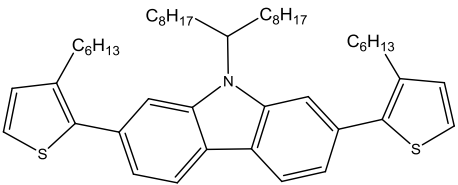
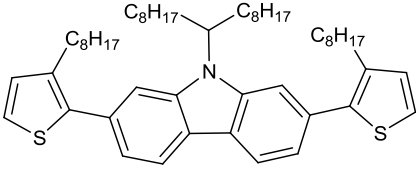
- 3,3''-dihexyl-2,2':5',2'':5'',2'''-quarterthiophene
- 1,6-pyrene
- 2,7-fluorene-9-one
- 4,7-dithien-2-yl-2,1,3-benzothiadiazole
- 4,7-bis(3-hexylthiophen-2-yl)-2,1,3-benzothiadiazole
- 2,7-(9-(heptadecan-9-yl)-9H-carbazole)
- 2,7-(9,9-dioctyl-9H-fluorene-2,7-diyl)
- 4,4'-dihexyl-2,2'-bithiophene
- 4,4'-dioctyl-2,2'-bithiophene

These monomers were paired together to form the fifteen alternating oligomers that were studied using Gaussian03.

Table 4.1: Oligomers studied using theoretical calculations.

Polymer	Structure
CP Alternating units: <ul style="list-style-type: none">• 1,6-pyrene• 2,7-(9-(heptadecan-9-yl)-9H-carbazole)	

<p>LP</p> <p>Alternating units:</p> <ul style="list-style-type: none"> • 1,6-pyrene • 2,7-(9,9-dioctyl-9H-fluorene-2,7-diyl) 	
<p>LF</p> <p>Alternating units:</p> <ul style="list-style-type: none"> • 2,7-fluoren-9-one • 2,7-(9,9-dioctyl-9H-fluorene-2,7-diyl) 	
<p>CF</p> <p>Alternating units:</p> <ul style="list-style-type: none"> • 2,7-fluoren-9-one • 2,7-(9-(heptadecan-9-yl)-9H-carbazole) 	
<p>TP</p> <p>Alternating units:</p> <ul style="list-style-type: none"> • 1,6-pyrene • 3,3''''-dihexyl-2,2':5',2'':5'',2'''-quarterthiophene 	
<p>CT</p> <p>Alternating units:</p> <ul style="list-style-type: none"> • 3,3''''-dihexyl-2,2':5',2'':5'',2'''-quarterthiophene • 2,7-(9-(heptadecan-9-yl)-9H-carbazole) 	
<p>LT</p> <p>Alternating units:</p> <ul style="list-style-type: none"> • 3,3''''-dihexyl-2,2':5',2'':5'',2'''-quarterthiophene • 2,7-(9,9-dioctyl-9H-fluorene-2,7-diyl) 	
<p>LB</p> <p>Alternating units:</p> <ul style="list-style-type: none"> • 4,7-dithien-2-yl-2,1,3-benzothiadiazole • 2,7-(9,9-dioctyl-9H-fluorene-2,7-diyl) 	

<p>CB</p> <p>Alternating units:</p> <ul style="list-style-type: none"> • 4,7-dithien-2-yl-2,1,3-benzothiadiazole • 2,7-(9-(heptadecan-9-yl)-9H-carbazole) 	 <p>The structure shows a central 2,1,3-benzothiadiazole ring connected at its 4 and 7 positions to two 2-thienyl groups. Each 2-thienyl group is further connected at its 2-position to a 9H-carbazole ring, which has a heptadecyl chain (C₁₇H₃₅) attached at the 9-position.</p>
<p>TF</p> <p>Alternating units:</p> <ul style="list-style-type: none"> • 3,3''''-dihexyl-2,2':5',2'':5'',2'''-quarterthiophene • 2,7-fluoren-9-one 	 <p>The structure shows a central fluorenone ring connected at its 2 and 7 positions to two 2,5-dithienyl groups. Each 2,5-dithienyl group has a hexyl chain (C₆H₁₃) attached at the 3-position.</p>
<p>TH</p> <p>Alternating units:</p> <ul style="list-style-type: none"> • 3,3''''-dihexyl-2,2':5',2'':5'',2'''-quarterthiophene • 4,7-bis(3-hexylthiophen-2-yl)-2,1,3-benzothiadiazole 	 <p>The structure shows a central 2,1,3-benzothiadiazole ring connected at its 4 and 7 positions to two 2-thienyl groups. Each 2-thienyl group is further connected at its 2-position to a 2,5-dithienyl group, which has a hexyl chain (C₆H₁₃) attached at the 3-position.</p>
<p>TB</p> <p>Alternating units:</p> <ul style="list-style-type: none"> • 4,7-dithien-2-yl-2,1,3-benzothiadiazole • 3,3''''-dihexyl-2,2':5',2'':5'',2'''-quarterthiophene 	 <p>The structure shows a central 2,1,3-benzothiadiazole ring connected at its 4 and 7 positions to two 2-thienyl groups. Each 2-thienyl group is further connected at its 2-position to a 2,5-dithienyl group, which has a hexyl chain (C₆H₁₃) attached at the 3-position.</p>
<p>TCT</p> <p>Symmetrical alternating unit:</p> <ul style="list-style-type: none"> • 4,4'-dihexyl-2,2'-bithiophene • 2,7-(9-(heptadecan-9-yl)-9H-carbazole) 	 <p>The structure shows a central 9H-carbazole ring connected at its 2 and 7 positions to two 2,5-dithienyl groups. Each 2,5-dithienyl group has a hexyl chain (C₆H₁₃) attached at the 3-position.</p>
<p>oTCT</p> <p>Symmetrical alternating unit:</p> <ul style="list-style-type: none"> • 4,4'-dioctyl-2,2'-bithiophene • 2,7-(9-(heptadecan-9-yl)-9H-carbazole) 	 <p>The structure shows a central 9H-carbazole ring connected at its 2 and 7 positions to two 2,5-dithienyl groups. Each 2,5-dithienyl group has an octyl chain (C₈H₁₇) attached at the 3-position.</p>

<p>oTLT</p> <p>Symmetrical alternating unit:</p> <ul style="list-style-type: none"> • 4,4'-dioctyl-2,2'-bithiophene • 2,7-(9,9-dioctyl-9H-fluorene-2,7-diyl) 	
--	--

The size of the oligomers was a concern when performing the theoretical calculations because the time to complete the calculation is dependent on the number of atoms within the molecule of interest. The number of atoms contained within the oligomers is listed in Table 4.2.

Table 4.2: Number of atoms within oligomeric units.

Polymer	Number of atoms (n=1)	Number of atoms (n=3)	Number of atoms (n=6)
CP	97	287	572
LP	95	281	560
LF	91	269	536
CF	93	275	548
TP	90	266	530
CT	137	407	812
LT	135	401	800
LB	96	284	566
CB	98	290	578
TF	86	254	506
TH	127	377	752
TB	91	269	536
TCT	123	365	728
oTCT	135	401	800
oTLT	133	395	788

Due to the size of the molecules that needed to be studied, the oligomers' geometries were optimized semi-empirically. The semi-empirical calculations were performed with the Austin Model 1 (AM1) method which provided an efficient method to determine the optimum geometry of the oligomers. The semi-empirical geometry optimizations provided a reasonable geometry to undergo energy calculations. The energy calculations were performed using density functional theory (DFT) with the 6-31G (d) basis set. The DFT energy calculations provided energy levels of the occupied and unoccupied electronic orbitals. From this data it was possible to determine the energy of the highest occupied molecular orbital (HOMO) and the lowest unoccupied molecular orbital (LUMO). The energy values produced by the calculations were in A.U. (Hartree) which was converted to eV by multiplying the values by 27.2116. Subsequently the band gap energy (E_g) was determined by calculating the energy difference between the HOMO and LUMO band levels. It was clearly observed that as the length of the oligomer was increased the energy of the band decreased. The energy associated with the π - π^* orbital gap (HOMO-LUMO gap) is decreased as the conjugation length with the polymer is increased. The results of the band gaps as oligomer size is increased is displayed in Figure 4.1.

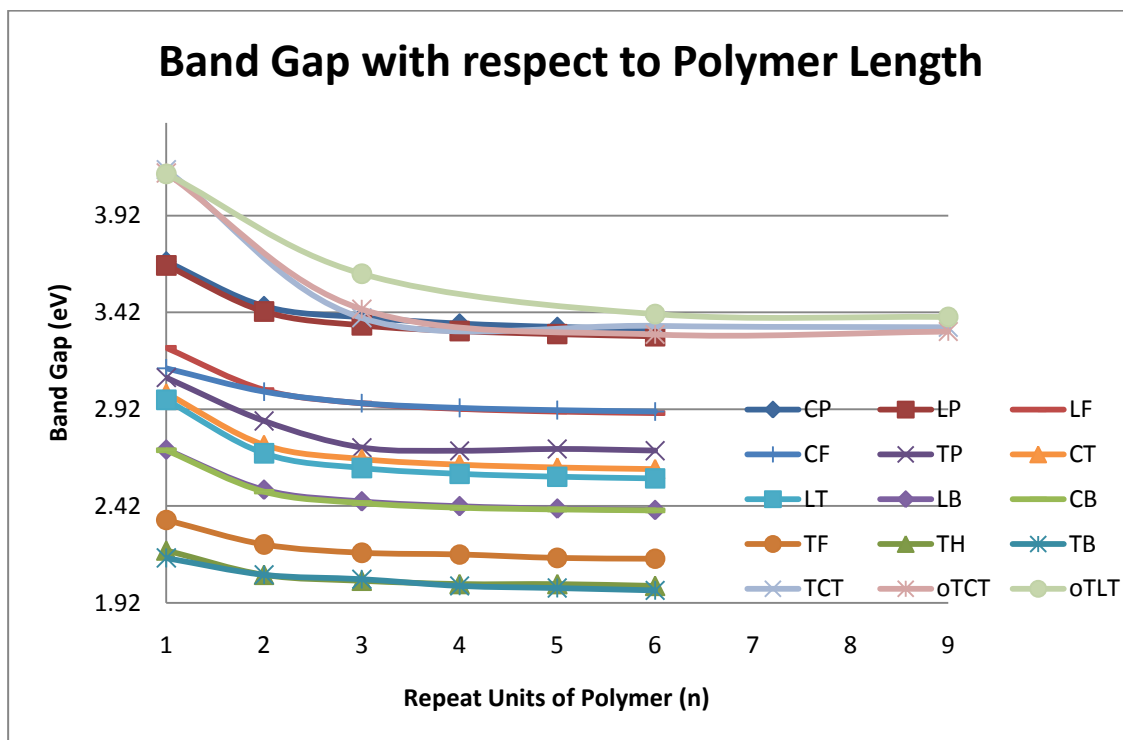


Figure 4.1: Band gap of oligomers as length (n) increases.

The graph clearly illustrates how the oligomer's band gap is decreased as the number of repeat units is increased. The addition of two oligomeric units to the original monomer drastically decreases the energy gap and this gap is further reduced as more monomers are added. The energy difference between the HOMO and LUMO level of each oligomer was determined to be relatively consistent at n=6. Therefore these values were used to compare the energy levels and band gaps of all the oligomers in the study. The band gaps are displayed in Figure 4.2, which also includes the calculated (DFT/6-31G (d)) and experimental band gap of PCBM, as well as the experimental band gap of poly-3-hexylthiophene (P3HT), and that of an ideal polymer for a bulk-heterojunction solar cell. Table 4.3 contains the energies of the HOMO level, LUMO level, and associated band gaps for the co-oligomers (n=6), P3HT, poly-3-octylthiophene (P3OT) and the

experimentally determined work functions of SWNTs, MWNTs, ITO, Al, and Ag. The table also contains predicted values for the maximum open circuit voltage (V_{OC}) of a polymer:PCBM solar cell. The maximum potential value for a PSC's V_{OC} is related to the energy difference between the HOMO of the donor (polymer) and the LUMO of the acceptor (PCBM). When raising the cell's V_{OC} by increasing the ΔE of the HOMO (donor) - LUMO (acceptor) gap it is important to consider the LUMO-LUMO gap between the donor and acceptor. The limiting value of this separation is that the energy difference between the two LUMOs must be greater than the coulombic attraction energy between the hole and electron of the exciton (approximately 0.3 eV in a conjugated polymer).

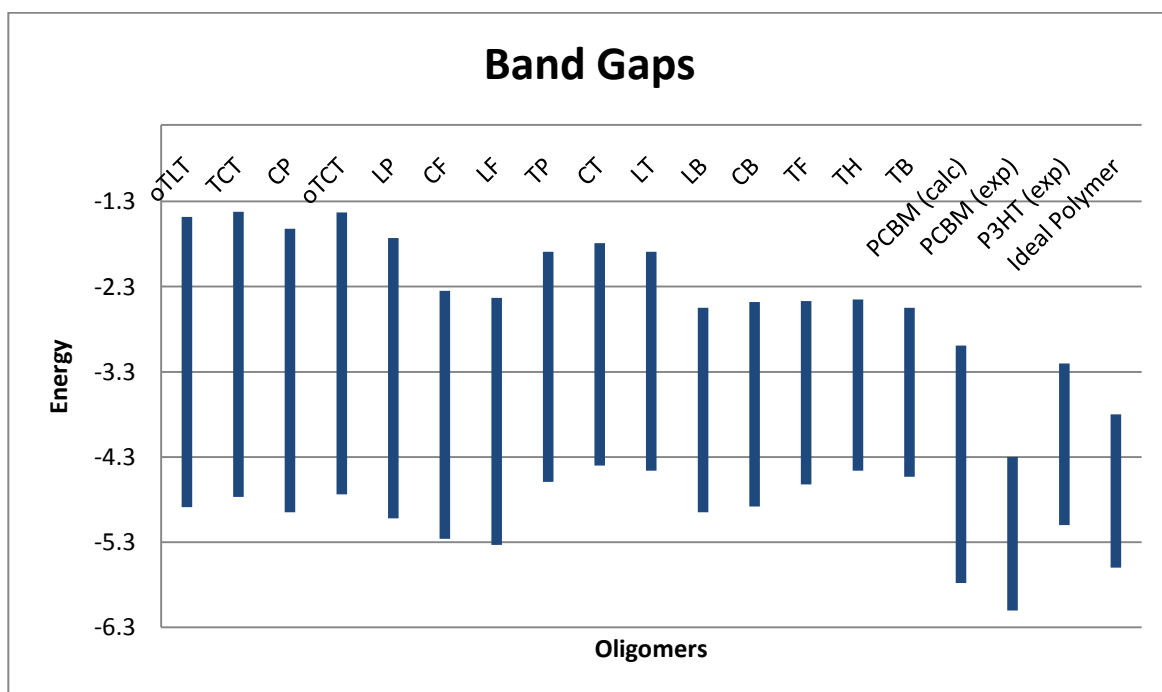


Figure 4.2: Calculated (DFT 6-31G (d)) HOMO and LUMO energy levels of the co-oligomers (n=6) and PCBM. Experimental energy levels associated with PCBM and P3HT, as reported in the literature, are also included. The bar heights are proportional to the band gap energy.

Table 4.3: Highest occupied molecular orbital (HOMO) and lowest unoccupied molecular orbital (LUMO) energies of the oligomers with six repeat units.

Polymer	HOMO (eV)	LUMO (eV)	Band Gap (eV)	Theoretical V_{OC} (from calc PCBM)	Theoretical V_{OC} (from exp PCBM)
CP	-4.95	-1.62	3.33	1.90	0.59
LP	-5.02	-1.73	3.29	1.78	0.47
LF	-5.33	-2.43	2.90	1.96	0.65
CF	-5.26	-2.35	2.91	1.75	0.44
TP	-4.59	-1.89	2.70	2.03	0.72
CT	-4.40	-1.79	2.61	2.27	0.96
LT	-4.46	-1.89	2.57	2.34	1.03
LB	-4.95	-2.55	2.40	1.60	0.29
CB	-4.88	-2.48	2.40	1.41	0.10
TF	-4.62	-2.47	2.15	1.47	0.16
TH	-4.46	-2.45	2.01	1.96	0.65
TB	-4.53	-2.55	1.98	1.89	0.58
TCT	-4.77	-1.42	3.35	1.63	0.32
oTCT	-4.74	-1.43	3.31	1.47	0.16
oTLT	-4.89	-1.48	3.41	1.54	0.23
P3HT (exp)	-5.10	-3.20	1.90	2.11	0.80
P3OT (exp)	-5.25	-2.85	2.40	2.26	0.95
Ideal Polymer	-5.8 to -5.2	-4.0 to -3.7	2.10 to 1.20	2.81 to 2.21	1.50 to 0.90
PCBM (calc)	-5.78	-2.99	2.79		
PCBM (exp)	-6.10	-4.30	1.80		
	Work Function (eV)				
SWNT (exp)	3.4 – 4.0				
MWNT (exp)	4.6 – 5.1				
ITO	4.7				
Al	4.3				
Ag	4.7				

4.1.2 Optical Absorptions

Another interesting characteristic of conjugated polymers linked to the HOMO-LUMO energy gap is the polymer's absorption of light. This absorption of light occurs in the ultra-violet and visible light regions of the electromagnetic spectrum. To determine this absorption theoretically time-dependent density functional theory (TD-DFT) was used. The calculations were performed with the 6-31G (d,p) basis set and examined forty excited states. The calculated absorption peaks were converted to Gaussian functions using the software GaussSum 2.2. An example of the converted data is shown in Figure 4.3, in which the absorption of TF (n=1 and n=3) is calculated.

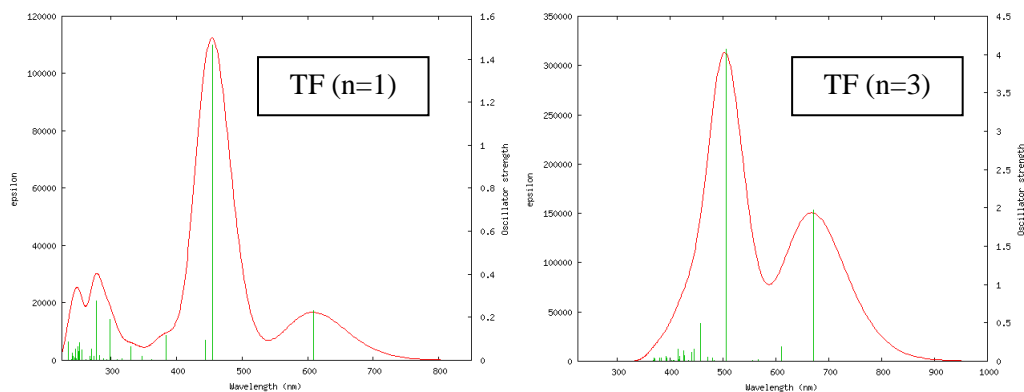


Figure 4.3: Conversion of absorption peaks to Gaussian functions.

Calculated absorptions demonstrate and emphasize the relationship between conjugation length and band gap. It is clear that there is a dramatic decrease in the energy associated with the optical absorption as the length of the oligomer is increased. The UV-Vis absorption spectrums were determined for oligomers units of n=1 and n=3 for LF, LP, CF, LB, CB, TF, TB, LT, TCT, oTLT, and oTCT. However for a few systems (CP, CT, TP, and TH) only the monomer's (n=1) absorption could be determined. This was the result of the size of the calculations and the

memory needed to perform the calculations. The greatest limitation of these calculations is their cost (time requirement).

4.1.3 Calculation Cost

The calculations were performed on the high performance computing virtual laboratory (HPCVL) at Queen’s University which was an essential resource to ensure completion of the demanding calculations. A calculation with a low level of theory, like the semi-empirical geometry optimizations, could be completed within a few hours or even minutes. Accordingly the DFT energy calculations could take anywhere from a few hours to several days. The demand presented by the TD-DFT calculations (used to determine absorption) meant that the computer had to struggle with some calculations for months. Table 4.4 provides insight into the cost of calculations, specifically providing the computing time required for the completed TD-DFT energy calculations. The cost of the calculations required to predict the absorption spectrum ranged from 1 day to over 90 days. The mean calculation time for the oligomers (n=3) was approximately 2 months. The high computational demand for these calculations illustrates the impracticality of this method to determine the optical absorption of conjugated polymers.

Table 4.4: Cost of TD-DFT energy calculations.

Job	HPCVL CPU time
TCT (n=1)	2 days 14 hours 19 minutes 10.3 seconds
oTLT (n=1)	25 days 11 hours 31 minutes 7.3 seconds
oTCT(n=1)	25 days 2 hours 38 minutes 2.1 seconds
CP (n=1)	2 days 21 hours 27 minutes 59.8 seconds
CT (n=1)	4 days 2 hours 8 minutes 54.1 seconds
LB (n=1)	2 days 7 hours 21 minutes 32.8 seconds
LF (n=1)	2 days 12 hours 16 minutes 19.1 seconds
LP (n=1)	1 days 21 hours 44 minutes 37.2 seconds
LT (n=1)	4 days 2 hours 43 minutes 57.4 seconds
TB (n=1)	1 days 22 hours 30 minutes 27.8 seconds

TF (n=1)	2 days 2 hours 1 minutes 17.9 seconds
TH (n=1)	2 days 23 hours 18 minutes 55.5 seconds
TP (n=1)	2 days 0 hours 9 minutes 28.8 seconds
CB (n=1)	1 days 19 hours 2 minutes 60.0 seconds
CF (n=1)	1 days 14 hours 3 minutes 17.7 seconds
TCT(n=3)	51 days 5 hours 57 minutes 42.9 seconds
oTLT (n=3)	67 days 4 hours 49 minutes 52.4 seconds
TB (n=3)	36 days 2 hours 12 minutes 11.4 seconds
LP (n=3)	53 days 8 hours 7 minutes 41.4 seconds
LF (n=3)	32 days 16 hours 6 minutes 39.9 seconds
LB (n=3)	33 days 0 hours 38 minutes 54.9 seconds
TF (n=3)	26 days 3 hours 57 minutes 46.2 seconds
oTCT (n=3)	79 days 8 hours 47 minutes 5.9 seconds
LT (n=3)	90 days 14 hours 40 minutes 56.6 seconds
CB (n=3)	41 days 7 hours 59 minutes 32.4 seconds
CF (n=3)	25 days 13 hours 18 minutes 34.7 seconds

4.1.4 Fragment Interactions

A final aspect of the theoretical study was the investigation of possible interactions between oligomers and carbon nanotubes. The first part of the interaction study was performed to determine if oligomers had a noticeable effect on one another. These calculations were done with the semi-empirical AM1 method to determine the optimal geometry of three oligomers that were in close proximity. Unfortunately, only results for one system (oTLT) were achieved. In this system, three oligomers of oTLT (n=3) were confined to a small region of space to examine any possible interactions between units. This calculation contained 1185 atoms and took 13 days 11 hours 12 minutes and 40.9 seconds to complete. The image of the optimized geometry is shown in Figure 4.4.

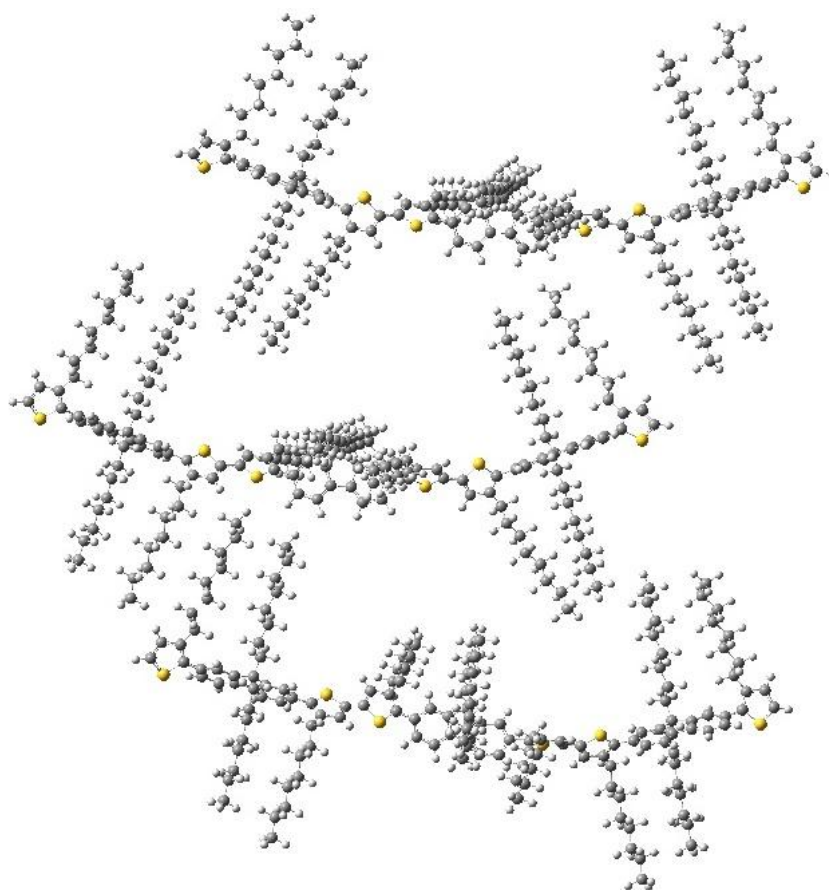


Figure 4.4: Optimized geometry of three oTLT ($n=3$) oligomers.

Along with oligomer-oligomer interactions, the interaction between the polymer and a single-walled carbon nanotube was investigated. This investigation required the construction and optimization of a carbon nanotube fragment. Geometry optimizations were attempted with both zigzag and armchair nanotubes, although only the armchair tubes yielded successful results. The armchair tubes that were investigated consisted of 168 ($n=1$), 504 ($n=3$), and 1008 ($n=6$) atoms. The first fragment ($n=1$) had a geometry optimization performed by DFT methods that took nearly five days. Based on this result the following geometry optimizations were performed semi-empirically, but still lasted up to twenty days ($n=6$).

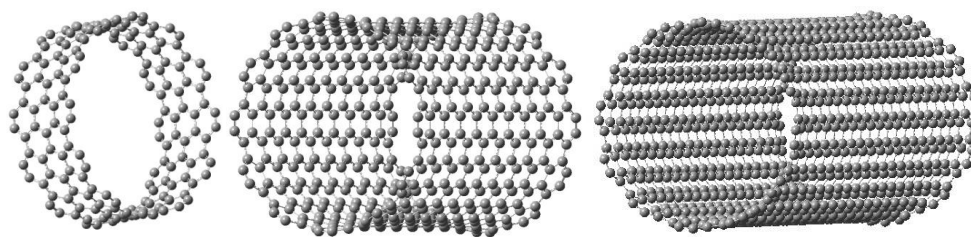


Figure 4.5: Armchair single-walled carbon nanotubes (n=1, 3, and 6) with semi-empirically (AM1) determined geometries.

Further calculations were performed to determine if there would be an interaction between the carbon nanotube and an oligomer. The n=3 oligomer of polymer TP, which contains a pyrene moiety, was positioned near the n=3 nanotube and then a geometry optimization was performed (AM1). The result illustrates an attraction caused by π - π stacking between the pyrene and carbon nanotube surface (Figure 4.6). This intermolecular interaction is attributed to π - π stacking between the polymer and CNT aromatic carbons. The distance between the pyrene (C_{283}) and SWCNT (C_{152}) was found to be 4.898 Å, which is relatively close to the π - π stacking distance exhibited between two porphyrin rings (3.4 - 3.6 Å) [58]. To provide more evidence of this interaction the use of force field calculations can be used in future studies.

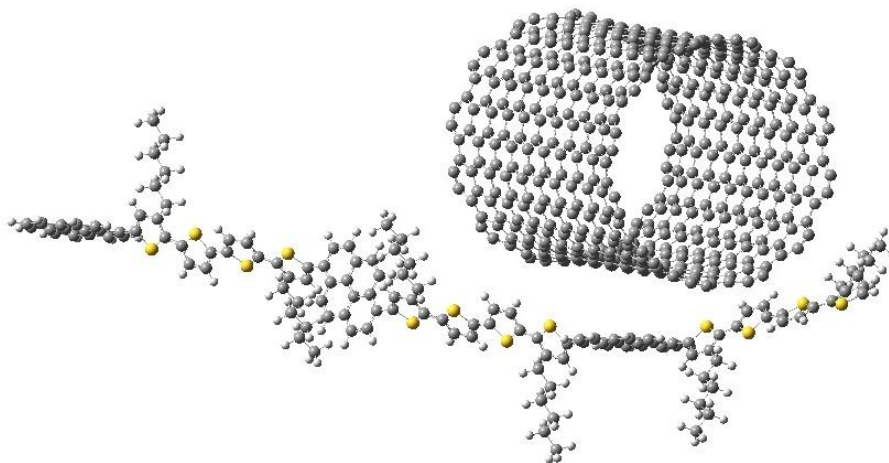


Figure 4.6: CNT interaction with TP (quaterthiophene-pyrene co-oligomer)

4.2 Polymer Synthesis

4.2.1 Synthetic Process

In conjunction with the theoretical calculations, an experimental study was performed that included the synthesis of eleven polymers. Many of the physical properties of the polymers that were synthesized in this investigation were predicted with the calculations. The synthesized polymers are LF, CP, LP, CF, LB, CB, TF, CT, TCT, oTCT, and oTLT. The three polymerization methods used to prepare the polymers were Stille cross-coupling, Suzuki-Miyaura cross-coupling, and oxidative coupling with anhydrous FeCl₃. Iron (III) chloride was used to oxidatively couple three polymers (TCT, oTCT, and oTLT), Suzuki coupling was used for eight (LF, LB, CP, CB, LP, CT, and CF) and one polymer (TF) was prepared via Stille and Suzuki coupling. The fluorescence of the polymers under ultraviolet light is shown in Figure 4.7.

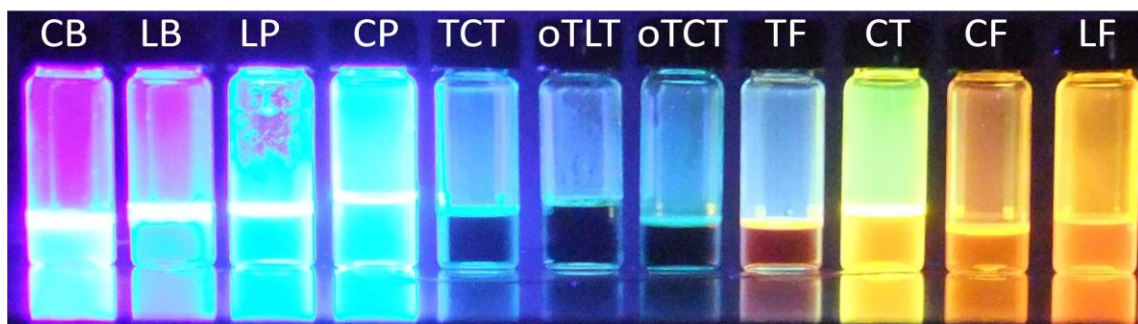


Figure 4.7: Fluorescence of synthesized conjugated polymers

The polymers prepared via oxidative coupling (using iron (III) chloride) required the preparation of symmetric monomers with a thiophene moiety on both ends. The thiophene provided the reactive site for the oxidative coupling between monomers to occur. For example, TCT (Figure 4.8) has a carbazole core with a hexyl-thiophene group on both ends in the 2 and 7 position.

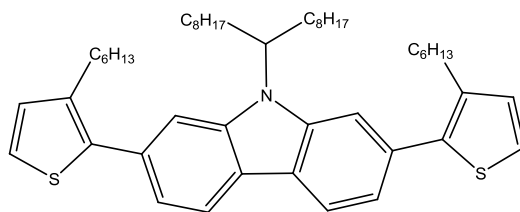


Figure 4.8: TCT monomer

For Suzuki coupling to function as a polymerization technique, it is necessary to have two uniquely disubstituted monomers to ensure that the polymer is an alternating copolymer and not a block copolymer. To ensure that the polymer achieves its desired design one monomer must be borynated on each end and the other monomer must have a halogen substituted on both ends. In this study, the borylated monomers were a pinacol borane derivative and bromine was used as the halogen.

One of the two monomers for the Stille cross-coupling reaction was also disubstituted with bromine, although the other monomer needed to be stannylated. For the only Stille polymerization, (3,3''-dihexyl-[2,2':5',2'':5'':2'''-quaterthiophene]-5,5'''-diyl)bis(tributylstannane) was synthesized from 3,3'''-dihexyl-2,2':5',2'':5'':2'''-quaterthiophene via a lithiation reaction followed by the addition tributyltin chloride. The major drawback of the Stille coupling was the use of the stannylated monomer and tin reaction by products that the reaction produces. The reaction conditions and catalyst usage for the various reactions is displayed in Table 4.5. The Suzuki and Stille reactions both required a Pd⁰ catalyst and heating, whereas the symmetric monomers were polymerized at room temperature solely in the presence of FeCl₃. The polymers were primarily purified by precipitation in methanol, although CP and LF were further purified with the use of a dialysis membrane. To purify the polymers via dialysis, the polymer was dissolved in THF and injected into a small pouch made from a membrane with pores to allow the small oligomers to travel through. The pouch was placed in a beaker of THF for a day to provide

adequate time for the oligomers to seep out of the bag. After the dialysis was complete, the remaining contents of the bag were removed (purified polymer).

Table 4.5: Polymerization reaction conditions

Polymer	Method	Solvent	Catalyst	Co-catalyst	Time (days)	Temperature (°C)
TF	Stille	Toluene	Pd(PPh ₃) ₄	None	6	90
TF	Suzuki	Toluene	Pd(PPh ₃) ₄	P(<i>o</i> -Tol) ₃	7	95
LF	Suzuki	Toluene	Pd(PPh ₃) ₄	None	7	95
LB	Suzuki	Toluene	Pd(PPh ₃) ₄	None	5	110
CP	Suzuki	Toluene	Pd(PPh ₃) ₄	None	5	110
CF	Suzuki	Toluene	Pd ₂ (dba) ₃	P(<i>o</i> -Tol) ₃	8	105
CT	Suzuki	Toluene	Pd ₂ (dba) ₃	P(<i>o</i> -Tol) ₃	6	90
LP	Suzuki	Toluene	Pd ₂ (dba) ₃	P(<i>o</i> -Tol) ₃	5	90
CB	Suzuki	Toluene	Pd ₂ (dba) ₃	P(<i>o</i> -Tol) ₃	4	90
TCT	Oxidative Coupling	Dichloromethane	FeCl ₃	None	1	23
oTCT	Oxidative Coupling	Dichloromethane	FeCl ₃	None	1	23
oTLT	Oxidative Coupling	Dichloromethane	FeCl ₃	none	1	23

The reaction mechanisms for the catalyzed polymer syntheses are very similar. The Stille reaction involves the oxidative addition of the halogenated monomer to the catalyst which is followed by transmetalation (Figure 4.9). In the transmetalation step, the alternating monomer is coordinated with the palladium as the halogen coordinates with the tin. The final step to form the new carbon-carbon bond is the reductive elimination of the two monomers from the palladium. This cross-coupling reaction is analogous to Suzuki coupling in which the tin is replaced with boron. The reaction to polymerize the symmetrical monomers with FeCl₃ involved a radical mechanism similar to the polymerization of thiophene to prepare polythiophene (Figure 4.10).

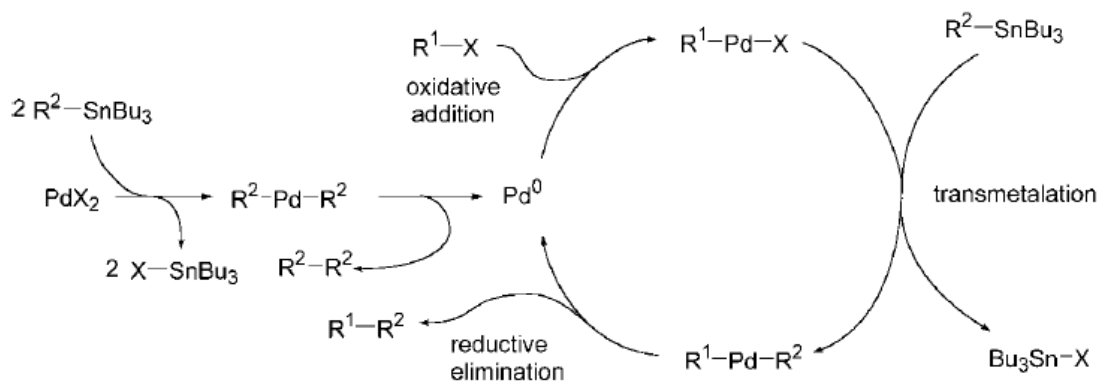


Figure 4.9: Stille cross-coupling mechanism [55].

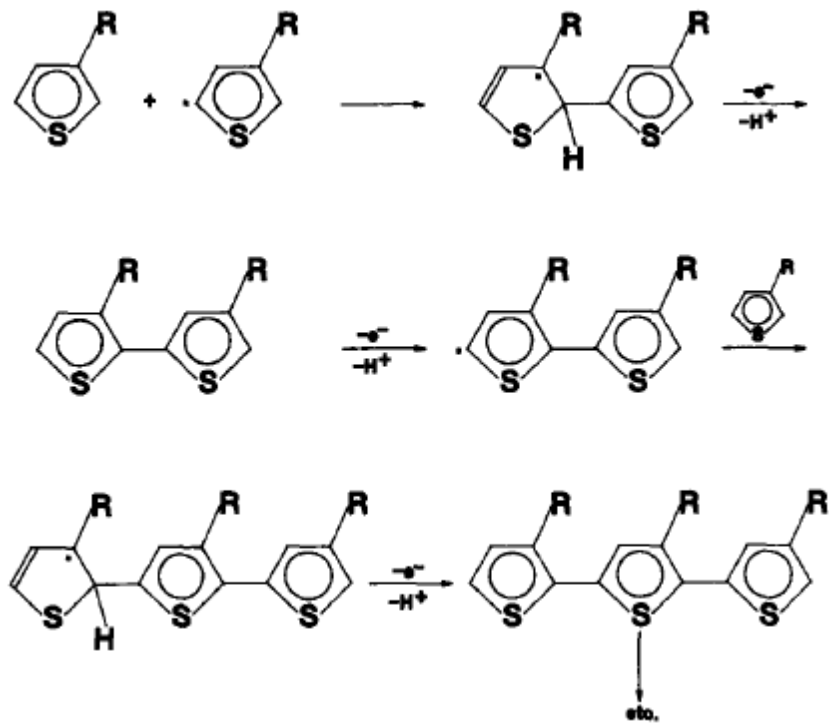


Figure 4.10: Oxidative coupling radical mechanism [53].

4.2.2 Absorption and Emission Spectra

An important experimental characteristic of the polymers is their ability to absorb and emit light. The absorption of the polymer provides insight into the π -conjugation and length of the polymer. The majority of the monomers in this study primarily absorb light in the ultra-violet region. However, this characteristic is dramatically altered by the formation of the alternating copolymers. It is particularly interesting to note the similarity between the predicted absorbance spectrum and those that were experimentally determined. Emission of light occurs from the polymers via fluorescence. The emission of the fluorescent light was detected as the samples of polymer in solution were exposed to 366 nm light. The fluorescent emission is always at a lower energy level than the absorption and furthermore as the band gap energy decreases the emission red shifts (shifts toward the infrared).

By comparing the experimental and theoretical absorption spectra of the polymer LP, it is clearly illustrated how useful the TD-DFT calculations were. Both the results for the monomer ($n=1$) and oligomer ($n=3$) are compared with the experimental results and are displayed in Figure 4.11. Figure 4.13 illustrates the similarity between the experimental and theoretical absorbance as well as the red shift of the polymer's fluorescence emission and thin film absorption. Table 4.6 illustrates the discrepancy between the theoretically determined band gaps (E_g) and those determined experimentally by UV-visible absorption spectroscopy. The band gap was calculated by plotting $\ln A$ versus the photon energy ($1240/\lambda$) and extrapolating the minimum energy of absorption. The majority of the theoretical band gaps are 0.6 eV greater than the experimental energy gaps, except for LB and CB whose theoretical E_g is less than the experimental E_g .

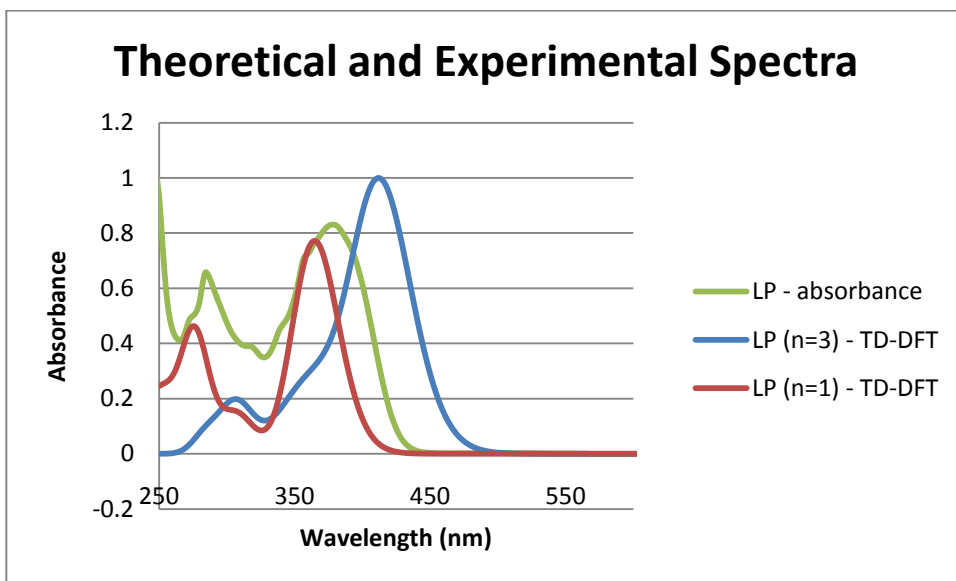
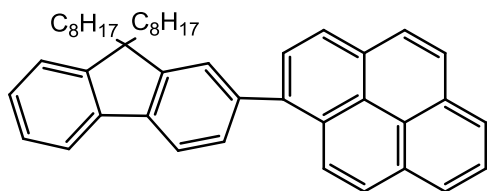


Figure 4.11: LP absorption comparison (theoretical and experimental).

LP (n=1)



LP (n=3)

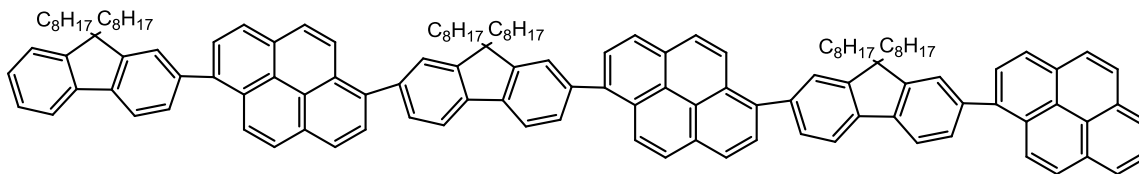


Figure 4.12: Structures of the LP monomer and oligomer (n=3).

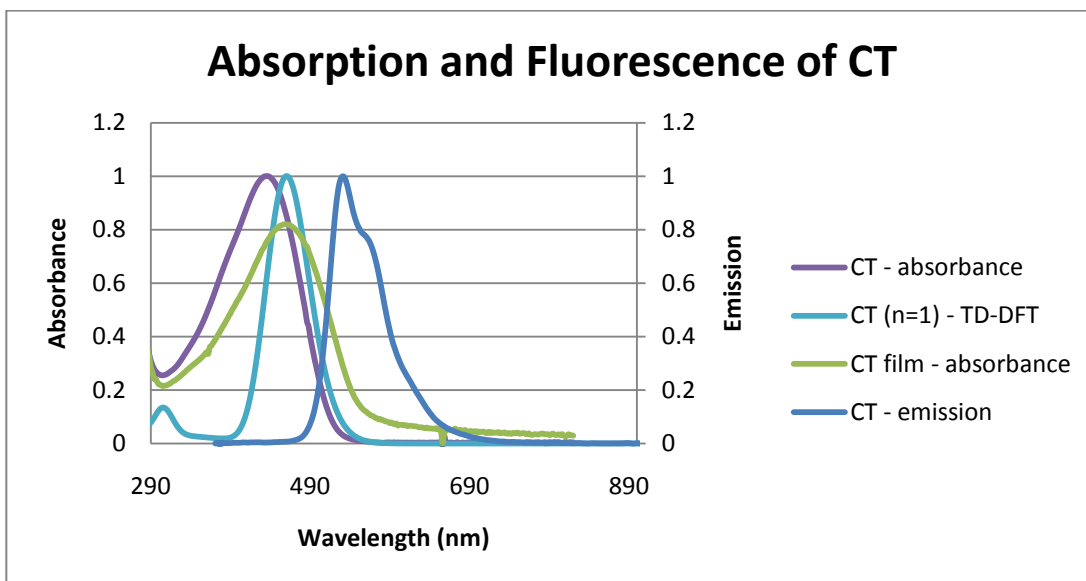


Figure 4.13: Absorbance and fluorescence comparison of CT.

CT (n=1)

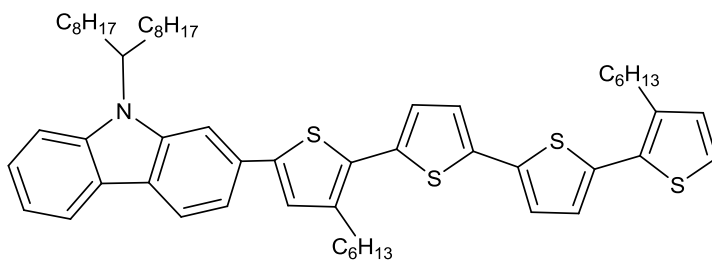


Figure 4.14: Structure of the CT monomer.

Table 4.6: Polymer band gaps (E_g) (determined by theoretical calculations and UV/Vis absorption spectroscopy) and their fluorescence emission (λ_{max}).

Polymer	Theoretical Band Gap (eV)	Experimental Band Gap (eV)	Difference in E_g (eV)	Fluorescence (λ_{max}) (nm)	Fluorescence (λ_{max}) (eV)
CP	3.33	2.75	0.58	449.93	2.76
LP	3.29	2.74	0.55	449.93	2.76
LF	2.90	2.12	0.78	578.85	2.14
CF	2.91	2.12	0.79	579.21	2.14
CT	2.61	2.20	0.41	531.1	2.34
LB	2.40	2.70	-0.30	436.26	2.84
CB	2.40	2.92	-0.52	429.96	2.88
TF (Stille)	2.15	1.64	0.51	507.66	2.44
TF (Suzuki)	2.15	2.06	0.09	495.32	2.50
TCT	3.35	2.58	0.77	497.87	2.49
oTCT	3.31	2.46	0.85	499.32	2.48
oTLT	3.41	2.50	0.91	500.77	2.48

4.2.3 MALDI analysis

The polymers produced in this investigation were characterized using several methods, one of which being MALDI. MALDI, more specifically MALDI-TOF, is a technique used in mass spectroscopy to determine the mass of large macromolecules and proteins. MALDI (matrix assisted laser desorption/ionization) attempts to provide a non-destructive method to examine the mass of polymers using time-of-flight (TOF) mass spectroscopy. The matrices used in this research were 2,5-dihydroxybenzoic acid (DHB) and α -cyano-4-hydroxycinnamic acid (CHCA) (refer to Figure 4.15) which help protect the polymers from fragmentation from the laser.

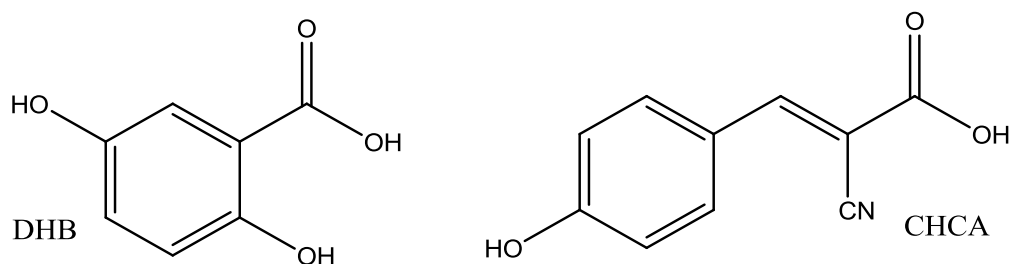


Figure 4.15: MALDI matrices (DHB and CHCA).

The results from the MALDI-TOF mass spectrometer failed to exhibit long polymeric units. This can be caused by many factors including a poorly selected matrix (as there are many possibilities) or poor TOF resolution. The MALDI spectrum of the TCT polymer exhibits peaks up to 2.6 kDa which implies that oligomers (approximately $n=4$) are successfully reaching the TOF (Figure 4.16). The capabilities of the MALDI were tested with MEH-PPV (purchased from Sigma-Aldrich) and P3HT, which resulted in similar spectra (primarily monomer).

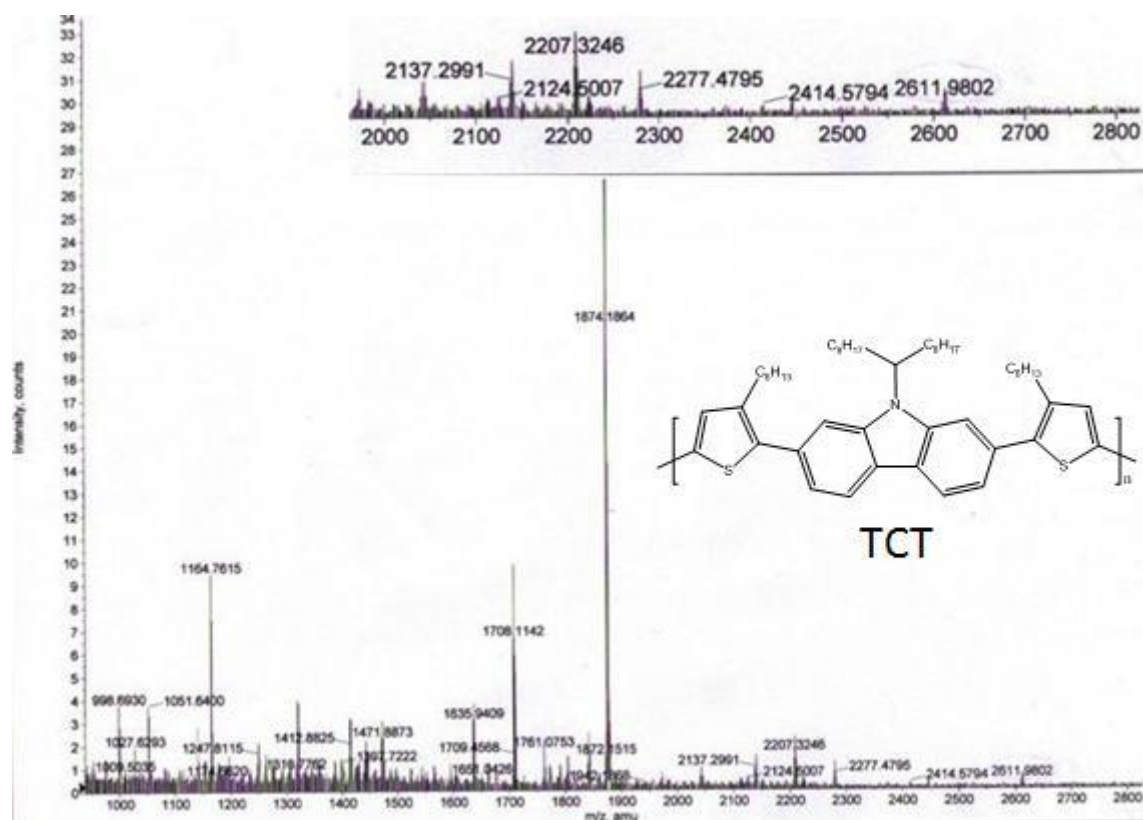


Figure 4.16: MALDI-TOF spectrum of the polymer TCT with a DHB matrix.

4.2.4 GPC results

Unlike the MALDI-TOF determination of mass, gel permeation chromatography (GPC) does not fragment the polymer at all. GPC relies on the theory of size exclusion chromatography in which molecules are passed through columns filled with gel. The gel contains pores which slow the progress of smaller molecules. Therefore, large molecules have a shorter retention time in a GPC column as opposed to small molecules that are retained for a longer period of time. This completely non-destructive method not only can be used to determine a polymer's average molar mass but also its polydispersity index (PDI). Due to the unknown retention characteristics of the polymers in this study, all the GPC results were compared to a polystyrene (PS) standard to determine the average masses.

The three mass values are statistically determined and are able to provide information concerning the polymers length (Table 4.7). The three masses are number average molecular mass (M_n), weight average molecular mass (M_w), and Z average molecular mass (M_z). These values can subsequently be used to determine the polydispersity (PDI) of the polymer sample, which is an indication of the variation in the degree of polymerization. The variation in size or PDI is most often determined by dividing the M_w by M_n . The results indicate that the Suzuki coupling provided a much smaller PDI than the oxidative coupling which implies that Suzuki coupling is more controlled than the coupling with iron (III) chloride.

Table 4.7: GPC determined masses and polydispersity of the synthesized polymers.

Polymer	M_n (g/mol)	M_w (g/mol)	M_z (g/mol)	M_w/M_n	M_z/M_n	Coupling
TCT	3 554	5 131	8 163	1.44	2.30	Oxidative
oTCT	5 441	17 440	42 010	3.21	7.72	Oxidative
oTLT	3 608	21 590	68 730	5.98	19.05	Oxidative
CP	1 228	1 579	2 189	1.29	1.78	Suzuki
LF	2 030	2 305	2 712	1.14	1.34	Suzuki
CF	42 480	42 670	42 870	1.01	1.01	Suzuki
TF	3 242	4 819	7 163	1.49	2.21	Stille
TF	1 816	2 219	2 909	1.22	1.60	Suzuki
LB	2 245	2 446	2 666	1.09	1.19	Suzuki
CT	3 296	4 888	6 951	1.48	2.11	Suzuki
LP	2 673	3 693	5 263	1.38	1.97	Suzuki
CB	1 762	1 867	1 989	1.06	1.13	Suzuki
P3HT	28 360	50 390	74 190	1.78	2.62	Suzuki
MEH-PPV	157 900	359 400	537 000	2.28	3.40	Suzuki

4.3 Solar Cells

4.3.1 Fabrication without SWCNTs

The cells fabricated in this study have provided preliminary results that provide insight into the photovoltaic activity of the prepared polymer composites (with and without SWCNTs). The polymer solar cells (PSCs) were characterized using a semi-conductor parameter analyzer. With such a device it was possible to determine the overall efficiency (%) of each cell as well as the maximum power (P_{\max}), open-circuit voltage (V_{OC}), short-circuit current density (I_{SC}), and the cell's fill factor (FF). Parameters of the polymer solar cells (not containing carbon nanotubes) showing photovoltaic activity are found in Table 4.8 (fabricated with an aluminum back electrode) and Table 4.9 (fabricated with a silver back electrode). The light source was held at a constant distance from the solar cell surface to ensure all cells received the same light intensity (60 mW/cm^2). An investigation into the effect of light intensity was performed which illustrated the dependence of the cell's power output on light intensity (as intensity is decreased the power output is reduced).

The solar cell's function can be influenced by many factors that include the homogeneity of the cell layers, composition of electrodes, and most importantly the morphology of the active layer. Defects in the active layer can significantly reduce the performance of a cell and can create short circuits. Parameters that must be carefully controlled when forming the film are solvent, concentration, speed, and ratio of PCBM to polymer in the mixture. With many different polymers it is very difficult to assume these parameters are consistent as each parameter may vary according to the polymer.

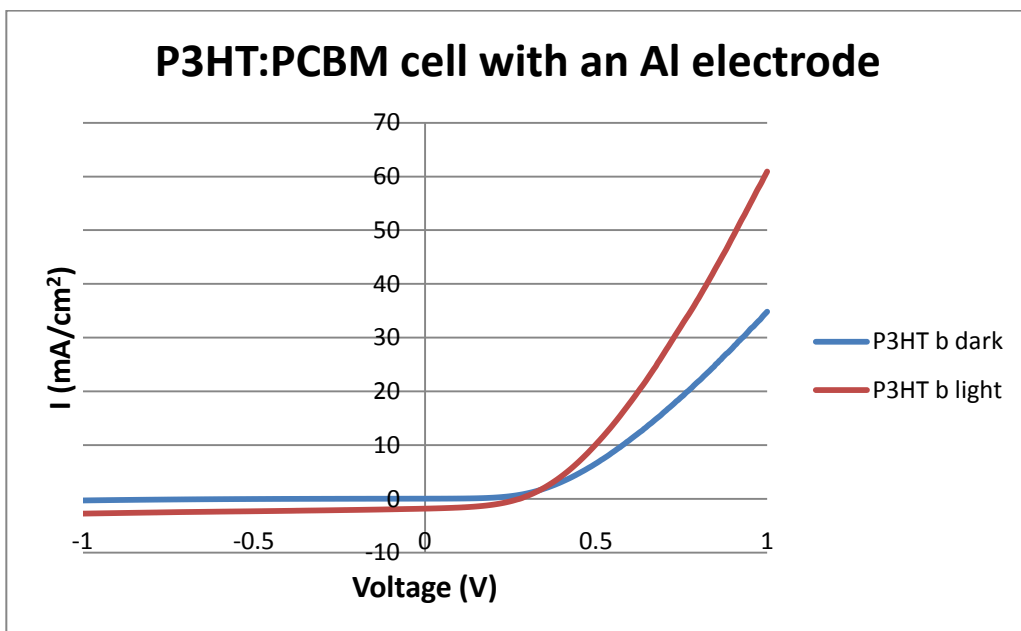


Figure 4.17: P3HT:PCBM solar cell with Al back electrode.

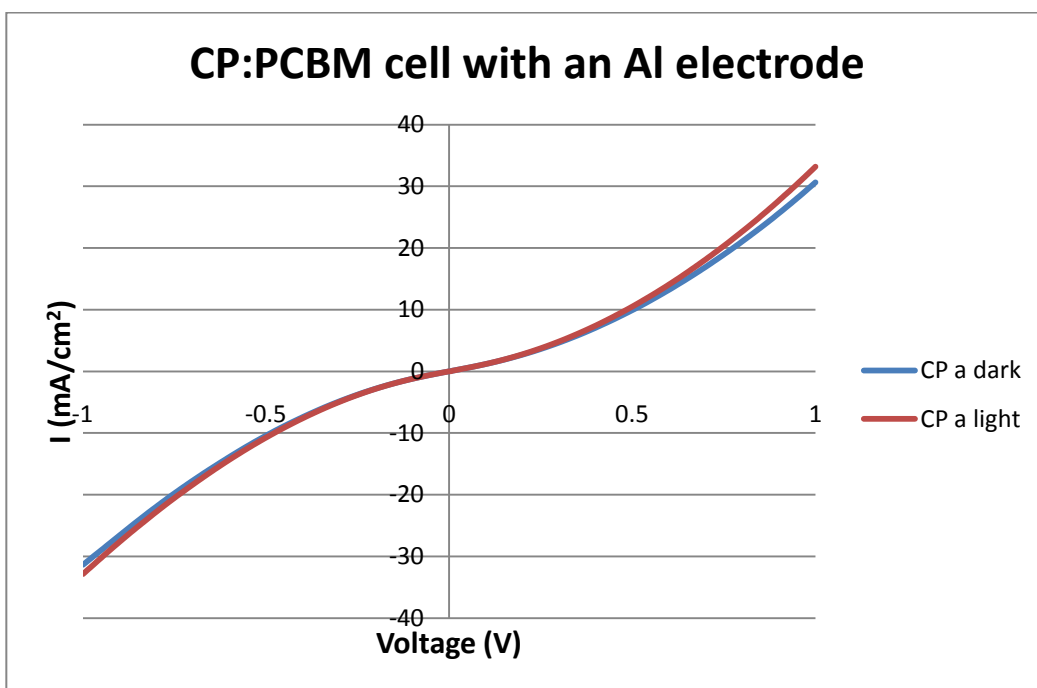


Figure 4.18: Non-functional CP:PCBM solar cell with Al back electrode.

Table 4.8: Parameters of BHJ solar cells (no SWNTs) with an aluminum back-electrode.

Cell	Efficiency (%)	P_{\max} (mW)	V_{oc} (V)	I_{sc} (mA/cm ²)	FF (%)
P3HT a	1.02	1.32E-1	0.270	-1.16	42.30
P3HT b	1.33	1.73E-1	0.275	-1.45	43.50
P3HT c	0.713	4.28E-2	0.265	-1.7826	45.25
P3HT d	0.749	4.49E-2	0.275	-1.8361	44.49
MEH-PPV 1	1.71E-3	2.22E-4	0.020	-0.061	18.30
MEH-PPV 2	0.1172	1.52E-2	0.705	-0.082	26.20
CF a	2.55E-6	1.28E-5	0.010	-0.006	21.07
CF b	2.30E-6	1.15E-5	0.010	-0.006	18.58
CT a	1.20E-3	6.00E-3	0.120	-0.183	27.22
CT b	2.39E-3	1.20E-2	0.190	-0.224	27.99

Table 4.9: Parameters of BHJ solar cells (no SWNTs) with a silver back-electrode.

Cell	Efficiency (%)	P_{\max} (mW)	V_{oc} (V)	I_{sc} (mA/cm ²)	FF (%)
CT a	5.52E-3	717.9E-6	0.035	-0.425	24.13
CT b	6.96E-3	904.6E-6	0.040	-0.458	24.67
P3HT a	3.82E-1	49.7E-3	0.120	-8.1961	25.26
P3HT b	1.22E-1	15.8E-3	0.090	-3.2044	27.40
MEH-PPV a	5.24E-2	6.81E-3	0.080	-1.7718	24.02
MEH-PPV b	2.46E-2	3.19E-3	0.045	-1.4803	24.01

4.3.2 Fabrication with SWCNTs

The characteristics of solar cells prepared with single-walled carbon nanotubes (SWNTs) that show photovoltaic activity are displayed in Table 4.10. The cells were characterized in the same method as the cells without CNTs. OPVs prepared with oTCT/PCBM and oTLT/PCBM films did not display any photovoltaic activity; however, cells containing oTCT/PCBM/SWCNT and oTLT/PCBM/SWCNT composites did indeed exhibit slight photovoltaic activity. The carbon nanotubes are thought to aid in the organization of the polymer chains within the active layer.

This increased regularity within the active layer is believed to occur by the structuring of the polymeric chains around the SWNTs. Research performed by Derbal-Habek and co-workers found the short-circuit current density (I_{SC}) and open circuit voltage (V_{OC}) of a P3HT/PCBM cells could be increased with the addition of single-walled carbon nanotubes [59]. The preliminary results of this study support the notion that SWCNTs can have an advantageous effect on the performance of polymer solar cells.

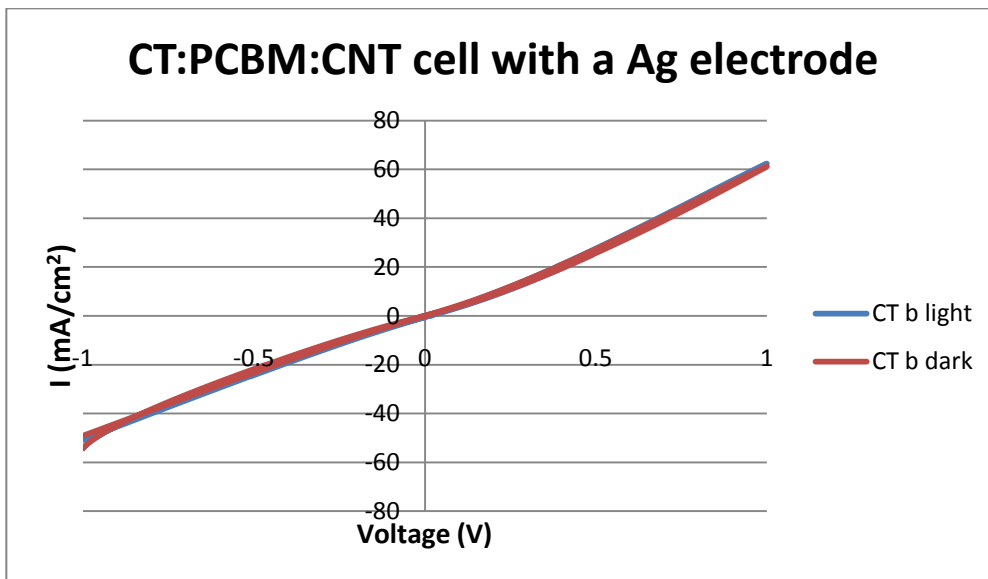


Figure 4.19: Functioning CT:PCBM:CNT solar cell with silver electrode.

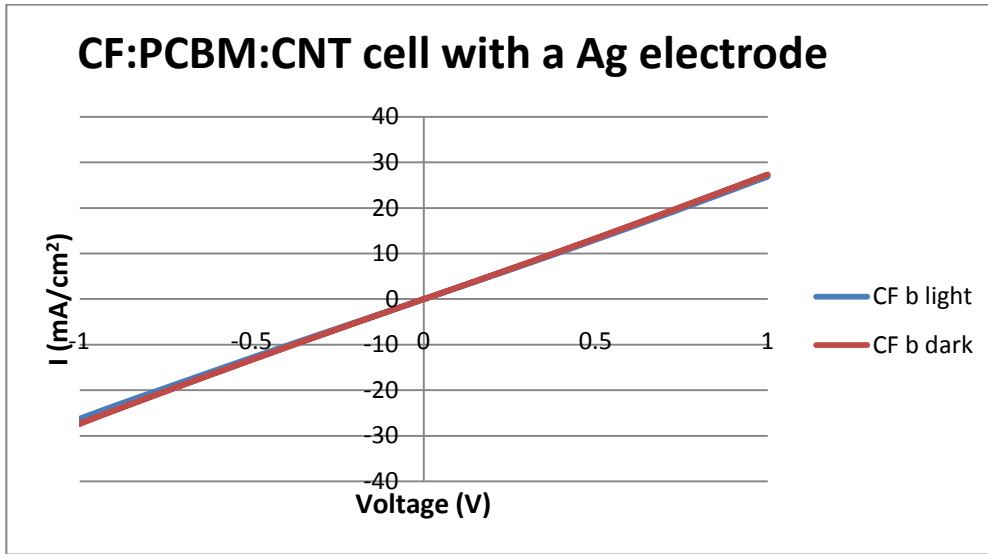


Figure 4.20: Short Circuit Solar Cell (CF:PCBM:CNT).

Table 4.10: Parameters of BHJ solar cells with a silver back-electrode that contain SWNTs.

Ag Cells	Efficiency (%)	P_{\max} (mW)	V_{oc} (V)	I_{sc} (mA/cm ²)	FF (%)
CT a	2.06E-3	267.4E-6	0.010	-0.489	27.30
CT b	2.70E-3	351.2E-6	0.010	-0.540	32.49
P3HT a	4.00E-2	5.20E-3	0.025	-3.287	31.65
P3HT b	3.54E-2	4.60E-3	0.035	-2.956	22.22
oTCT a	1.36E-7	17.74E-9	0.065	-736.4E-9	185.32
oTCT b	3.05E-6	396.3E-9	0.105	-19.96E-9	94 541.00
oTLT a	3.66E-6	476.3E-9	0.005	-0.00153	31.14
oTLT b	2.70E-6	350.5E-9	-0.405	24.18E-9	17895.00
MEH-PPV a	8.59E-4	111.7E-6	0.005	-0.466	23.95
MEH-PPV b	2.47E-3	320.7E-6	0.015	-0.561	19.04

Chapter 5

Conclusions and Future Work

5.1 Conclusions

The investigation carried out in this project allowed for the development of π -conjugated polymers and their implementation in organic solar cells. The eleven synthesized polymers, as well as four others, were investigated using theoretical methods that included semi-empirical geometry optimizations, DFT energy calculations, and TD-DFT optical absorption predictions. The absorption predictions gave credence to our experimental results in which the absorption of the longer polymer chains underwent a redshift from the monomer absorption.

With several of the prepared polymers, bulk-heterojunction photovoltaic cells were fabricated and their photovoltaic activity was investigated. Many of the fabricated cells exhibited positive results (i.e. photovoltaic efficiency) which illuminates the photovoltaic behavior of the polymer and provides evidence for their future use in polymer solar cells.

Several polymers (CF, CT, TCT, LP, oTCT, oTLT, P3HT, and MEH-PPV) were used to solubilize single-walled carbon nanotubes (SWNTs). Solubility of the nanotubes was achieved by the polymers' ability to wrap the tubes, disrupt the bundles (ropes of tubes), and allow for the creation of a homogeneous mixture. Polymer:PCBM:SWNT mixtures were prepared and utilized as the active layer in BHJ solar cells. Some of the cells that incorporated the nanotube composites displayed photovoltaic activity.

Following assembly of the polymer solar cells containing active layer composites (with and without carbon nanotubes) it was clearly evident that the polymers lacking the ability to form a uniform film were unable to achieve high photovoltaic efficiencies. The solar cells that short

circuiting and showed no photovoltaic activity contained polymer films with defects. In some cases, pin hole defects in the polymer film can lead to the demise of the cell and create short circuits. Not only was the film forming character of polymer pivotal to the solar cell's successful fabrication, but the required removal of oligomers from the polymer mixtures is also important. Upon solvent evaporation small oligomers and monomers that are present in the active layer can crystallize and cause defects in the film. Short-circuits were also exhibited in some of the cells prepared with carbon nanotubes. The length of the nanotubes was problematic because the CNTs enabled the formation of a continuous connection between the anode and cathode.

5.2 Future Work

The future direction of this project will allow for the optimization of both the polymerization and solar cell fabrication methods. To prepare efficient PSCs the polymer synthesis will be optimized to prepare long conjugated polymers (with a low PDI) that have good film forming character. The interaction between the polymer and acceptor within the film will be further investigated by various spectroscopic techniques. For example, fluorescence spectroscopy will provide insight into the charge generation mechanisms within the polymer/PCBM and polymer/PCBM/SWCNT composites. Quenching of the polymer's luminescence within the composites provides evidence that there is charge transfer from the polymer to the acceptor moiety within the active layer. The current project's goal was not to optimize the fabrication method of the cells, but was used as a means to develop polymers and test their photovoltaic activity. Therefore the next steps in the project will focus on developing preparation methods for each polymer to ensure that the morphology of the cell's active layer is uniform and that phase segregation occurs between the polymer and acceptor.

References

- [1] Bube, R.H. Photovoltaic Materials, Imperial College Press, London (1998)
- [2] Yu, P.Y.; Cardona, M. Fundamentals of Semiconductors: Graduate Texts in Physics 4th ed., Springer-Verlag Berlin Heidelberg (2010)
- [3] Teegarden, D. Polymer Chemistry: Introduction to an Indispensable Science, National Science Teachers Association, Arlington (2004)
- [4] Brabec, C.J.; Dyakonov, V.; Parisi, J.; Saricifci, N.S. Organic Photovoltaics: Concepts and Realizations, Springer-Verlag Berlin Heidelberg, New York (2003)
- [5] Thompson, B.C.; Fréchet, J.M.J. 'Polymer-fullerene composite solar cells.' *Angewandte Chemie International Edition*, 47, 58 (2008)
- [6] Shaheen, Sean E.; White, Matthew S.; Olsen, Dana C.; Kopidakis, N.; Ginley, David S. 'Inverted bulk-heterojunction plastic solar cells.' *SPIE –The International Society for Optical Engineering Newsroom*, 10.1117/2.1200705.0756 (2007)
- [7] Hadziioannou, G.; Malliaras, G.G. *Semiconducting Polymers: Chemistry, Physics and Engineering Vol. 2*, Wiley-VCH, Weinheim (2007)
- [8] Hadziioannou, G.; Malliaras, G.G. *Semiconducting Polymers: Chemistry, Physics and Engineering Vol. 1*, Wiley-VCH, Weinheim (2007)
- [9] François, B.; Widawski, G.; Rawiso, M.; Cesar, B. 'Block-copolymers with conjugated segments: Synthesis and structural characterization.' *Synthetic Metals*, 69, 463 (1995)
- [10] Stalmach, U.; de Boer, B.; Videlot, C.; van Hutten, P. F.; Hadziioannou, G. 'Semiconducting diblock copolymers synthesized by means of controlled radical polymerization techniques.' *Journal of the American Chemical Society*, 122, 5464 (2000)
- [11] Georges, M. K.; Moffat, K. A.; Veregin, R. P. N.; Kazmaier, P. M.; Hamer, G. K., 'Narrow molecular weight resins by a free radical polymerization process; the effect of nitroxides and organic acids on the polymerization', *Polymeric Materials Science and Engineering* , 69, 305 (1993)
- [12] Liu, J.; Sheina, E.; Kowalewski, T.; McCullough, R. D. 'Tuning the electrical conductivity and self-assembly of regioregular polythiophene by block copolymerization: nanowire morphologies in new di- and triblock copolymers.' *Angewandte Chemie International Edition*, 41, 329 (2002)

- [13] Oberlin, A.; Endo, M.; Koyama, T. 'Filamentous growth of carbon through benzene decomposition', *Journal of Crystal Growth*, 32, 335 (1976)
- [14] Burroughes, J. H.; Bradley, D. D. C.; Brown, A. R.; Marks, R. N.; Mackay, K.; Friend, R. H.; Burns, P. L.; Holmes, A. B. 'Light-emitting diodes based on conjugated polymers'. *Nature*, 347, 539 (1990)
- [15] Friend, R. H.; Gymer, R. W.; Holmes, A. B.; Burroughes, J. H.; Marks, R. N.; Taliani, C.; Bradley, D. D. C.; Dos Santos, D. A.; Brédas, J. L.; Lögdlund, M.; Salaneck, W. R. 'Electroluminescence in conjugated polymers'. *Nature*, 397, 121 (1999)
- [16] Dresselhaus, M.S.; Dresselhaus, G.; Avouris, P. *Carbon Nanotubes: Synthesis, Structure, Properties, and Applications*. Springer-Verlag Berlin Heidelberg, Berlin (2001)
- [17] O'Connell, M.J. *Carbon Nanotubes: Properties and Applications*, Taylor and Francis Group, LLC, Boca Raton (2006)
- [18] Wildöer, J. W. G.; Venema, L. C.; Rinzler, A. G.; Smalley, R. E.; Dekker, C., 'Electronic structure of atomically resolved carbon nanotubes', *Nature*, 391, 59 (1998)
- [19] Saito, S.; Zettl, A. *Carbon Nanotubes: Quantum Cylinders of Graphene*, Elsevier, Oxford (2008)
- [20] Harris, P.J.F. *Carbon Nanotube Science: Synthesis, Properties and Applications*, Cambridge University Press, New York (2009)
- [21] Kitiyanan, B.; Alvarez, W. E.; Harwell, J. H.; Resasco, D. E. 'Controlled production of single-wall carbon nanotubes by catalytic decomposition of CO on bimetallic Co–Mo catalysts', *Chemical Physics Letters*, 317, 497 (2000)
- [22] Bachilo, S. M.; Balzano, L.; Herrera, J. E.; Pompeo, F.; Resasco, D. E.; Weisman, R. B. 'Narrow (n,m)-distribution of single-walled carbon nanotubes grown using a solid supported catalyst', *Journal of the American Chemical Society*, 125, 11186 (2003)
- [23] Kam, N. W. S.; Dai, H. J. 'Carbon nanotubes as intracellular protein transporters: generality and biological functionality', *Journal of the American Chemical Society*, 127, 6021 (2005)
- [24] Zheng, M.; Jagota, A.; Semke, E. D.; Diner, B. A.; Mclean, R. S.; Lustig, S. R.; Richardson, R. E.; Tassi, N. G., 'DNA-assisted dispersion and separation of carbon nanotubes' *Nature Materials*, 2, 338 (2003)

- [25] Zheng, M.; Jagota, A.; Strano, M. S.; Santos, A. P.; Barone, P.; Chou, S. G.; Diner, B. A.; Dresselhaus, M. S.; Mclean, R. S.; Onoa, G. B.; Samsonidze, G. G.; Semke, E. D.; Usrey, M.; Walls, D. J., 'Structure-based carbon nanotube sorting by sequence-dependent DNA assembly', *Science*, 302, 1545 (2003)
- [26] Strano, M. S.; Zheng, M.; Jagota, A.; Onoa, G. B.; Heller, D. A.; Barone, P. W.; Usrey, M. L., 'Understanding the nature of the DNA-assisted separation of single-walled carbon nanotubes using fluorescence and Raman spectroscopy', *Nano Letters*, 4, 543 (2003)
- [27] Liu, J.; Rinzler, A.G.; Dai, H.; Hafner, J. H.; Bradley, R. K.; Boul, P.J.; Lu, A.; Iverson, T.; Shlimov, K.; Huffman, C. B.; Rodriguez-Macias, F.; Shon, Y.-S.; Lee, T. R.; Colbert, D. T.; Smalley, R. E. 'Fullerene pipes', *Science*, 280, 1253 (1998)
- [28] Viswanathan, G.; Chakrapani, N.; Yang, H.; Wei, B.; Chung, H.; Cho, K.; Ryu, C. Y.; Ajayan, P. M. 'Single-step in situ synthesis of polymer-grafted single-wall nanotube composites', *Journal of the American Chemical Society*, 125, 9258 (2003)
- [29] Jin, Z.; Huang, L.; Goh, S. H.; Xu, G.; Ji, W. 'Characterization and nonlinear optical properties of a poly(acrylic acid)-surfactant-multi-walled carbon nanotube complex' *Chemical Physics Letters*, 332, 461 (2000)
- [30] Chen, R. J.; Zhang, Y.; Wang, D.; Dai, H. 'Noncovalent sidewall functionalization of single-walled carbon nanotubes for protein immobilization', *Journal of the American Chemical Society*, 123, 3838 (2001)
- [31] O'Connell, M. J.; Boul, P.; Ericson, L. M.; Huffman, C.; Wang, Y.; Haroz, E.; Kuper, C.; Tour, J.; Ausman, K. D.; Smalley, R. E. 'Reversible water-solubilization of single-walled carbon nanotubes by polymer wrapping', *Chemical Physics Letters*, 342, 265 (2001)
- [32] Star, A.; Stoddart, J. F.; Steuerman, D.; Diehl, M.; Boukai, A.; Wong, E. W.; Yang, X.; Chung, S.-W.; Choi, H.; Heath, J. R. 'Preparation and properties of polymer-wrapped single-walled carbon nanotubes', *Angewandte Chemie, International Edition*, 40, 1721 (2001)
- [33] Ago, H.; Shaffer, M. S. P.; Ginger, D. S.; Windle, A. H.; Friend, R. H. 'Electronic interaction between photoexcited poly(*p*-phenylene vinylene) and carbon nanotubes', *Physical Review B*, 61, 2286 (2000)
- [34] Kymakis, E.; Amaratunga, G. A. J. 'Single-wall carbon nanotube/conjugated polymer photovoltaic devices', *Applied Physics Letters*, 80, 112 (2002)

- [35] Nogueira, A. F.; Lomba, B. S.; Mauro, A. S.-O.; Correia, C. R. D. 'Polymer solar cells using single-wall carbon nanotubes modified with thiophene pendent groups', *Journal of Physical Chemistry C*, 111, 18431 (2007)
- [36] Patyk, R. L.; Lomba, B. S.; Nogueira, A. F.; Furtado, C. A.; Santos, A. P.; Mello, R. M. Q.; Micaroni, L.; Hummelgen, I. A. 'Carbon nanotube-polybithiophene photovoltaic devices with high open-circuit voltage', *Physica Status Solidi RRL: Rapid Research Letters*, 1, R43 (2007)
- [37] Pradhan, B.; Batabyal, S. K.; Pal, A. J. 'Functionalized carbon nanotubes in donor/acceptor-type photovoltaic devices', *Applied Physics Letters*, 88, 093106/1 (2006)
- [38] Li, C.; Chen, Y.; Wang, Y.; Iqbal, Z.; Chhowalla, M.; Mitra, S. 'A fullerene-single wall carbon nanotube complex for polymer bulk heterojunction photovoltaic cells', *Journal of Materials Chemistry*, 17, 2406 (2007)
- [39] Arranz-Andrés, J.; Blau, W. J. 'Enhanced device performance using different carbon nanotube types in polymer photovoltaic devices', *Carbon*, 46, 2067 (2008)
- [40] Berson, S.; de Bettignies, R.; Bailly, S.; Guillerez, S.; Joussetme, B. 'Elaboration of P3HT/CNT/PCBM composites for organic photovoltaic cells', *Advanced Functional Materials*, 17, 3363 (2007)
- [41] Kymakis, E.; Amaratunga, G. A. J. 'Carbon nanotubes as electron acceptors in polymeric photovoltaics', *Reviews on Advanced Materials Science*, 10, 300 (2005)
- [42] Kymakis, E.; Servati, P.; Tzanetakis, P.; Koudoumas, E.; Kornilios, N.; Rompogiannakis, I.; Franghiadakis, Y.; Amaratunga, G. A. J. 'Effective mobility and photocurrent in carbon nanotube-polymer composite photovoltaic cells', *Nanotechnology*, 18, 435702 (2007)
- [43] Gaussian 03, Revision C.2, M.J. Frisch *et al.*, Gaussian, Inc., Wallingford, CT, 2003
- [44] Dewar, M.; Thiel, W. 'MINDO/3 study of the addition of singlet oxygen (1.DELTA.gO2) to 1,3-butadiene'. *Journal of the American Chemical Society*, 99, 2338 (1977)
- [45] Roothaan, C. C. J. 'New Developments in Molecular Orbital Theory'. *Reviews of Modern Physics*, 23, 69 (1951)
- [46] a) Becke, A. D. 'Density-functional thermochemistry. III. The role of exact exchange'. *Journal of Chemical Physics*, 98, 5648 (1993) b) Lee, C.; Yang, W.; Parr, R. P. 'Development of the Colle-Salvetti correlation-energy formula into a functional of the electron density'. *Physical Review B*, 37, 785 (1988)

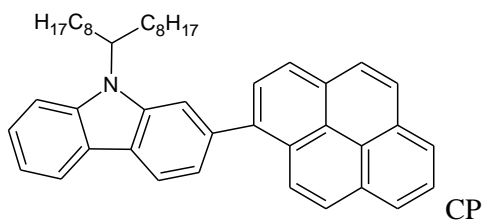
- [47] O'Boyle, N. M.; Tenderholt, A. L.; Langner, K. M. 'cclib: A library for package-independent computational chemistry algorithms.' *Journal of Computational Chemistry*, 29, 839 (2008)
- [48] Tamao, K.; Sumitani, K.; Kumada, M. 'Selective carbon-carbon bond formation by cross-coupling of Grignard reagents with organic halides. Catalysis by nickel-phosphine complexes'. *Journal of the American Chemical Society*, 94, 4374 (1972)
- [49] Bundgaard, E. and Krebs, F. C. 'Low-band-gap conjugated polymers based on thiophene, benzothiadiazole, and benzobis(thiadiazole)'. *Macromolecules*, 39, 2823 (2006)
- [50] Blouin, N.; Michaud, A.; Leclerc, M. 'A low-bandgap poly(2,7-carbazole) derivative for use in high-performance solar cells'. *Advanced Materials*, 19, 2295 (2007)
- [51] Hanif, M.; Lu, P.; Li, M.; Zheng, Y.; Xie, Z.; Ma, Y.; Li, D.; Li, J. 'Synthesis, characterization, electrochemistry and optical properties of a novel phenanthrenequinone *alt*-dialkylfluorene conjugated copolymer'. *Polymer International*, 56, 1507 (2007)
- [52] Andreani, F.; Salattelli, E.; Lanzi, M. 'Novel poly(3,3''- and 3',4'-dialkyl-2,2':5',2''-terthiophene)s by chemical oxidative synthesis: evidence for a new step towards the optimization of this process'. *Polymer*, 37, 661 (1996)
- [53] Niemi, V. M.; Knuutila, P.; Osterholm, J.-E.; Korvola, J. 'Polymerization of 3-alkylthiophenes with FeCl₃'. *Polymer*, 33, 1559 (1992)
- [54] Casado, A. L.; Espinet, P.; Gallego, A. M. 'Mechanism of the Stille reaction. 2. Couplings of aryl triflates with vinyltributyltin. Observation of intermediates. A more comprehensive scheme'. *Journal of the American Chemical Society*, 122, 11771 (2000)
- [55] Espinet, P and Echavarren, A. M. 'The Mechanisms of the Stille reaction'. *Angewandte Chemie International Edition*, 43, 4704 (2004)
- [56] Miyaura, N. and Suzuki, A. 'Palladium-catalyzed cross-coupling reactions of organoboron compounds'. *Chemical Reviews*, 95, 2457 (1995)
- [57] Goodson, F. E.; Wallow, T. I.; Novak, B. M. 'Application of "Transfer-free" Suzuki coupling protocols toward the synthesis of "unambiguously linear" poly(p-phenylenes)'. *Macromolecules*, 31, 2047 (1998)
- [58] Hunter, C. A. and Sanders, J. K. M. 'The Nature of π - π Interactions'. *Journal of the American Chemical Society*, 112, 5525 (1990)

- [59] Derbal-Habak, H.; Bergeret, C.; Cousseau, J.; Nunzi, J.-M. 'Improving the current density J_{sc} of organic solar cells P3HT:PCBM by structuring the photoactive layer with functionalized SWCNTs'. *Solar Energy Materials and Solar Cells*, doi: 10.1016/j.solmat.2010.12.047 (2011)
- [60] Krebs, F.C. *Polymer Photovoltaics: A Practical Approach*, Society of Photo-Optical Instrumentation Engineers, Bellingham (2008)
- [61] Katon, J.E. *Organic Semiconducting Polymers*, Marcel Dekker Inc., New York (1968)
- [62] Bloor, D.; Blythe, T. *Electrical Properties of Polymers*, Cambridge University Press, New York (2005)
- [63] Moliton, A. *Optoelectronics of Molecules and Polymers*, Springer-Verlag Berlin Heidelberg, New York (2006)
- [64] Farchioni, R.; Grosso, G. *Organic Electronic Materials: Conjugated Polymers and Low Molecular Weight Organic Solids*, Springer-Verlag Berlin Heidelberg, New York (2001)
- [65] Hamagachi, C. *Basic Semiconductor Physics 2nd ed.*, Springer-Verlag Berlin Heidelberg (2010)
- [66] Bhushan, B. *Springer Handbook of Nanotechnology*, Springer-Verlag Berlin Heidelberg (2007)
- [67] Bhushan, B. *Springer Handbook of Nanotechnology*, Springer-Verlag Berlin Heidelberg (2010)
- [68] Jäger-Waldau, A. *PV Status Report 2009: Research, Solar Cell Production and Market Implementation of Photovoltaics*, European Union (2009) <http://re.jrc.europa.eu/refsys/>

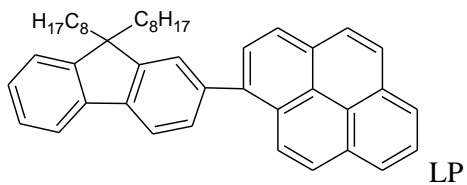
Appendix A

Supplementary Data

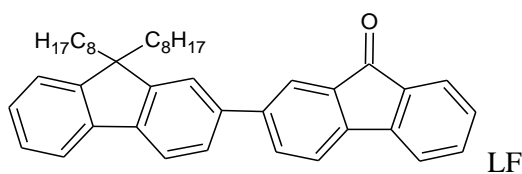
HOMO and LUMO energy levels of oligomers determined theoretically using DFT calculations (6-31G (d))



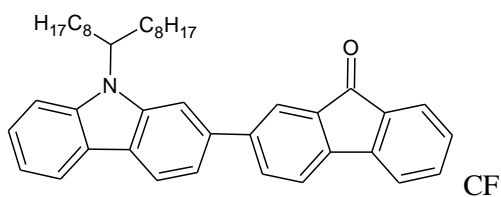
n	HOMO (eV)	LUMO (eV)	Band Gap (eV)
1	-5.16	-1.48	3.68
2	-5.00	-1.55	3.45
3	-4.98	-1.58	3.39
4	-4.96	-1.60	3.36
5	-4.96	-1.61	3.35
6	-4.95	-1.62	3.33



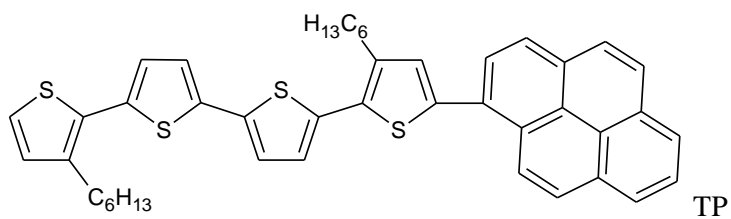
n	HOMO (eV)	LUMO (eV)	Band Gap (eV)
1	-5.20	-1.53	3.66
2	-5.07	-1.65	3.42
3	-5.04	-1.69	3.35
4	-5.03	-1.71	3.32
5	-5.03	-1.72	3.31
6	-5.02	-1.73	3.30



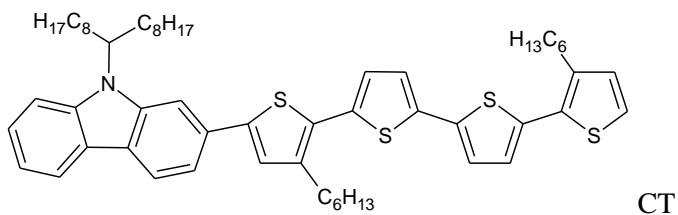
n	HOMO (eV)	LUMO (eV)	Band Gap (eV)
1	-5.55	-2.32	3.24
2	-5.39	-2.37	3.02
3	-5.35	-2.40	2.95
4	-5.34	-2.42	2.92
5	-5.33	-2.42	2.91
6	-5.33	-2.43	2.90



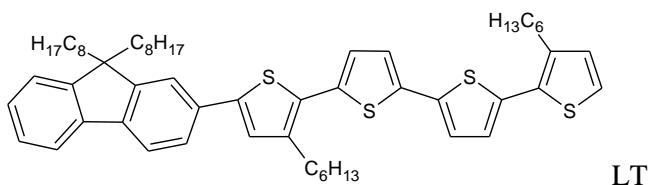
n	HOMO (eV)	LUMO (eV)	Band Gap (eV)
1	-5.41	-2.28	3.13
2	-5.33	-2.32	3.01
3	-5.29	-2.34	2.95
4	-5.27	-2.34	2.93
5	-5.26	-2.35	2.92
6	-5.26	-2.35	2.91



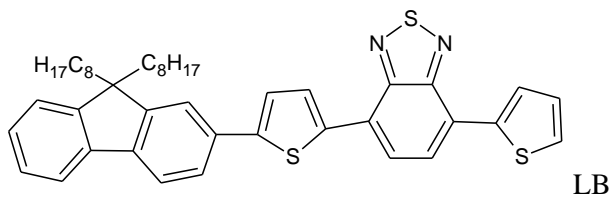
n	HOMO (eV)	LUMO (eV)	Band Gap (eV)
1	-4.75	-1.67	3.08
2	-4.68	-1.82	2.86
3	-4.58	-1.86	2.72
4	-4.58	-1.88	2.71
5	-4.59	-1.88	2.71
6	-4.59	-1.89	2.71



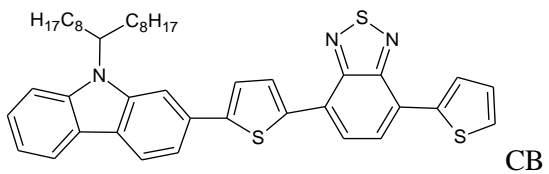
n	HOMO (eV)	LUMO (eV)	Band Gap (eV)
1	-4.56	-1.56	3.00
2	-4.45	-1.71	2.74
3	-4.42	-1.76	2.66
4	-4.41	-1.78	2.63
5	-4.40	-1.78	2.62
6	-4.40	-1.79	2.61



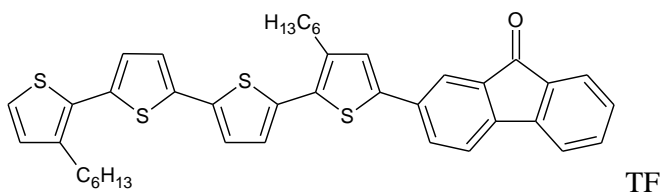
n	HOMO (eV)	LUMO (eV)	Band Gap (eV)
1	-4.60	-1.63	2.97
2	-4.50	-1.81	2.69
3	-4.47	-1.86	2.62
4	-4.46	-1.88	2.59
5	-4.46	-1.89	2.57
6	-4.46	-1.89	2.56



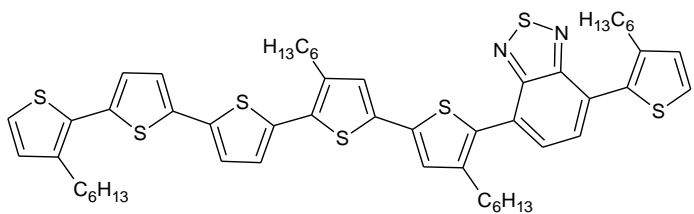
n	HOMO (eV)	LUMO (eV)	Band Gap (eV)
1	-5.17	-2.46	2.71
2	-5.01	-2.51	2.50
3	-4.97	-2.53	2.44
4	-4.96	-2.54	2.42
5	-4.95	-2.55	2.40
6	-4.95	-2.55	2.40



n	HOMO (eV)	LUMO (eV)	Band Gap (eV)
1	-5.12	-2.42	2.70
2	-4.94	-2.45	2.49
3	-4.90	-2.47	2.43
4	-4.89	-2.48	2.41
5	-4.88	-2.48	2.40
6	-4.88	-2.48	2.40

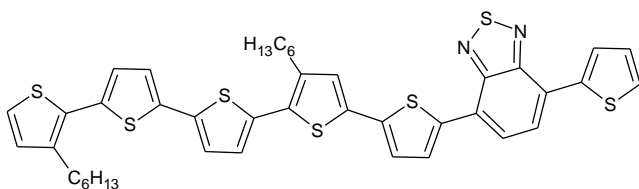


n	HOMO (eV)	LUMO (eV)	Band Gap (eV)
1	-4.70	-2.35	2.35
2	-4.64	-2.42	2.22
3	-4.63	-2.45	2.18
4	-4.63	-2.46	2.17
5	-4.62	-2.47	2.15
6	-4.62	-2.47	2.15



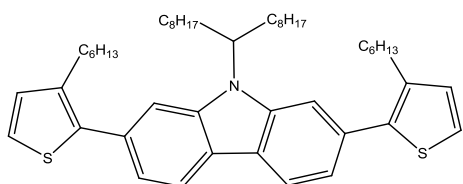
TH

n	HOMO (eV)	LUMO (eV)	Band Gap (eV)
1	-4.57	-2.38	2.19
2	-4.49	-2.43	2.06
3	-4.47	-2.44	2.03
4	-4.47	-2.45	2.02
5	-4.47	-2.45	2.02
6	-4.46	-2.45	2.01



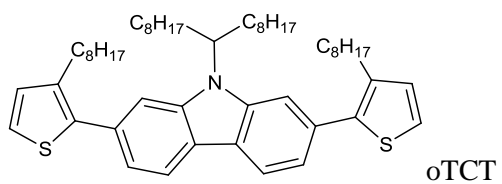
TB

n	HOMO (eV)	LUMO (eV)	Band Gap (eV)
1	-4.62	-2.47	2.15
2	-4.58	-2.52	2.06
3	-4.57	-2.53	2.04
4	-4.55	-2.54	2.01
5	-4.54	-2.54	2.00
6	-4.53	-2.55	1.98

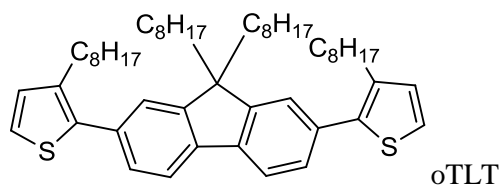


TCT

n	HOMO (eV)	LUMO (eV)	Band Gap (eV)
1	-5.28	-1.12	4.16
3	-4.78	-1.39	3.39
6	-4.77	-1.42	3.35
9	-4.77	-1.43	3.34



n	HOMO (eV)	LUMO (eV)	Band Gap (eV)
1	-5.27	-1.13	4.14
3	-4.79	-1.36	3.43
6	-4.74	-1.43	3.31
9	-4.74	-1.42	3.32

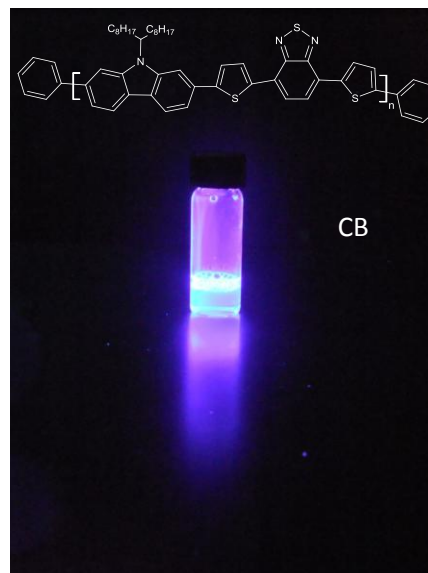
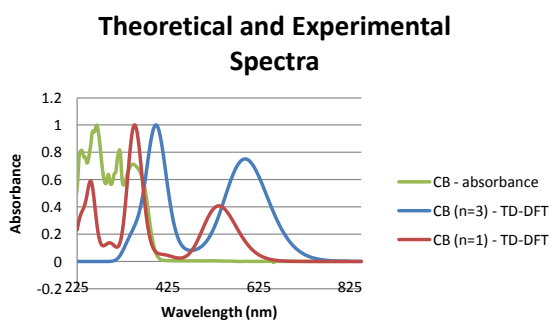
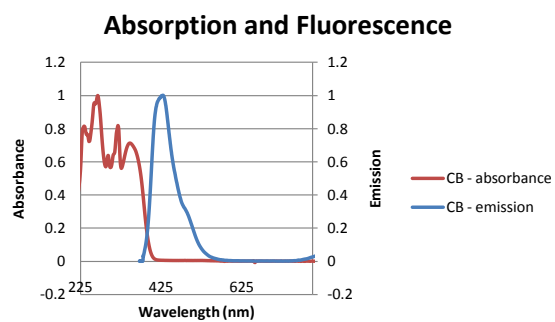


n	HOMO (eV)	LUMO (eV)	Band Gap (eV)
1	-5.38	-1.24	4.14
3	-5.05	-1.43	3.62
6	-4.89	-1.48	3.41
9	-4.88	-1.49	3.39

UV-Visible absorption spectra (theoretical and experimental) and fluorescence of polymers

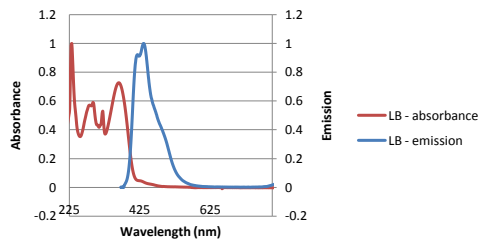
polymers

CB

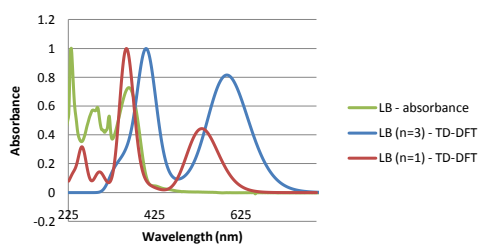


LB

Absorption and Fluorescence

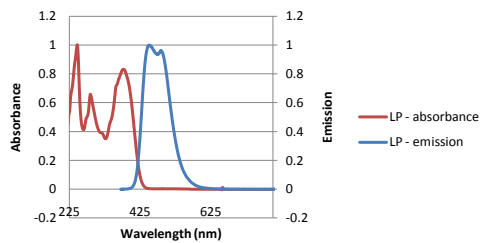


Theoretical and Experimental Spectra

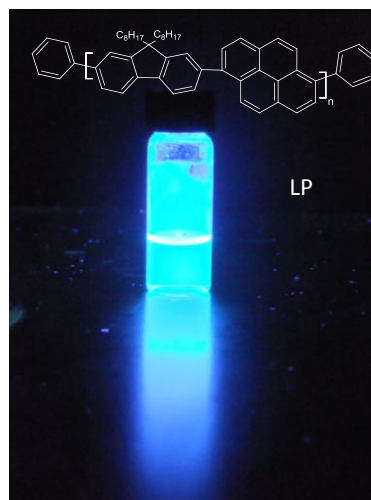
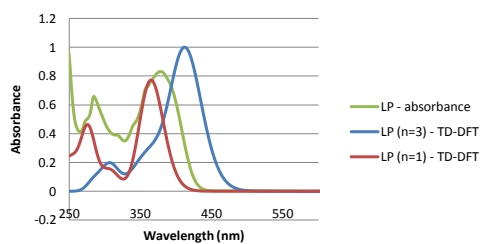


LP

Absorption and Fluorescence

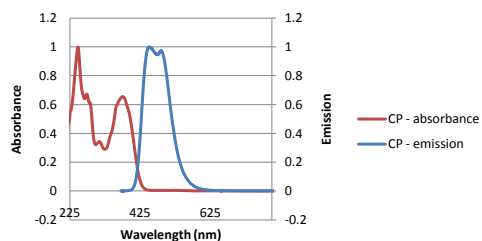


Theoretical and Experimental Spectra

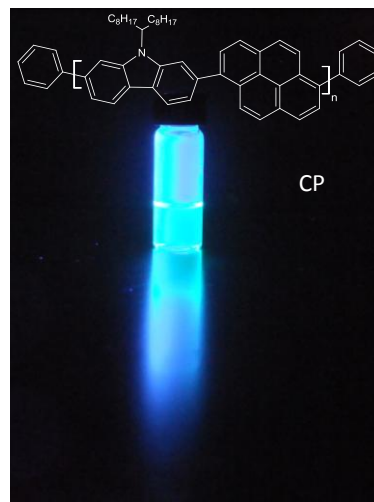
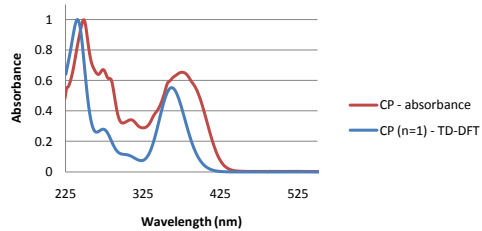


CP

Absorption and Fluorescence

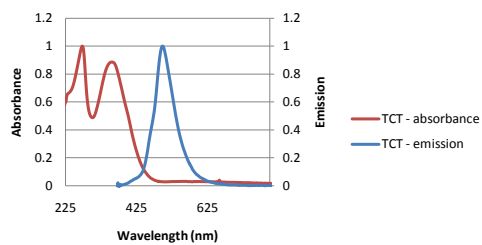


Theoretical and Experimental Spectra

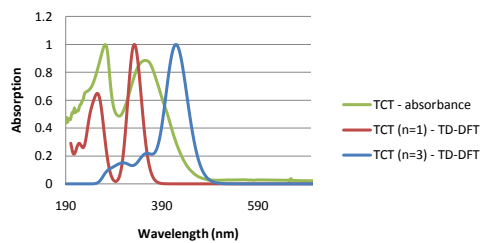


TCT

Absorption and Fluorescence

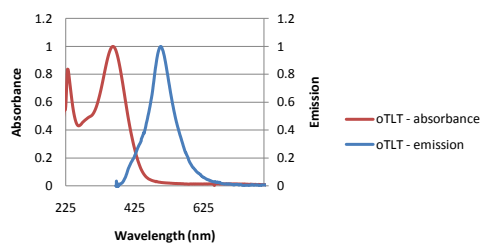


Theoretical and Experimental Spectra

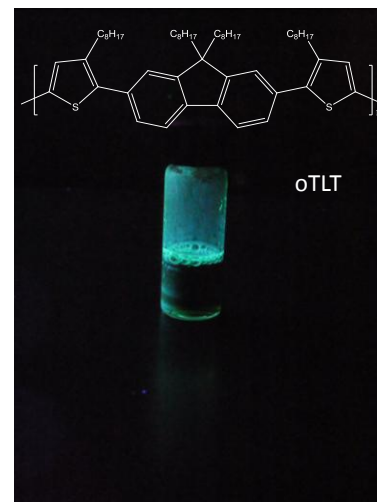
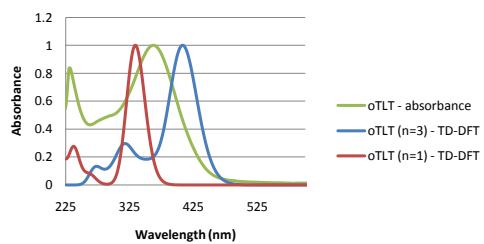


oTLT

Absorption and Fluorescence

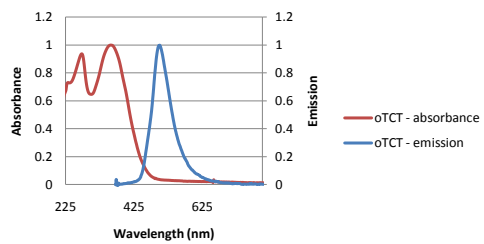


Theoretical and Experimental Spectra

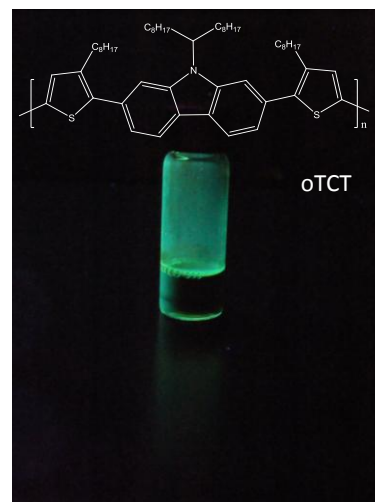
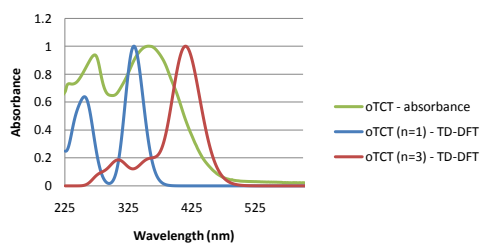


oTCT

Absorption and Fluorescence

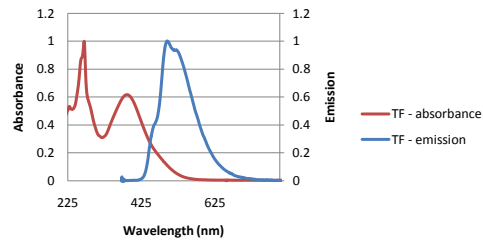


Theoretical and Experimental Spectra

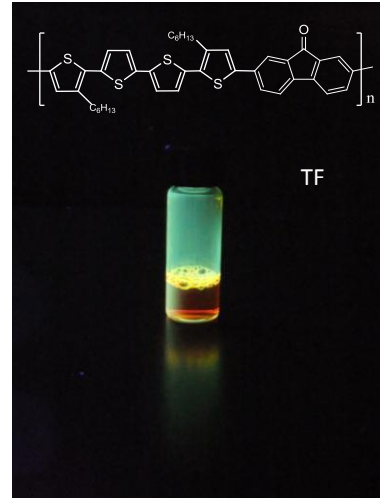
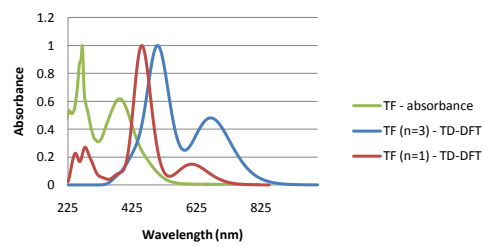


TF - Suzuki

Absorption and Fluorescence

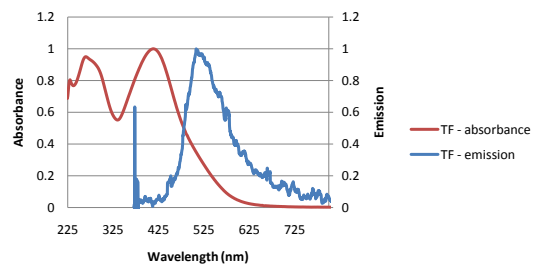


Theoretical and Experimental Spectra

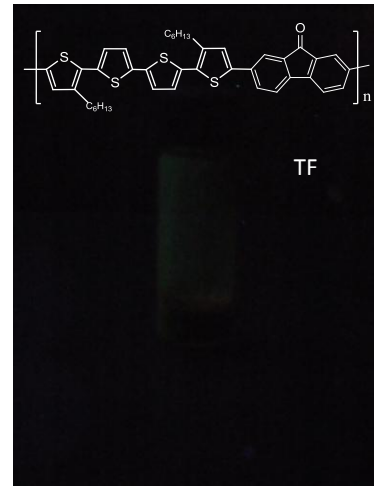
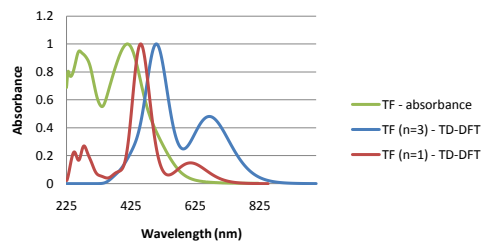


TF - Stille

Absorption and Fluorescence

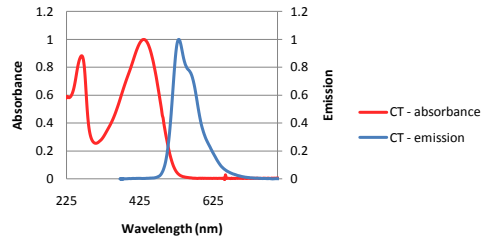


Theoretical and Experimental Spectra

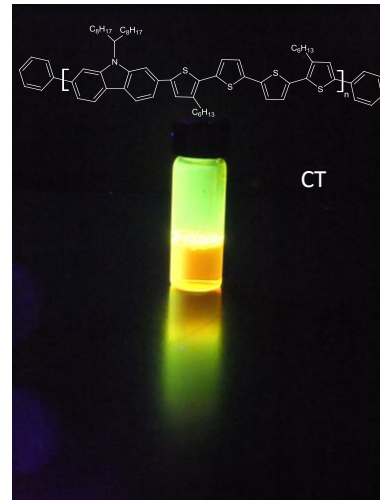
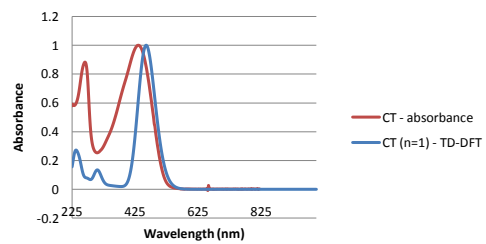


CT

Absorption and Emission

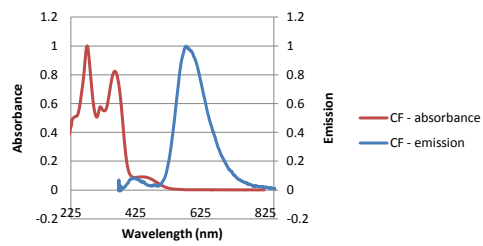


Theoretical and Experimental Spectra

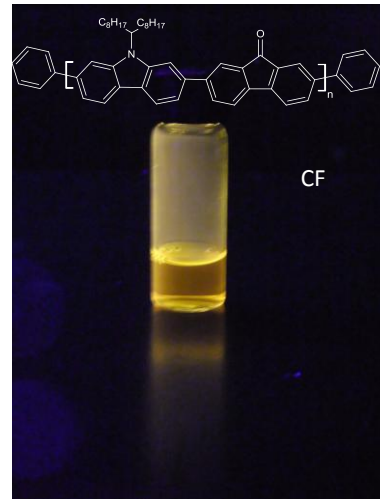
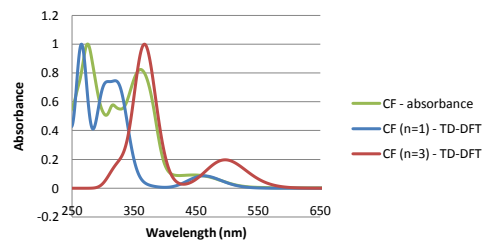


CF

Absorption and Fluorescence

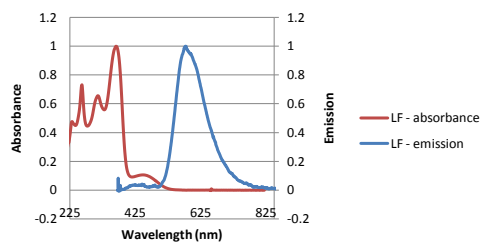


Theoretical and Experimental Spectra

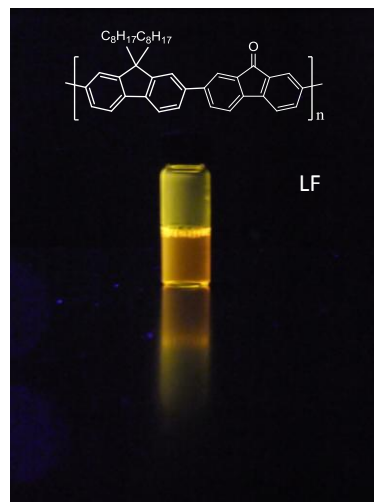
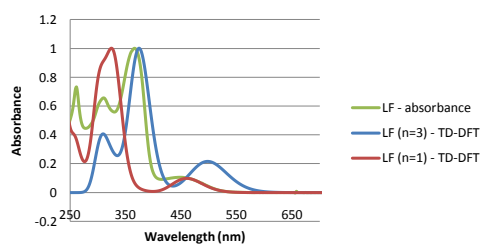


LF

Absorption and Fluorescence

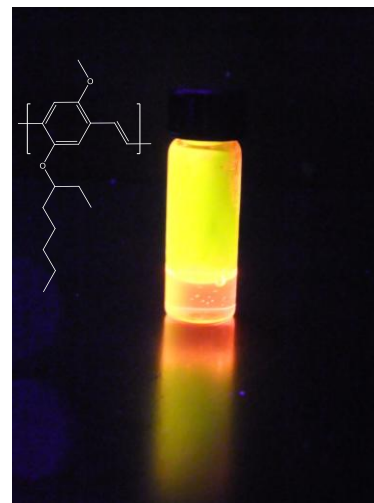
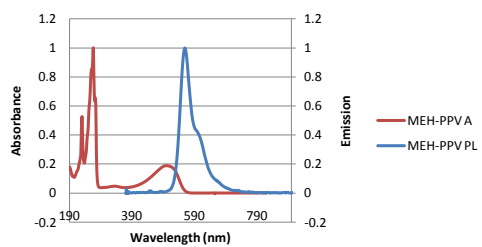


Theoretical and Experimental Spectra

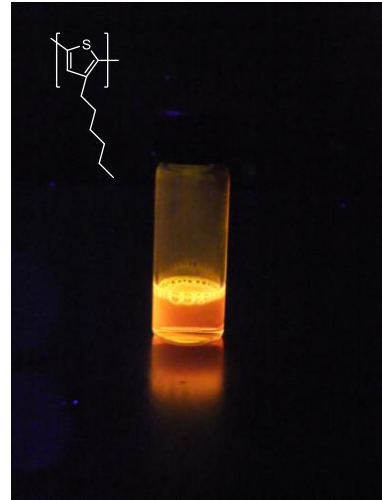
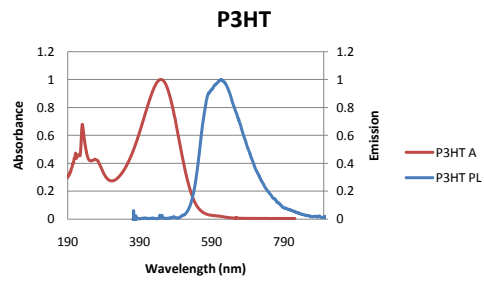


MEH-PPV

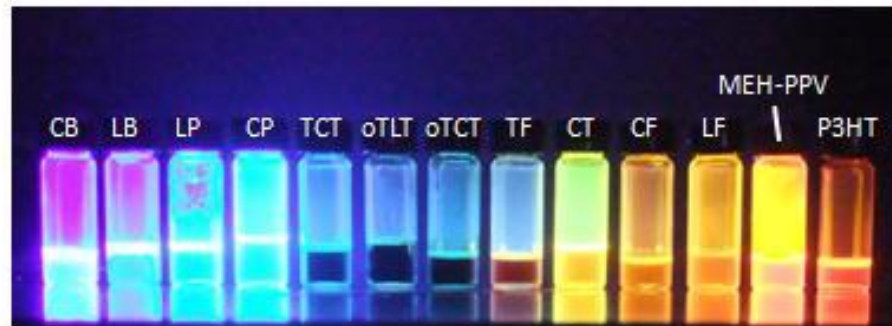
MEH-PPV



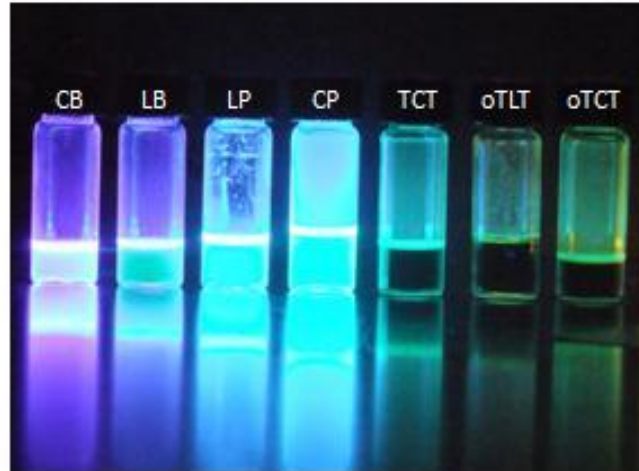
P3HT



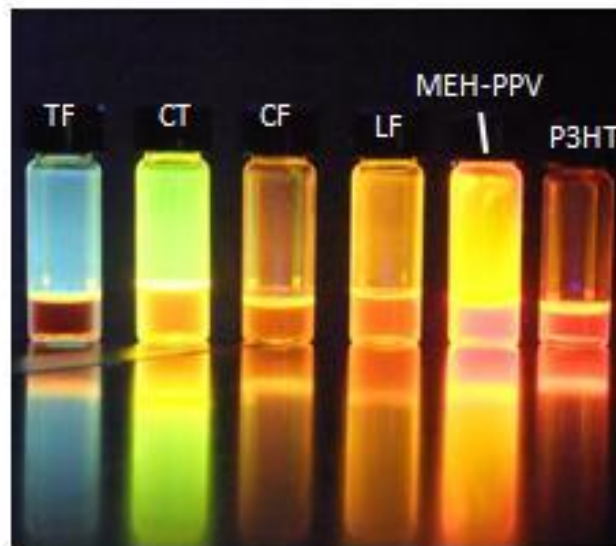
Group of Polymers



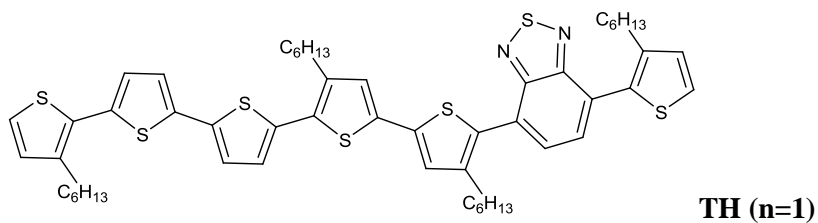
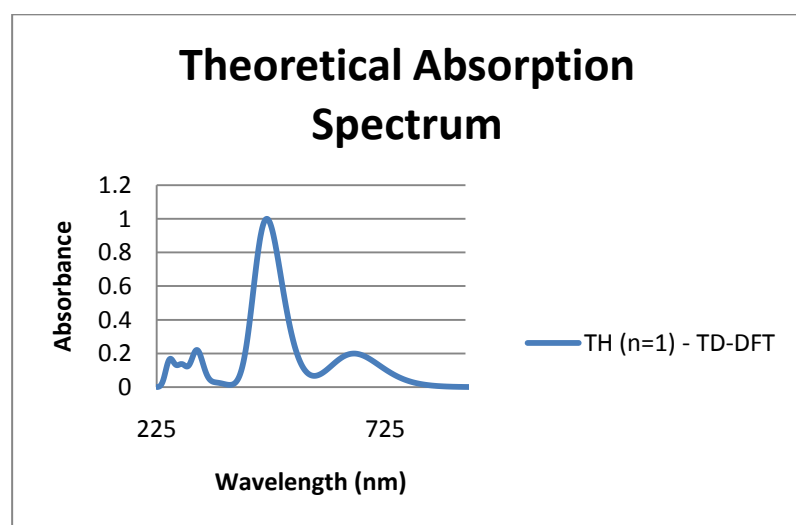
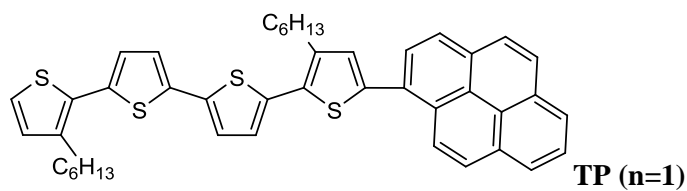
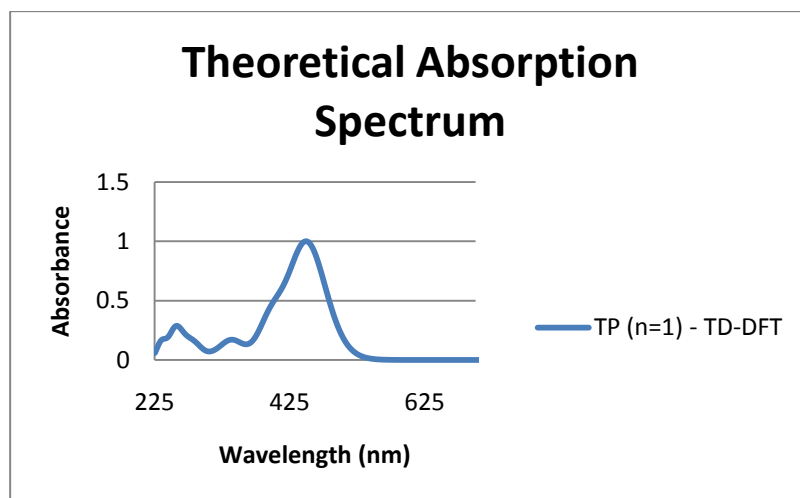
Blue to Green



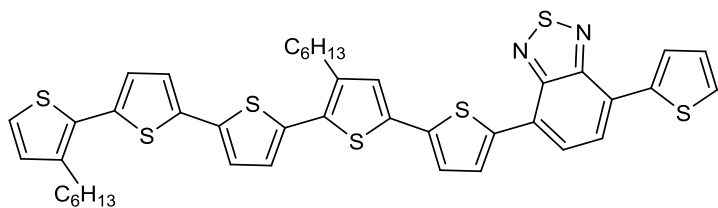
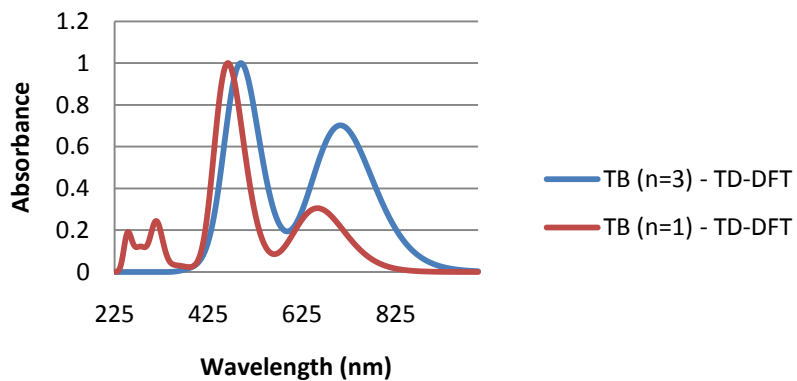
Yellow to Red



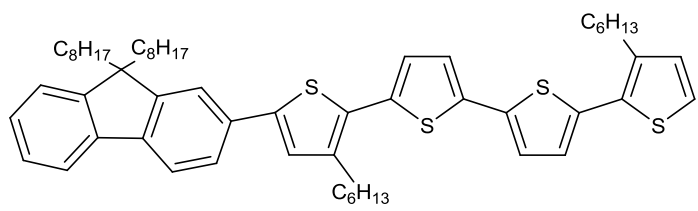
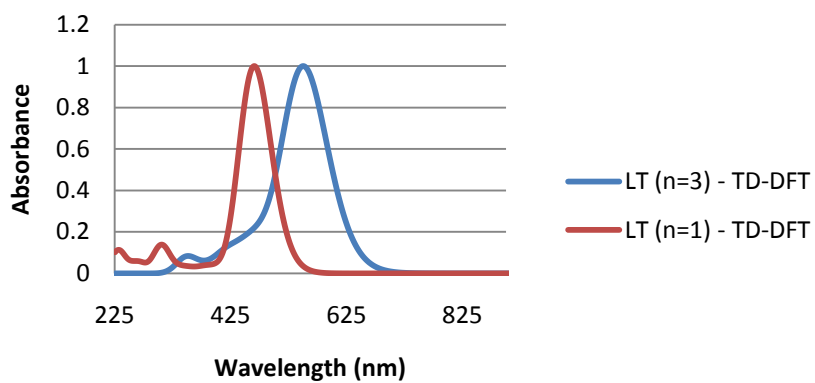
Theoretical optical absorption of polymers not synthesized



Theoretical Absorption Spectra



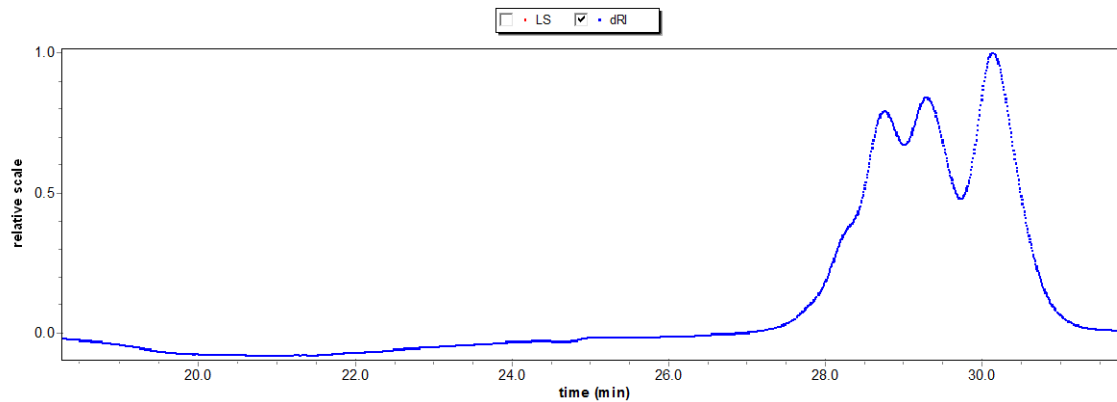
Theoretical Absorption Spectra



GPC Results

CB

Define Peaks



CHCl₃ Column

Peak limits (min) 27.181 - 29.739

Polydispersity

Mw/Mn 1.059(6%)

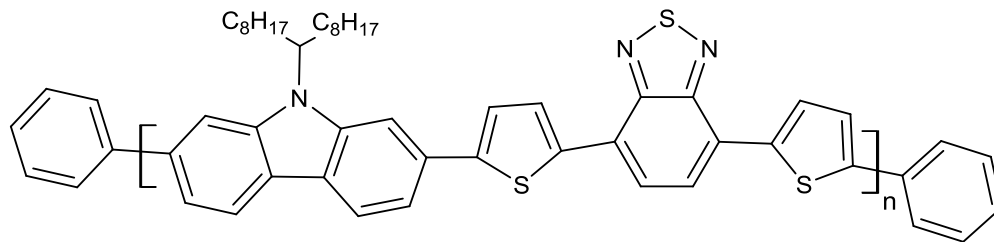
Mz/Mn 1.129(10%)

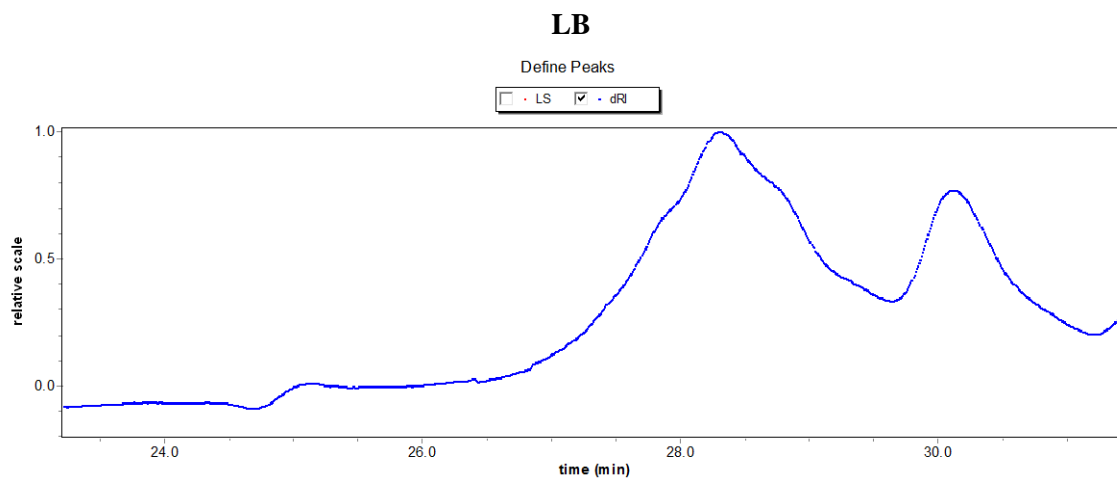
Molar mass moments (g/mol)

Mn 1.762e+3(4%)

Mw 1.867e+3(4%)

Mz 1.989e+3(9%)





CHCl₃ Column

Peak limits (min) 26.879 - 29.612

Polydispersity

Mw/Mn 1.089(6%)

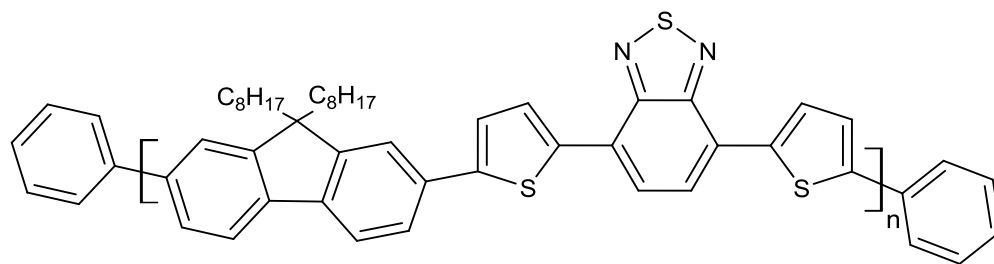
Mz/Mn 1.187(10%)

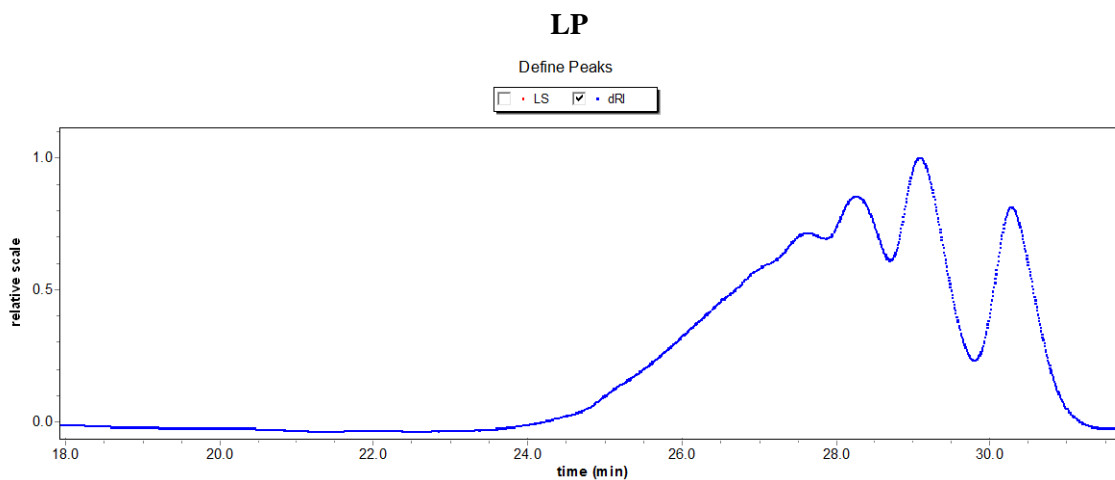
Molar mass moments (g/mol)

Mn 2.245e+3(4%)

Mw 2.446e+3(4%)

Mz 2.666e+3(9%)





CHCl₃ Column

Peak limits (min) 23.940 - 29.788

Polydispersity

Mw/Mn 1.382(6%)

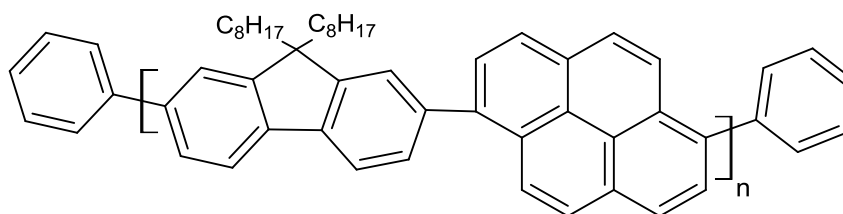
Mz/Mn 1.969(10%)

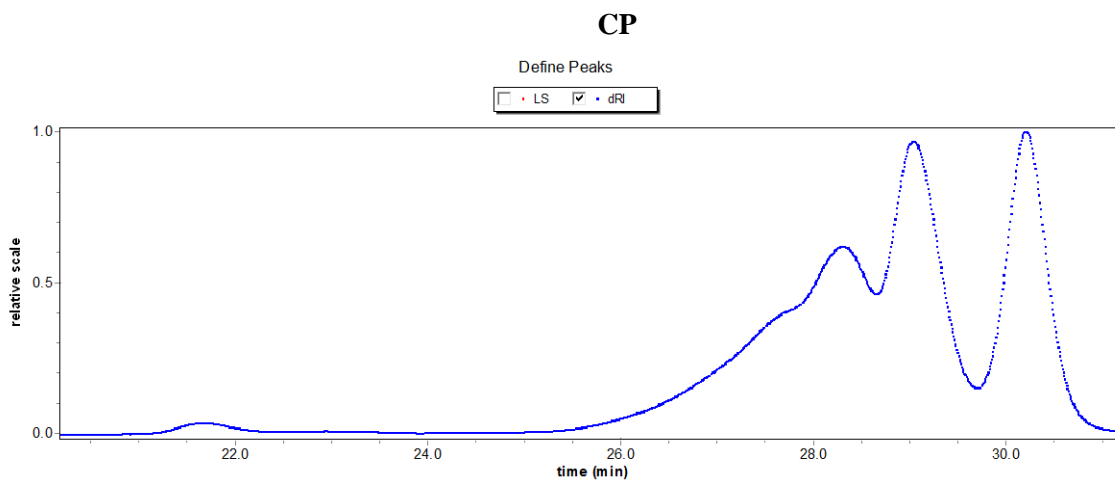
Molar mass moments (g/mol)

Mn 2.673e+3(4%)

Mw 3.693e+3(4%)

Mz 5.263e+3(9%)





THF Column

Peak limits (min) 25.149 - 29.662

Polydispersity

Mw/Mn 1.287(30%)

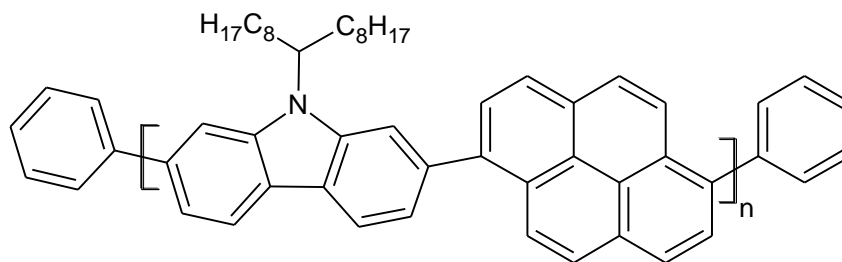
Mz/Mn 1.783(52%)

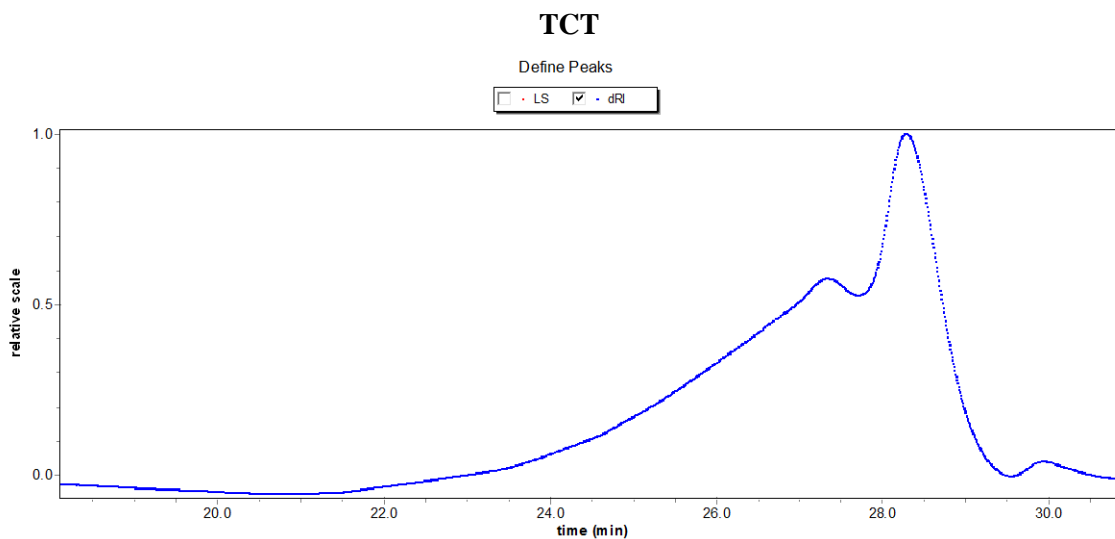
Molar mass moments (g/mol)

Mn 1.228e+3(21%)

Mw 1.579e+3(21%)

Mz 2.189e+3(47%)





CHCl₃ Column

Peak limits (min) 21.188 - 29.489

Polydispersity

Mw/Mn 1.444(6%)

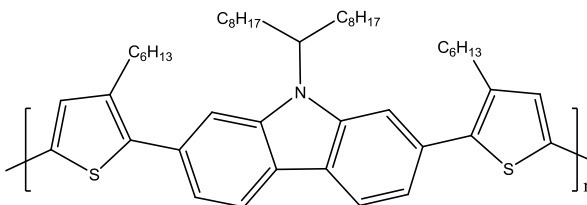
Mz/Mn 2.297(10%)

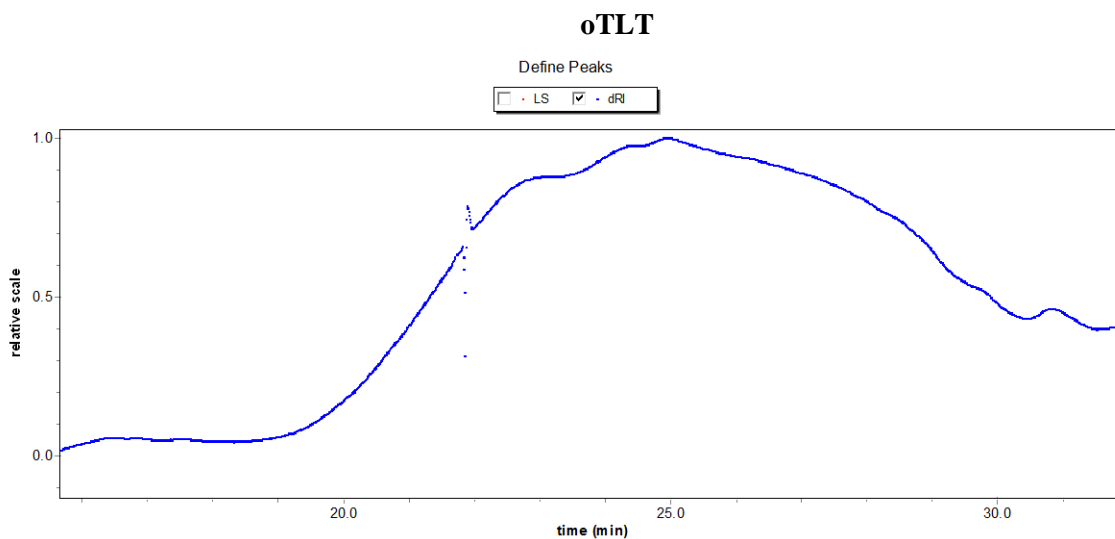
Molar mass moments (g/mol)

Mn 3.554e+3(4%)

Mw 5.131e+3(4%)

Mz 8.163e+3(9%)





CHCl₃ Column

Peak limits (min) 18.458 - 31.562

Polydispersity

Mw/Mn 5.983(6%)

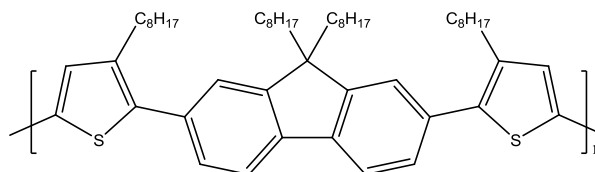
Mz/Mn 19.048(10%)

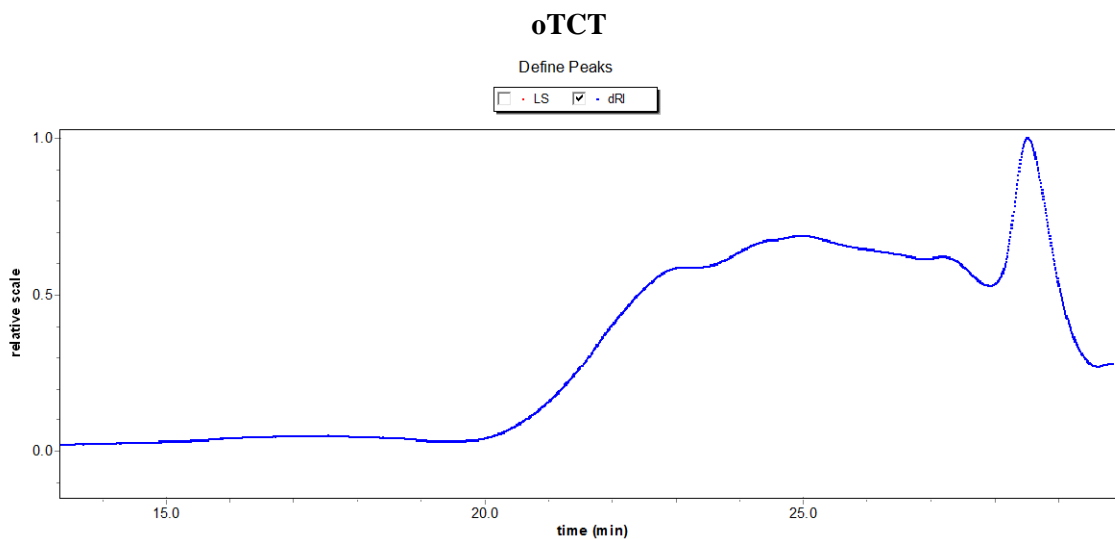
Molar mass moments (g/mol)

Mn 3.608e+3(4%)

Mw 2.159e+4(4%)

Mz 6.873e+4(9%)





CHCl₃ Column

Peak limits (min) 19.783 - 29.581

Polydispersity

Mw/Mn 3.206(6%)

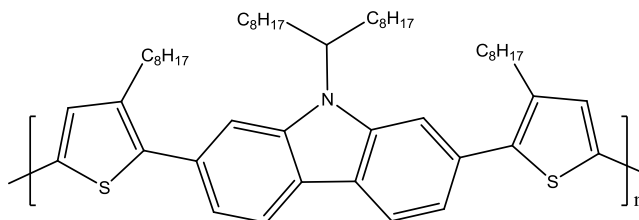
Mz/Mn 7.722(10%)

Molar mass moments (g/mol)

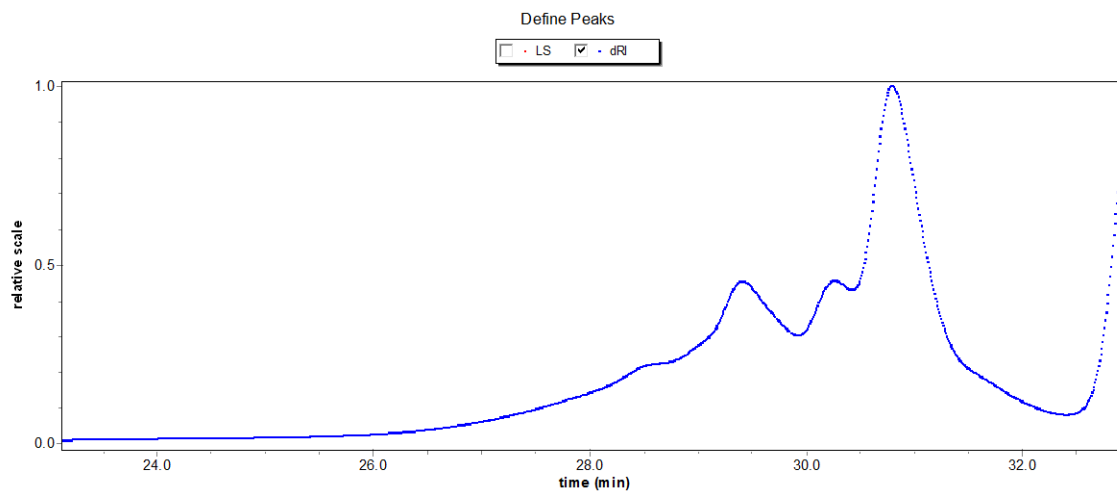
Mn 5.441e+3(4%)

Mw 1.744e+4(4%)

Mz 4.201e+4(9%)



TF - Suzuki



CHCl₃ Column

Peak limits (min) 25.891 - 29.931

Polydispersity

Mw/Mn 1.222(6%)

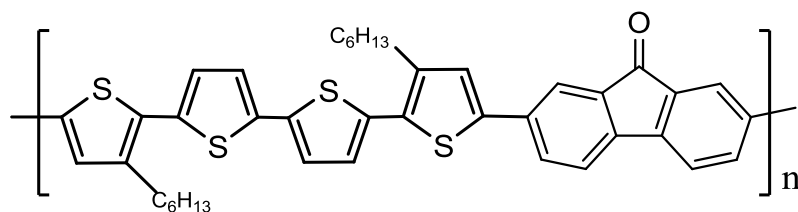
Mz/Mn 1.602(10%)

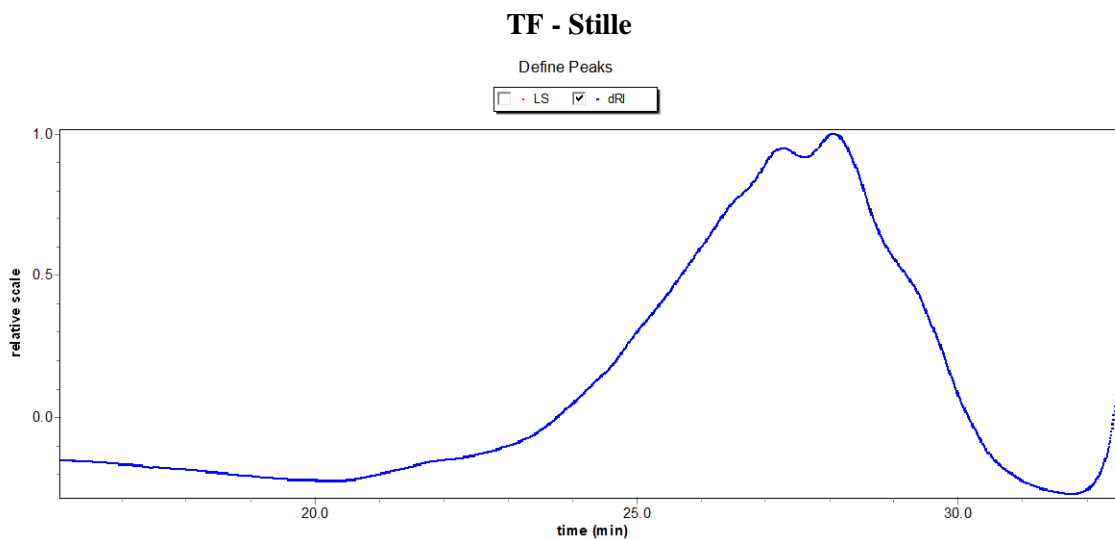
Molar mass moments (g/mol)

Mn 1.816e+3(4%)

Mw 2.219e+3(4%)

Mz 2.909e+3(9%)





CHCl₃ Column

Peak limits (min) 22.772 - 30.657

Polydispersity

Mw/Mn 1.487(6%)

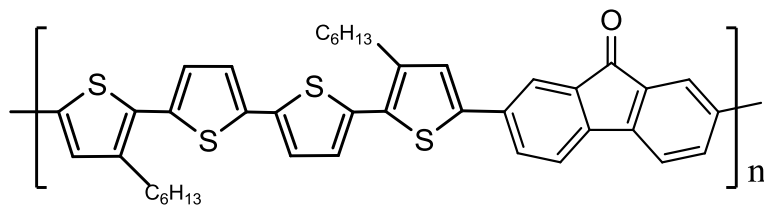
Mz/Mn 2.210(10%)

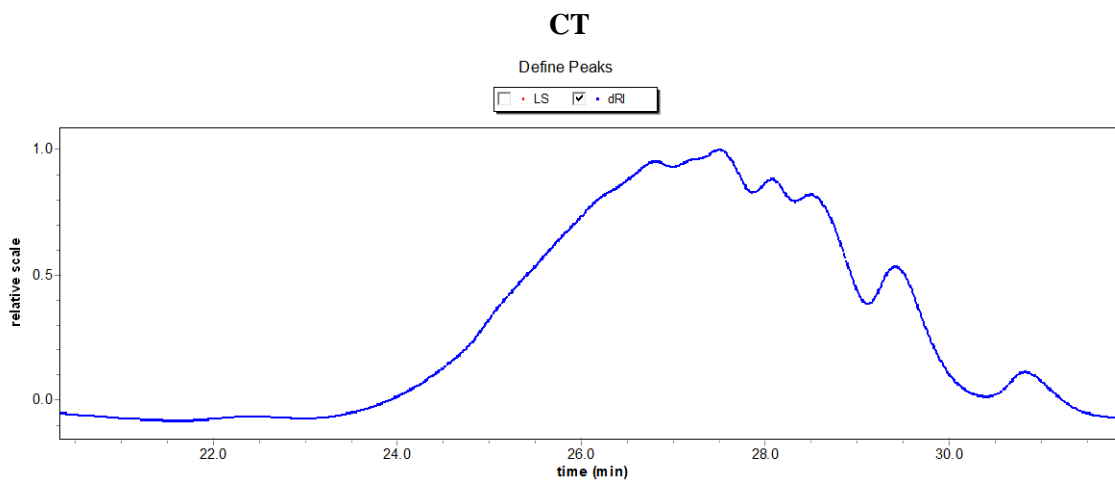
Molar mass moments (g/mol)

Mn 3.242e+3(4%)

Mw 4.819e+3(4%)

Mz 7.163e+3(9%)





CHCl₃ Column

Peak limits (min) 23.155 - 30.341

Polydispersity

Mw/Mn 1.483(6%)

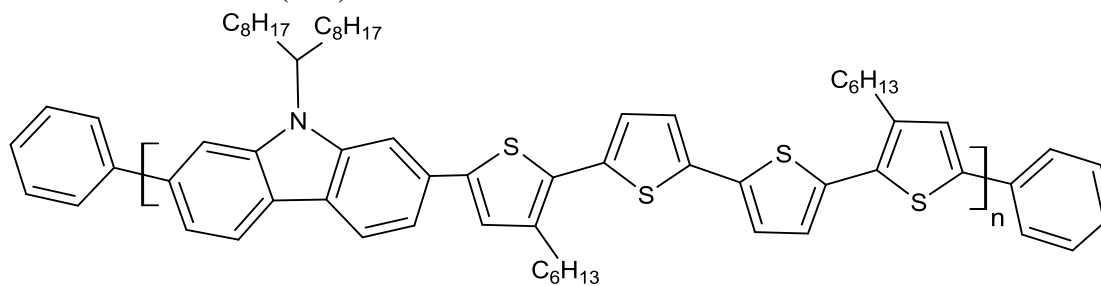
Mz/Mn 2.109(10%)

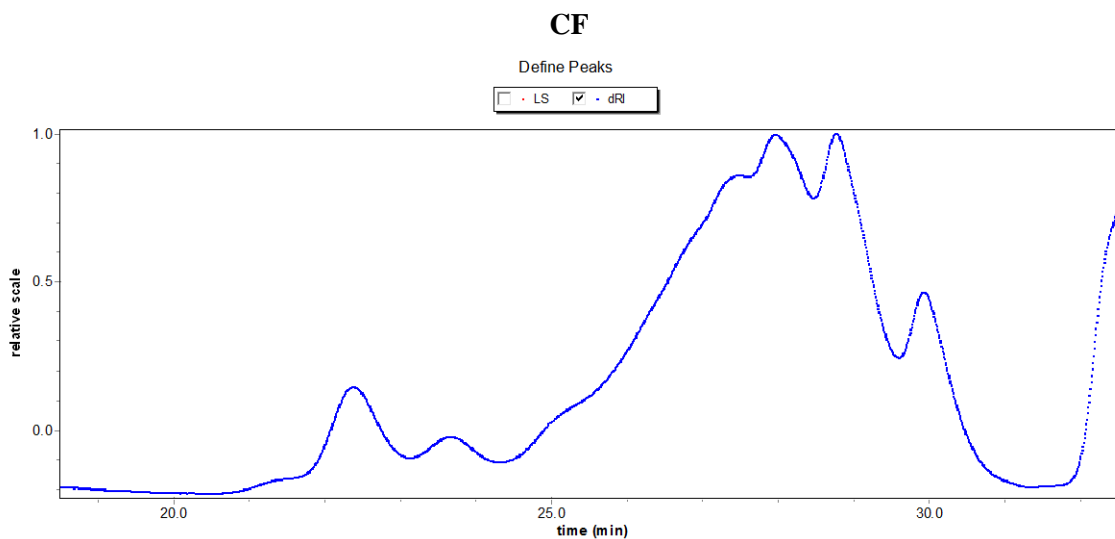
Molar mass moments (g/mol)

Mn 3.296e+3(4%)

Mw 4.888e+3(4%)

Mz 6.951e+3(9%)





CHCl₃ Column

Peak limits (min) 20.590 - 23.130

Polydispersity

Mw/Mn 1.005(6%)

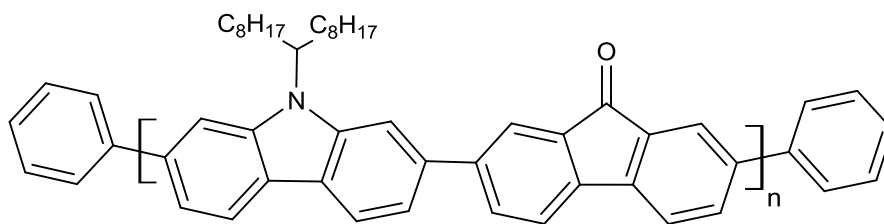
Mz/Mn 1.009(10%)

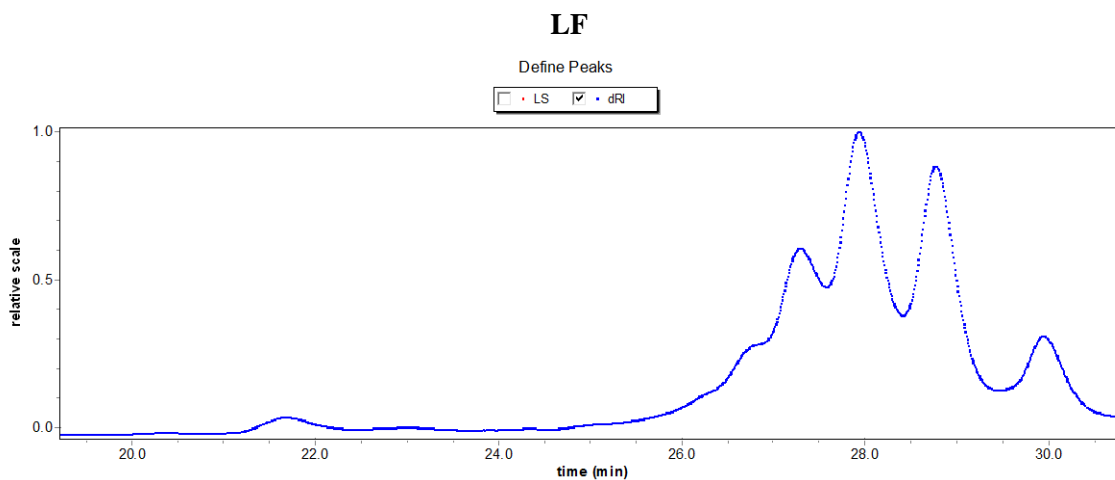
Molar mass moments (g/mol)

Mn 4.248e+4(4%)

Mw 4.267e+4(4%)

Mz 4.287e+4(9%)





THF Column

Peak limits (min) 25.369 - 28.453

Polydispersity

Mw/Mn 1.135(30%)

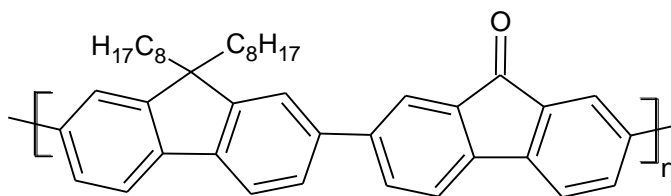
Mz/Mn 1.336(52%)

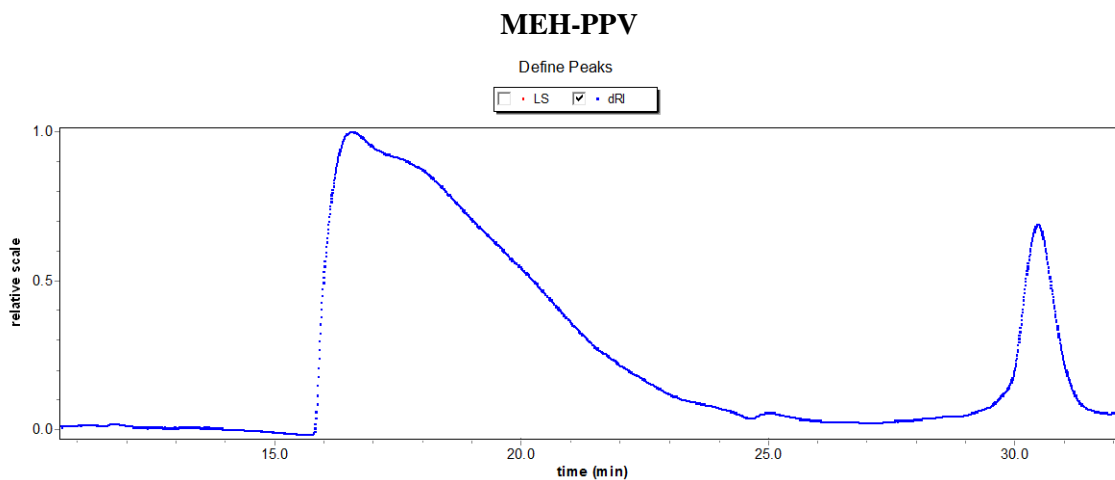
Molar mass moments (g/mol)

Mn 2.030e+3(21%)

Mw 2.305e+3(21%)

Mz 2.712e+3(47%)





CHCl₃ Column

Peak limits (min) 15.823 - 24.386

Polydispersity

Mw/Mn 2.277(6%)

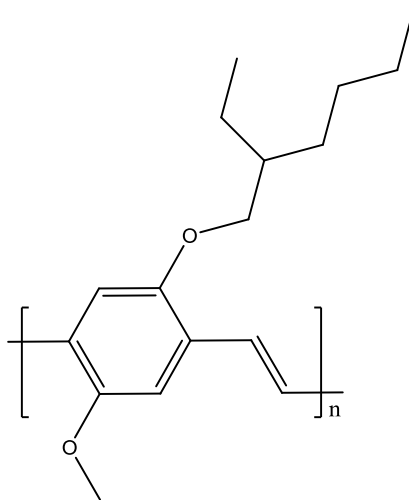
Mz/Mn 3.402(10%)

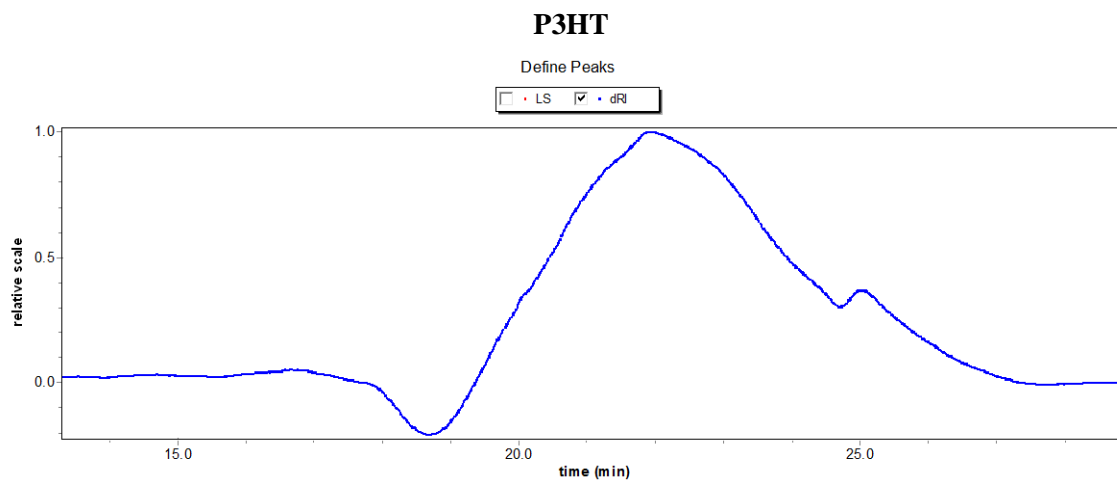
Molar mass moments (g/mol)

Mn 1.579e+5(4%)

Mw 3.594e+5(4%)

Mz 5.370e+5(9%)





CHCl₃ Column

Peak limits (min) 17.589 - 27.735

Polydispersity

Mw/Mn 1.777(6%)

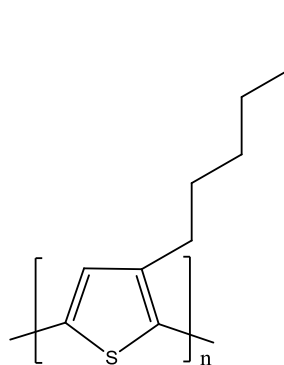
Mz/Mn 2.616(10%)

Molar mass moments (g/mol)

Mn 2.836e+4(4%)

Mw 5.039e+4(4%)

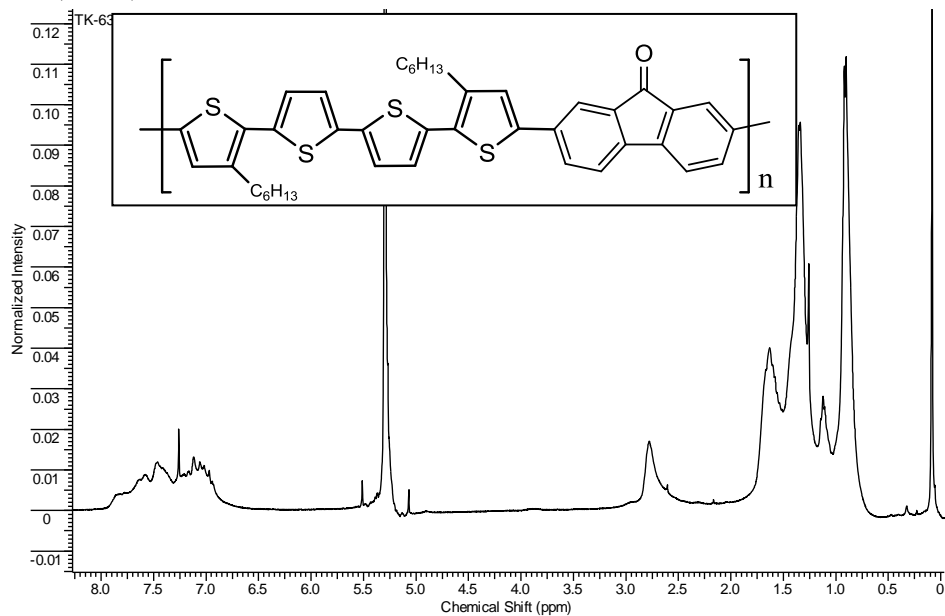
Mz 7.419e+4(9%)



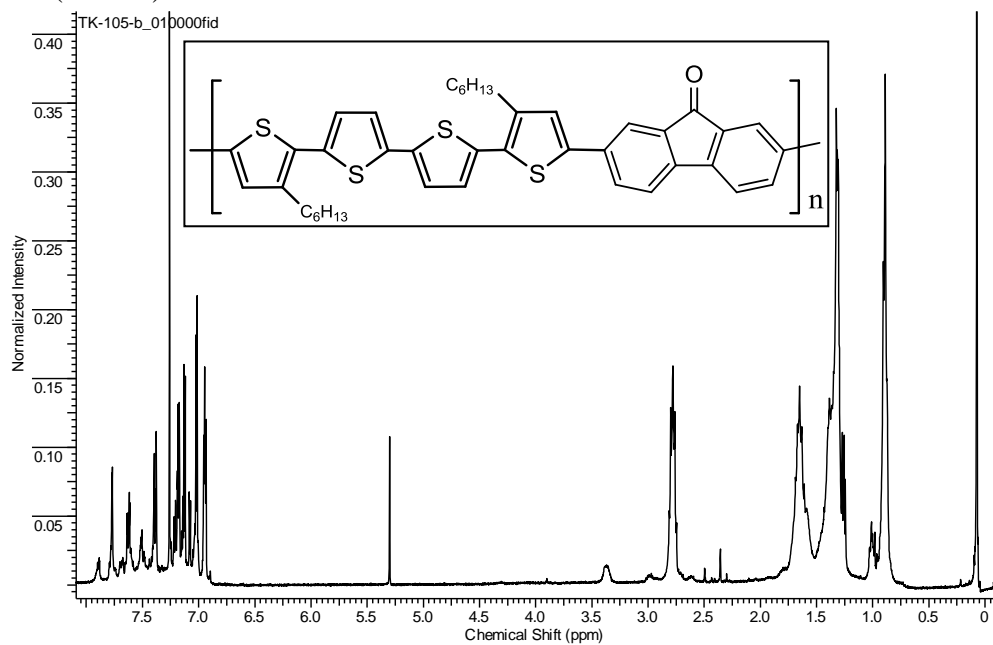
¹H NMR Spectra of Polymers

The peak broadening evident among the polymer spectra is indicative of polymerization.

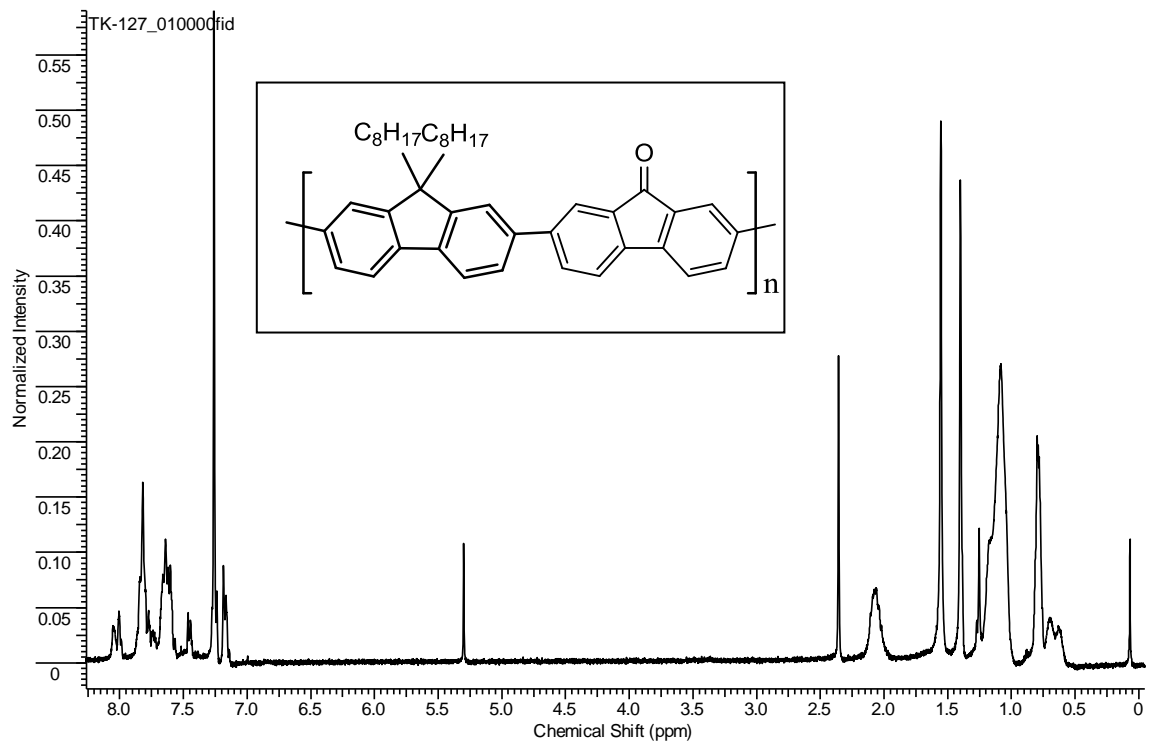
TF (Stille)



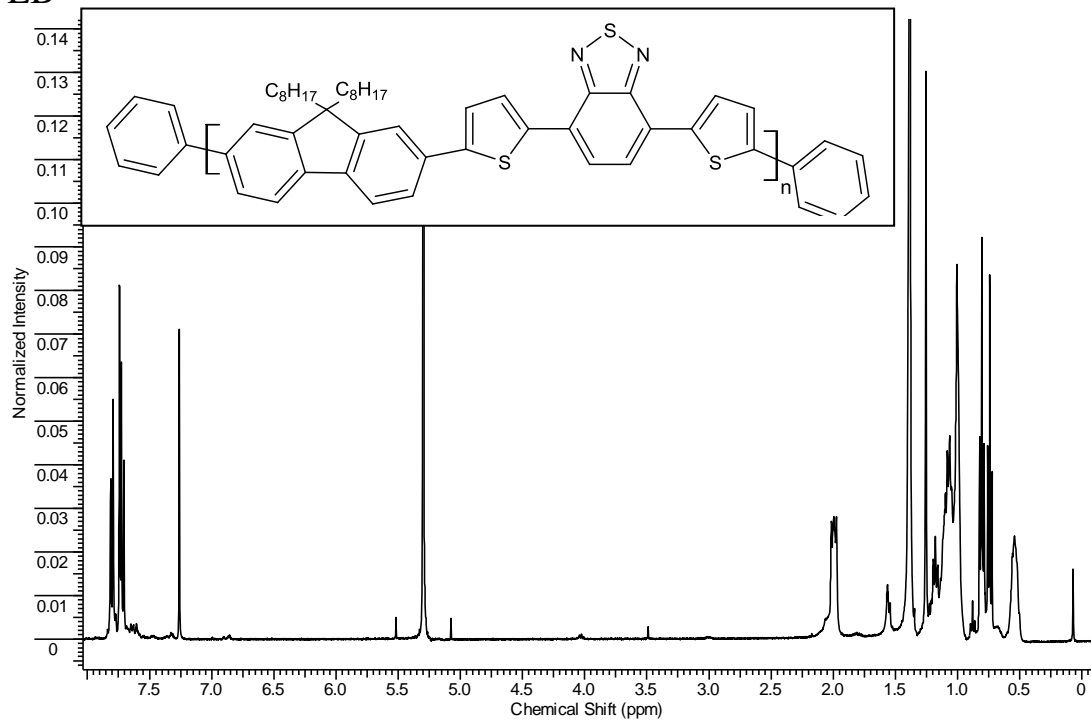
TF (Suzuki)



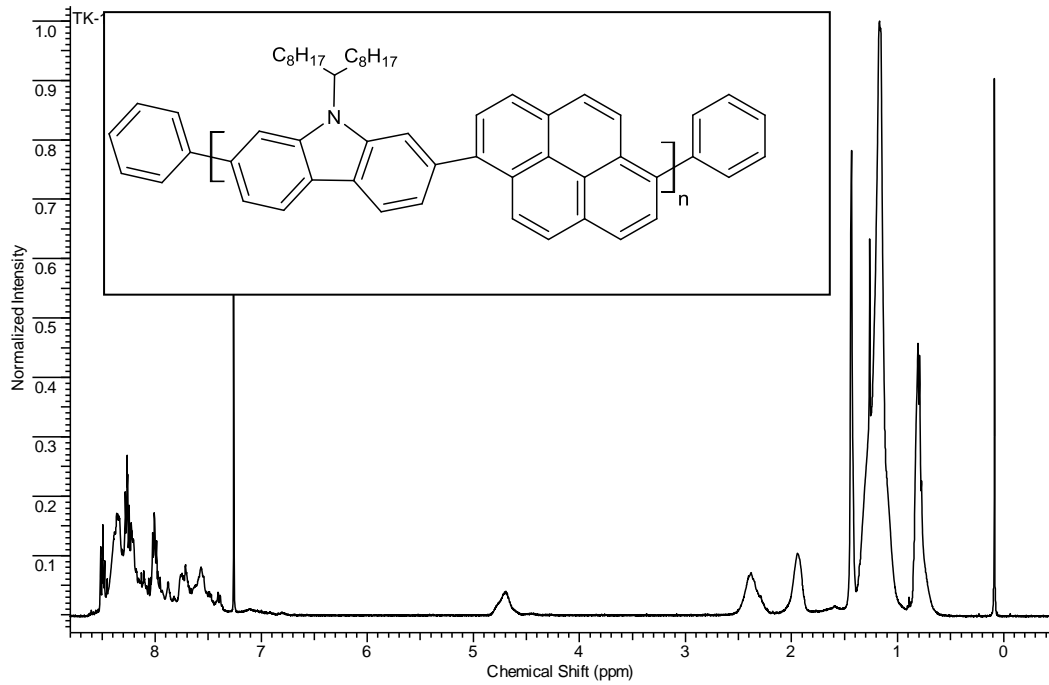
LF



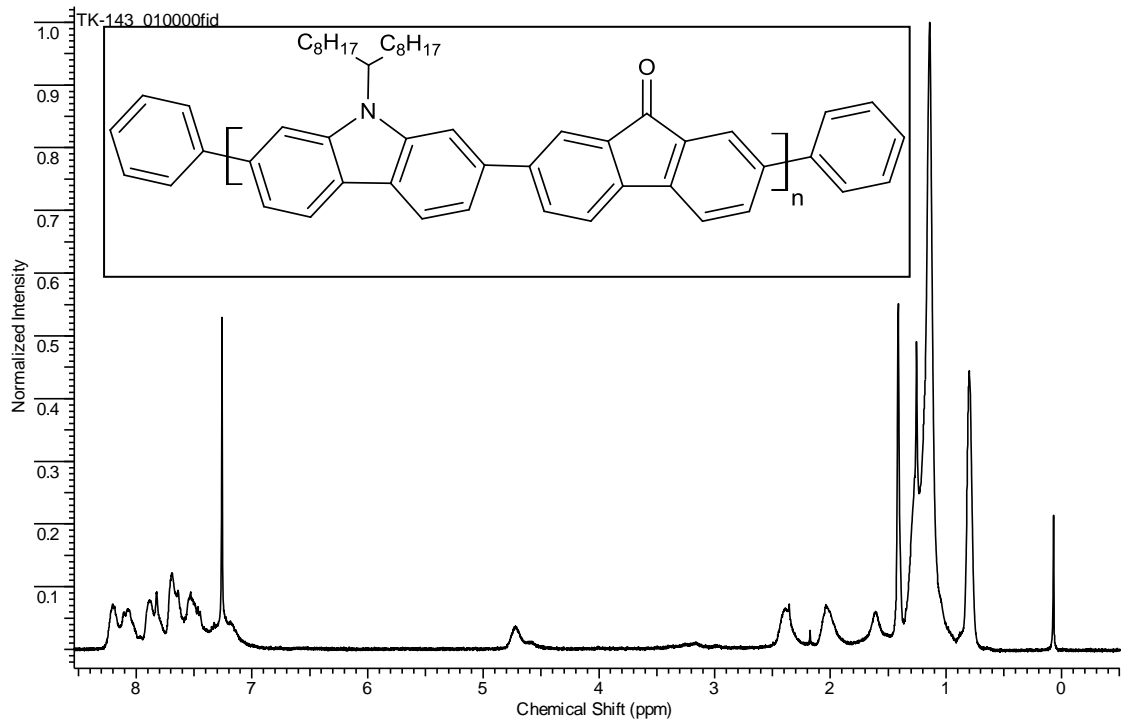
LB



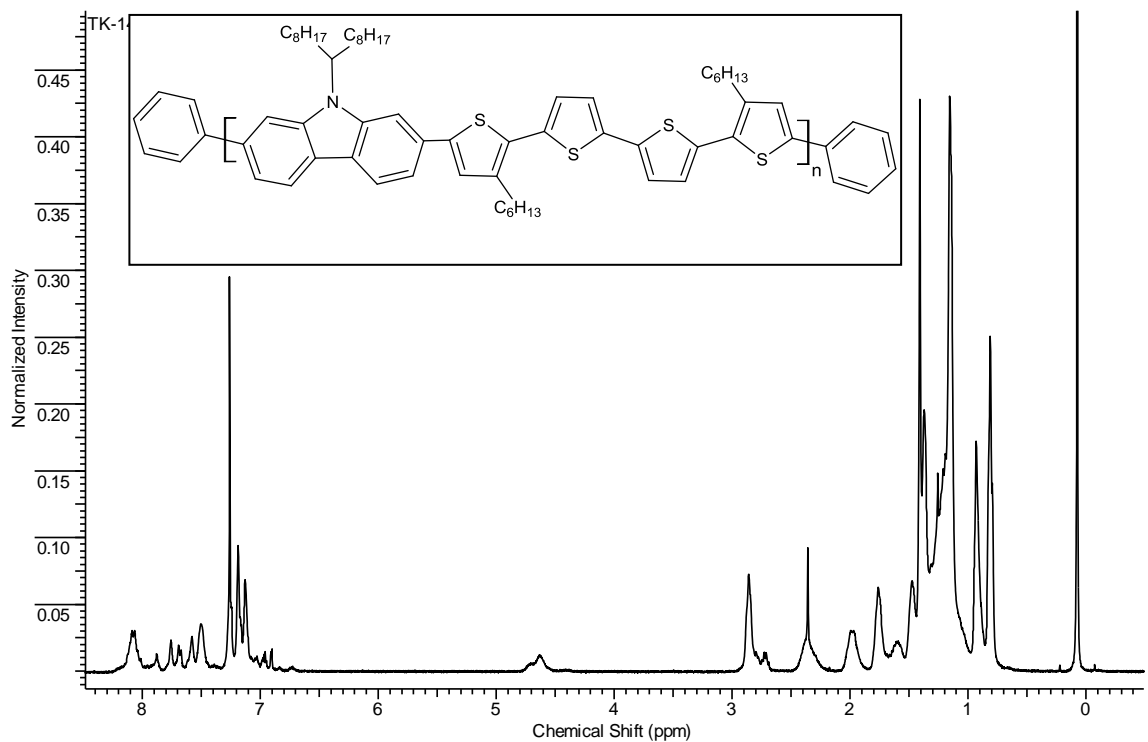
CP



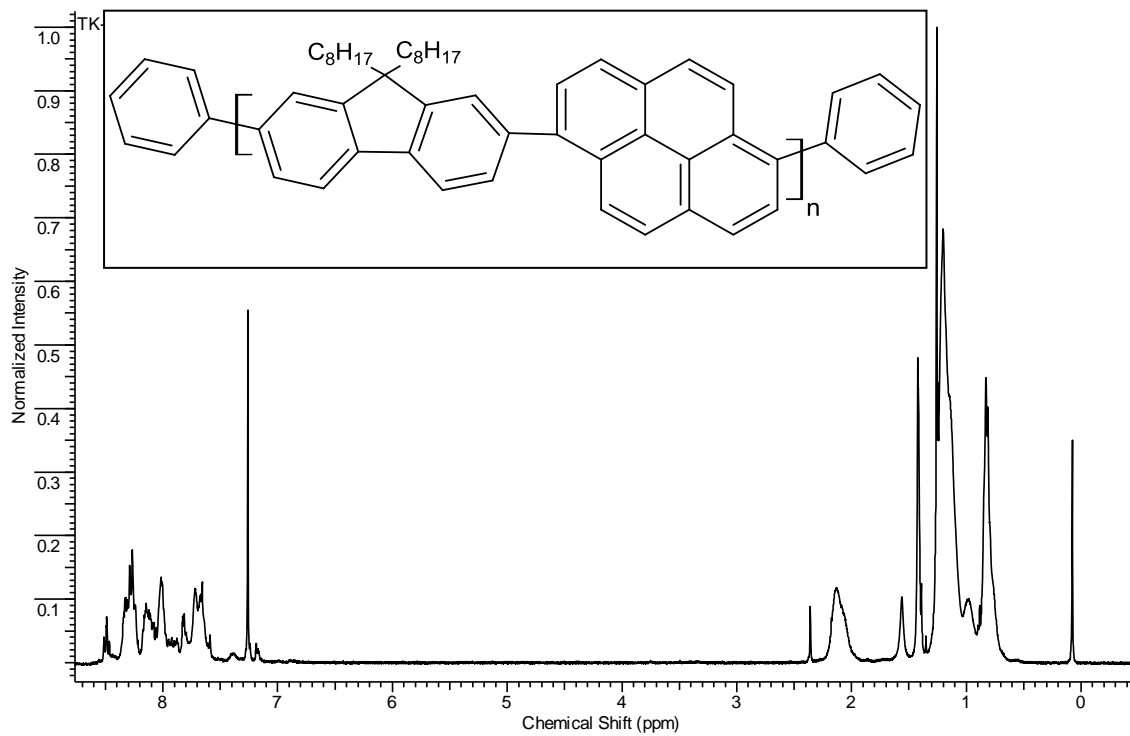
CF

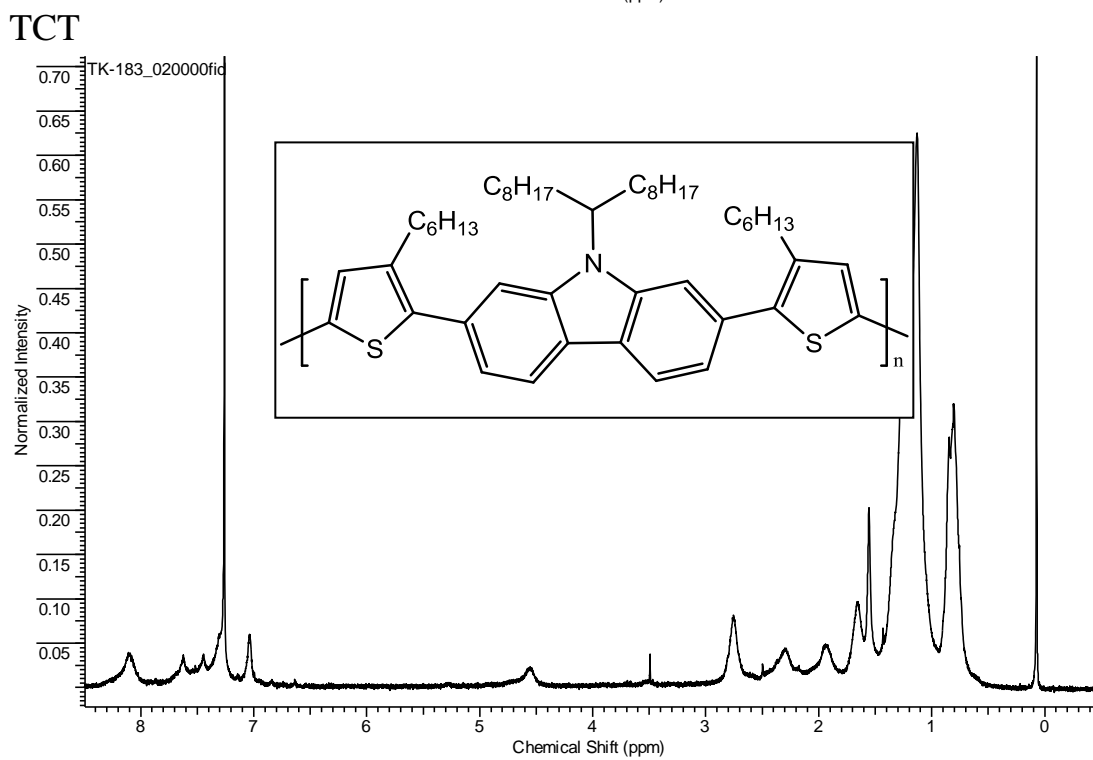
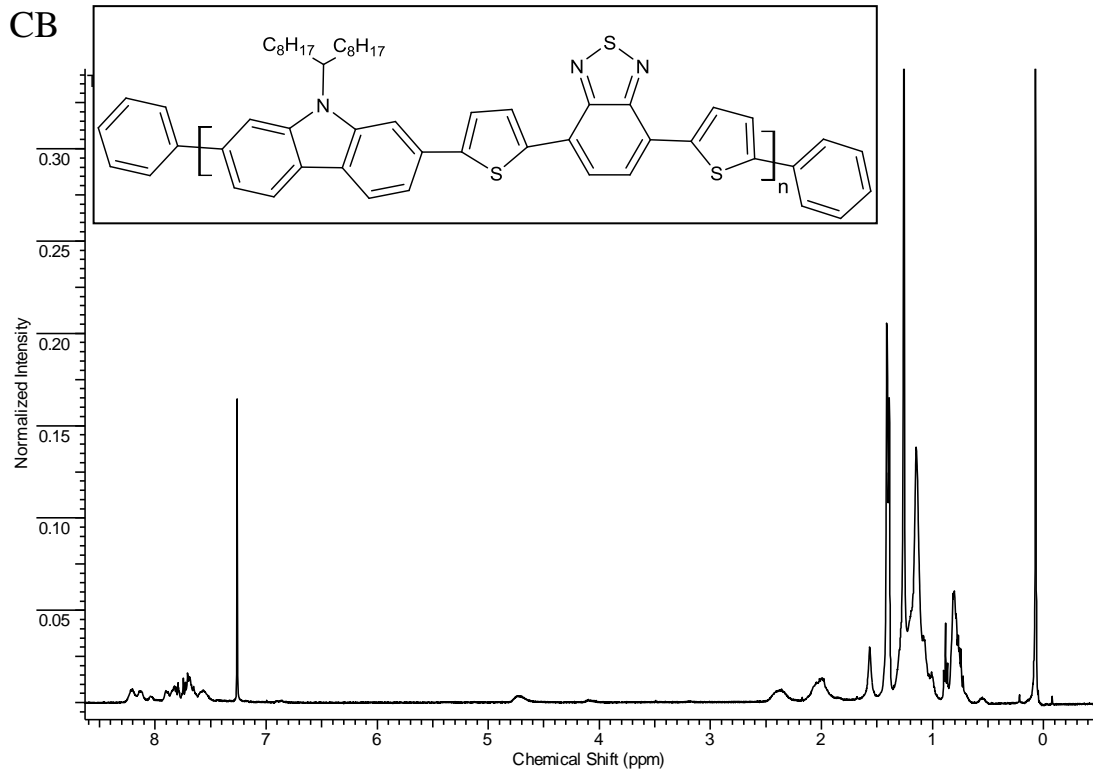


CT

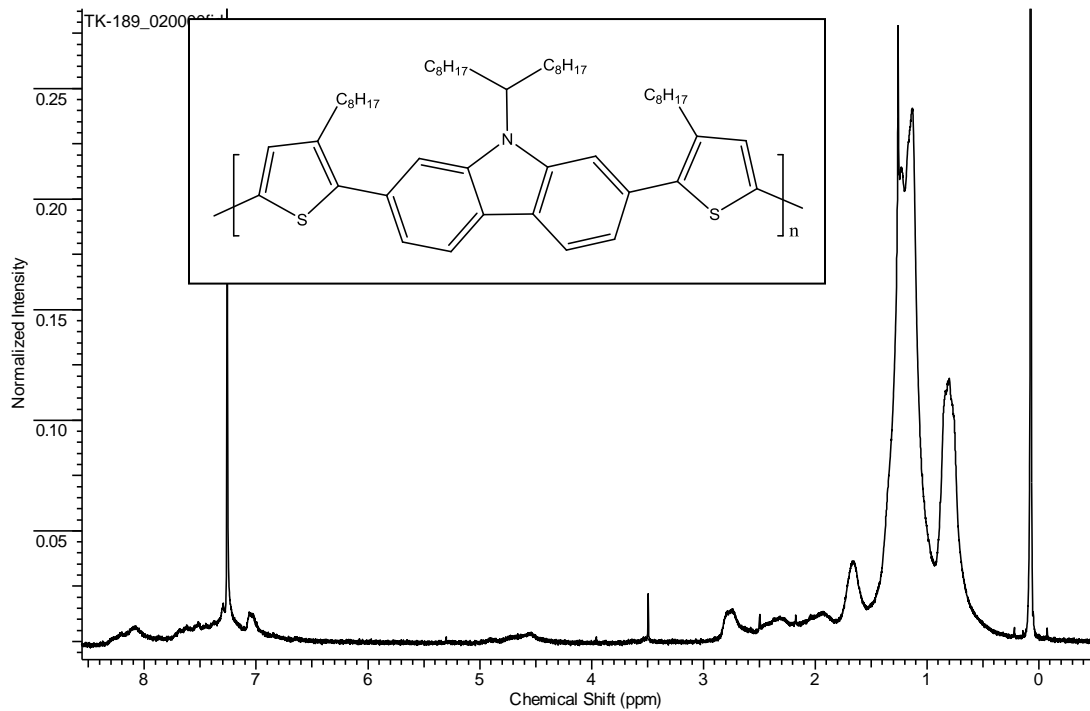


LP

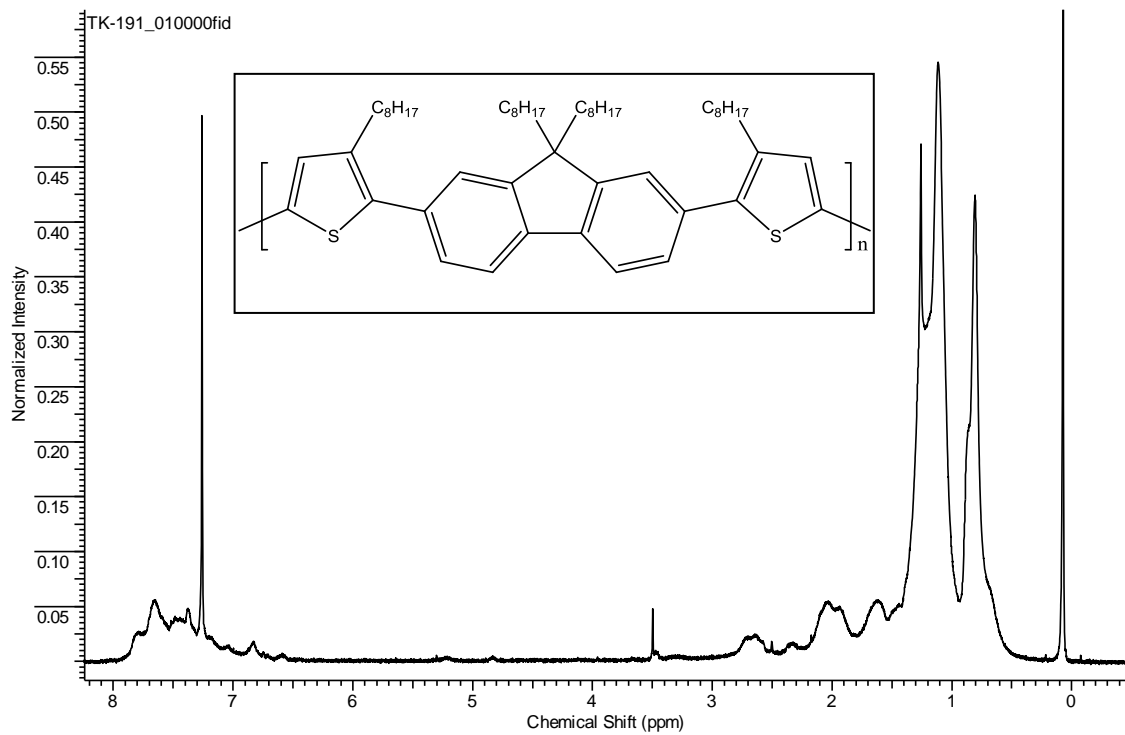




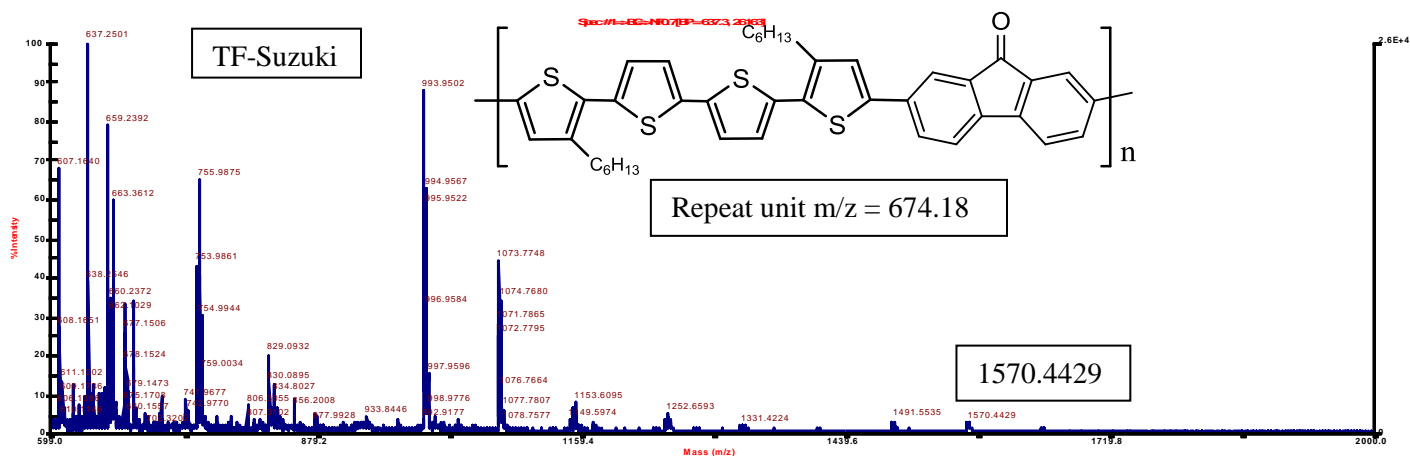
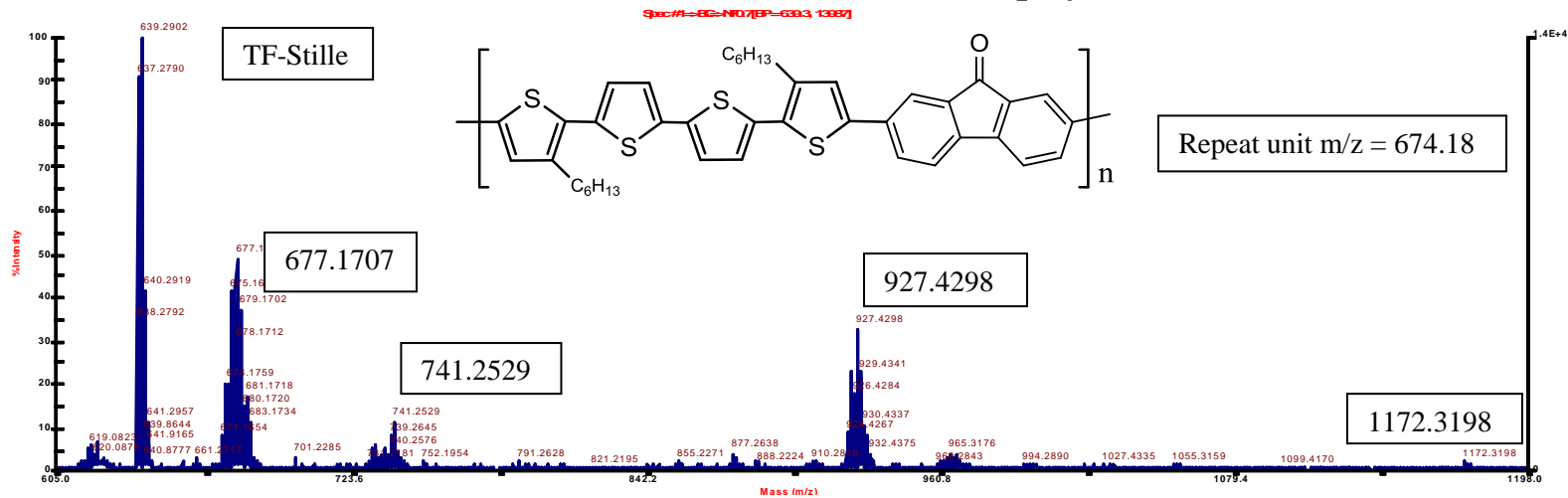
oTCT



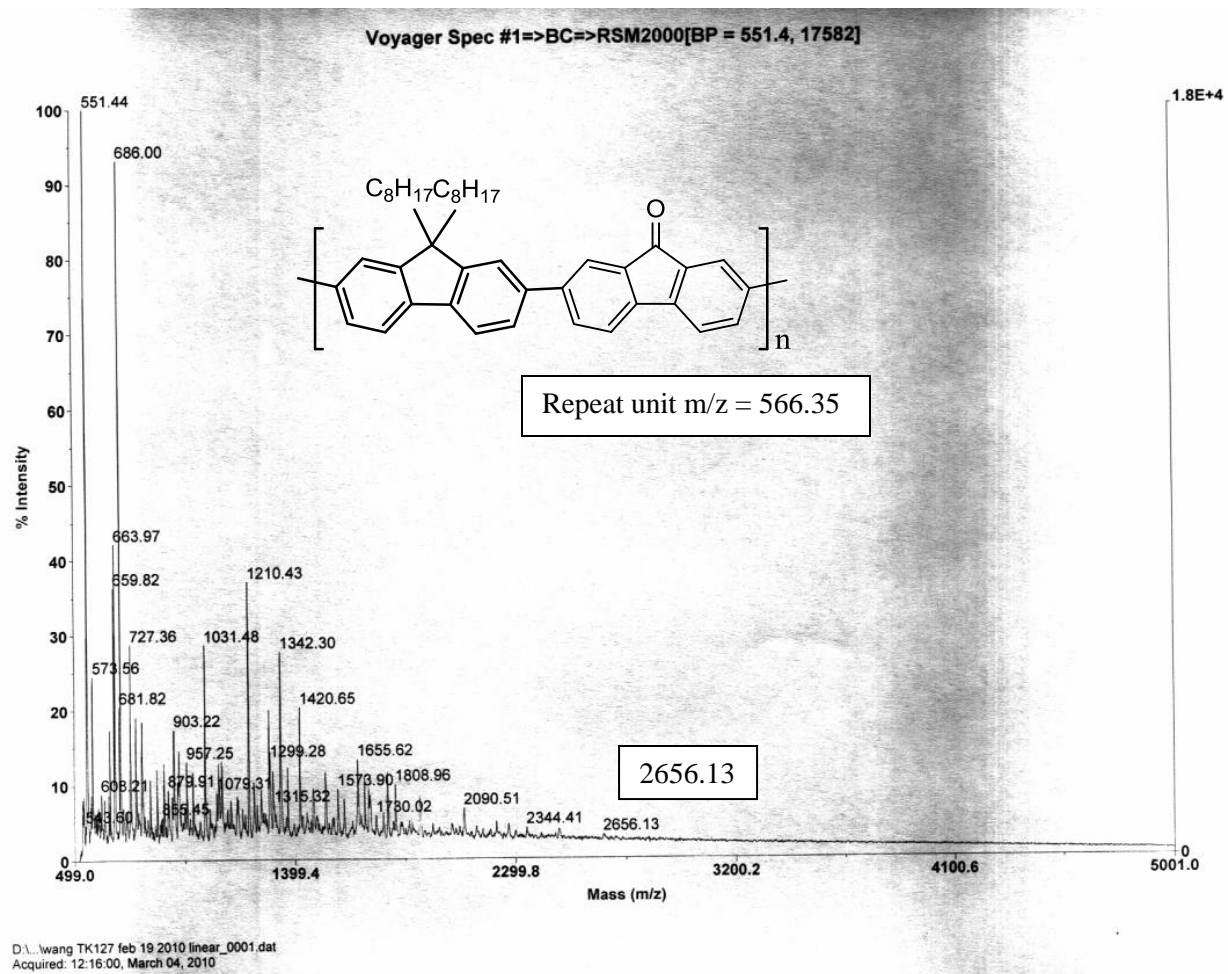
oTLT



MALDI-TOF results for selected polymers

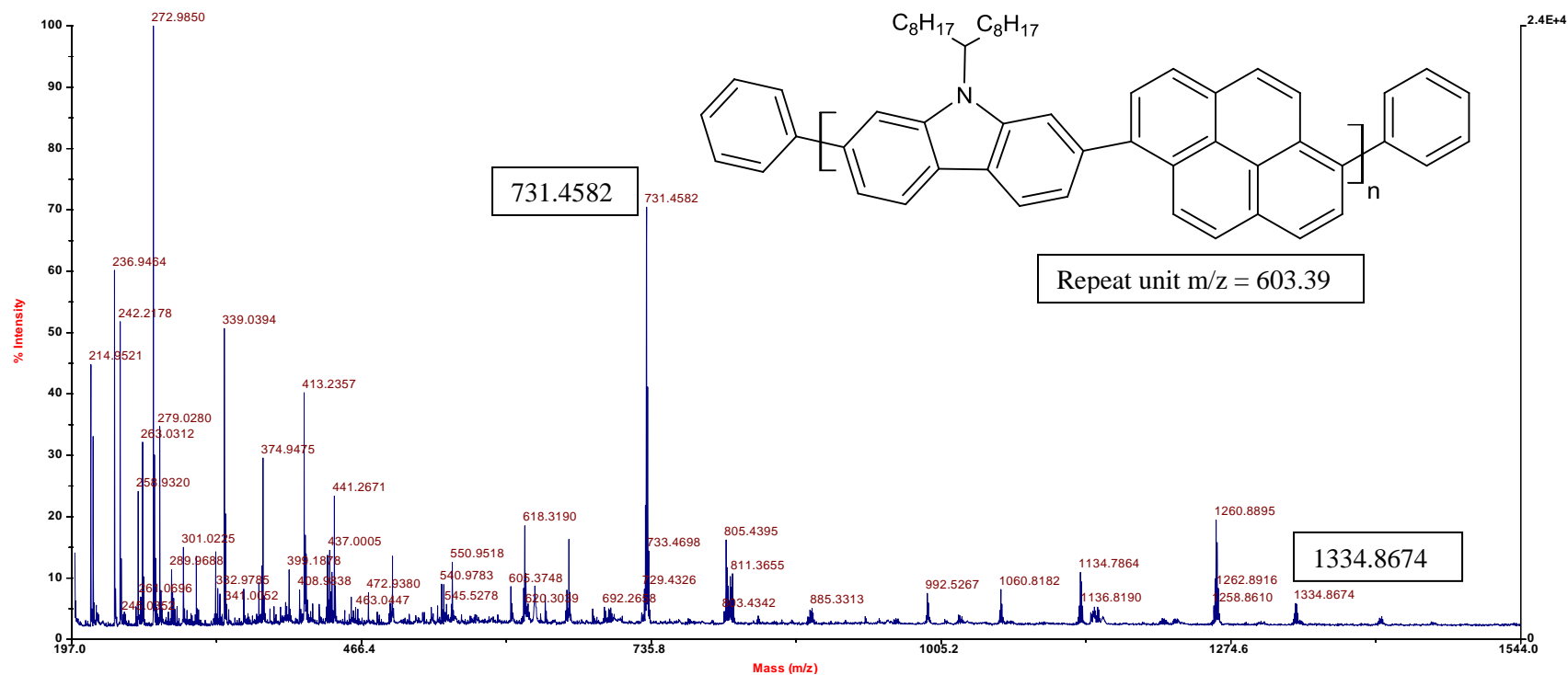


LF

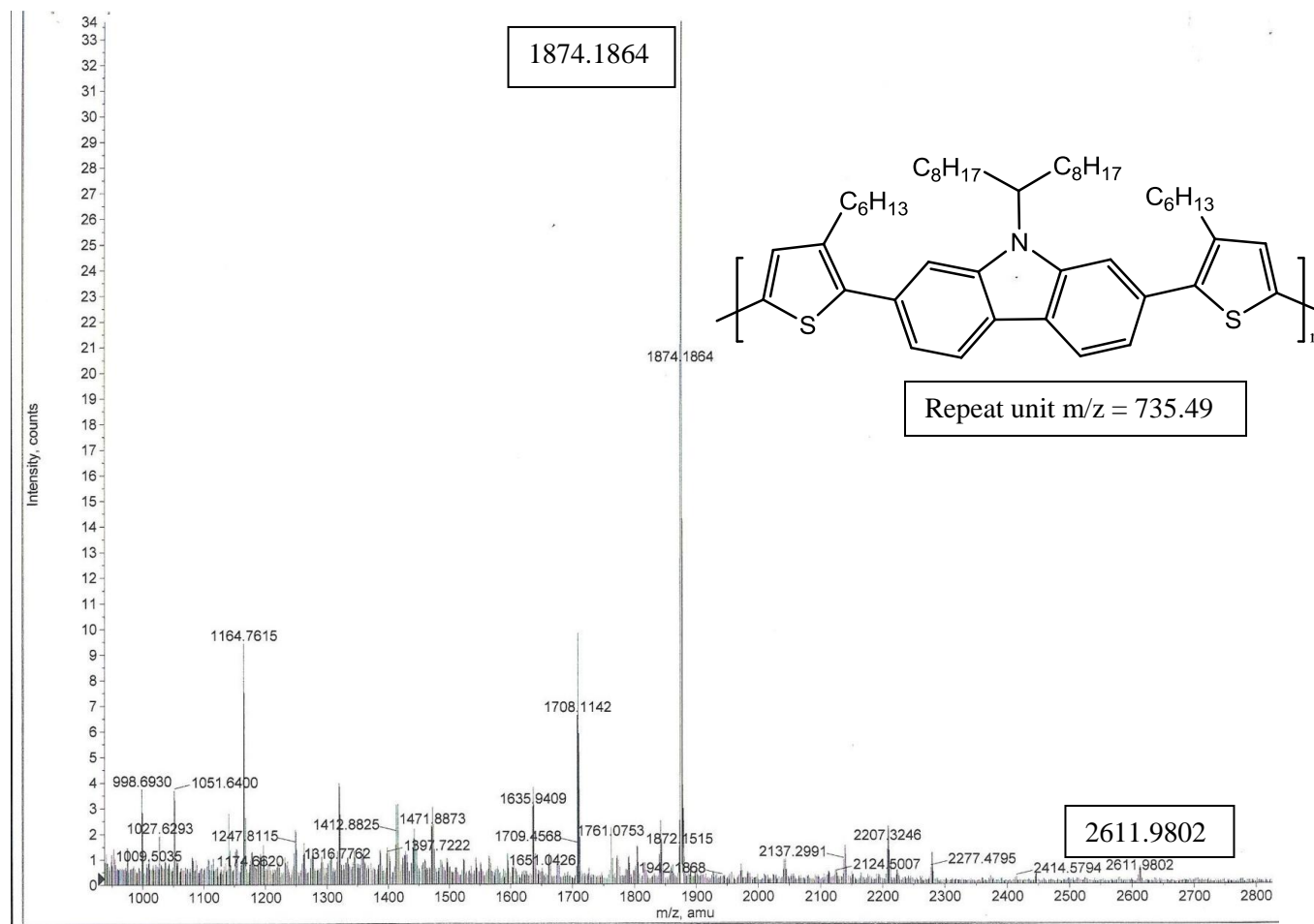


CP

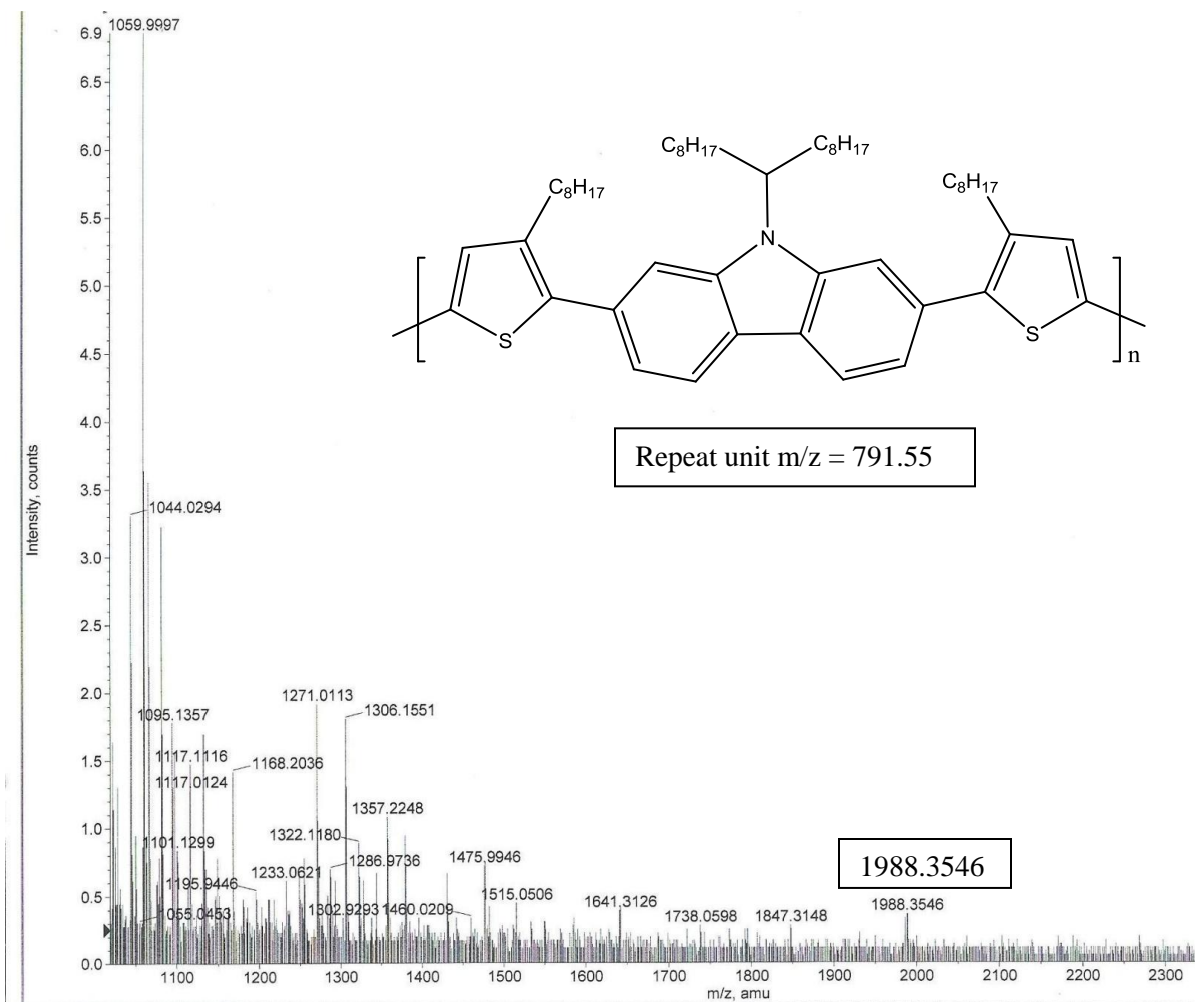
Voyager Spec #1[BP = 273.0, 23524]



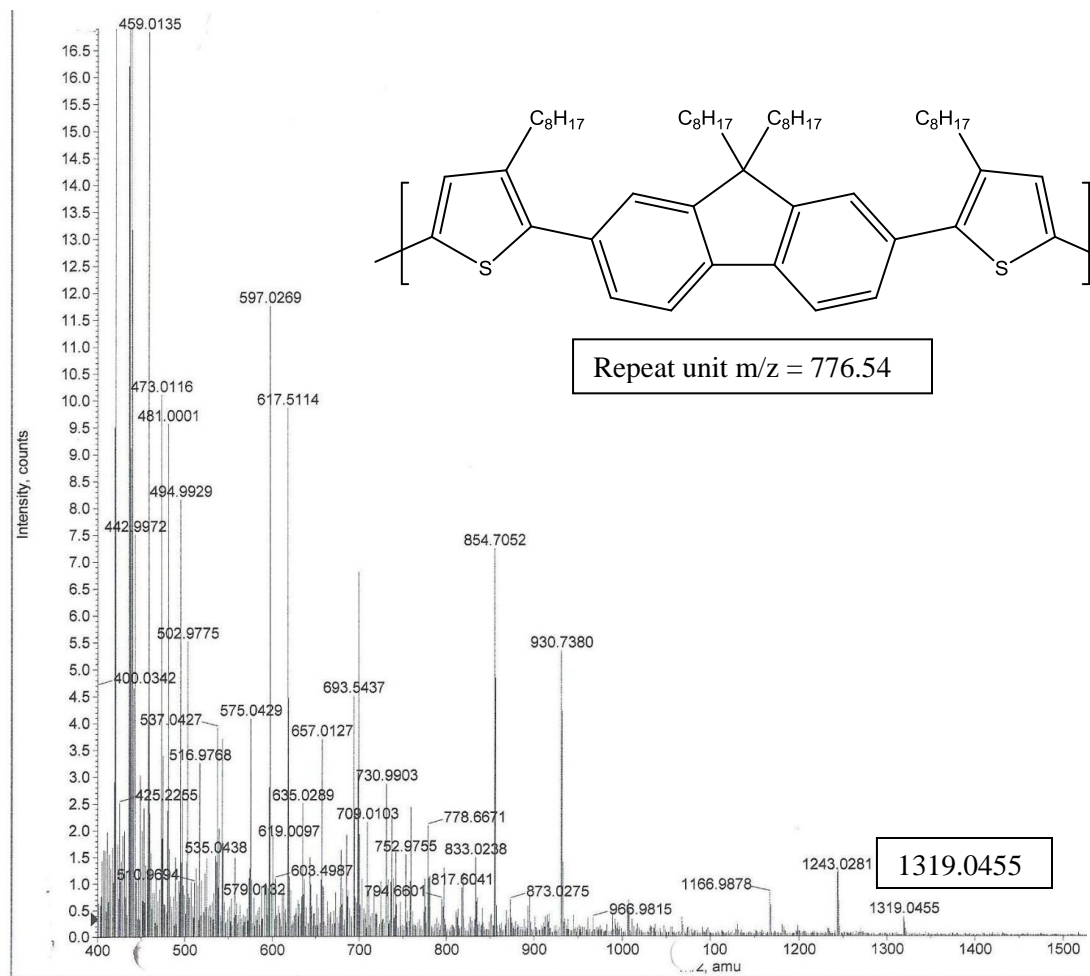
TCT



oTCT

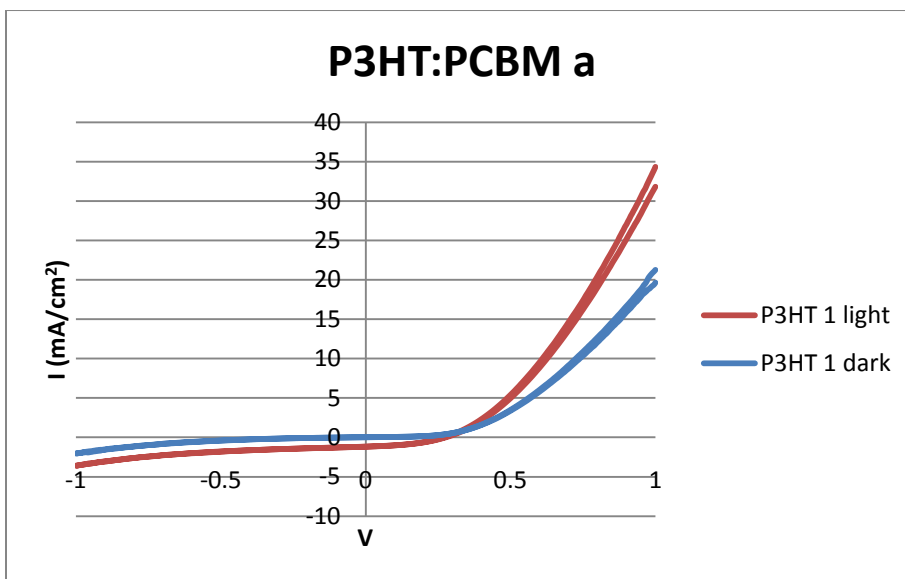
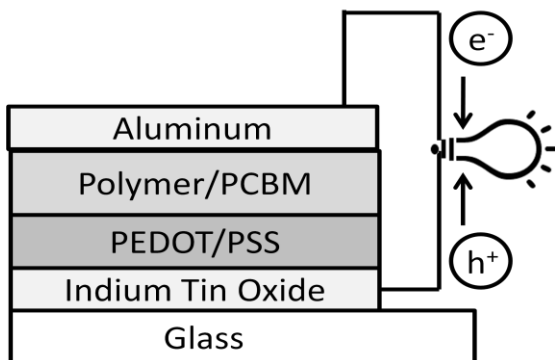


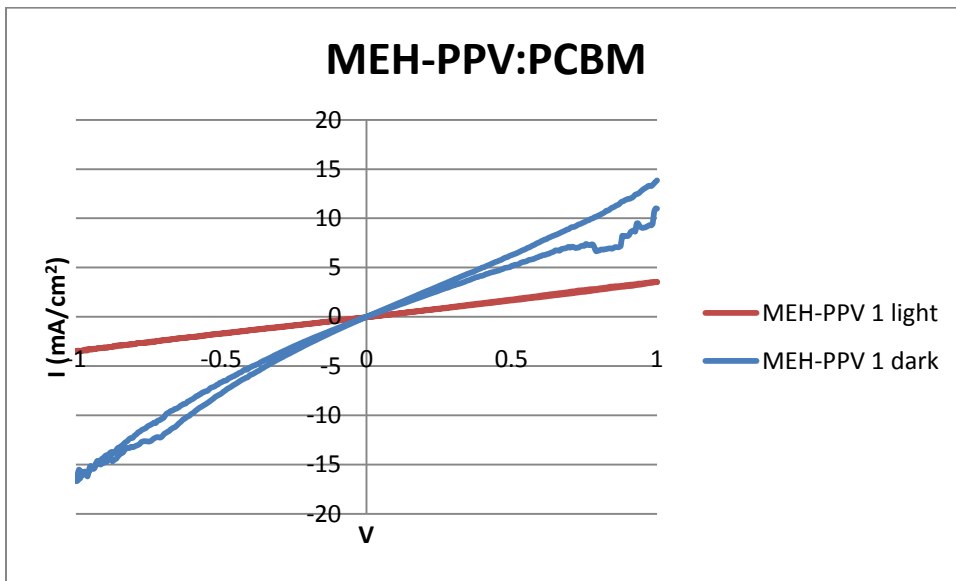
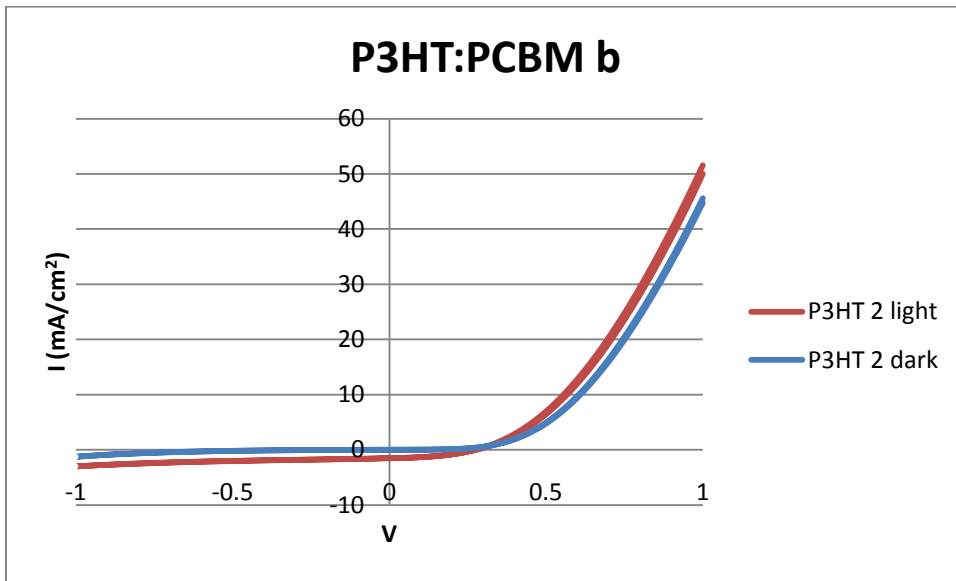
oTLT

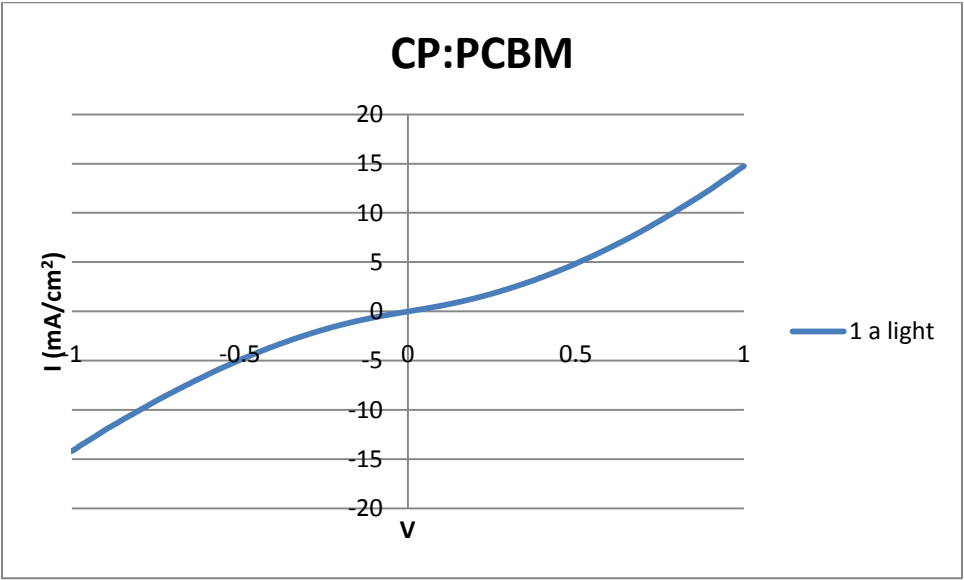
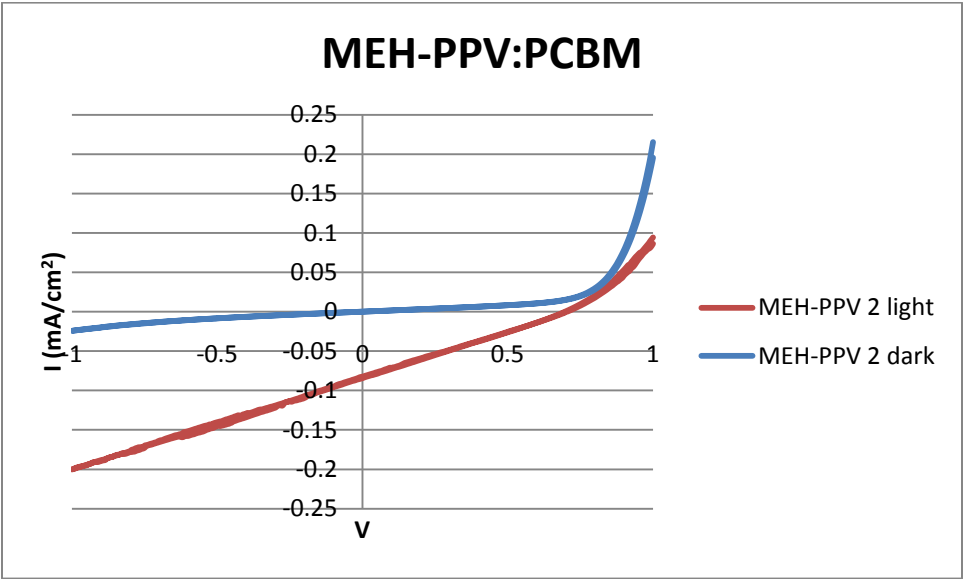


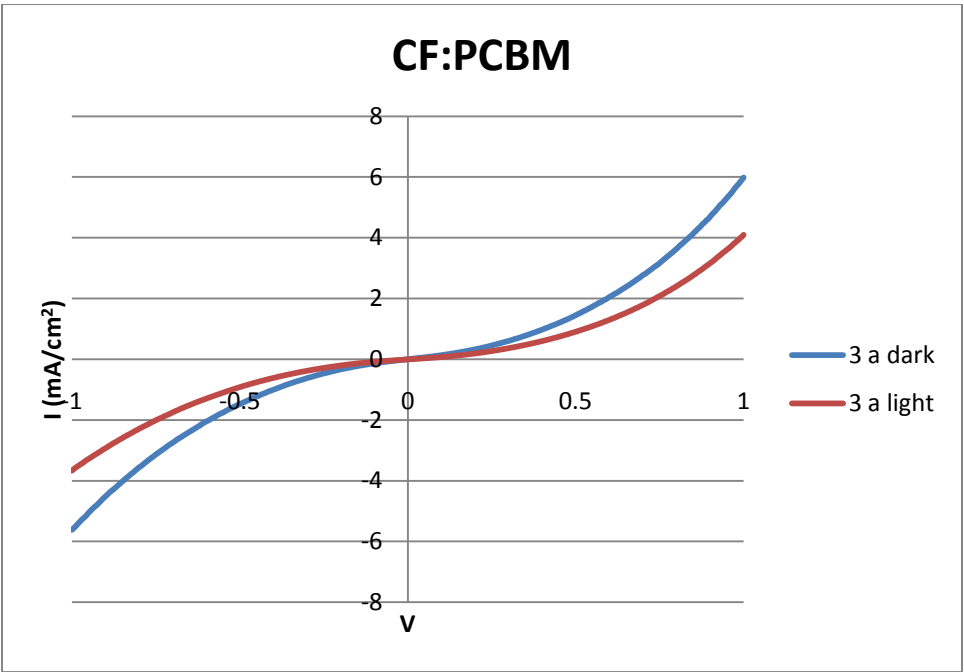
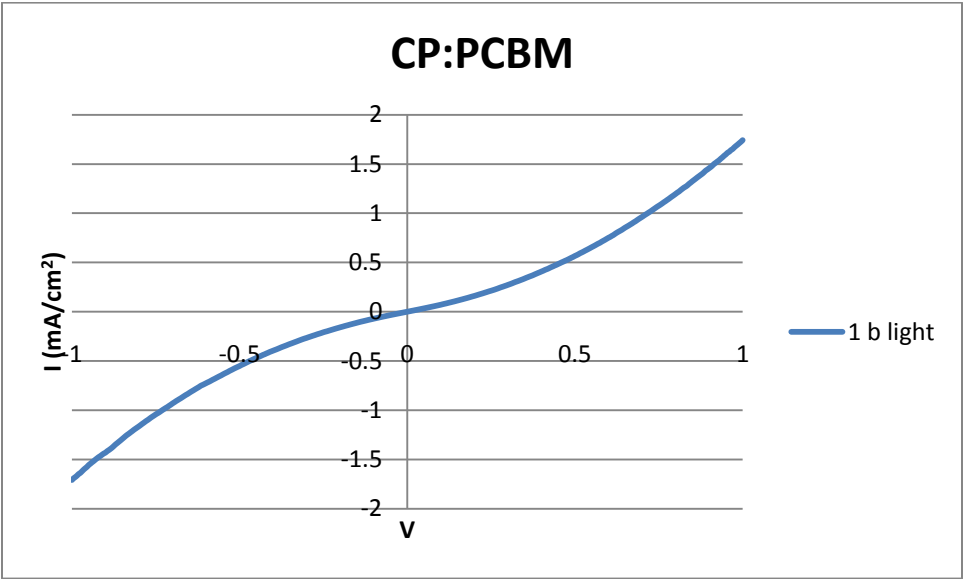
Solar Cells

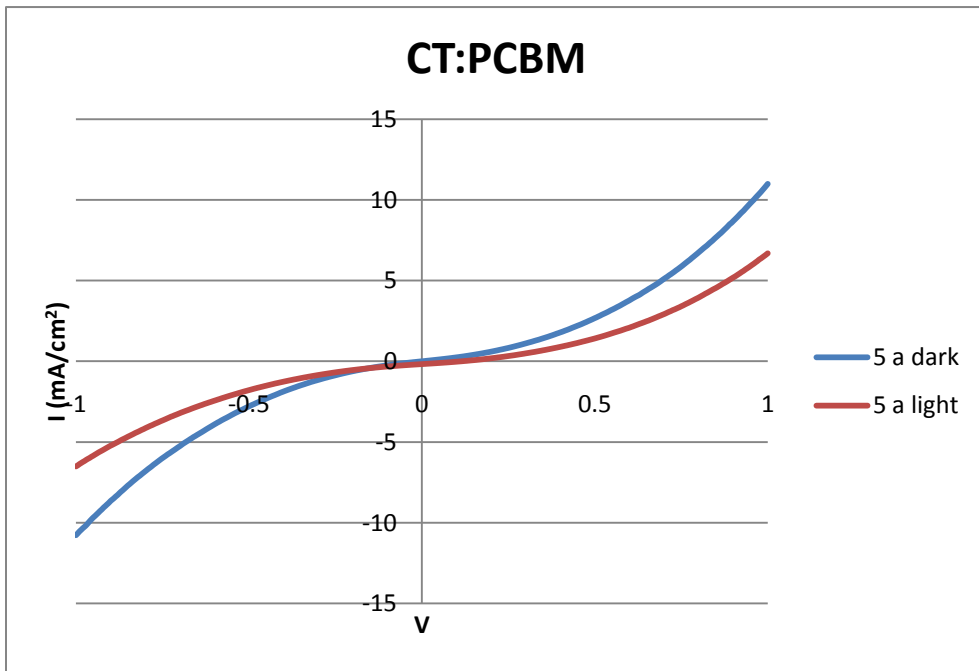
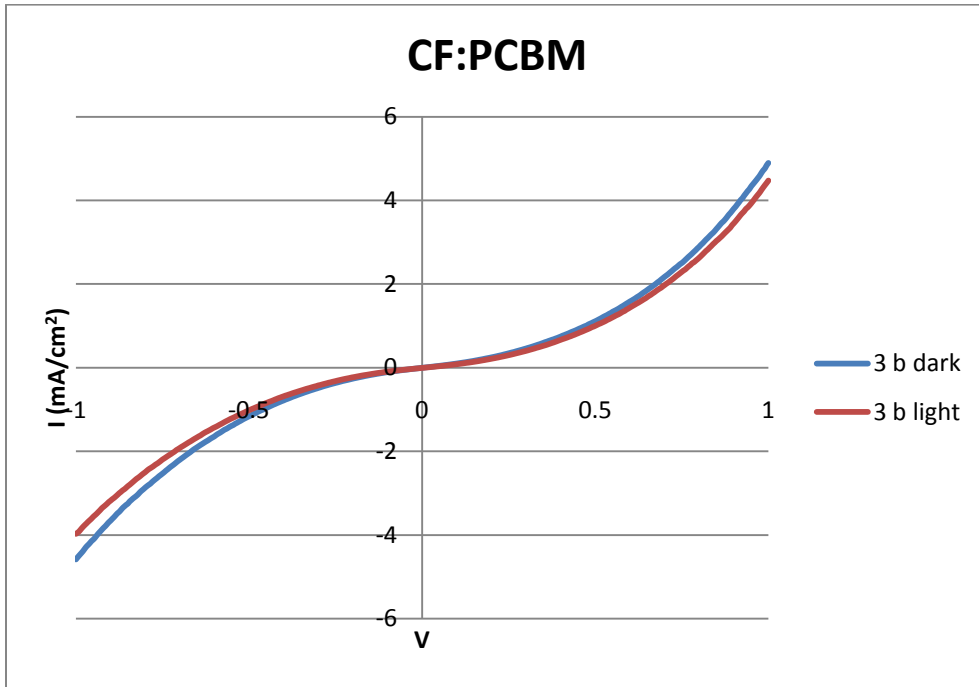
Aluminum electrode

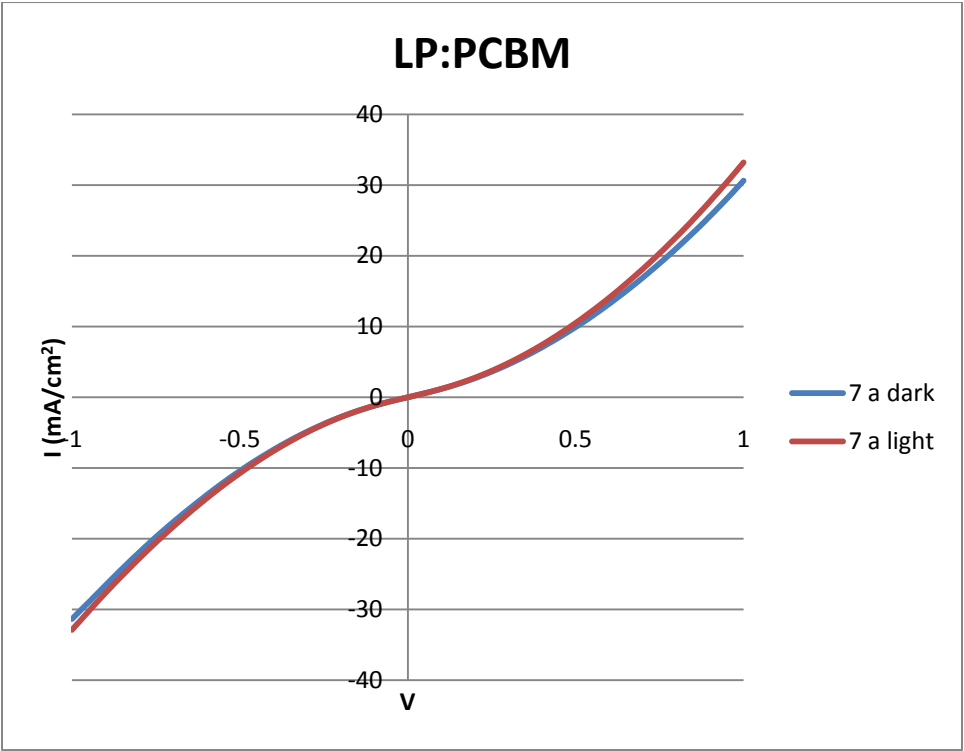
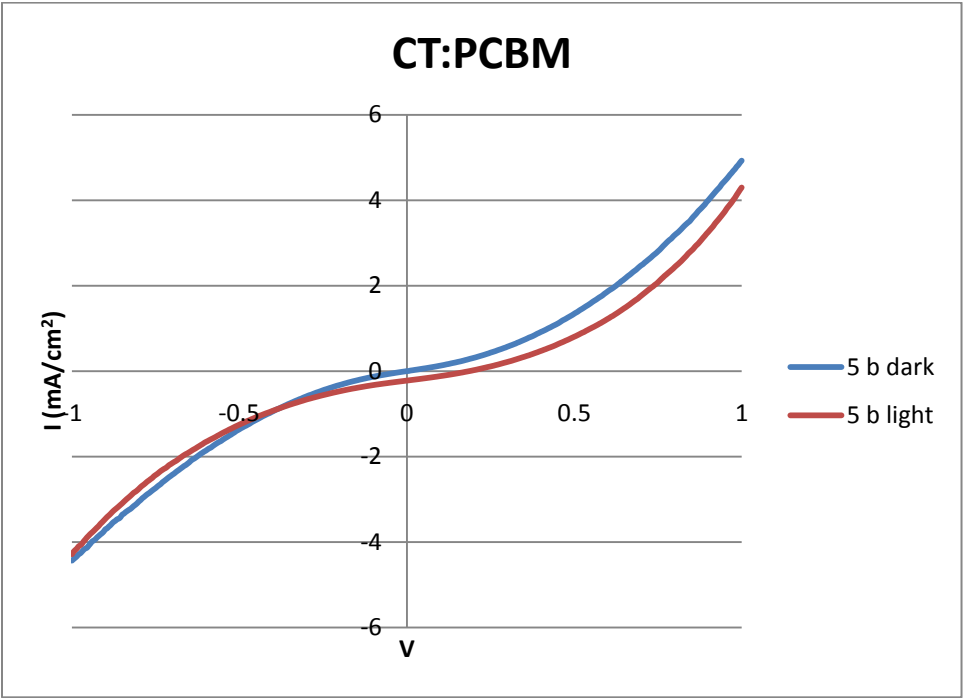


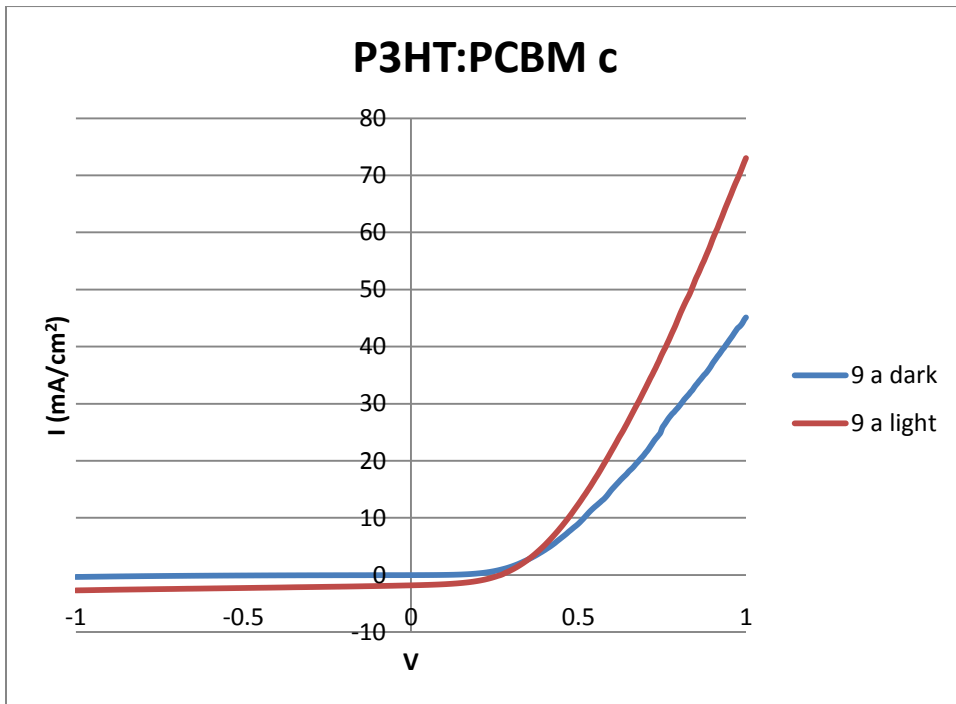
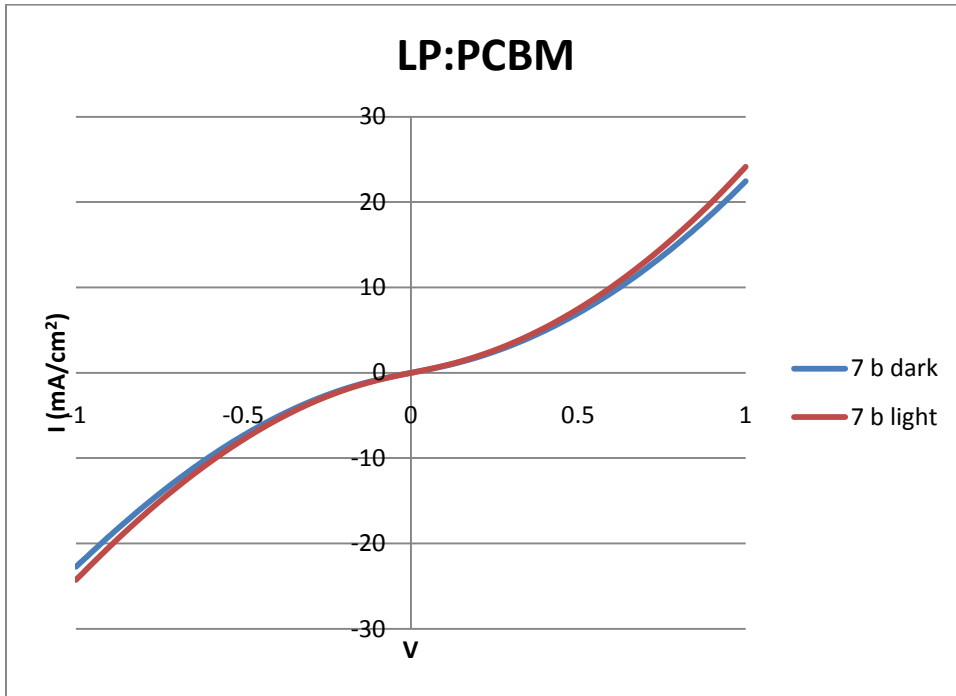


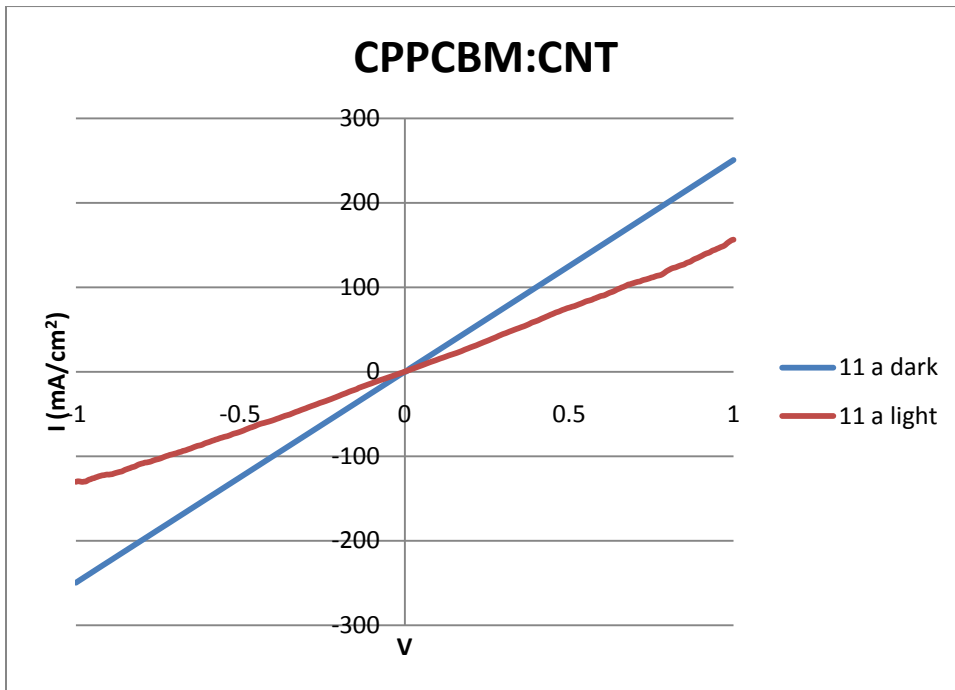
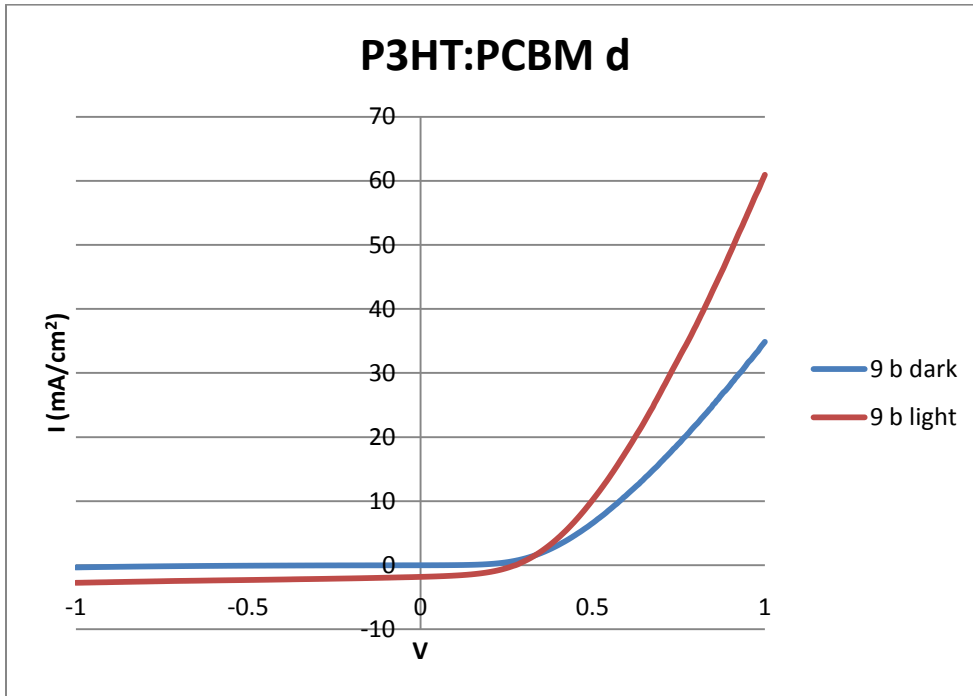


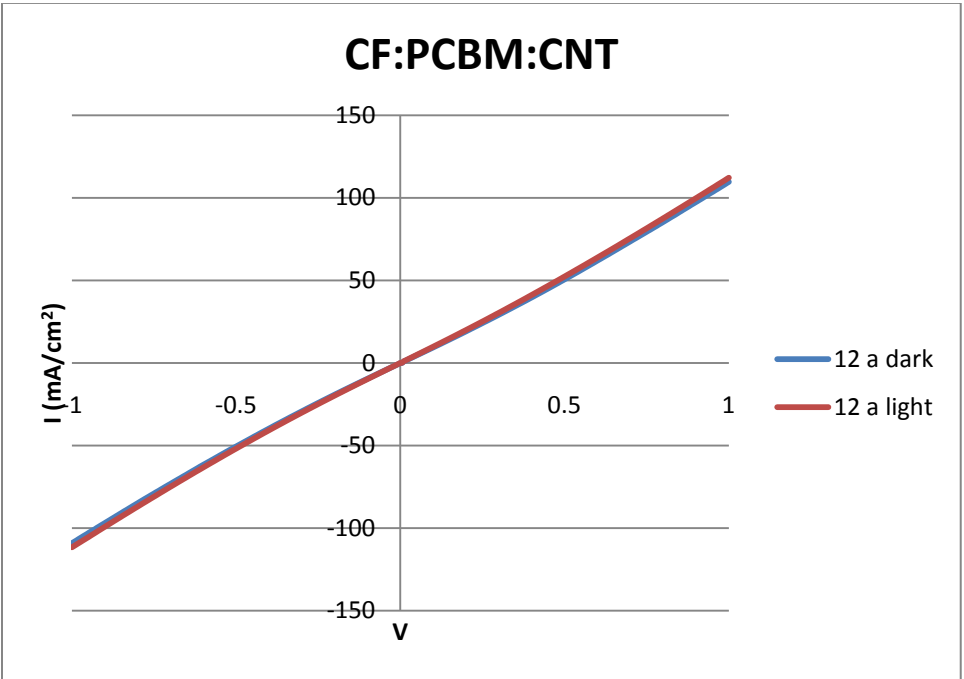
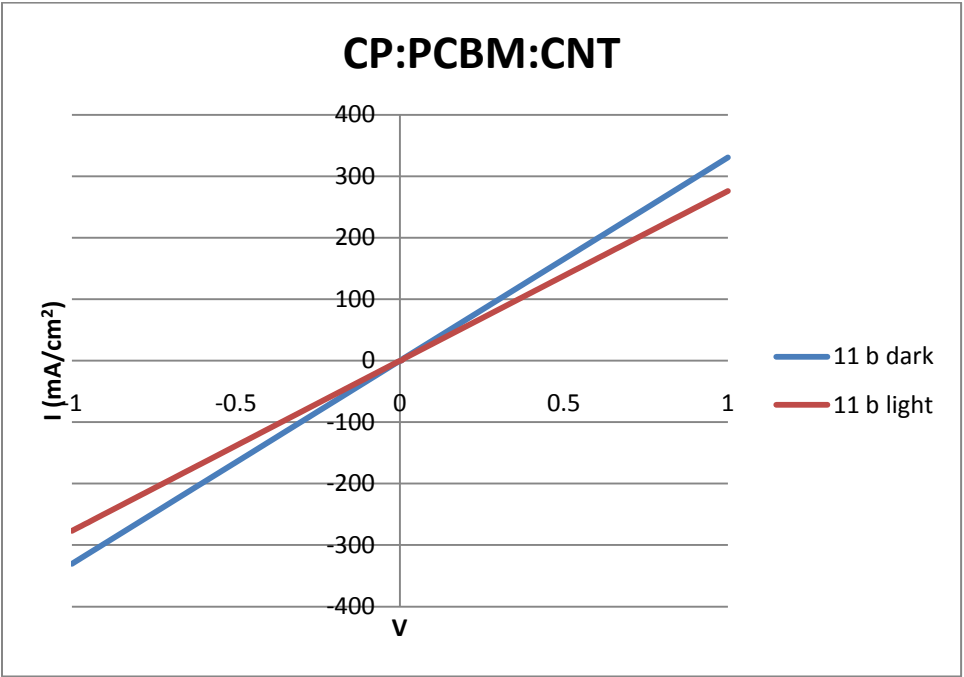


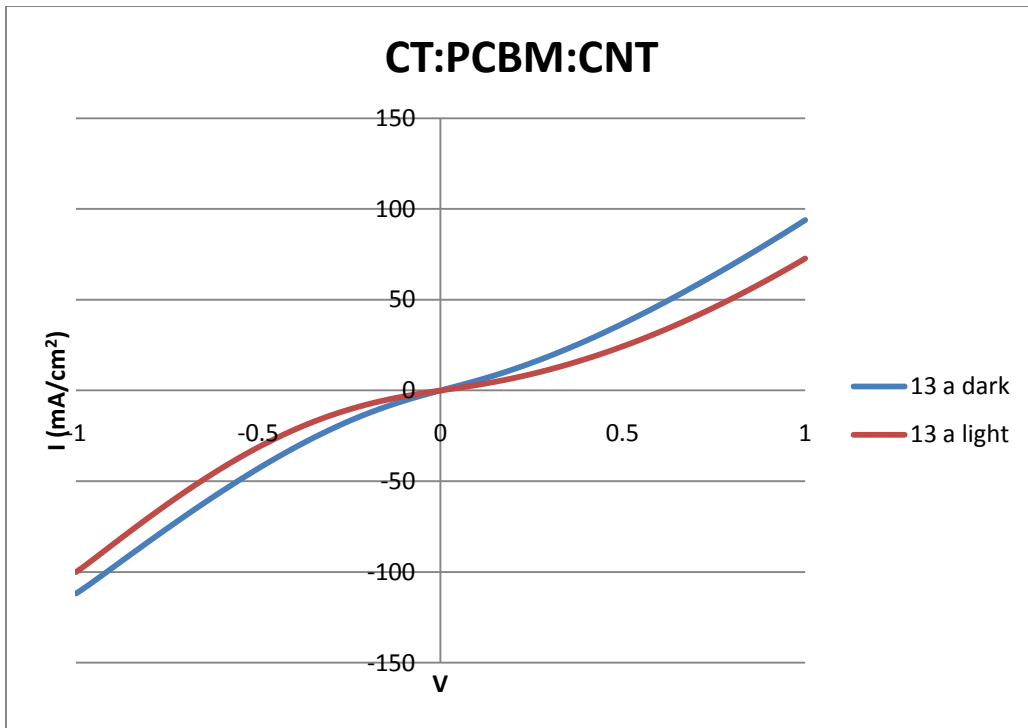
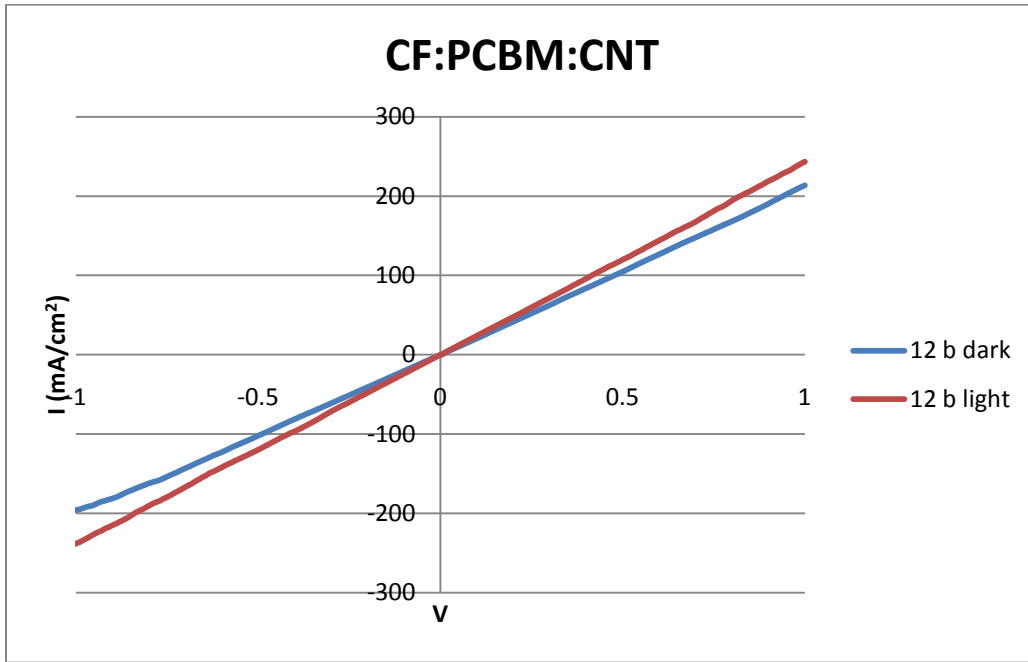


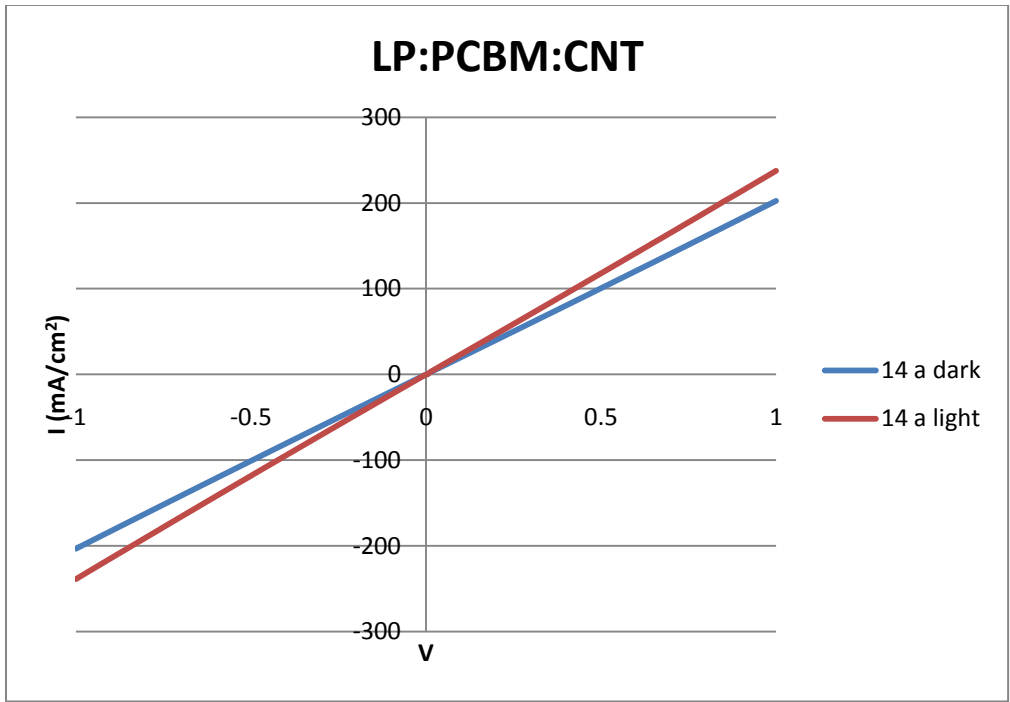
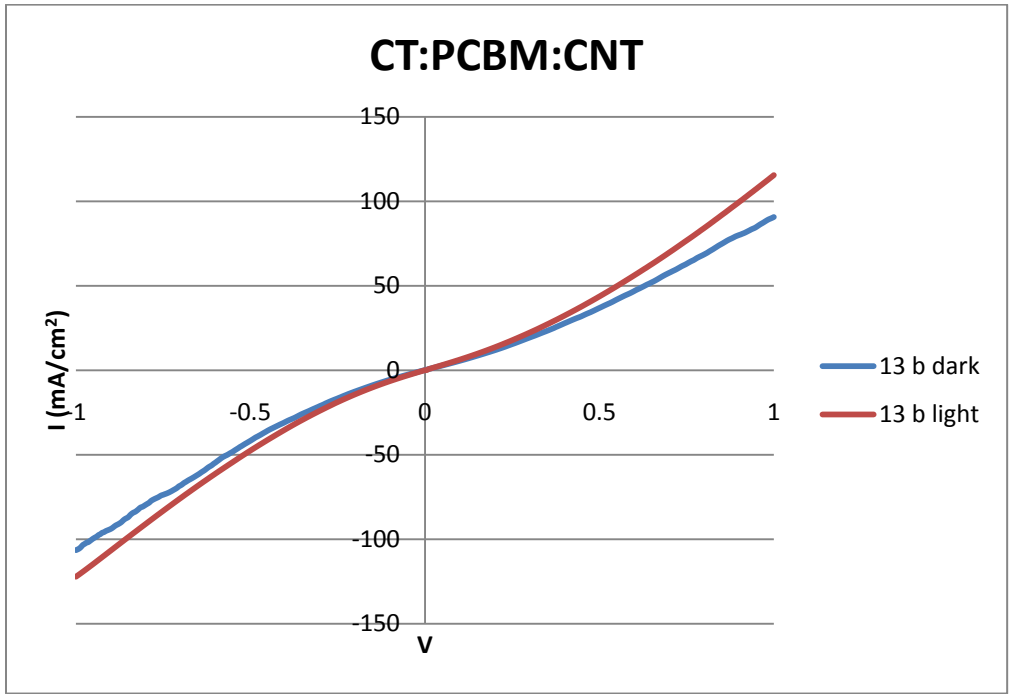


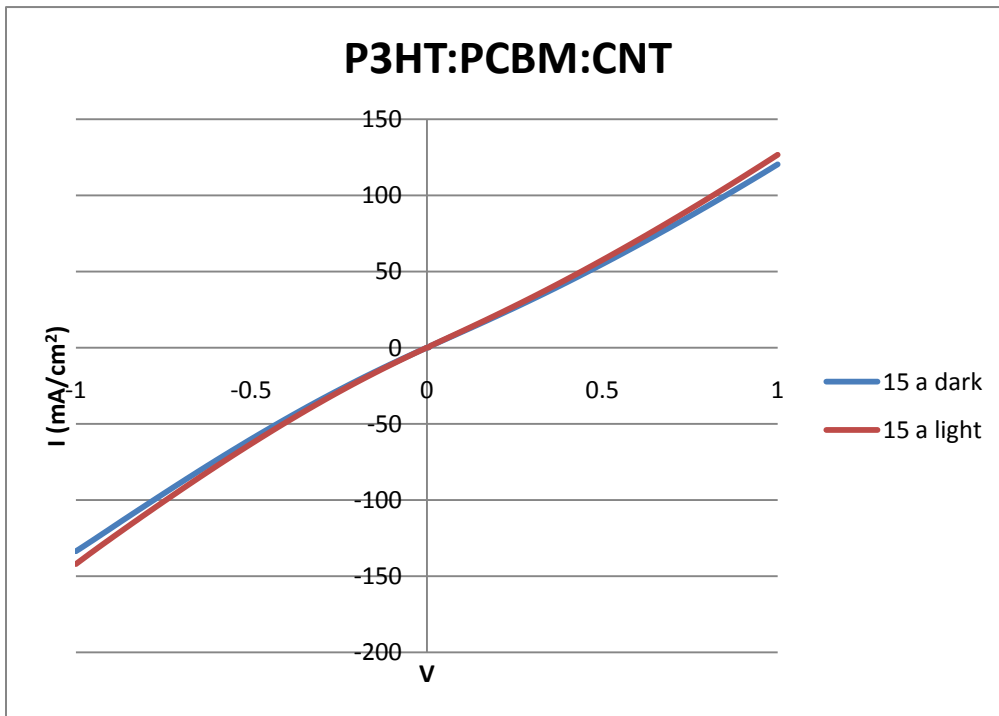
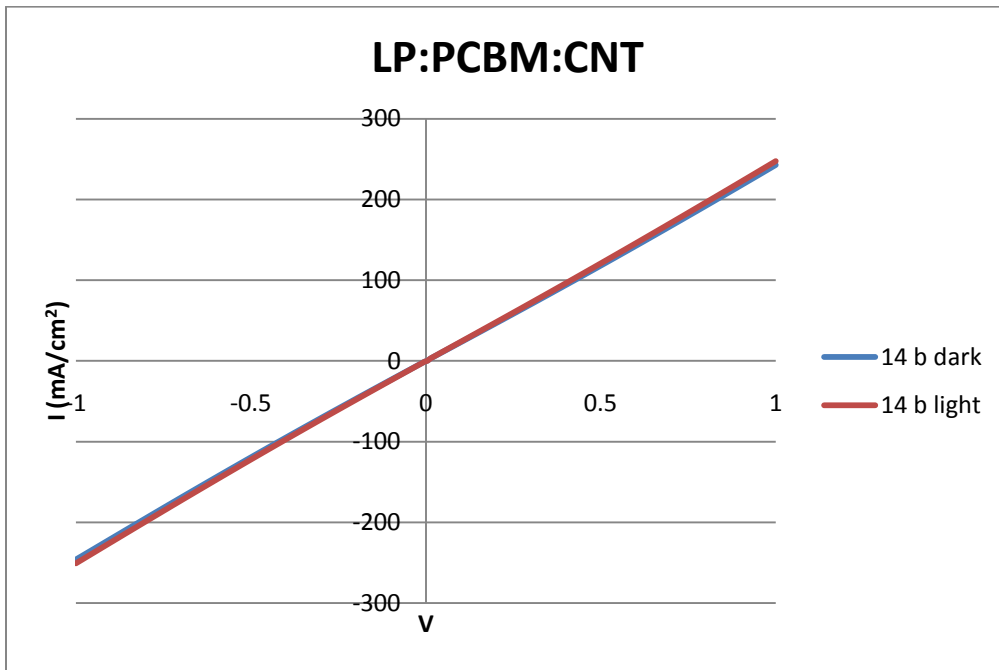


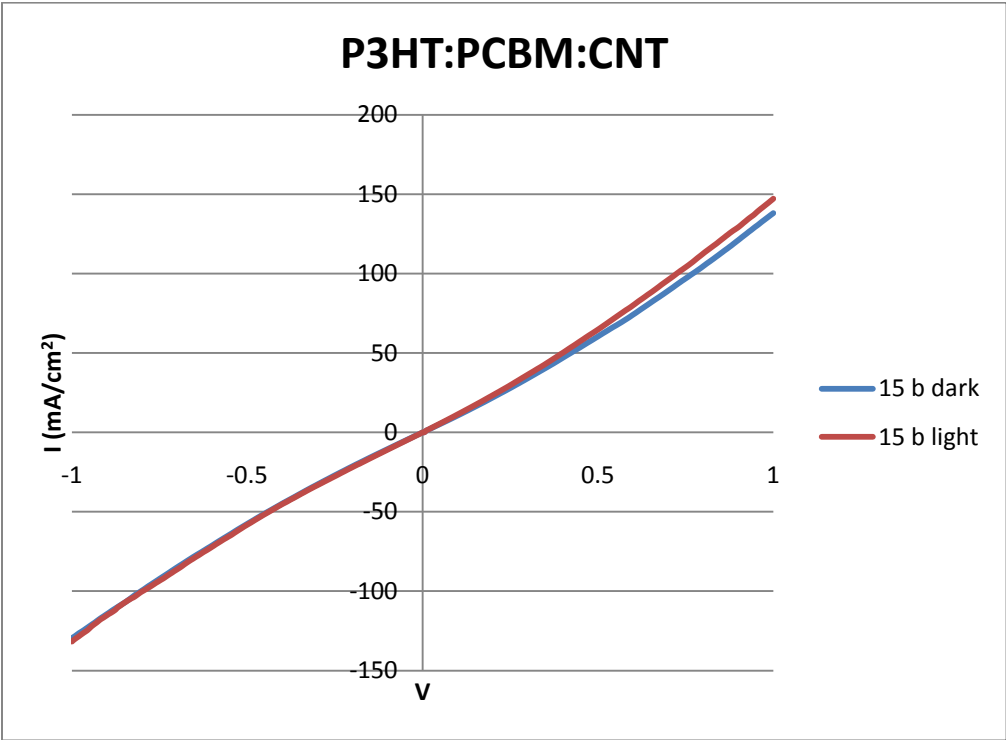




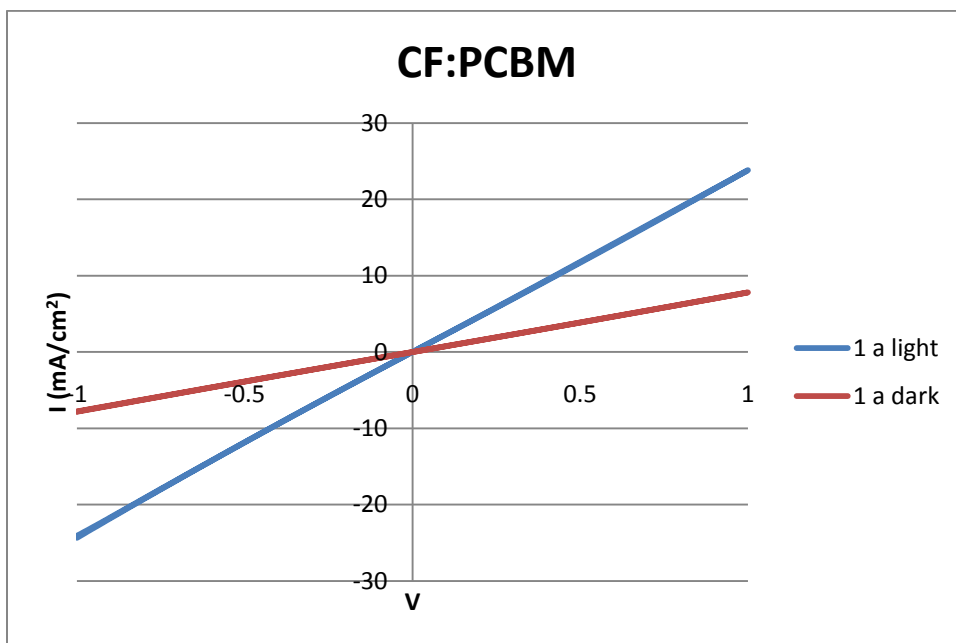
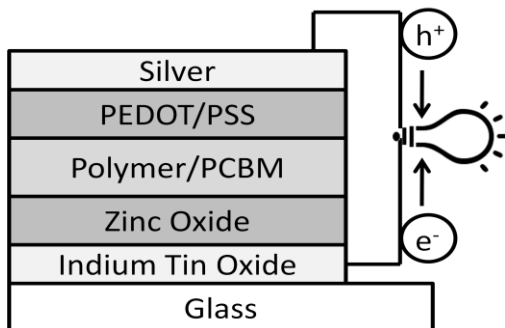


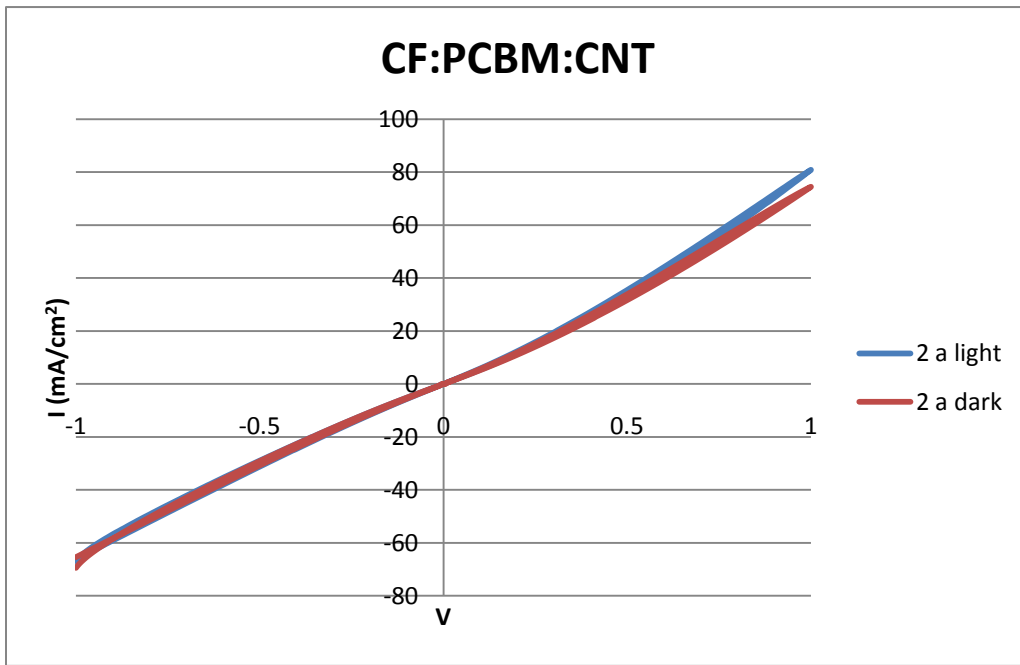
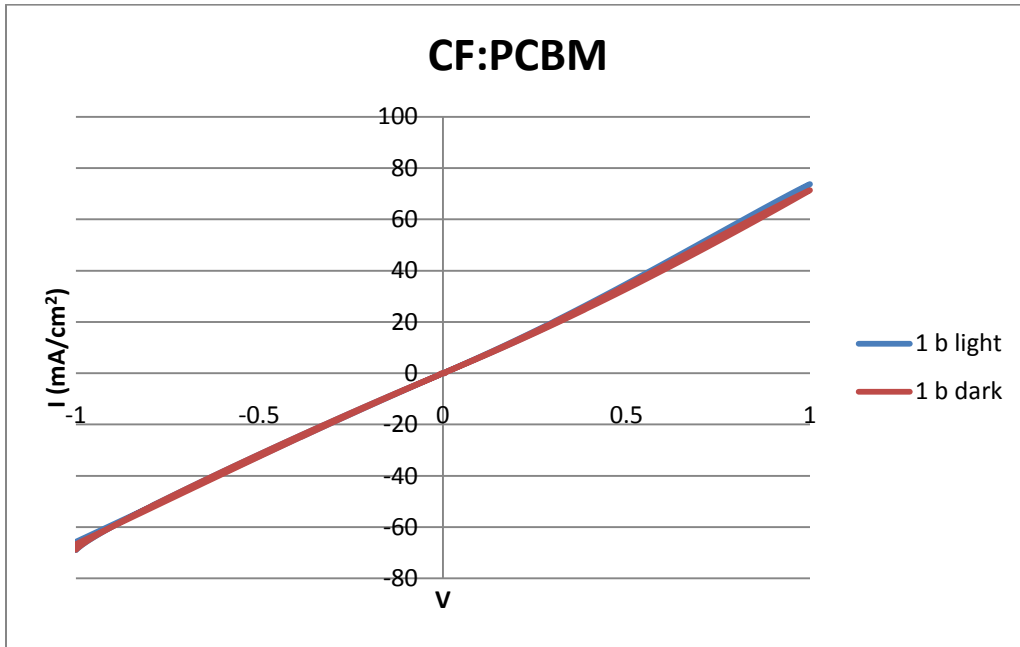


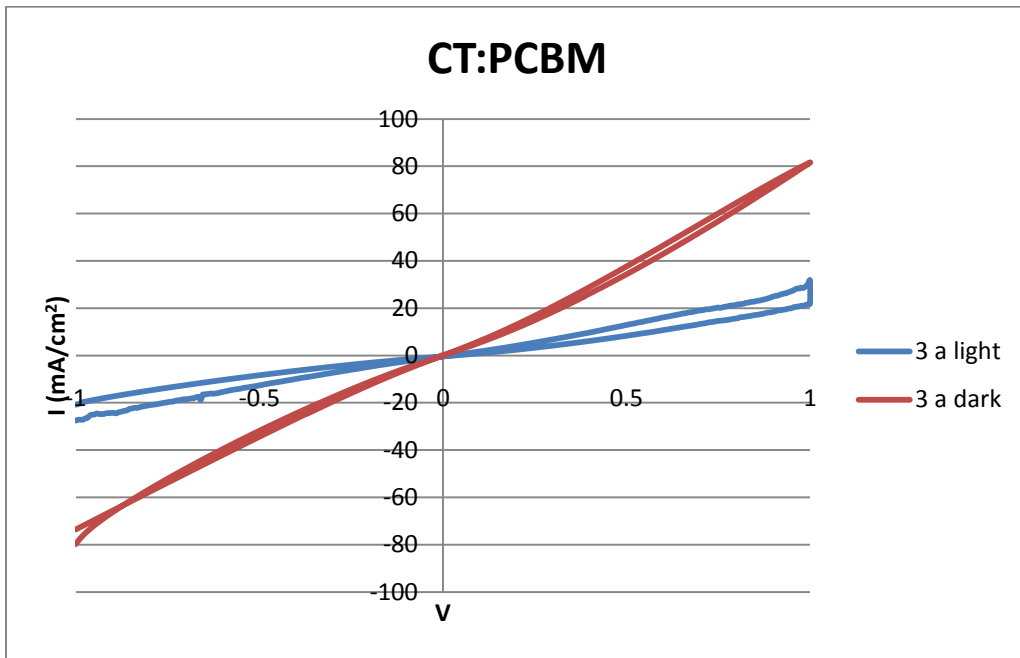
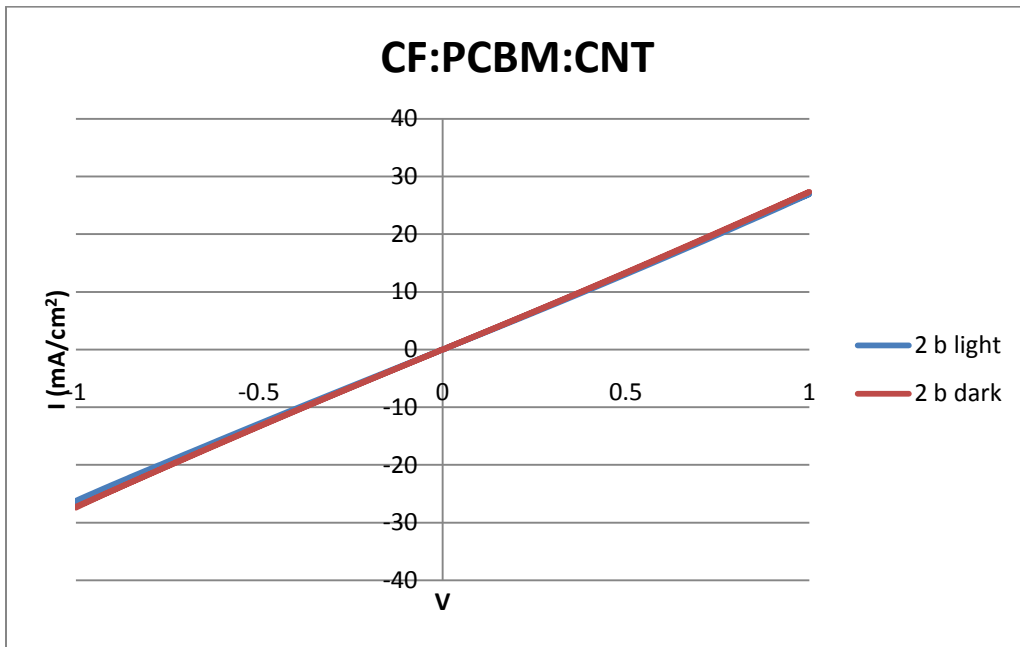


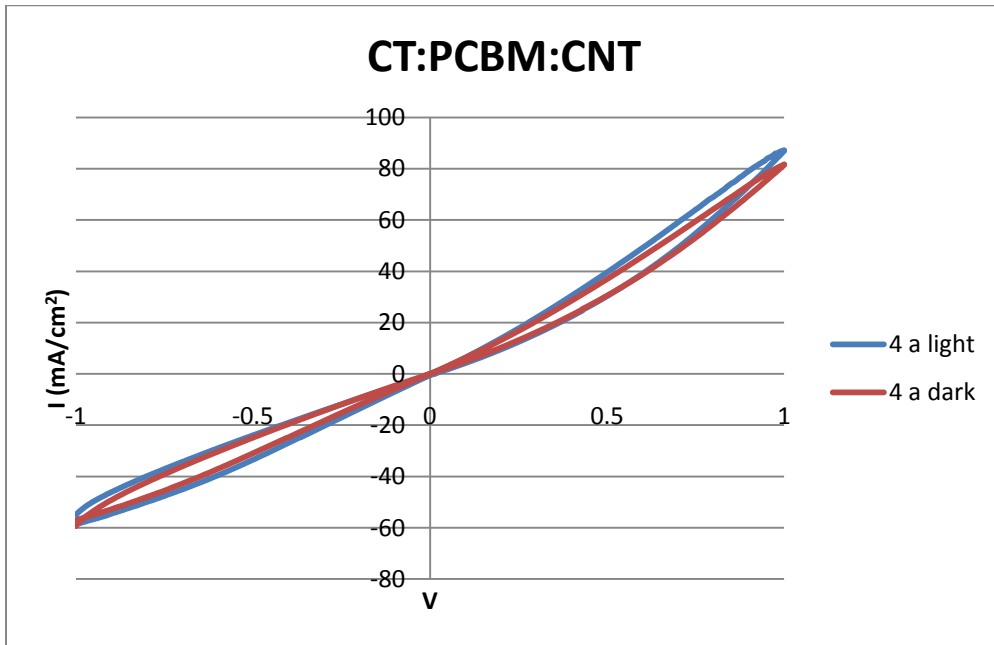
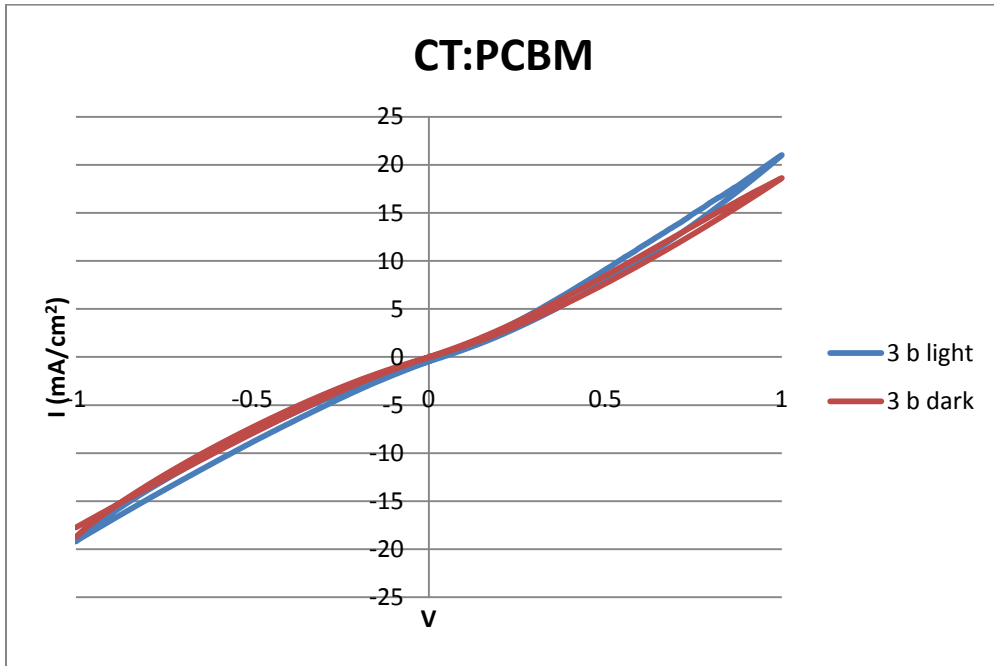


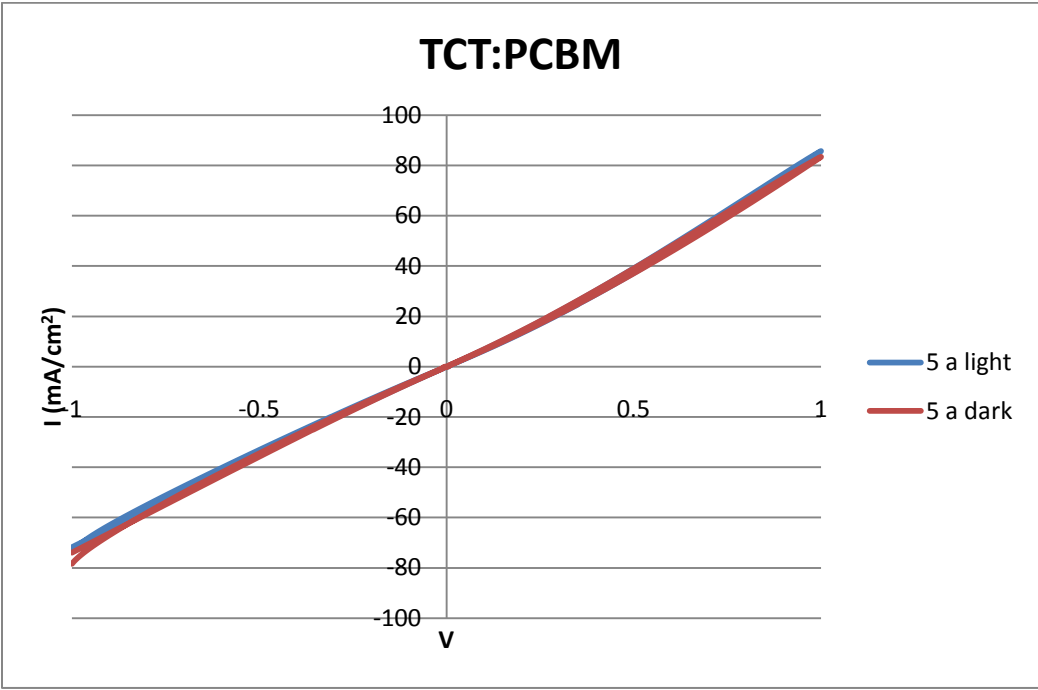
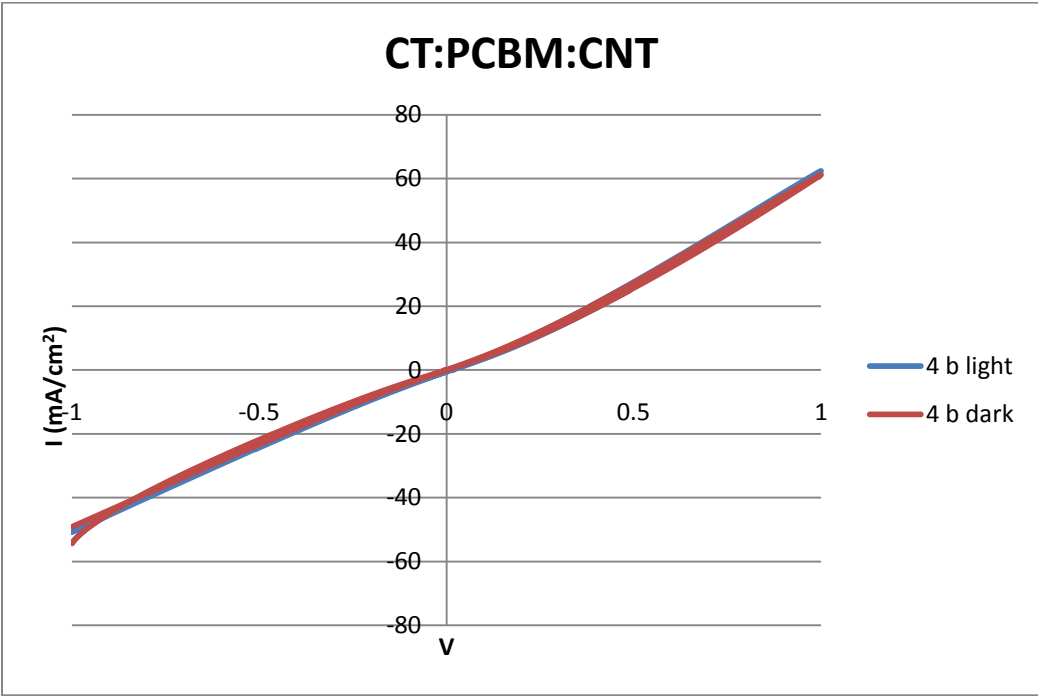
Silver Electrode

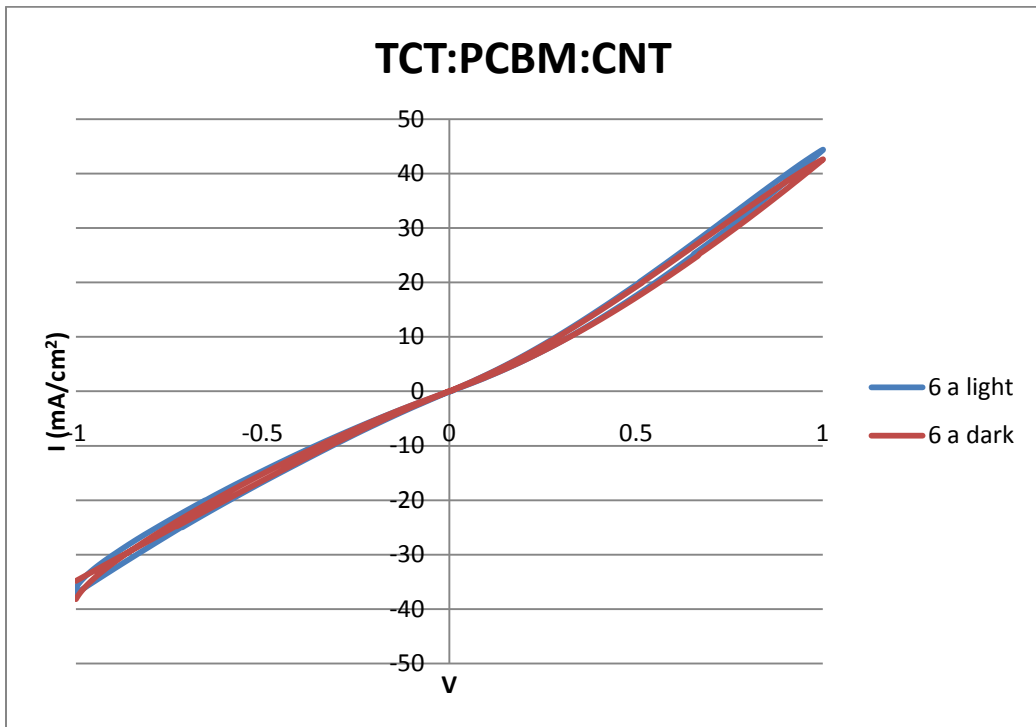
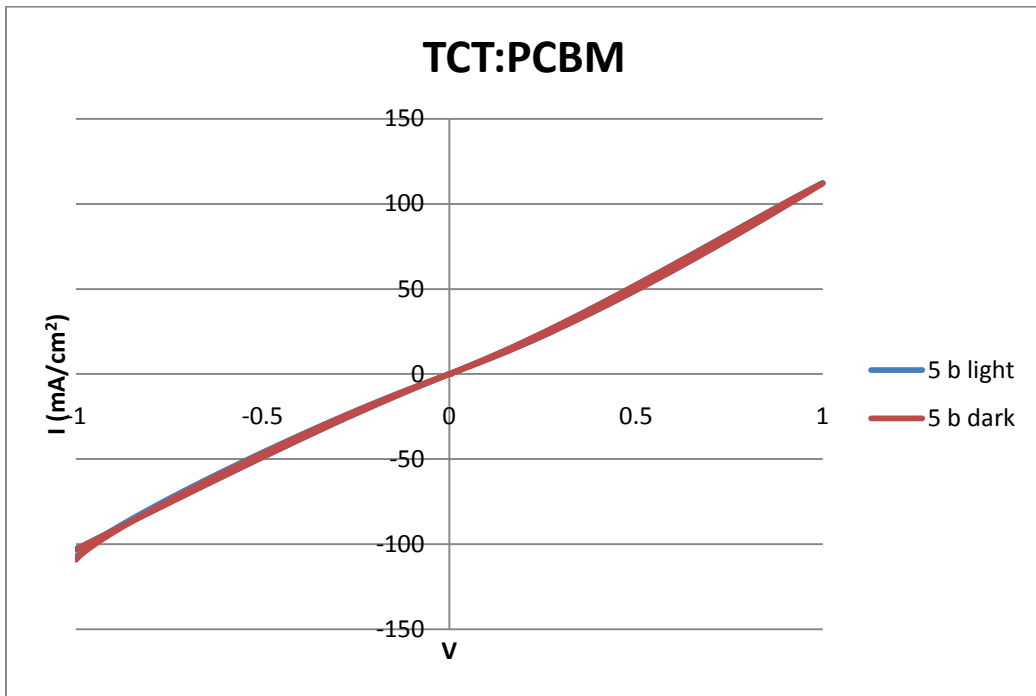


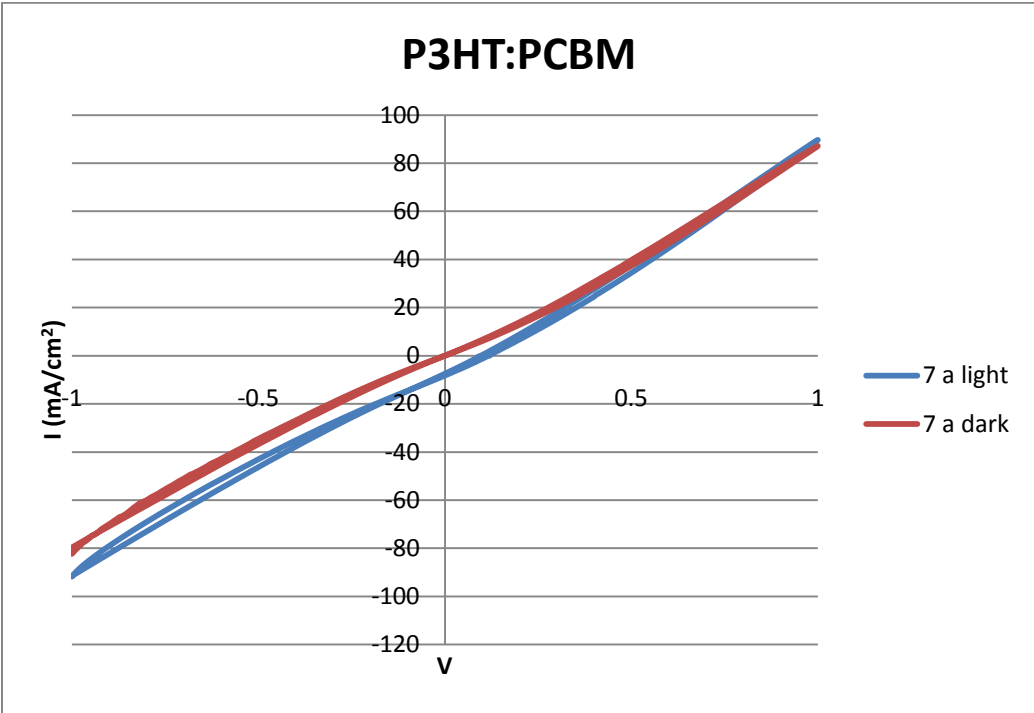
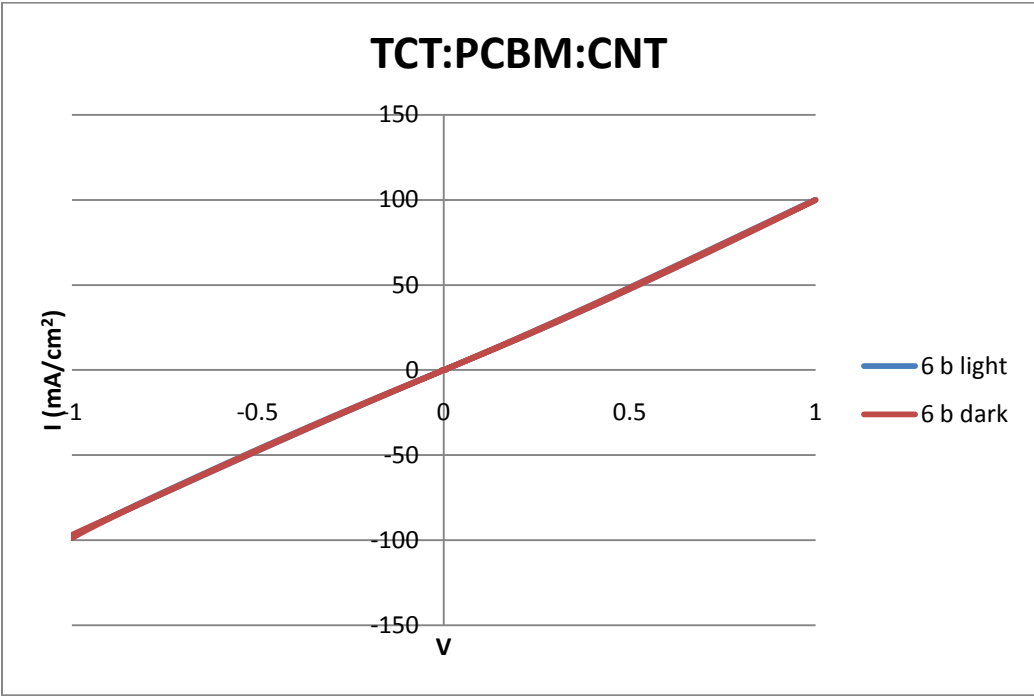


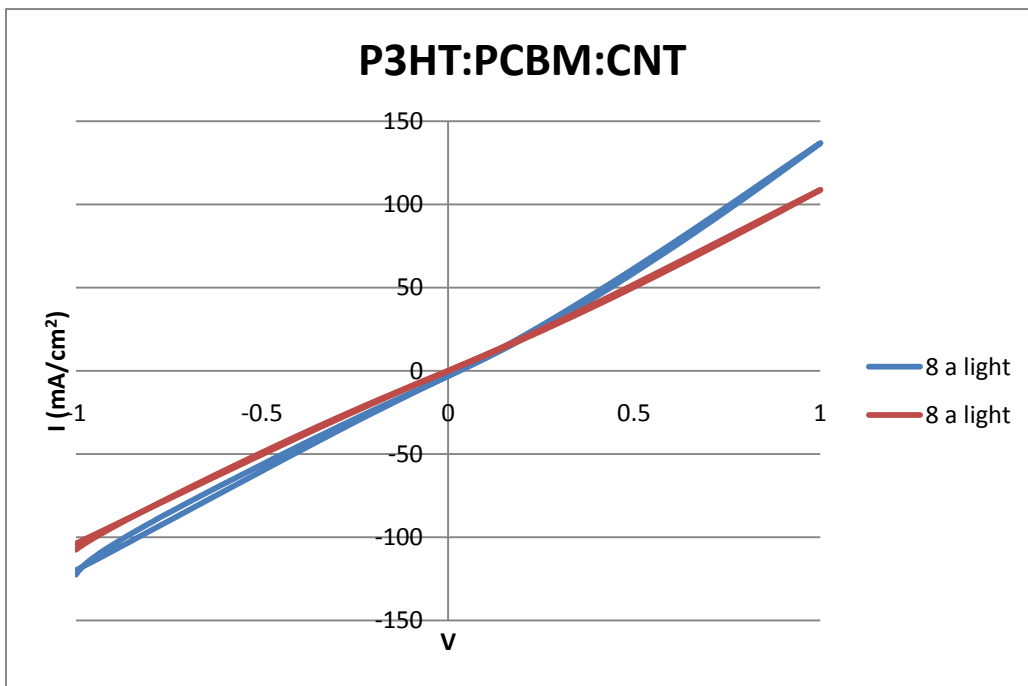
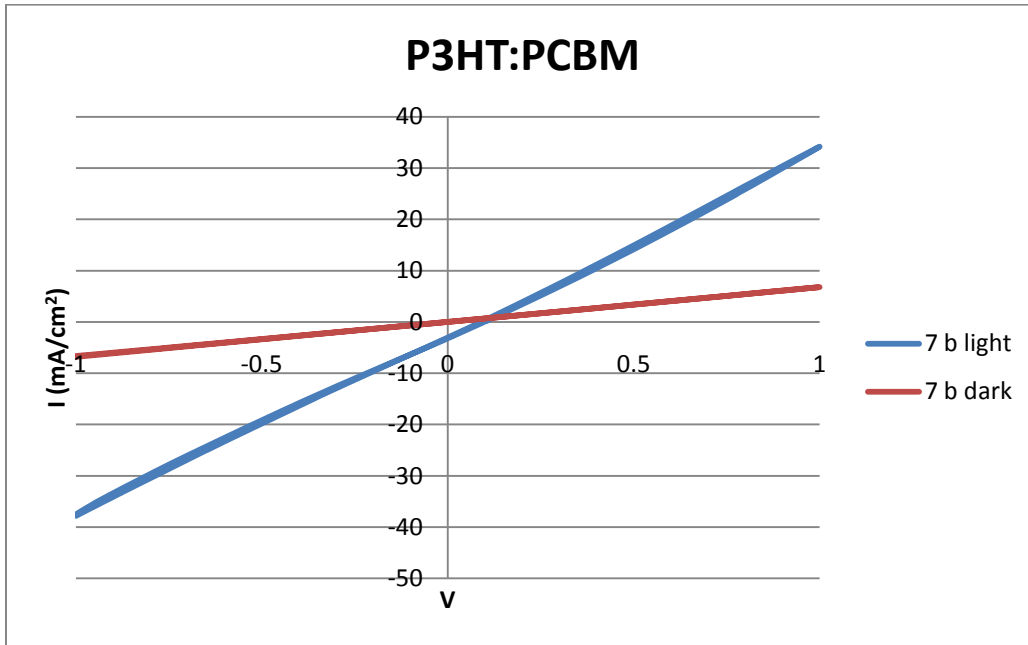


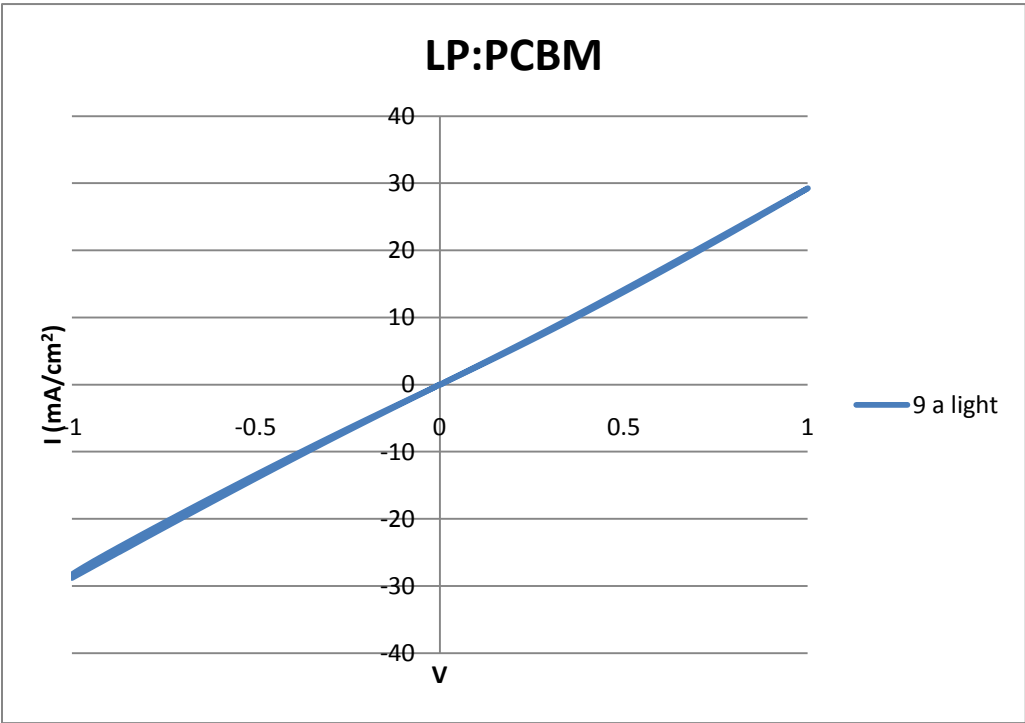
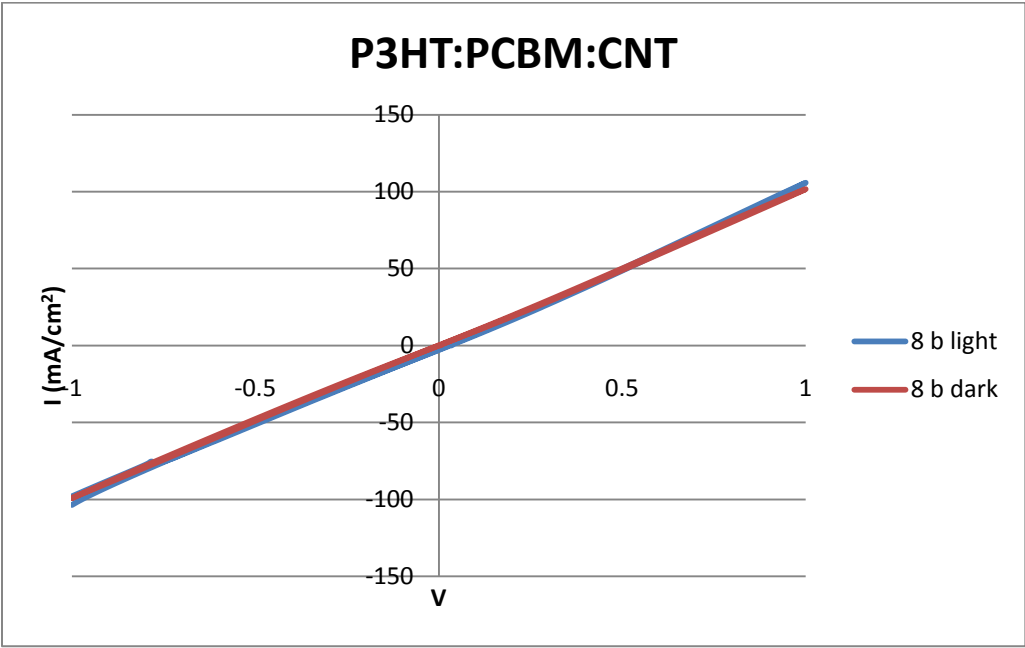


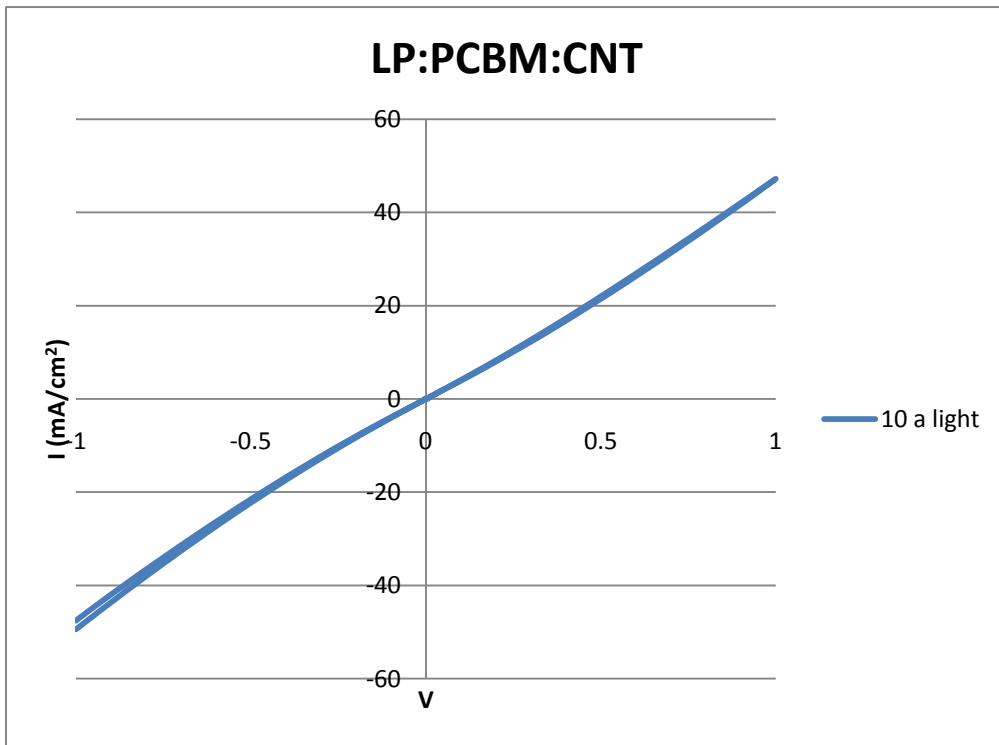
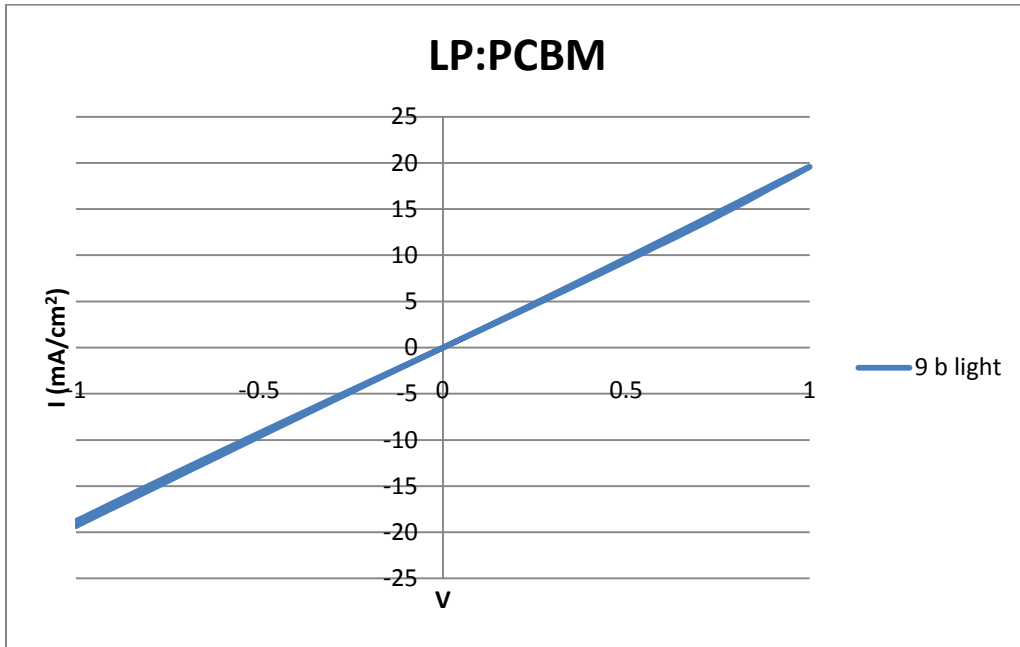


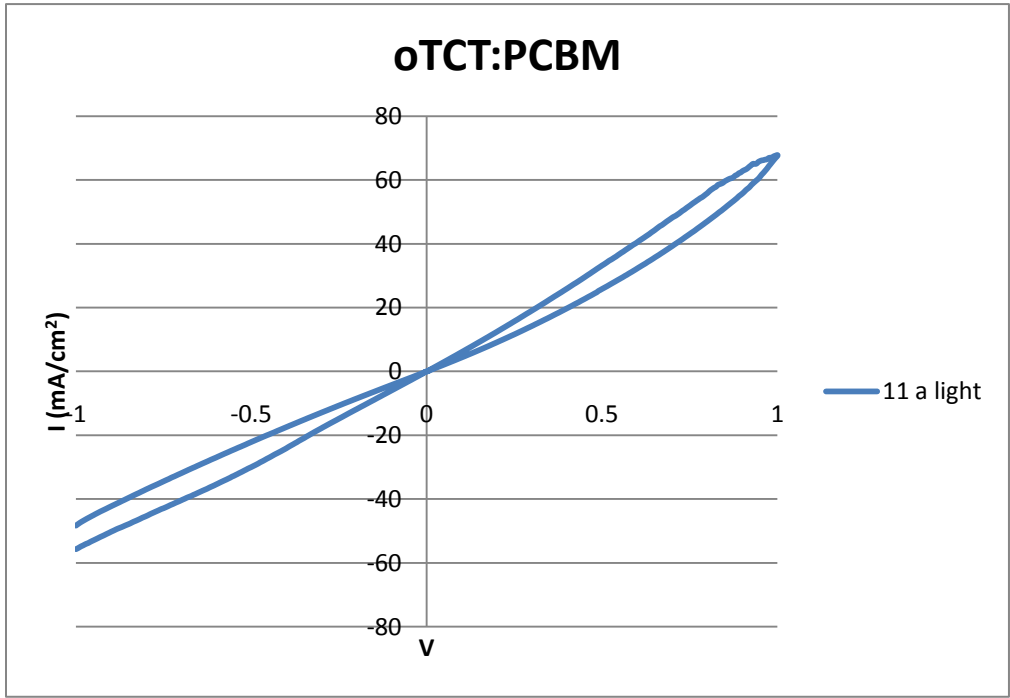
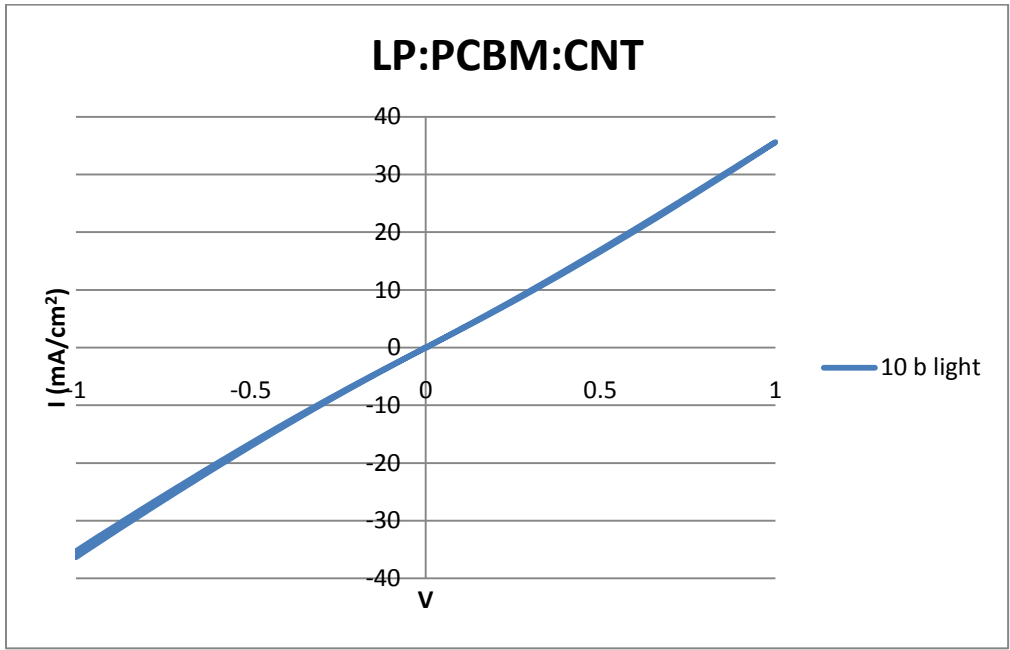


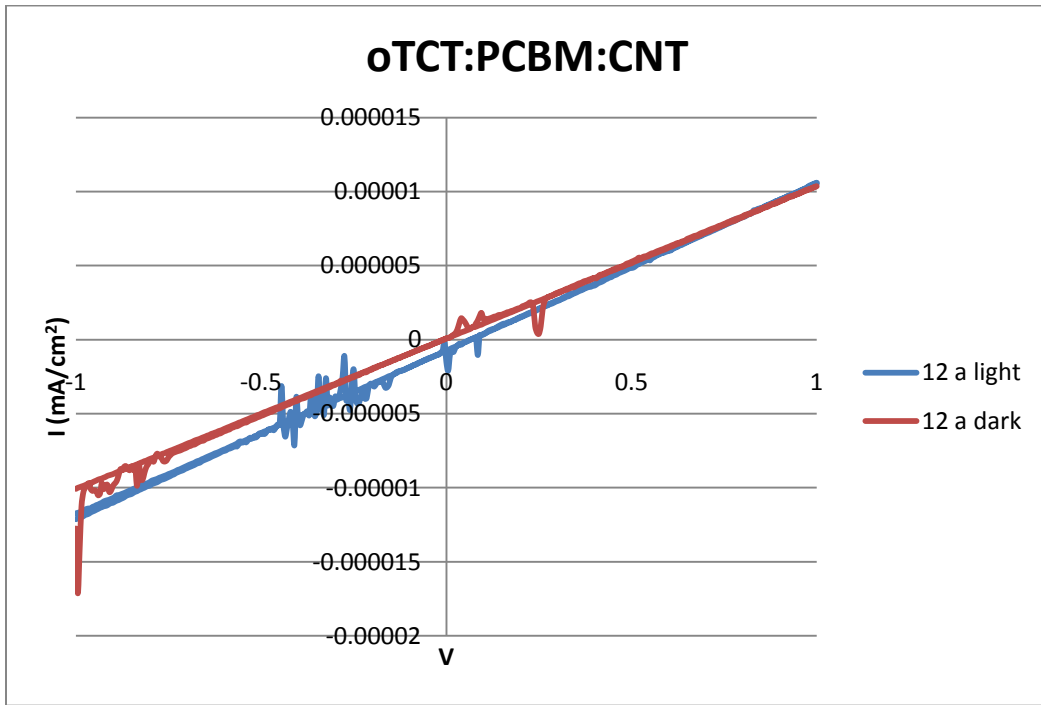
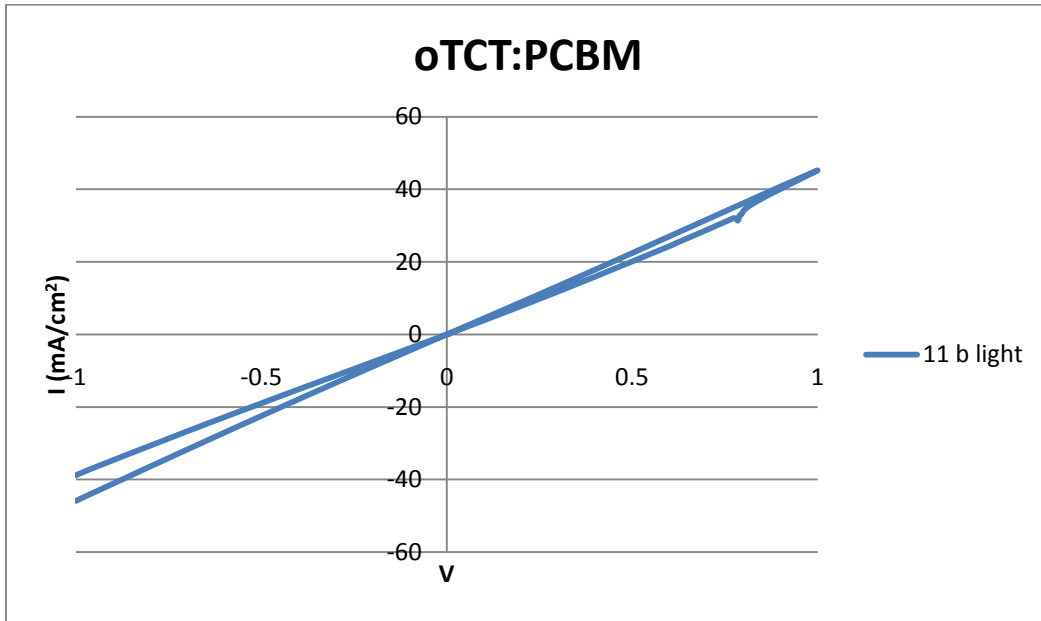


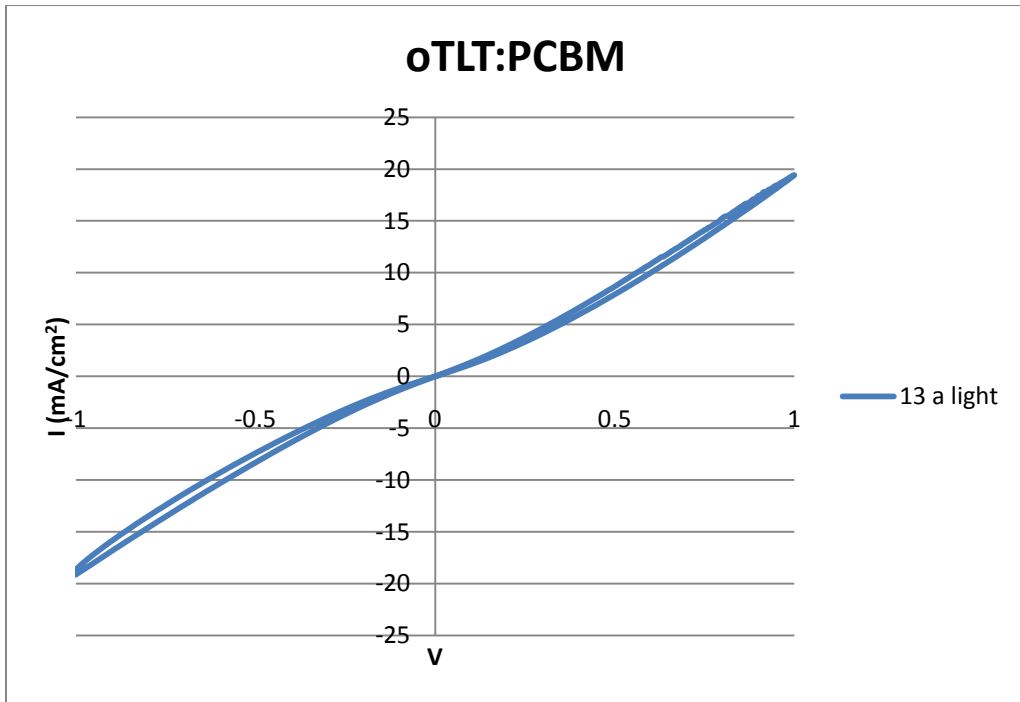
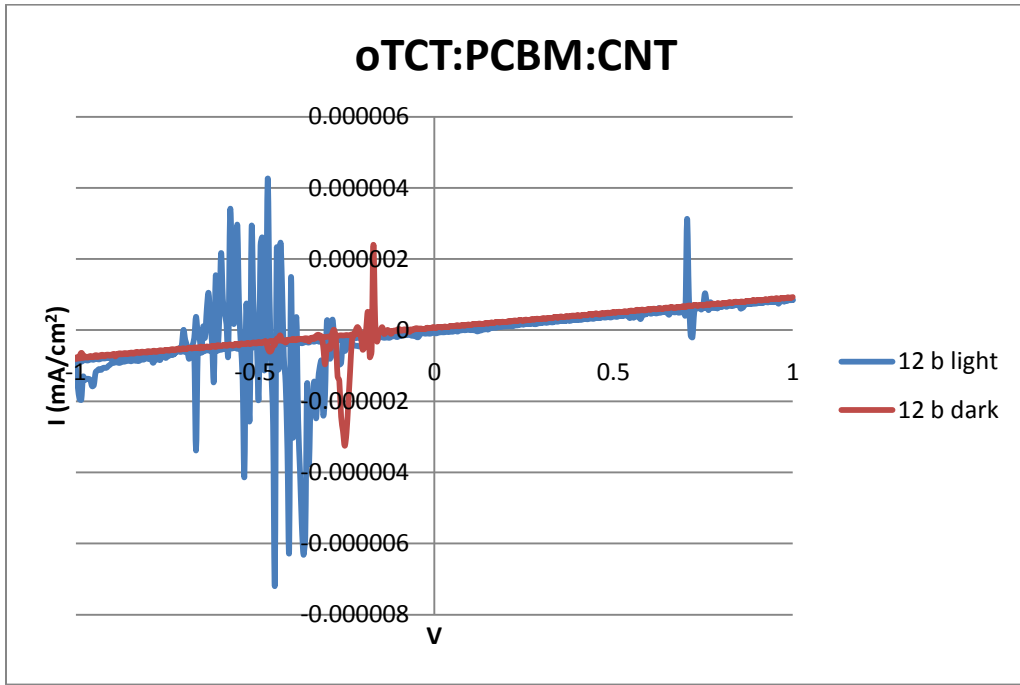


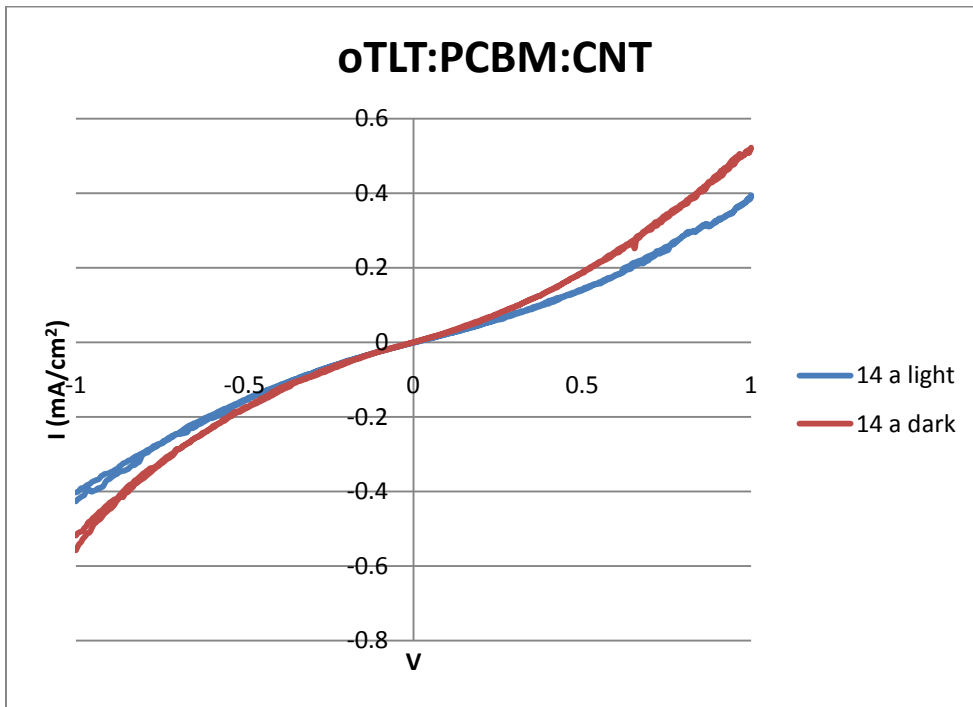
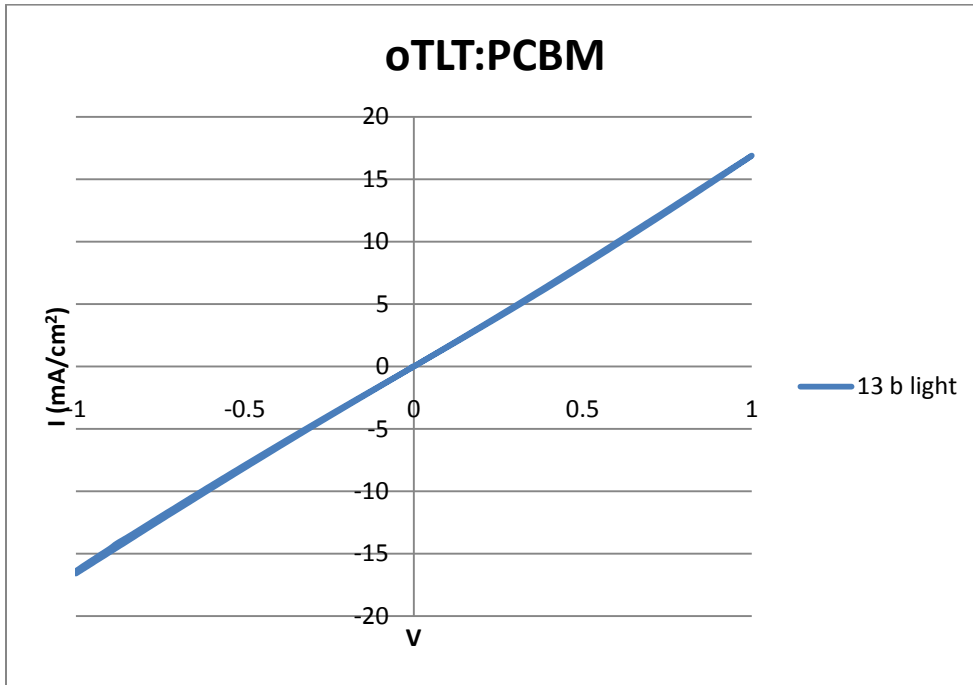


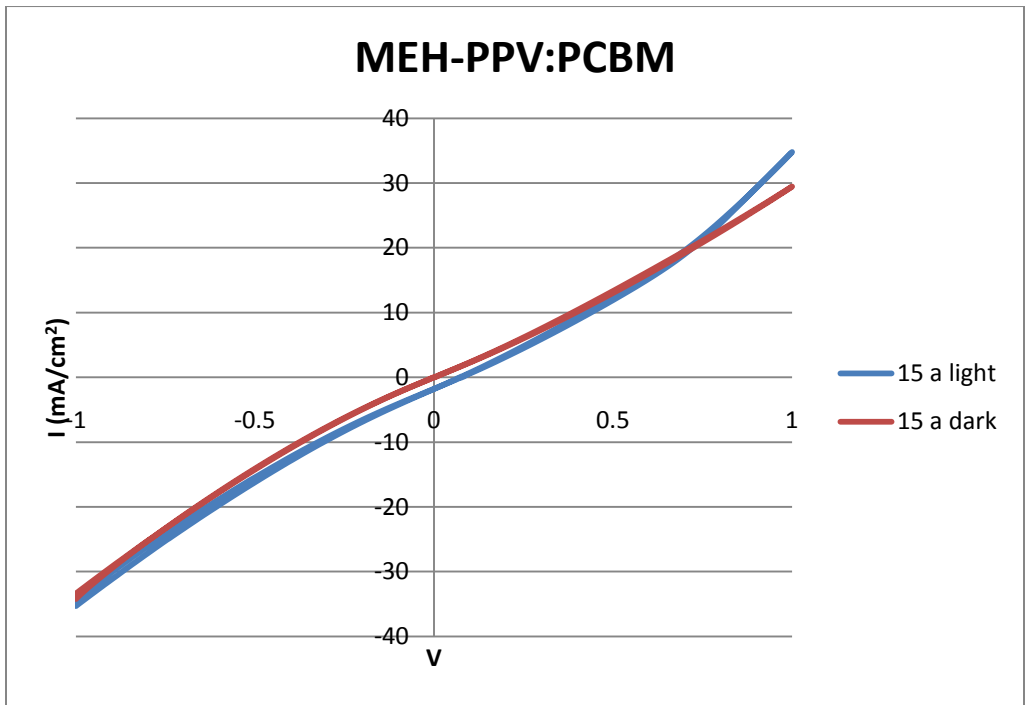
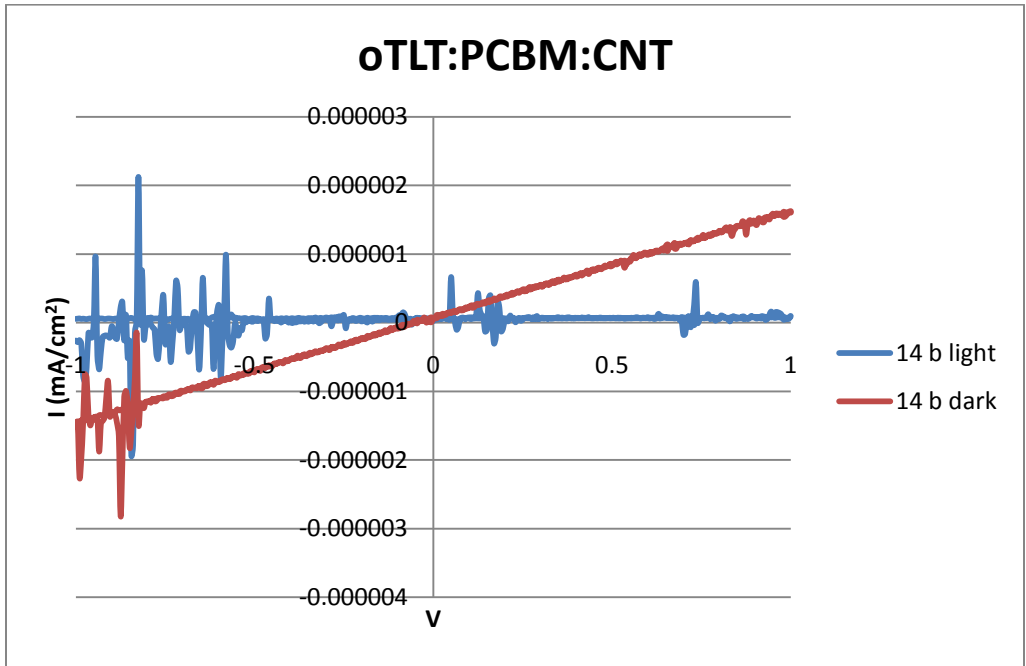


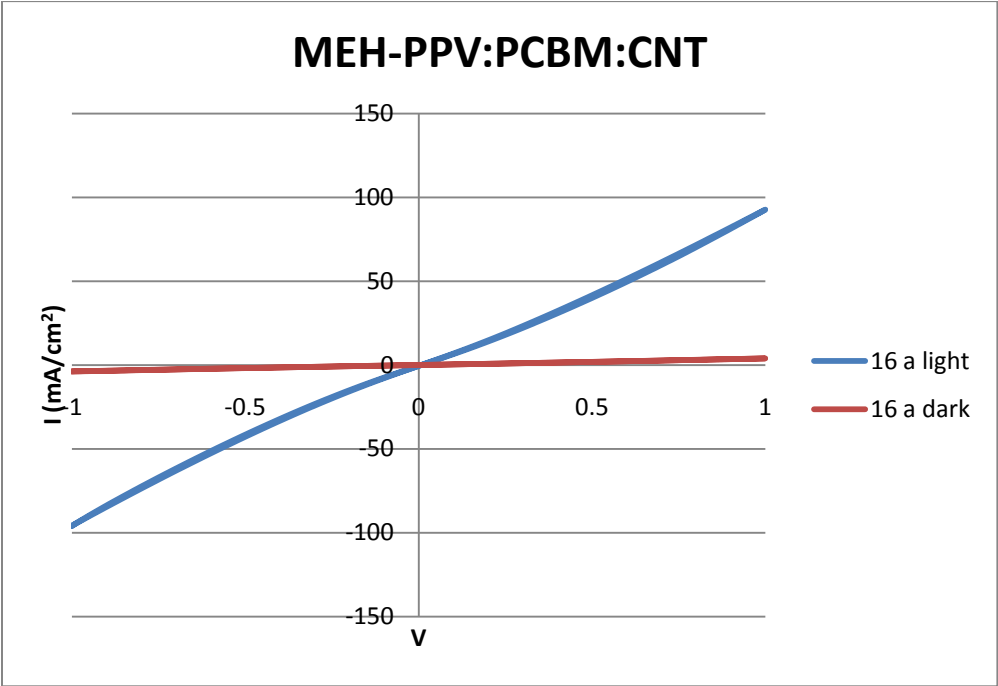
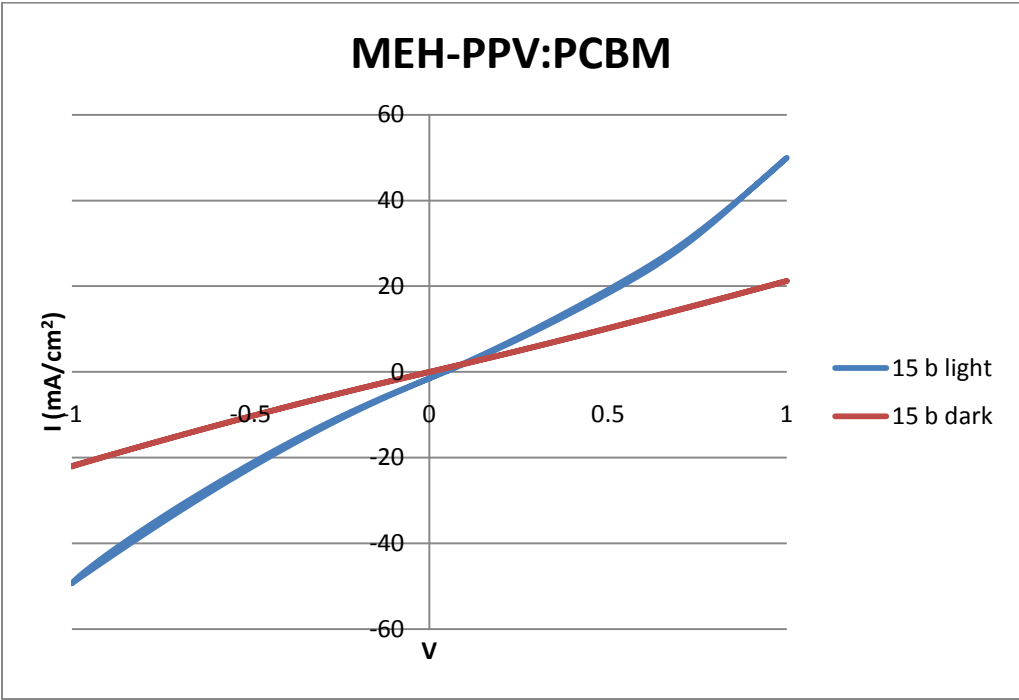


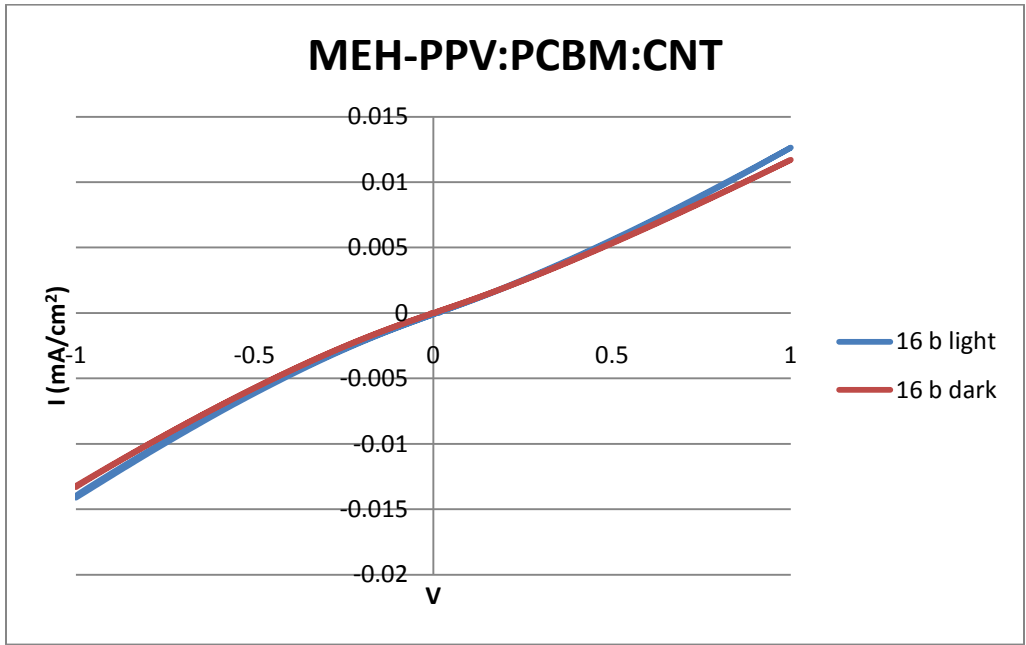






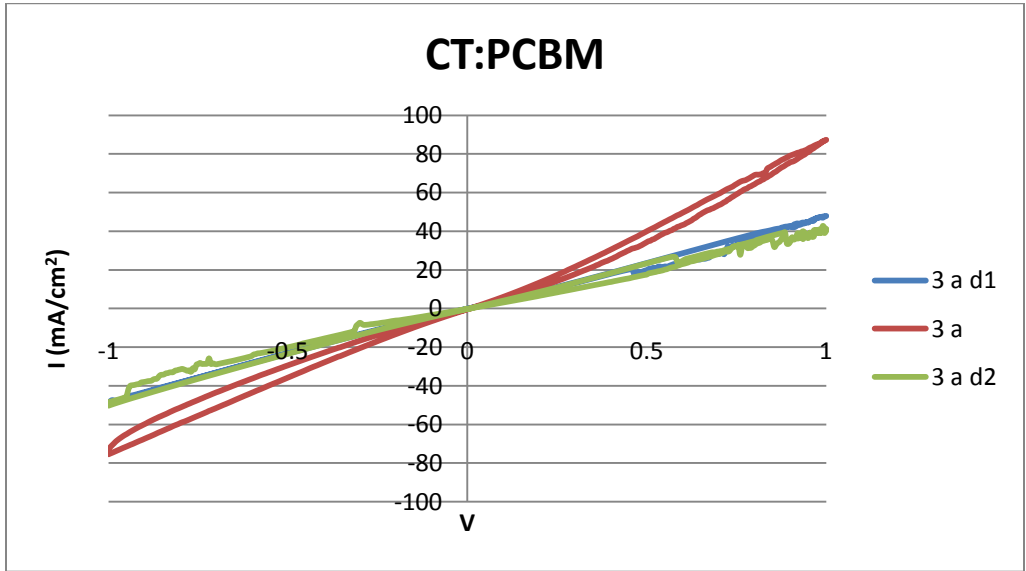


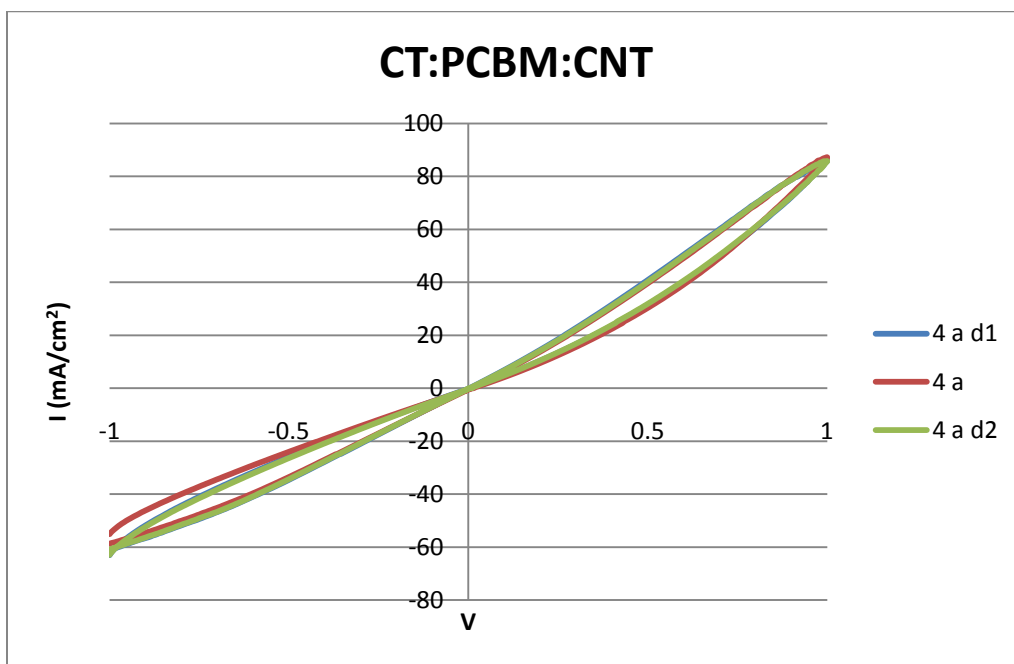
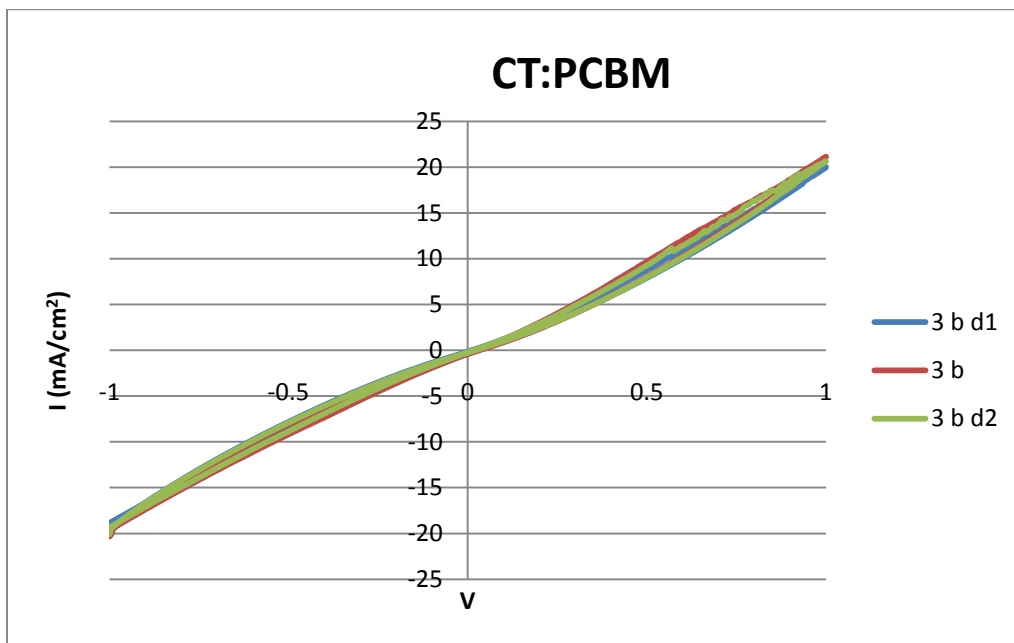


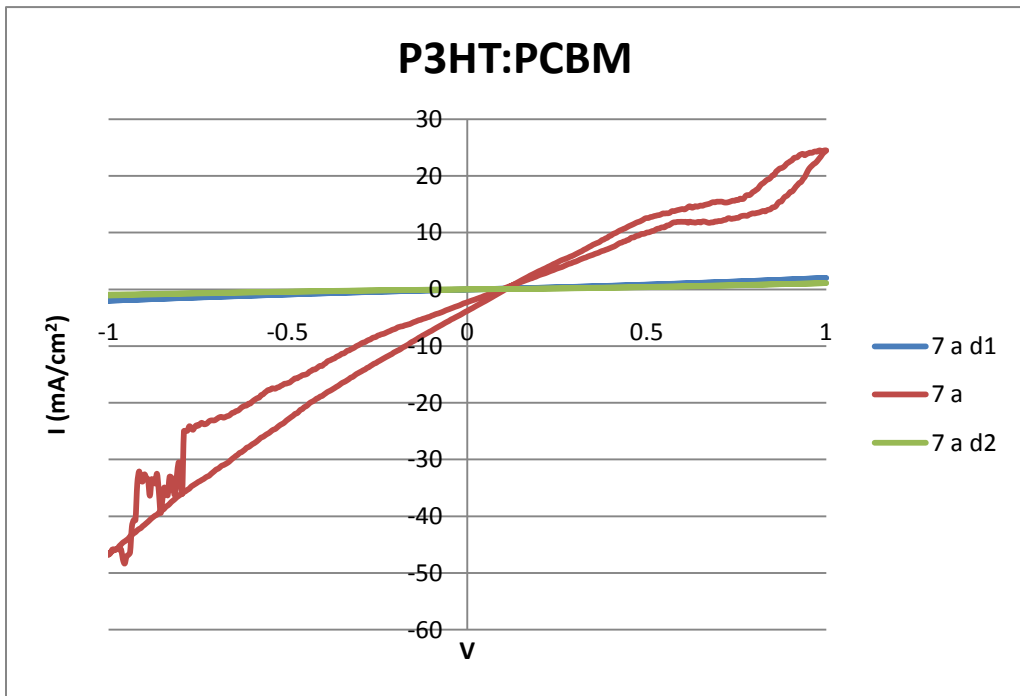
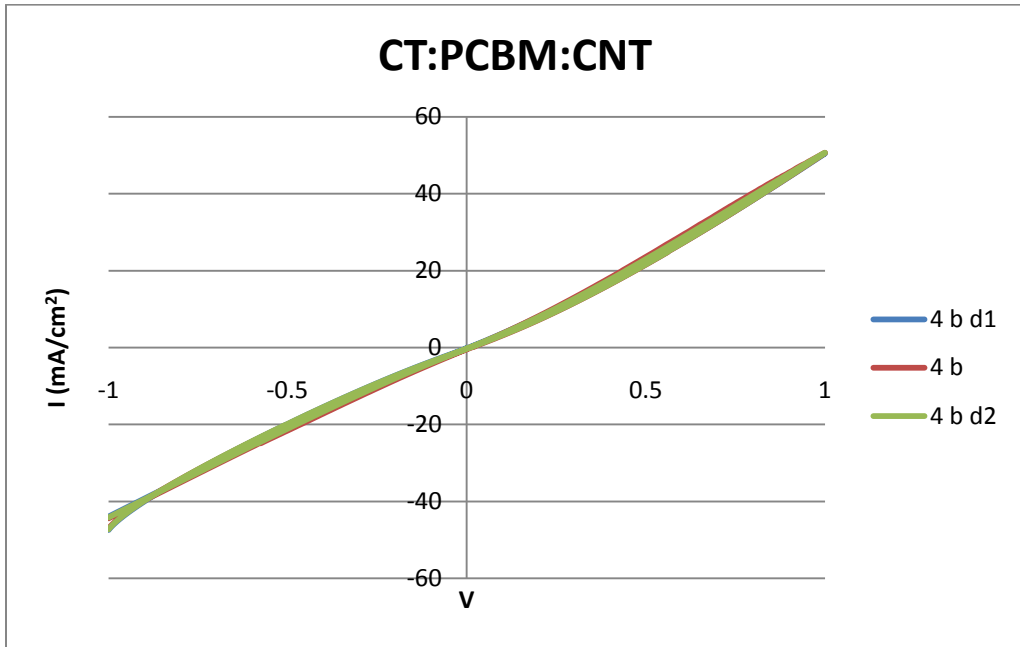


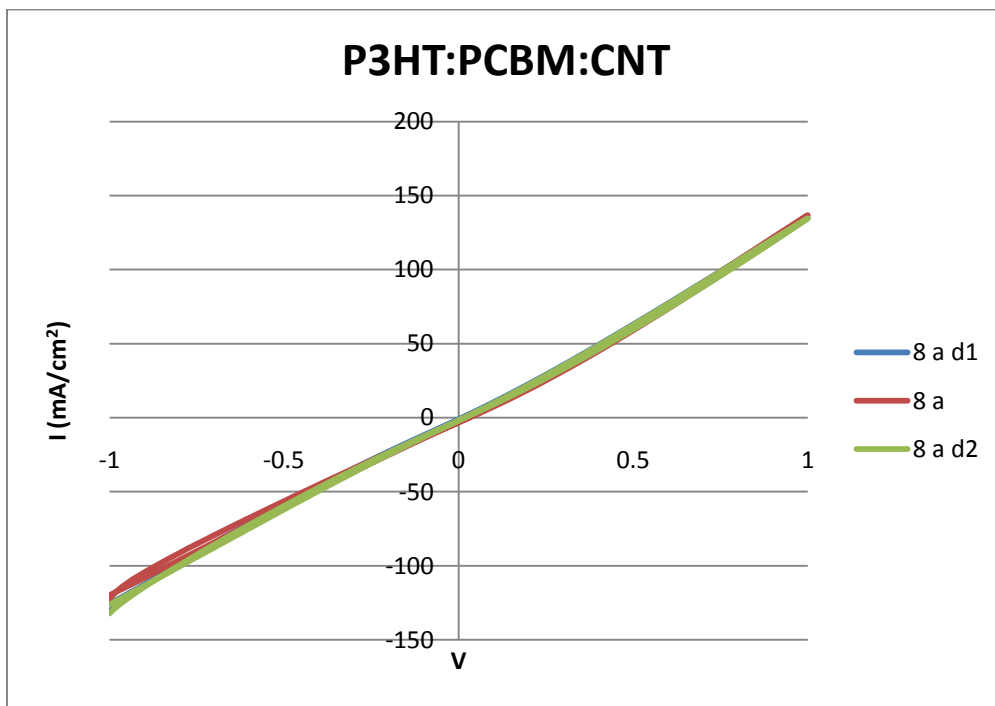
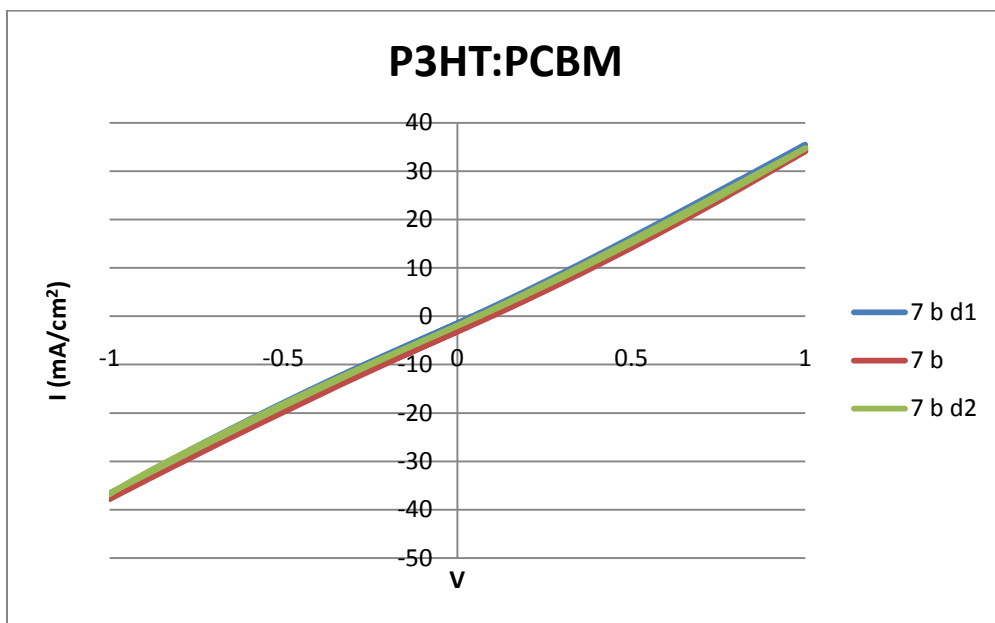
Silver Electrode – Variation in Intensity

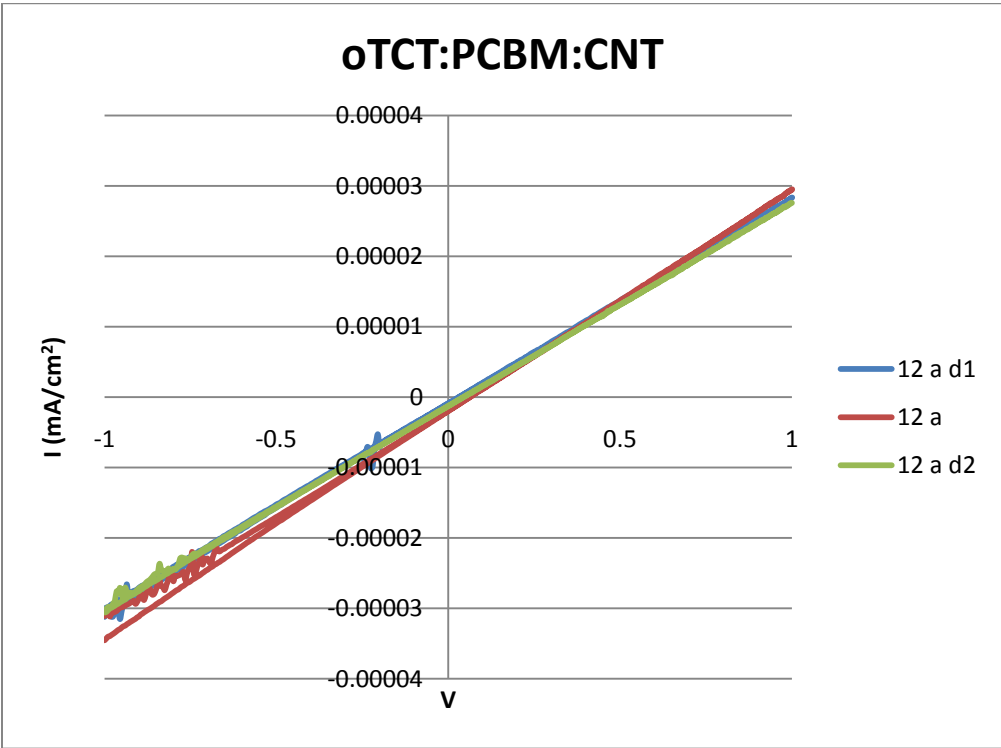
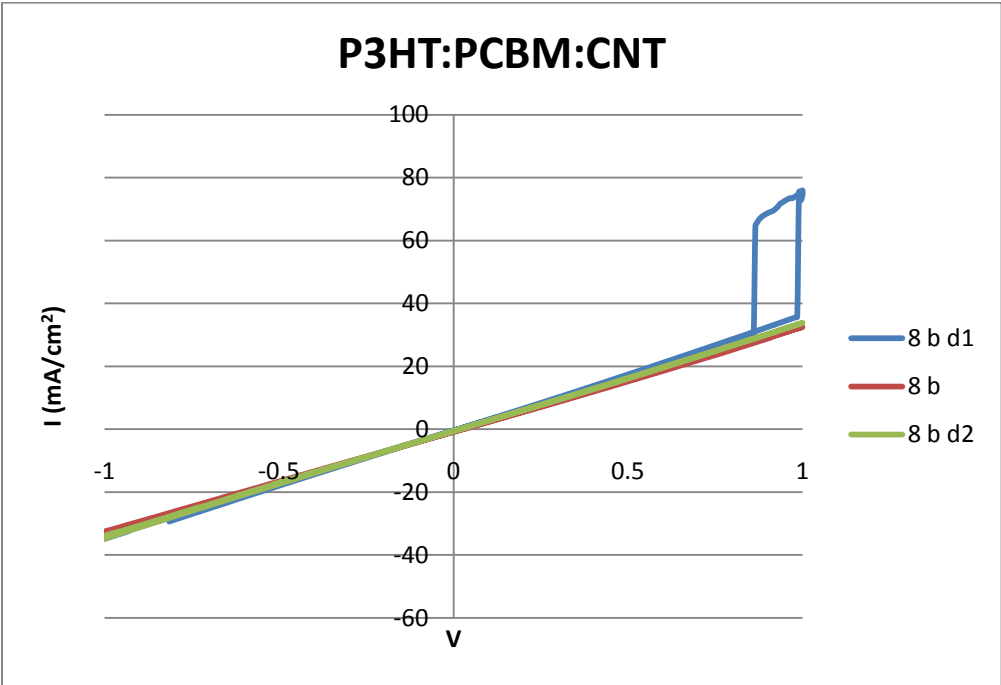
Initial distance = 45 cm, d1 = 140 cm, d2 = 85 cm

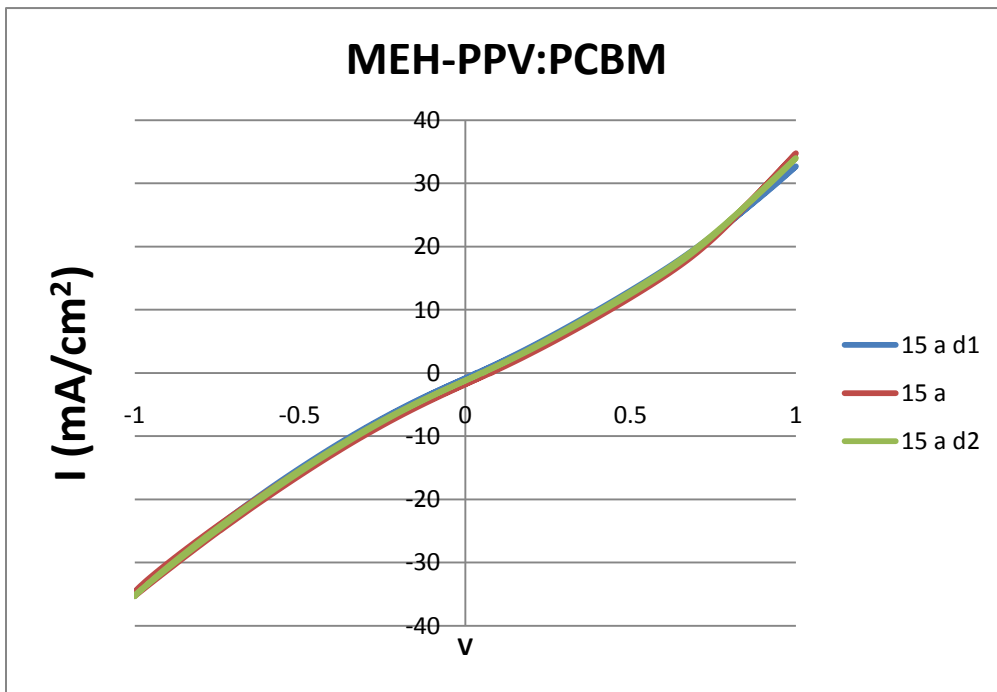
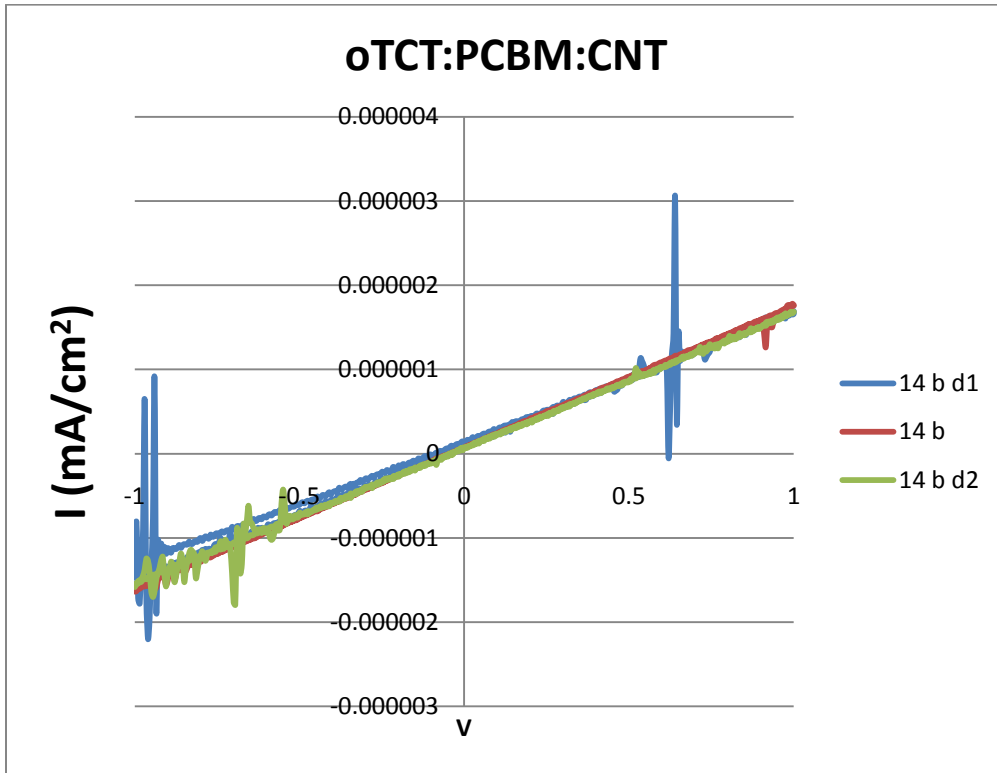


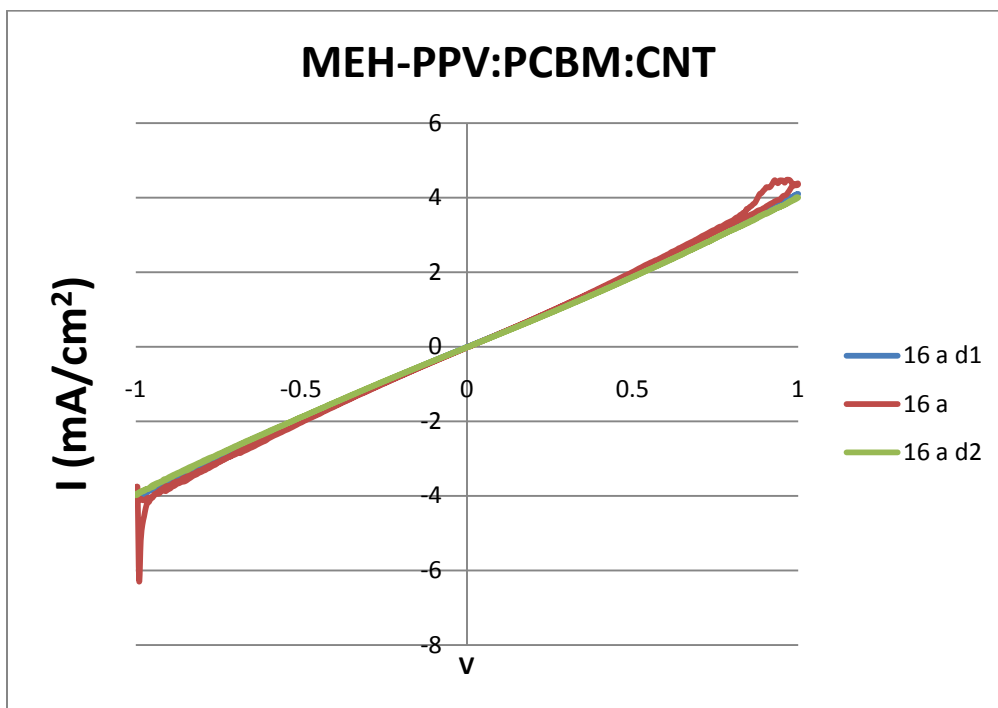
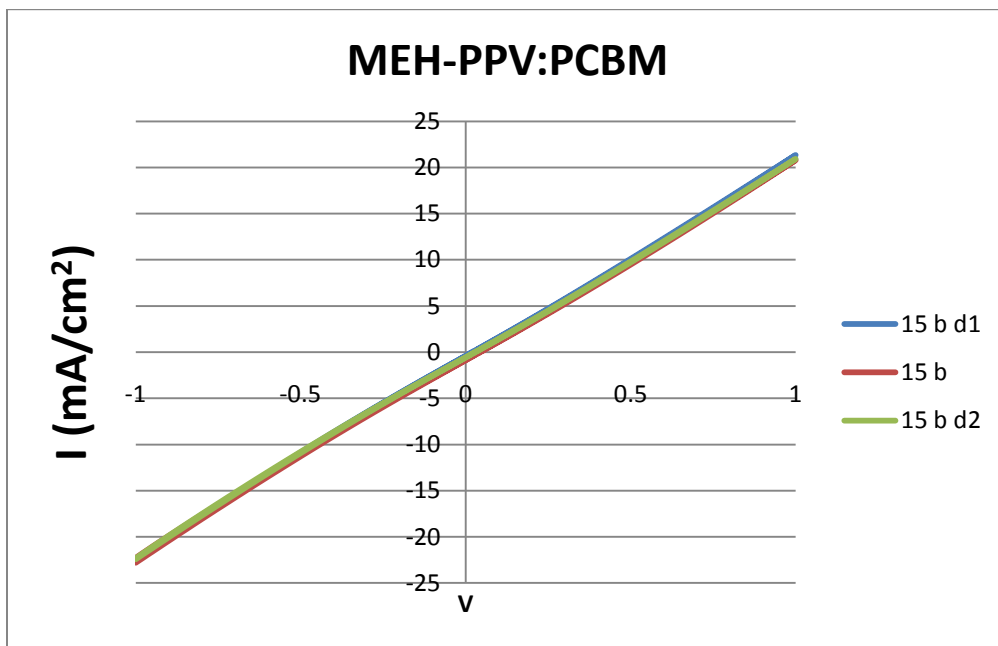












MEH-PPV:PCBM:CNT

